UNIVERSITÄT HAMBURG
DEPARTMENT PHYSIK

Structural Characterization of Hydride Composite Systems for Hydrogen Storage using Synchrotron- and Neutron Radiation Facilities

Dissertation

zur Erlangung des Doktorgrades

des Department Physik

der Universität Hamburg

vorgelegt von

Fahim Karimi

aus Kabul

Hamburg

2018

Angaben zum Promotionsverfahren

Gutachter der Dissertation:	1) Prof. Andreas Schreyer 2) Prof. Thomas Klassen
Gutachter der Disputation:	1) Prof. Andreas Schreyer 2) Prof. Chiara Milanese
Datum der Disputation:	20.07.2018
Vorsitzender des Prüfungsausschusses:	Prof. Michael A. Rübhausen
Vorsitzender des Promotionsausschusses:	Prof. Wolfgang Hansen
Dekan des Fachbereichs Physik:	Prof. Heinrich Graener

Zusammenfassung

Die volumetrische Dichte vom gasförmigen Wasserstoff kann durch dessen Speicherung in Metallhydriden erheblich erhöht werden (von ~ 0,08 kg H_2 / m^3 im gasförmigen Zustand bis zu ~ 150 kg H_2 / m^3 im Metallwirt, chemisch gebunden). Metallhydride übertreffen somit die volumetrischen Dichten von komprimiertem- (40 kg H_2 / m^3) oder flüssigem Wasserstoff (~ 70 kg H_2 / m^3) sowie deren Aspekte der Lagerungssicherheit. Daher sind Metallhydride prädestinierte Kandidaten für emissionsfreie Energiespeichersysteme für mobile Anwendungen. Auf Bor basierte komplexe Leichtmetallhydride sind aufgrund ihrer hohen gravimetrischen- und volumetrischen Wasserstoffspeicherkapazitäten für mobile Anwendungen von besonderem Interesse. Nachteilig für ihre mobile Anwendung ist jedoch ihre hohe Reaktionsenthalpien, die ihre Speichersysteme ungünstig und bisweilen unmöglich machen. Um ihre Reaktionsenthalpien zu verringern, bei Beibehaltung ihre hohen gravimetrischen Wasserstoffkapazitäten, kann additives Metallhydrid mit dem jeweiligen komplexen Hydrid gemischt werden. Während des Dehydrierungsprozesses kann das zusätzliche Metallhydrid das komplex-Hydrid durch eine exotherme Reaktion destabilisieren, was zu einer Reduktion der Gesamtreaktionsenthalpie führen kann. Dieser Ansatz wird als "Reactive Hydride Composite" (RHC) bezeichnet. Tatsächlich könnten auf dieser Weise die Reaktionsenthalpien zahlreiche zusammengesetzte Metallhydride reduziert werden. Die Dehydrierungs-/Rehydrierungsreaktionskinetik von RHCs ist im allgemeinem jedoch sehr langsam. In der vorliegenden Arbeit wurden $LiBH_4$-MgH_2 (Li-RHC) und $Ca(BH_4)_2$-MgH_2 (Ca-RHC), welche die beiden wichtigsten Mitglieder der RHC-Familie mit ihren jeweiligen gravimetrischen Kapazitäten von ~ 11 Gew.% H_2 und ~ 8,4 Gew.% H_2, im Detail untersucht. Durch Zugabe einer geringen Menge von NbF_5 konnte die Dehydrierung/Rehydrierungsreaktionskinetik signifikant verbessert werden. Die Funktionsweise dieses Additives wurde unter Verwendung mehrere experimentelle Methoden in großen Forschungseinrichtungen (wie z.B.: *in-situ*-SR-PXD, EXAFS, SAXS/ASAXS und SANS/USANS)) sowie Labormaßstab-Apparaturen (Sievert-Typ, DSC/DTA, SEM/TEM, MS und NMR) detailliert untersucht. Beide Komposit-Systeme wurden von kristallinen, amorphen und/oder nanoskopischen Strukturen bis hin zu makroskopischen Bereichen strukturell untersucht. Die Kombination, Interpretation und Kondensation der Ergebnisse, die mit Hilfe der oben genannten Methoden gewonnen worden, erlaubten einen Zusammenhang zwischen der Nanostruktur der Komposit Systeme mit und deren Dehydrierungskinetik/Rehydrierungskinetik herzustellen. Weiterhin, wurde der chemische Zustand des Additivs und dessen Größenverteilung bestimmt. Darüber hinaus konnten die Zerfallsprodukte von $Ca(BH_4)_2$ erstmals stabilisiert werden, indem MgH_2 durch Zusatz von Nickel destabilisiert wurde, und somit Mg_2NiH_4 als Destabilisierungsmittel für Ca $(BH_4)_2$ verwendet wurde. Auch wurden zwei neue Syntheseverfahren zur Herstellung von Borid-nanopartikeln gezeigt. Schließlich wurden die RHCs nach ihren spezifischen thermodynamischen Verhaltensweisen in drei Unterklassen eingeteilt: "wechselseitig destabilisiert - RHC" (m-RHC), "single-RHC" (s-RHC) und "additive- RHC (a-RHC).

Die Erkenntnisse aus dieser Arbeit tragen zu einem umfassenden Verständnis der Wirkungsweise von Übergangsmetall-Halogenide auf die Reaktionsmechanismus/Reaktionskinetik bezüglich Wasserstoffaufnahme bzw. Abgabe der Hydrid-Komposit-Systeme bei. Somit dient diese Arbeit als Grundlage bzw. sie bietet eine Orientierung für die zukünftigen Untersuchungen auf diesem Gebiet bzw. von solchen Systemen. Aus dieser Arbeit geht auch einen neuen Destabilisierungspfad hervor, der die thermodynamischen Eigenschaften von RHC-Systemen weiter zu optimieren erlaubt. Darüber hinaus bietet diese Arbeit einen neuen Syntheseweg von Übergangsmetall-Borid-Nanopartikeln, der eine neue Möglichkeit eröffnet die Wirkungsweise dieser Nanopartikeln (auf die Desorption/Absorptionskinetik von RHCs) in Modellsystemen zu untersuchen.

Abstract

Hydrogen stored in metal hydrides improves significantly its volumetric density (from ~ 0.08 kg H_2/ m^3 at gaseous state up to ~ 150 kg H_2/ m^3 chemically bonded in metal host). Metal hydrides also surpass by far volumetric densities of hydrogen stored in compressed form (40 kg H_2/ m^3) or in liquid state (~ 70 kg H_2/ m^3), as well as their storage safety aspects. Therefore, metal hydrides are potential candidates for emission-free energy storage systems in future applications. Boron-based light-weight metal complex hydrides are of particular interest for mobile applications, owing to their high gravimetric hydrogen storage capacities at high volumetric densities. However, their reaction enthalpies are rather high to be applied in mobile storage systems. In order to reduce their reaction enthalpies by maintaining their high gravimetric hydrogen capacities, an additive metal hydride can be mixed with the respective complex hydride. During the dehydrogenation process of the composite system the additive metal hydride can destabilize the complex hydride by an exothermic reaction, leading to an overall reduction of the reaction enthalpy. This approach is termed as "Reactive Hydride Composites" (RHC). Indeed, the reaction enthalpies of numerous hydride composite systems could be reduced by using this destabilization approach. However, the dehydrogenation/rehydrogenation reaction kinetics of RHCs suffers along their reaction paths by various activation barriers.

In the present work, $LiBH_4$-MgH_2 (Li-RHC) and $Ca(BH_4)_2$-MgH_2 (Ca-RHC) were investigated, in detail, which are the two most promising members of boron-based RHC family with their respective gravimetric capacities of ~ 11 wt. % H_2 and ~ 8.4 wt. % H_2. By addition of a small amount of NbF_5, the dehydrogenation/hydrogenation reaction kinetics of both systems was considerably enhanced.

Using several experimental methods at large scale research facilities (synchrotron radiation facilities and neutron research reactor facilities (*in situ* SR-PXD, EXAFS, SAXS/ASAXS and SANS/USANS)) and lab scale apparatus (Sievert type apparatus, DSC/DTA, SEM/TEM, MS, and NMR) enabled characterization of crystalline, amorphous and/or nanoscopic structures in both composite systems from Ångstrom region to nanoscopic range and up to macroscopic sizes. The combination, interpretation and condensation of the results obtained by such reach methods allowed gaining unique insights in to complex interactions between the additives, their chemical states, size distribution and the hydride matrix and their correlations, in turn, with dehydrogenation/hydrogenation kinetics of the systems.

Additionally, for the first time, the decomposition products of $Ca(BH_4)_2$ could be stabilized by destabilizing MgH_2, hence using Mg_2NiH_4 as a destabilization agent for $Ca(BH_4)_2$. Furthermore, two new synthesis methods were proposed to produce transition metal boride nanoparticles and complex borohydrides, respectively. Lastly, the RHCs were organized and divided, according to their specific thermodynamical behaviours, in the following three distinct subclasses: "mutually destabilized-RHC" (m-RHC), "single-RHC" (s-RHC), and "additive-RHC (a-RHC).

Prior to this research less was known about the reasons hidden behind the positive effects of transition metal halides on hydrogen release and uptake kinetics of RHCs. The insights gained by this work contributes to a much deeper understanding of structural effects of transition metal halides with respect to kinetic behaviour of composite systems and, thus, it provides a guidance for upcoming investigations in this field or of hydride composite systems, in general. This work also offers new destabilization route to further optimize the thermodynamic properties of RHC systems. In addition, this thesis provides a new pathway to synthesize transition metal boride nanoparticles, which opens possibilities to study their effects on dehydrogenation/hydrogenation kinetics in RHC model systems and their own properties with regard to other application fields such as super conductivity etc. at the molecular level.

Content

List of publications

1. F. Karimi, P. K. Pranzas, A. Hoell, U. Vainio, E. Welter, V. S. Raghuwanshi, C. Pistidda, M. Dornheim, T. Klassen and A. Schreyer, *Journal of Applied Crystallography*, 2014, **47**, 67-75.
2. F. Karimi, P. Klaus Pranzas, C. Pistidda, J. A. Puszkiel, C. Milanese, U. Vainio, M. Paskevicius, T. Emmler, A. Santoru, R. Utke, M. Tolkiehn, C. B. Minella, A.-L. Chaudhary, S. Boerries, C. E. Buckley, S. Enzo, A. Schreyer, T. Klassen and M. Dornheim, *Physical Chemistry Chemical Physics*, 2015, **17**, 27328-27342.
3. F. Karimi, M. V. C. Riglos, J. Puszkiel, A. Santoru, A. Hoell, C. Milanese, C. Pistidda, P. K. Pranzas,M. Dornheim, T. Klassen and a. A. Schreyer, *submitted to: Journal of Physical Chemistry C*, 2018.
4. F. Karimi, J. Puszkiel, A. Santoru, M. V. C. Riglos, C. Milanese, C. Pistidda, P. K. Pranzas,M. Dornheim, T. Klassen and a. A. Schreyer; To be *submitted to: Journal of Physical Chemistry C*, 2018.
5. F. Karimi, N. Bergemann, A. Santuro, C. Pistidda, C. Milanese, K. P. Pranzas, A. Schreyer, T. Klassen and a. M. Dornheim; *To be submitted to: Journal of Hydrogen Energy*, 2018.
6. F. Karimi, P. K. Pranzas, J. Puszkiel, M. V. C. Riglos, A. Santoru, D. F. Mildner, C. Pistidda, M. Dornheim, T. Klassen and a. A. Schreyer, *To be submitted in: Journal of Nano Energy*, 2017.
7. A. Santoru, C. Pistidda, M. H. Sorby, M. R. Chierotti, S. Garroni, E. Pinatel, F. Karimi, H. Cao, N. Bergemann, T. T. Le, J. Puszkiel, R. Gobetto, M. Baricco, B. C. Hauback, T. Klassen and M. Dornheim, *Chemical Communications*, 2016, **52**, 11760-11763.
8. N. Bergemann, C. Pistidda, C. Milanese, T. Emmler, F. Karimi, A. L. Chaudhary, M. R. Chierotti, T. Klassen and M. Dornheim, *Chemical Communications*, 2016, **52**, 4836-4839.
9. M. Paskevicius, U. Filsø, F. Karimi, J. Puszkiel, P. K. Pranzas, C. Pistidda, A. Hoell, E. Welter, A. Schreyer, T. Klassen, M. Dornheim and T. R. Jensen, *International Journal of Hydrogen Energy*, 2016, **41**, 4159-4167.
10. K. Suarez-Alcantara, M. H. Sørby, C. Pistidda, F. Karimi, I. Saldan, B. C. Hauback, T. Klassen and M. Dornheim, *The Journal of Physical Chemistry C*, 2015, **119**, 11430-11437.
11. J. A. Puszkiel, F. C. Gennari, P. A. Larochette, J. M. Ramallo-López, U. Vainio, F. Karimi, P. K. Pranzas, H. Troiani, C. Pistidda, J. Jepsen, M. Tolkiehn, E. Welter, T. Klassen, J. Bellosta von Colbe and M. Dornheim, *Journal of Power Sources*, 2015, **284**, 606-616.
12. N. Busch, J. Jepsen, C. Pistidda, J. A. Puszkiel, F. Karimi, C. Milanese, M. Tolkiehn, A.-L. Chaudhary, T. Klassen and M. Dornheim, *Journal of Alloys and Compounds*, 2015, **645, Supplement 1**, S299-S303.
13. J. Puszkiel, F. C. Gennari, P. Arneodo Larochette, H. E. Troiani, F. Karimi, C. Pistidda, R. Gosalawit–Utke, J. Jepsen, T. R. Jensen, C. Gundlach, M. Tolkiehn, J. Bellosta von Colbe, T. Klassen and M. Dornheim, *Journal of Power Sources*, 2014, **267**, 799-811.
14. C. Pistidda, F. Karimi, S. Garroni, A. Rzeszutek, C. Bonatto Minella, C. Milanese, T. T. Le, L. H. Rude, J. Skibsted, T. R. Jensen, C. Horstmann, C. Gundlach, M. Tolkiehn, P. K. Pranzas, A. Schreyer, T. Klassen and M. Dornheim, *The Journal of Physical Chemistry C*, 2014, **118**, 28409-28417.
15. C. Pistidda, D. Pottmaier, F. Karimi, S. Garroni, A. Rzeszutek, M. Tolkiehn, M. Fichtner, W. Lohstroh, M. Baricco, T. Klassen and M. Dornheim, *International Journal of Hydrogen Energy*, 2014, **39**, 5030-5036.
16. J. Puszkiel, F. Gennari, P. A. Larochette, F. Karimi, C. Pistidda, R. Gosalawit-Utke, J. Jepsen, T. R. Jensen, C. Gundlach, J. B. von Colbe, T. Klassen and M. Dornheim, *International Journal of Hydrogen Energy*, 2013, **38**, 14618-14630.
17. R. Gosalawit-Utke, C. Milanese, P. Javadian, J. Jepsen, D. Laipple, F. Karimi, J. Puszkiel, T. R. Jensen, A. Marini, T. Klassen and M. Dornheim, *International Journal of Hydrogen Energy*, 2013, **38**, 3275-3282.
18. M. Sale, C. Pistidda, A. Taras, E. Napolitano, C. Milanese, F. Karimi, M. Dornheim, S. Garroni, S. Enzo and G. Mulas, *Journal of Alloys and Compounds*, 2013, **580, Supplement 1**, S278-S281.
19. R. Gosalawit-Utke, C. Milanese, T. K. Nielsen, F. Karimi, I. Saldan, K. Pranzas, T. R. Jensen, A. Marini, T. Klassen and M. Dornheim, *International Journal of Hydrogen Energy*, 2013, **38**, 1932-1942.
20. J. A. Puszkiel, M. V. C. Riglos, F. Karimi, A. Santoru, C. Pistidda, T. Klassen, J. M. B. v. Colbe and a. M. Dornheim; *Journal of Material Chemistry A*, 2017.
21. J. A. Puszkiel, M. V. C. Riglos, J. R. López, M. Mizrahi, F. Karimi, A. Santoru, A. Hoell, F. C. Gennari, P. A. Larochette, C. Pistidda, T. Klassen, J. M. B. v. Colbe and a. M. Dornheim; *Journal of Physical Chemistry Chemical Physics*, 2017.
22. C. Bonatto Minella, E. Pellicer, E. Rossinyol, F. Karimi, C. Pistidda, S. Garroni, C. Milanese, P. Nolis, M. D. Baró, O. Gutfleisch, K. P. Pranzas, A. Schreyer, T. Klassen, R. Bormann and M. Dornheim, *The Journal of Physical Chemistry C*, 2013, **117**, 4394-4403.

23. Le. T. T, C. Pistidda, F. Karimi, S. P. Gharibdoust, B. Richter, C. Milanese, A. Santoru, J. Puszkiel, A. Hoell, J. Skibsted, A. Etsuo, T. Klassen and a. M. Dornheim, *Journal of physical chemistry C* 2018.
24. R. Gosalawit−Utke, T. K. Nielsen, K. Pranzas, I. Saldan, C. Pistidda, F. Karimi, D. Laipple, J. Skibsted, T. R. Jensen, T. Klassen and M. Dornheim, *The Journal of Physical Chemistry C*, 2012, **116**, 1526-1534.
25. P. K. Pranzas, U. Bösenberg, F. Karimi, M. Münning, O. Metz, C. B. Minella, H.-W. Schmitz, F. Beckmann, U. Vainio, D. Zajac, E. Welter, T. R. Jensen, Y. Cerenius, R. Bormann, T. Klassen, M. Dornheim and A. Schreyer; *Advanced Engineering Materials*, 2011, **13**, 730-736.

26. Hujun Cao, Weijin Zhang, Claudio Pistidda, Julián Puszkiel, Chiara Milanese, Antonio Santoru, Fahim Karimi, Maria Victoria Castro Riglos, Gökhan Gizer, Edmund Welter, Jozef Bednarcik, Martin Etter, Ping Chen, Thomas Klassen and Martin Dornheim; *Journal of Physical Chemistry Chemical Physics*, 2017

27. Antonio Santoru, Claudio Pistidda, Matteo Brighi, Michele R. Chierotti, Michael Heere, Fahim Karimi, Hujun Cao, Giovanni Capurso, Anna-Lisa Chaudhary, Gökhan Gizer, Sebastiano Garroni, Magnus H. Sørby, Bjørn C. Hauback, Radovan Černý, Thomas Klassen and Martin Dornheim; *Journal of Inorganic Chemistry*, 2018

28. J. L. Carrillo-Bucio, I. Saldan, C. Pistidda, F. Karimi, K. Suárez-Alcántara, M. Dornheim, and T. Klassen; *The Journal of Physical Chemistry C*, 2017

Lis of presentations

1. Oral presentation at the Gordon Research Conference 2011, (Hydrogen-Metal systems), at Stonehill College (Boston, USA). Title: Structural investigation of RHC by means of Photons and Neutron.
2. Oral presentation at the HASYLAB User Meeting 2012, (Scattering methods in material science), at DESY (Hamburg, Germany). Title: ASAXS investigation of NbF_5 doped $LiBH_4$-MgH_2 and $Ca(BH_4)_2$-MgH_2 composite system.
3. Poster presentation at the International Symposium on Metal-Hydrogen systems conference 2012, at Kyoto (Japan). Title: EXAFS investigation of doped $Ca(BH_4)_2$-MgH_2 composite system for solid-state hydrogen storage
4. Oral presentation at Deutsche Gesellschaft für Materialkunde (DGM) 2013 (German Material Science Society), (Energy Materials), at Darmstadt (Hessen, Germany). Title: Characterization of hydrogen storage materials using scattering and imaging techniques.
5. Poster presentation at BESSY Synchrotron User Meeting 2014, at Berlin (Germany). Title: ASAXS investigation of RHC systems.

1. Motivation and scope of the work

Most of global consumed energy is currently covered by combustion of fossil fuels and by nuclear fission. These energy resources, however, are limited and their massive consumption leads to pollution of our environment. Considering these facts, sustainable and environment friendly ("clean") energy concepts are urgently needed. Use of hydrogen as an energy carrier is one of the most promising possible solutions. This is due to the following facts:

i). Hydrogen is an excellent energy carrier owing to its extremely high energy density per unit mass (33.3 kWh/kg), in comparison to natural gas (13.9 kWh/kg) and liquid fossil fuels (12.4 kWh/kg)[16, 17].

ii). Hydrogen is the most abundance element on the earth (in the universe)

iii). The combustion product of hydrogen is just water: $\mathrm{H_2} + \frac{1}{2}\mathrm{O_2} \rightarrow \mathrm{H_2O} + \mathrm{Energy}$

Using sustainable energy sources such as sun, wind, and biomass etc. for hydrogen production will close an entirely renewable energy circuit. This will help to reduce the anthropogenic environmental pollution drastically. The main reason, why hydrogen is not being applied so far as energy carrier in a wide variety of application fields, is its extremely low volumetric energy density (~0.003 kWh/dm^3) and its low ignition energy (~ 0.02 mJ at hydrogen/air ≈ 29 % volume ratio; a spark is sufficient for ignition) in comparison to gasoline (~9 kWh/dm^3, 0.24 mJ (gasoline vapour)) at normal conditions, for instance.[18] There are basically two classical approaches to enhance the volumetric energy density of gaseous hydrogen:

1) pressurizing it up to ~700 bar at 15 °C (1.2 kWh/dm^3)[19], or
2) liquefying it at cryogenic temperatures (2.4 kWh/dm^3) [19]

Both methods are energy expensive and the safety concepts for respective tanks are not straightforward for on-board application. Therefore, to design safe storage tank systems based on these classical methods requires thick tank walls and/or usage of sophisticated materials, which becomes soon highly cost-intensive and/or heavy, hence unfeasible. An alternative approach is to store hydrogen chemically in metals (metal hydrides). This method significantly improves the volumetric energy density (4.0 kWh dm^{-3}, for $\mathrm{LiBH_4}$)[20] in comparison to aforementioned concepts. Furthermore, the safety concerns are considerably reduced relative to classical storage systems, due to chemical storage of hydrogen in the metallic lattice. Among metal hydrides, light metal hydrides are of especial interest for mobile applications. This is mainly due their high gravimetric hydrogen capacities.

In this work, mixtures of light metal hydrides the so-called "Reactive Hydride Composite" (RHC) systems are the subject of research. In the framework of this investigation the two most important members of this material class are investigated; namely: $\mathrm{2LiBH_4{+}MgH_2}$ (Li-RHC), and $\mathrm{Ca(BH_4)_2{+}MgH_2}$ (Ca-RHC) hydride composite systems with addition of small amount of transition metal halide (TMH) as additive or dopants.

The main focus of this research is directed toward structural characterisation of pure and doped Li-RHC and Ca-RHC systems, respectively. The aim is to draw relationships between structural properties of the investigated RHC systems and their respective kinetic behaviour and to find possible explanations for the function of the used dopants (additives) on the hydrogenation/dehydrogenation kinetics of the RHC systems. Aside this central matter, reaction mechanism, and calorimetrical properties of the pure and doped RHC systems are studied, in some detail. At the borders of the framework of this study, decomposition products of the Ca-RHC system with respect to different thermodynamic conditions are investigated in order to find reaction paths with stabilized decomposition products of the system. To accomplish the objectives of this work, various experimental techniques were used.

Small-Angle scattering (SAS) methods were applied to gain integral information about the micro- and nanostructure of the specimens. Anomalous Small-Angle X-ray Scattering (ASAXS) was used to reveal the size distribution of the additives in the hydride matrices. For the first time, to the best of the author's knowledge, successful ASAXS measurements at the K-edge of calcium in the metal-hydride systems is performed in this work to study the nanostructure of the matrix. (Ultra) Small-Angle Neutron Scattering (USANS/SANS) is applied to investigate micro/nano structure of the pure and doped Li-RHC matrix. X-ray Absorption Spectroscopy is used to study chemical state and local environment of the additive in the hydride matrices. Transmission Electron Microscopy (TEM), Scanning Electron Microscopy (SEM), and Electron Dispersion Spectroscopy (EDS) methods were applied to probe locally the morphology of the specimens. Nuclear Magnetic Resonance (NMR) was used to determine the chemical state of the low atomic number elements that were not detectable with other methods due to their nano-crystalline/amorphous nature.

In situ Synchrotron Radiation Powder X-ray Diffraction (SR-PXD), Differential Scanning Calorimetry (DSC), Differential Thermal Analysis (DTA), and Mass spectrometry (MS) were used to characterize the reaction mechanism of the pure and doped RHC systems.

2. Theory

2.1. Metal hydrogen interactions

The interaction between hydrogen molecules and metals proceeds in several steps. By approaching the surface of a metal, hydrogen molecules interact with the metal *via* Van der Waals force (VWF) (typical strengths of VWF are in the range of 0.4-6 kJ/mol interacting in distances between 0.3 and 0.6 nm). This state is the so called "physisorbed state" of the molecular hydrogen in the hydrogen-metal system. After passing an activation-barrier toward the metal surface the dissociation of molecular hydrogen takes place, due to the electronic interaction of the hydrogen molecules with the metal atoms. This stage of interaction is the so-called "chemisorbed state" of hydrogen in the hydrogen-metal system. Subsequently, atomic hydrogen can diffuse through the sub-layers of metallic surface into the host lattice.

At the initial state of chemisorption (at constant temperature T), where the ratio of metal-to-hydrogen (M/H) is relative small (M/H < 10 %), hydrogen atoms are dissolved in the metal (solid solution: α-phase). According to the Gibbs phase rule:

$$F = 2 + N - P \tag{1}$$

Where F is the degree of freedom of the system, N corresponds to number of involved species in the system (here metal and hydrogen) and P is number of present phases in the system (here: gaseous hydrogen and α-phase). The hydrogen-metal system has therefore 2 degrees of freedom. Thus, both, partial hydrogen pressure and the α-phase rise by increasing the onset hydrogen pressure of the system. Conversely, this leads to an expansion of the metallic unit cell by roughly ~ 2-3 Å [21] and at a certain concentration of M/H it is energetically favourable for the metal-hydrogen system to form the metal hydride phase (β-phase) with a higher M/H concentration. At this stage α- and β-phase coexist, and therefore the system gains an additional phase on the expense of the loss of a degree of freedom ($F = 2 + N(2) - P(3) = 1$). Therefore, further increase of the applied hydrogen pressure leads to growing hydride phase. Hence, this region of the coexistence of α-phase and β-phase is marked by the so called "plateau-pressure", and is characterized by equilibrium between the gaseous hydrogen ($H_{2(g)}$), pure metal ($Me_{(s)}$) and metal in the β-phase ($Me\beta_{(s)}$):

$$H_{2(g)} + Me_{(s)} \leftrightarrows Me\beta_{(s)} \tag{2}$$

The width of the plateau gives an idea about the stored hydrogen and its position provides information about stability of the hydride phase (at a given temperature). After exhausting of the β-phase and fading of the α-phase, the hydrogen-metal system is reduced by a phase but then again it gains an additional degree of freedom. Hence, the subsequent increase of applied hydrogen pressure leads to, simultaneously, dissolving hydrogen in the β-phase and abrupt rising of the partial hydrogen pressure in the hydrogen-metal system. These processes can be measured by the method of so called "Pressure-Composition-Isotherm" diagram (PCI-diagram). From the measured PCI-curves the thermodynamic quantities such as enthalpy and entropy changes of a given system can be experimentally determined by using Van't Hoff equation. Due to the importance of Van't Hoff equation for the Metal-Hydrogen systems, in the following a simple derivation of this equation is given.

2.2. Thermodynamics of metal hydrides

It can be shown, that the chemical potential of one component system is given by:

$$\mu(T,p) = \mu_{i,0} + k_B T \, ln(a) \tag{3}$$

Where, a, describes the activity of the material under non-ideal conditions, and it is determined by measuring the chemical potential with respect to a standard state ($\mu_{i,0}$):

$$a = exp\left(\frac{\mu - \mu_{i,0}}{k_B T}\right) \tag{4}$$

Using the chemical potentials above for the hydrogen gas, metal and metal hydride phases in the law of mass action one finds the heterogeneous equilibrium of the metal-hydrogen system by:

$$\Delta G = \Delta G_{Me\beta} - \left(\Delta G_{H_2} + \Delta G_{Me}\right) = -RTln\left(\frac{a_{Me\beta}}{a_{Me}(p/p_0)}\right) \tag{5}$$

Since the solids don't change their concentration in a heterogeneous reaction, their activity coefficients are set to be one ($a_{Me} = 1; a_{Me\beta} = 1$) and equation (5) can be rewritten as:

$$\Delta G = -RTln\left(\frac{p_0}{p}\right) = RTln\left(\frac{p}{p_0}\right) \tag{6}$$

Where ΔG states for the standard Gibbs energy of formation, which is defined as:

$$\Delta G = \Delta H - T\Delta S \tag{7}$$

Here, ΔH and ΔS are the standard enthalpy and standard entropy of formation, respectively. Combination and rearrangement of the equations (6) and (7) leads to:

$$ln\left(\frac{p}{p_0}\right) = \frac{\Delta H_f^0}{RT} - \frac{\Delta S_f^0}{R} \tag{8}$$

This equation is the so called "Van't Hoff equation", which allows the experimental determination of standard enthalpy and standard entropy of formation of a metal-hydrogen system. Measuring the plateau pressure at minimum three different isothermal conditions, and logarithmic plotting of the plateau pressure versus the reciprocal temperature (1/T) gives a straight line. The slope and the intercept of the Van't Hoff plot correspond to standard enthalpy and standard entropy of formation, respectively. The value of formation of enthalpy mirrors the strength of the metal-hydrogen interaction in the hydride phase. For all metal hydrides the change in standard entropy of formation is approximately $\Delta S_f^0 = 130\ \mathrm{J\ K^{-1}mol^{-1}}$ which is comparable to the standard entropy of hydrogen ($S_{H_2}^0 = 130\ \mathrm{J\ K^{-1}mol^{-1}}$). This is not surprising; since the entropy term bares the amount of all information which includes all micro states that are needed to characterize the most probable macro state of the system at given conditions. By the formation of a hydride phase, only the gaseous molecular hydrogen loses the most significant degree of information in the system, therefore, the change in entropy for all metal hydride systems are distributed around a specific value.

2.3. Hydride forming elements

Numerous elements in the periodical system of elements (PSE) build binary compounds with hydrogen which are termed as hydrides. The hydrides are divided and distinguished by the nature of their chemical bonds (see Figure 1). All Alkaline- and Alkaline earth metals form ionic hydrides (saline hydride), except MgH_2 and BeH_2. Both of them exhibit partially ionic and partially covalent bonds, respectively.[22,23] Ionic hydrides are thermally stable and forming solids with high melting- and boiling point. The elements of the third to seventh main group in the PSE form covalent hydrides.

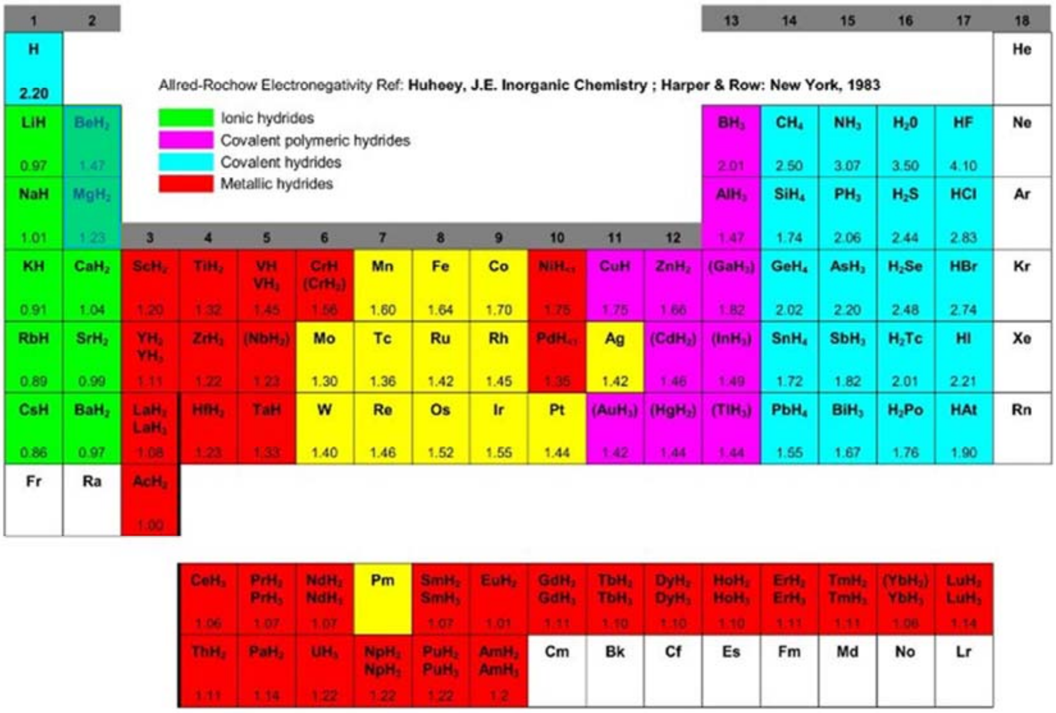

1	2	3	4	5	6	7	8	9	10	11	12	13	14	15	16	17	18
H 2.20																	He
LiH 0.97	BeH_2 1.47											BH_3 2.01	CH_4 2.50	NH_3 3.07	H_20 3.50	HF 4.10	Ne
NaH 1.01	MgH_2 1.23											AlH_3 1.47	SiH_4 1.74	PH_3 2.06	H_2S 2.44	HCl 2.83	Ar
KH 0.91	CaH_2 1.04	ScH_2 1.20	TiH_2 1.32	VH VH_2 1.45	CrH (CrH_2) 1.56	Mn 1.60	Fe 1.64	Co 1.70	$NiH_{<1}$ 1.75	CuH 1.75	ZnH_2 1.66	(GaH_3) 1.82	GeH_4 2.02	AsH_3 2.20	H_2Se 2.48	HBr 2.74	Kr
RbH 0.89	SrH_2 0.99	YH_2 YH_3 1.11	ZrH_2 1.22	(NbH_2) 1.23	Mo 1.30	Tc 1.36	Ru 1.42	Rh 1.45	$PdH_{<1}$ 1.35	Ag 1.42	(CdH_2) 1.46	(InH_3) 1.49	SnH_4 1.72	SbH_3 1.82	H_2Tc 2.01	HI 2.21	Xe
CsH 0.86	BaH_2 0.97	LaH_2 LaH_3 1.08	HfH_2 1.23	TaH 1.33	W 1.40	Re 1.46	Os 1.52	Ir 1.55	Pt 1.44	(AuH_3) 1.42	(HgH_2) 1.44	(TlH_3) 1.44	PbH_4 1.55	BiH_3 1.67	H_2Po 1.76	HAt 1.90	Rn
Fr	Ra	AcH_2 1.00															
			CeH_3 1.06	PrH_2 PrH_3 1.07	NdH_2 NdH_3 1.07	Pm	SmH_2 SmH_3 1.07	EuH_2 1.01	GdH_2 GdH_3 1.11	TbH_2 TbH_3 1.10	DyH_2 DyH_3 1.10	HoH_2 HoH_3 1.10	ErH_2 ErH_3 1.11	TmH_2 TmH_3 1.11	(YbH_2) YbH_3 1.06	LuH_2 LuH_3 1.14	
			ThH_2 1.11	PaH_2 1.14	UH_3 1.22	NpH_2 NpH_3 1.22	PuH_2 PuH_3 1.22	AmH_2 AmH_3 1.2	Cm	Bk	Cf	Es	Fm	Md	No	Lr	

Allred-Rochow Electronegativity Ref: **Huheey, J.E. Inorganic Chemistry ; Harper & Row: New York, 1983**

🟩 Ionic hydrides
🟪 Covalent polymeric hydrides
🟦 Covalent hydrides
🟥 Metallic hydrides

Figure 1. Periodical system of elements and their respective hydrides.[24]

They are mostly non-metal-hydrogen compounds and exist under normal conditions in the liquid or in the gaseous state. With some exception (*e. g.* water (H_2O), this is due to adapted hydrogen bonds), the covalent hydrides have usually low melting- and boiling point. Metallic hydrides are formed by interaction of hydrogen with transition metals (TMs) or inner transition metals (lanthanides and actinides). The hydrogen exists in the TMs lattice as a donator (H^+) to the Fermi see of the TMs. Therefore, they show the typical characteristics of TMs such as conductivity, hardness, magnetic properties and lustre. With exception of americium hydride (AmH_2), europium hydride (EuH_2) and uranium hydride (UH_3), metallic hydrides cannot be strictly termed as compounds, because TMs don't react stoichiometric with hydrogen but they form a large range of nonstoichiometric compounds.

2.4. Metal hydrides

All the metal-hydrogen systems are named as metal hydrides (or for simplicity just "hydrides"). Depending on the chemistry of metal hydrides, they can be classified in, at least, four groups: non-interstitial binary hydrides, interstitial binary hydrides, intermetallic hydrides and complex hydrides. These groups are defined further in detail in the following subsections.

2.4.1. **Non-interstitial binary hydrides**

Non-interstitial hydrides are basically all the binary hydrides (only one metal-hydrogen system) of the main groups. They have either ionic or covalent bonds. However, for hydrogen storage in mobile application only the light metal-hydrogen systems are of importance. Hence, the focus on metal hydrides of interest can be reduced to the first three rows of alkaline- and alkaline earth metals. Since, LiH, NaH, KH and CaH_2 are all ionic in nature; their thermal stabilities are consequently rather high and beryllium is highly toxic to be considered as reversible hydrogen storage media for mobile applications. Thus, only remaining candidate of the non-interstitial hydride group is MgH_2. Fortunately it has an intermediate bond character between ionic and covalent, so that its thermal stability is significantly reduced in comparison to all other light metal hydrides. Therefore, MgH_2 is considered as one of the most promising reversible hydrogen storage materials for mobile applications.[25] Therefore, the following subsection is dedicated to present some properties of MgH_2 in more detail with respect to hydrogen storage.

2.4.1.1. Magnesium hydride (MgH_2)

In addition to those advantages mentioned in the previous section magnesium is also one of the most abundance light metals on the earth.[26] Furthermore, MgH_2 shows the highest gravimetric hydrogen content (7.6 wt. %, and thus the highest energy density (9 MJ/kg of Mg)) among the metal hydrides and its volumetric density (106 kgH_2/m^3) is approximately twice high than the liquid hydrogen (70 kg H_2/m^3) [27-30]. MgH_2 condenses under normal condition in tetragonal crystal structure (α-polymorph of MgH_2 (space group $P4_2/mnm$)), and under pressure it transforms to γ-MgH_2, β-MgH_2, and δ-MgH_2 with the corresponding crystal structures of orthorhombic (*Pbcn*), cubic (space group *Pa-3a*) or orthorhombic HP1 with the space group $Pbc2_1$ and orthorhombic (space group *Pbca*), respectively. [29, 31-37] The thermodynamic properties of MgH_2 have been investigated by several groups, and the average desorption enthalpy and entropy values at 1 bar H_2, determined by van't Hoff relation; reported are -76 kJ mol^{-1} H_2 and 138 J (K^{-1} mol^{-1} H_2) at 300-350 °C [7, 28, 38-44]. The enthalpy value (-76 kJ mol^{-1} H_2) of MgH_2 is too high to be used for on board applications. The ideal enthalpy value needed for mobile applications has to be in the range of 25-45 kJ mol^{-1} H_2, in order to meet the DOE targets for mobile applications.[45-47] At the present, storage of renewable energies (solar energy, for instance) [48] is one of the major tasks to be solved in order to take a big step forward toward a green energy era. MgH_2 is therefore well suited to store high amount of energy (~ 0.9 kWh (kg^{-1} Mg), according to:

$$\mathrm{MgH_2} + 75\ \mathrm{kJ}\ (\mathrm{mol^{-1}\ H_2}) \rightarrow^{\text{Energy storage}} \leftarrow_{\text{Energy release}} \mathrm{Mg} + \mathrm{H_2} \qquad (9)$$

The solar energy can be stored *via* photovoltaic plates during the summer and the stored heat can be used during the winter to warm up the house, for instance. Moreover, it can be stored in a very interesting temperature range (300 - 500 °C) with respect to hydrogen pressure. In this temperature range the heat energy can be transformed more effectively to mechanical or electrical energy.[49] Despite these positive aspects of MgH_2, with respect to the energy storage sector, its reversible hydrogen sorption kinetic is rather slow for being used in a broad application range. Numerous additives were investigated to overcome this kinetic obstacle of the MgH_2-Mg system. [50, 51] Among them Nb_2O_5 showed the best de/rehydrogenation kinetic performance of MgH_2, [52-56] which provides a base to use it in a wide range of applications.

2.4.2. Interstitial binary hydrides (metallic hydrides)

All transitions metals, with the exception of the copper- and zinc group, form binary hydrides which are termed to be interstitial hydrides or metallic binary hydrides. In these hydrides, hydrogen is stored either in tetrahedral or in octahedral interstitial sites of the transition metal. Due to occupancy of hydrogen in the interstitial sites of the metal lattice, the unit cell of the host metal expands gradually with the hydrogen concentration in the metal. Exceptions to this rule are some rare earth metal hydrides in which their unit cell decreases with occupancy of hydrogen in the interstitial sites (lanthanide contraction).[57-59] In the following subsection two prominent interstitial hydrides are presented in some detail.

2.4.2.1. Yttrium hydride (YHx) and palladium hydride (PHx)

Interstitial metals cannot strictly be termed as chemical compounds. This is due to their continuous hydrogen absorption through the transition metals. They are rather called "non-stoichiometric" metal hydrides MH_x, where x can vary between 0 and 3(exception to this are: AmH_2, EuH_2 and UH_3). This feature of non-stoichiometric metallic hydrides -continuous absorption of hydrogen- leads to a series of interesting physical properties of them. For instance, a thin film of YH_2 changes its metallic property through the hydrogenation reaction to a semiconductor by reaching the YH_3. Correspondingly, the optical properties of the thin film changes from entirely reflecting mirror to a transparent window.[60] This is due to change in the electronic band gape of the metallic YH_2. The transparency of Pd coated yttrium window occurs not gradually but is a complex function of incident photon energy and concentration of hydrogen in the interstitial sites of yttrium metal. Another noticeable interstitial hydride system is the Pd-H system, which has been widely investigated in the past and it is perhaps the best investigated metal hydride system, so far.[61] PdH_x can be formed under atmospheric hydrogen pressure at room temperature conditions (observed 1866 by Thomas Graham).[62] As the molecular hydrogen approaches the surface of Pd it dissociates with almost no activation barrier.[63, 64] After dissociation of molecular hydrogen, the atomic hydrogen is absorbed in the interstitial octahedral sites of the fcc-lattice of Pd. Therefore, PdH_x has a high volumetric hydrogen capacity, in comparison to gaseous, compressed or liquid hydrogen. Furthermore, due to its outstanding dissociative possessions Pd is also widely used as a catalyst for hydrogen sorption reactions, hydrogen purification, hydrogen sensors, and in electrocatalyst in low temperature fuel cells.[65-69]

2.4.3. Intermetallic hydrides

In 1958 Libowitz *et al.* [70] could reversibly hydrogenate, for the first time, the binary intermetallic compound (ZrNi). In the following years a bunch of new intermetallic hydrides were published.[71] Before proceeding, the difference between intermetallic compounds and alloys should be clarified. In the case of alloys the constituents have a continuous composition range (*e.g.*: in the case of a binary alloy, composed of constituents A and B, they can form an alloy of $A_{1-x}B_x$ whereby, $x \in]0\,;1[$), whereas intermetallic compounds have only certain composition (in the case of a binary intermetallic compound, composed of constituents A and B, they can only form: AB, AB_2, AB_3, AB_5, for instance). The so called pseudo-Laves phases of intermetallic compounds can interestingly have even higher volumetric hydrogen density (120 g/L) in comparison to liquid hydrogen (71 g/L).[72] As a prominent example of intermetallic hydrides, in the following Mg_2NiH_4 is presented in some detail.

2.4.3.1. *Magnesium-Nickel-hydride (Mg_2NiH_4)*

The drawback of MgH_2 as hydrogen storage material for mobile application is its high thermodynamic stability, as was pointed out in subsection 2.3.1.1. In year 1968 Reily and Wiswall [42] published a work on reversible hydrogen uptake and release of Mg_2Ni alloy by the following reaction:

$$\mathrm{Mg_2Ni + 2H_2 \leftrightarrow Mg_2NiH_4} \qquad (10)$$

By method of PCI (Pressure-Composition-Isotherm) they could determine the enthalpy value of reaction (10) to be -64.5 kJ / mol H_2, which is 11.5 kJ / mol H_2 lower in comparison to the value of pure MgH_2. Therefore, Mg_2NiH_4 decomposes, depending on the dopant, in the temperature range of 200-250 °C under static vacuum condition.[73, 74] However, the gravimetric hydrogen capacity is dropped down to 3.6 wt. %, due to the addition of a heavy element. The idea behind the destabilization of stable metal hydrides is to alloy two metals which form separately highly unstable metal hydrides (such as NiH_2) and relative stable metal hydrides (such as MgH_2), respectively. The resulting enthalpy of formation of such ternary hydrides can be described by the rule of Miedema.[75] Beside reaction (10), there are two alternative ways to synthesize $MgNiH_4$. This can be done either through mechano-synthesis by ball milling (BM) under nitrogen atmosphere or by using solid-state high-pressure synthesis (HPS): [76, 77]

$$\mathrm{2MgH_2 + Ni \xrightarrow{BM,HPS} Mg_2NiH_4} \qquad (11)$$

Depending on the synthesize method, (11) can produce either low-temperature (LT) phase or high-temperature (HT) phase of Mg_2NiH_4. The LT-phase of Mg_2NiH_4 at 1bar of H_2 atmosphere starts to transform roughly above 250 °C into a cubic structure HT-phase. Besides Mg_2NiH_4, Mg-Ni system can form further hydride phases $Mg_xNi_yH_z$, with compositions such as $Mg_2NiH_{0.3}$, $Mg_6Ni_3H_{0.9}$, and $MgNi_2H_{3.2}$.[78-80]

2.4.4. **Complex hydrides**

In 1997 Bogdanović and Schwickardi reported successful reversible hydrogen storage in the catalysed complex metal hydride ($NaAlH_4$).[81]

$$\mathrm{NaAlH_4 \leftrightarrow NaAl_3H_6 + H_2 \leftrightarrow NaH + Al + 3H_2} \qquad (12)$$

Since then numerous complex metal hydrides were investigated as potential hydrogen storage materials.[17, 82]. Light complex metal hydrides are especially suited for hydrogen storage in mobile applications. This is, especially, due to their high gravimetric hydrogen capacities. Since boron is the lightest hydrogen forming complex ($[BH_4]^-$) it has the highest gravimetric hydrogen storage capacity, when combining with alkaline- or alkaline earth metals. In particular Li^{+1}, Na^{+1}, K^{+1} from the alkaline metal group and Mg^{+2} and Ca^{+2} (Beryllium is not considered, due to its toxicity) from the alkaline earth metals are outstanding candidates for the formation of high capacity complex hydrides.[83] The group of $[BH_4]^{-1}$ is known as tetrahydroborates group or more commonly as the group of borohydrides. Schlesinger *et al.* [84-86] reported during 1940-1953 for the first time successful synthesis of borohydrides. Among the borohydrides $LiBH_4$ and $Ca(BH_4)_2$ posse the most interesting characteristics as hydrogen storage material. They have relative high gravimetric hydrogen capacities ($LiBH_4$:18.5 wt. % and $Ca(BH_4)_2$: 10.5 wt. %) which are far above the target established by the DOE (6.0 wt. % for 2010 and 9.0 wt. % for 2015; wt. % expressed as kg H_2/kg System).[87] Moreover, they show high volumetric energy content (3.8 kWh dm^{-3} and 4.6 kWh dm^{-3}) than liquid hydrogen (2.37 kWh dm^{-3}), hydrogen at 20 MPa (0.53 kWh dm^{-3}) and natural gas at 20 MPa (2.3 kWh dm^{-3}).[82] Therefore in the following subsections some more light is shed on these complex borohydrides.

2.4.4.1. *Lithium borohydride ($LiBH_4$)*

Lithium borohydride's enthalpy of formation at room temperature from its elements is approximately -194 kJ / mol BH_4.[88, 89] It undergoes by increasing temperature a structural phase transformation from orthorhombic symmetry (*Pnma* space group) to hexagonal symmetry at 380 K (107 °C) (*$P6_3mc$* space group) and its physical phase transformation accrues at 550 K (277 °C) from solid to liquid before liberating the hydrogen content above 700 K (427 °C).[20, 82, 90] The only decomposition product of $LiBH_4$ which could be detected *via* XRD is LiH.[91] The state of boron, however, was not detectable (*via* XRD) hinting to its amorphous/nanocrystalline structure after decomposition of $LiBH_4$. By using first principle calculation Ohba *et al.*[92] and by means of DFT calculation Ozolins *et al.*[93] determined, respectively, $Li_2B_{12}H_{12}$ to be one of the most stable intermediate compounds upon dehydrogenation of $LiBH_4$. Though, Ozolins *et al.* [93] claimed that their structure of $Li_2B_{12}H_{12}$ is by 7 k J mol^{-1} H_2 energetically favourable than the one reported in the following reference.[92] The existence of $Li_2B_{12}H_{12}$ as being an intermediate compound upon desorption of $LiBH_4$ was shown experimentally by Orimo *et al.* [94] and Hwang *et al.*[95] Ohba *et al.* [15] calculated the minimum enthalpy of formation of the following equation with δ being the mol fraction of H_2:

$$(1-\delta)[\mathrm{LiH}+\mathrm{B}]+\delta\mathrm{H}_2 \rightarrow \frac{1-\delta}{x}\mathrm{LiB}_x\mathrm{H}_y + \frac{(1-\delta)(x-1)}{x}\mathrm{LiH} \qquad (13)$$

With $\delta = (y-1)/(2x+y-1)$ and $x \geq 1$. They have found $Li_2B_{12}H_{12}$ to be the most stable intermediate phase among all other possible phases along the sorption reaction path of $LiBH_4$. Therefore, the desorption reaction paths of $LiBH_4$ can be described by the following reaction steps:

$$\mathrm{LiBH}_4 \leftrightarrow 1/12\mathrm{LiB}_{12}\mathrm{H}_{12} + 5/6\mathrm{LiH} + 13/12\mathrm{H}_2 \leftrightarrow \ \mathrm{LiH} + \mathrm{B} + 3/2\mathrm{H}_2 \qquad (14)$$

Furthermore, during dehydrogenation of $LiBH_4$ highly toxic boranes can be formed. [82, 96] A rehydrogenation of the final dehydrogenated product is reported to occur only above 650 °C and at 15 MPa of hydrogen pressure. [91, 97] These, properties of $LiBH_4$ make its use challenging for mobile applications.

2.4.4.2. Calcium borohydride $Ca(BH_4)_2$

Calcium borohydride's enthalpy of formation from its elements is -142 kJ / mol BH_4 [98]. It bares three polymorphs (α, β and γ-$Ca(BH_4)_2$) at room temperature. Upon heating at roughly 125 °C the polymorphic phase transformation of α-$Ca(BH_4)_2$ and γ-$Ca(BH_4)_2$ to more stable β-$Ca(BH_4)_2$ takes place. [99, 100] The β-$Ca(BH_4)_2$ starts to release hydrogen at about 350 °C. The dehydrogenation reaction can progress along several possible reaction paths. These possible reaction paths are listed in Table 1.

Table 1. Possible reaction paths and the corresponding theoretical enthalpies of dehydrogenation reaction of $Ca(BH_4)_2$. In reaction 4 the compound $CaB_{12}H_{12}$ has several polymorphs with, respectively, different reaction enthalpy values (from reference [101])

#	**Reaction**	**Cell volume [Å^{-3}]/ f.u**	**ΔH (0 K) in kJ/mol H_2**
1	$Ca(BH_4)_2 \rightarrow Ca + 2B + 4H_2$		83.3
2	$Ca(BH_4)_2 \rightarrow CaH_2 + 2B + 3H_2$		56.1
3	$Ca(BH_4)_2 \rightarrow \frac{2}{3}CaH_2 + \frac{1}{3}CaB_6 + \frac{10}{3}H_2$		37.9
4	$Ca(BH_4)_2 \rightarrow \frac{1}{6}X_i = (CaB_{12}H_{12}) + \frac{5}{6}\,CaH_2 + \frac{13}{6}\,H_2$		
(4a)	$X_1 =$ C2/m-50	216.45	39.1
(4b)	$X_2 =$ P2-50	233.15	36.9
(4c)	$X_3 =$ Pm-100	243.56	37.7
4d	$X_4 =$ C2/m-100	231.13	36.5
4e	$X_5 =$ Pm-100	237.97	36.9
4f	$X_5 =$ P1-100	233.37	36.3
4g	$X_5 =$ C2/c-100	231.74	35.8

Reaction (4) (Table 1) shows the decomposition of $Ca(BH_4)_2$ in to CaH_2, H_2 and to calcium *dodeca-closo-borane* ($CaB_{12}H_{12}$). Wang *et al.*[101] calculated a group of possible $CaB_{12}H_{12}$ polymorphs which are competitive, regarding their enthalpy values, with the reaction path (3). By variation of the mol fraction δ of the molecular hydrogen (similar to formula 2-11 for $LiBH_4$) in CaH_2+B and CaH_2+CaB_6, , respectively, Wang *et al.*[101] could determine the enthalpy of formation for a series of CaB_xH_y compounds. Due to fairly high stability of $CaB_{12}H_{12}$ not all of hydrogen capacity of $Ca(BH_4)_2$ can be reversibly exhausted at moderate conditions. Using Nucleus Magnetic Resonance technique (NMR), the existence of $CaB_{12}H_{12}$ was also experimentally confirmed by Minella *et al.*[102] Over the de/rehydrogenation process the stable desorption products ($CaB_{12}H_{12}$ and amorphous boron) accumulate and do not participate in the hydrogenation cycle. Thus the system leads with cycling to irreversible final state.

2.5. Method of reactive additives

In the year 1967, the method of reactive additives (alloying) of single-phase metal hydrides was reported in order to modify their thermodynamic stability. [29, 42, 103-108]

$$aA_xB_y + bH_2 \leftrightarrow cA_vH_z + dA_nB_m \qquad (15)$$

This approach is schematically displayed in Figure 2.

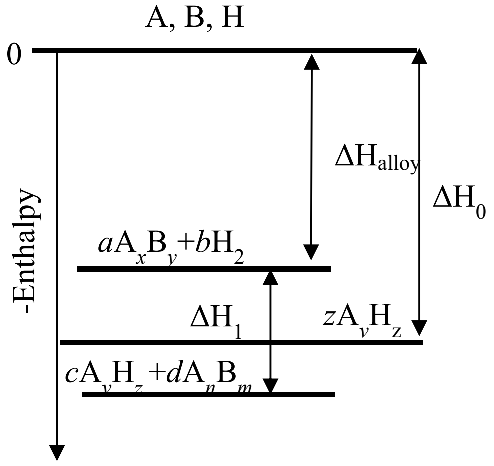

Figure 2. Schematic illustration of destabilization of a metal hydride by reactive additive method.

This concept takes advantage of an alloy which has two different stable states in the hydrogenated and dehydrogenated state, respectively. The additive dA_nB_m forms during the dehydrogenation process of the metal hydride (cA_vH_z) another stable alloy (aA_xB_y). Hence, the endothermic process of dehydrogenation (ΔH_0) is partially compensated by the exothermic formation of the alloy (aA_xB_y) (ΔH_{alloy}), which leads to an overall reduction of the reaction enthalpy (ΔH_1). With other words: the dehydrogenation product of the metal hydride (cA_vH_z) is stabilized by the formation of a more stable alloy (aA_xB_y), in comparison to the element (A). Reilly *et al.* [107, 109] used this approach, for the first time, to stabilize the reaction product of MgH_2 by using $MgCu_2$ as a reactive additive (see reaction (16)).

$$3Mg_2Cu + 3H_2 \leftrightarrow 3MgH_2 + MgCu_2 \qquad (16)$$

Two other prominent examples of this destabilization concept are:[110, 111]

$$Mg_2Si + 2H_2 \leftrightarrow 2MgH_2 + Si \qquad (17)$$

$$Mg_2Al_3 + 2H_2 \leftrightarrow 2MgH_2 + 3Al \qquad (18)$$

Whereby, reactions (17) and (18) have less stable hydrogenated states due to the elemental presence of the alloying metal in comparison to reaction (16). The main drawback of this method is the non-ability of the additive to absorb hydrogen, which significantly reduces the total gravimetric hydrogen capacity of the system. The method of destabilization by alloying circumvents this obstacle, and it is the subject of the following subsection.

2.6. Method of destabilization by alloying

In order to optimize the gravimetric hydrogen capacity of the system, it is favourable to find an alloy which in turn forms a hydride phase in the hydrogenated state:

$$a\mathrm{A}_x\mathrm{B}_y + b\mathrm{H}_2 \leftrightarrow \mathrm{cA}_d\mathrm{B}_e\mathrm{H}_f \tag{19}$$

The scheme of this concept is presented in Figure 3. Due to the removal of the additional weight of the non-hydrogen containing additive, the overall hydrogen capacity is increased and at the same time the enthalpy of the system is reduced.

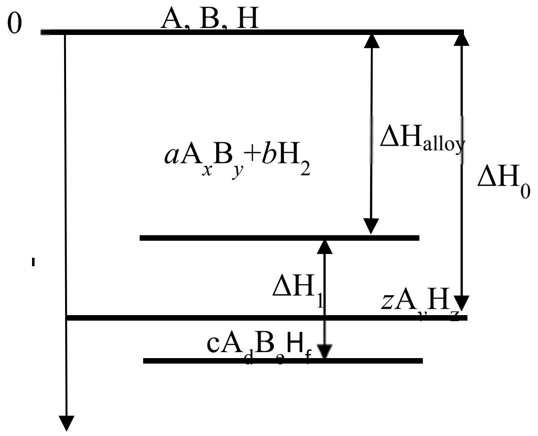

Figure 3. Illustration of destabilization of a metal hydride by alloying.

A prominent example of this concept is the Mg-Ni-H system: [42]

$$\mathrm{Mg_2Ni} + 2\mathrm{H_2} \leftrightarrow \mathrm{Mg_2NiH_4} \tag{20}$$

The dehydrogenation reaction of $\mathrm{Mg_2NiH_4}$ proceeds at much lower temperatures in comparison to $\mathrm{MgH_2}$, as was discussed in subsection 2.3.3. Also this method has the disadvantage of reducing the overall hydrogen capacity of the system due to the additional mass of the alloying element.

2.6.1. Method of destabilization by partial cation/anion substitution

A theoretical investigation, performed by Nakamori *et al.*[112] on the stability of borohydrides revealed a linear dependency between the heat of formation ($\Delta\mathrm{H}_{\mathrm{Me(BH_4)_2}}$) of $\mathrm{Me(BH_4)_2}$, where Me stands for a metal, and their Pauling number.

$$\Delta H^{f}{}_{Me(BH_4)_2}\;[\,kJ(mol\,BH4)^{-1}\,] = 248.7\,\chi_p - 390.8 \qquad (21)$$

The same research group delivered, soon after their theoretical predictions, the experimental evidence of the stability of borohydrides based on the proportionality between the enthalpy of formation and the Pauling number of electronegativity by measuring the decomposition temperatures of the borohydrides. These results gave a new guideline for alteration of the stability of complex hydrides by partially substitution of either cation or anion side of the complex compounds. The prior strategy led to investigation of a bunch of bimetallic complex hydrides. In particular the group of bialkali alanates showed some alteration in their thermodynamic behaviour.[113-121] Also some correlation between the thermodynamic stability of bialkali complex hydrides and their structural properties was reported [122]. The studies of Rude *et al.* [123] and other researchers [112, 117, 124], on the other hand, showed that the average desorption temperatures of the bialkali metal borohydrides are approximately the same as for monoalkali metal borohydrides. Efforts have been taken to substitute partially the anion side of the complex metal hydrides by halides in order to modify their thermodynamic properties. Partial anion-substitution in the complex borohydrides systems were achieved by chloride, bromide and iodide. [125-127] Theoretical calculations based on density functional theory (DFT) predicted also a fluorine anion substitution. [128, 129] However, no evidence of H^--anion substitution by F^--anion could be observed by experimental results of Pranzas *et al.*[130] and others.[131-133] Their experimental results indicate that the addition of fluorine (*via* transition metal fluorides) in the complex hydrides leads, during mechanicomilling or upon de/rehydrogenation cycling, to stable alkaline/earth alkaline metal fluoride species. Therefore the impact of transition metal fluorides on the decomposition kinetics of complex metal hydrides is yet unclear. In conclusion, the stability of the complex metal hydrides and their intermediate products precludes the reversible reaction with hydrogen at moderate temperatures and pressures. So far, many attempts have been made to face the poor thermodynamic properties (reversibility) and sluggish material kinetic of the system.[134-136] In the following section the concept of reactive hydride composite is introduced which allows a thermodynamic tuning of complex metal hydrides.

2.6.2. Concept of Reactive Hydride Composites (RHC)

The concept of reactive alloying had the disadvantage of reducing the overall hydrogen capacity of the system due to additional mass of the alloying element. An alternative method to avoid a dramatic degradation of hydrogen content and to stabilize the dehydrogenation products of the hydride system at the same time is the approach of the so called “Reactive Hydride Composite” (RHC). In this approach, a metal hydride with high gravimetric hydrogen capacity is used as a reactive additive material. During the endothermic dehydrogenation process a mutual exothermic reaction of the hydride composite system occurs which stabilizes the reaction products. This in turn reduces the overall enthalpy of the reaction. A schematic diagram of this approach is displayed in the Figure 4.

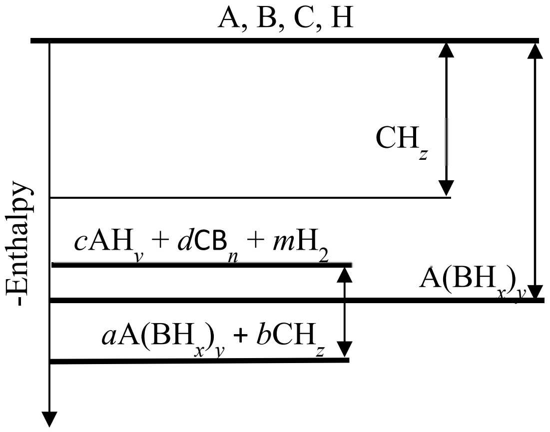

Figure 4. Diagram of destabilization by the concept of Reactive Hydride Composite (RHC).

An example of this approach is the reaction of the hydride composite system $LiNH_2$-LiH.[137-139]

$$\mathrm{LiNH_2 + LiH \leftrightarrow Li_2NH + H_2} \qquad (22)$$

The decomposition of each compound $LiNH_2$ and LiH takes place at about 350 °C and 900 °C, respectively. However, the composite system $LiNH_2$-LiH starts to decompose at temperatures at about 150 °C. In contrast to enthalpy values of $LiNH_2$ (-186 kJ / mol NH_3 [140]) and LiH (-190 kJ / mol of H_2)[141] the corresponding enthalpy value of the composite system according to reaction (22) is only -45 kJ / mol H_2 (determined using PCI-method by Chen *et al*)[139] with a theoretical capacity of 6.5 wt. % of H_2. It should be noted that without the reactive hydride (LiH) the lithium amide ($LiNH_2$) would decompose in to lithium imide (Li_2NH) and ammonia (NH_3). Therefore, not only the thermodynamic stability of the system is altered (reduced) by stabilizing the desorption product (Li_2NH) but it ensures also the reversible hydrogen storage in the Li-N-H system. Complex borohydrides have, however, much higher gravimetric capacities in comparison to Li-N-H system, as was pointed out in subsection 2.3.4. In the following subsections the reactive hydride composite systems $LiBH_4$-MgH_2 and $Ca(BH_4)_2$-MgH_2 are presented in more detail, which are the subjects of investigation in this thesis.

2.6.3. Introduction to Li-RHC and Ca-RHC systems

US Department Of Energy (DOE) has declared a minimum limit for gravimetric- and volumetric capacities for mobile hydrogen storage systems up to 5.5 wt. % H_2 and 40 g (H_2/L), respectively, by 2017 (ultimate: 7.5 wt % (H_2) and 70 Kg (H_2)/m^3) [45-47]. Reactive hydride composites fulfil these DOE targets, as can be deduced from Figure 5.

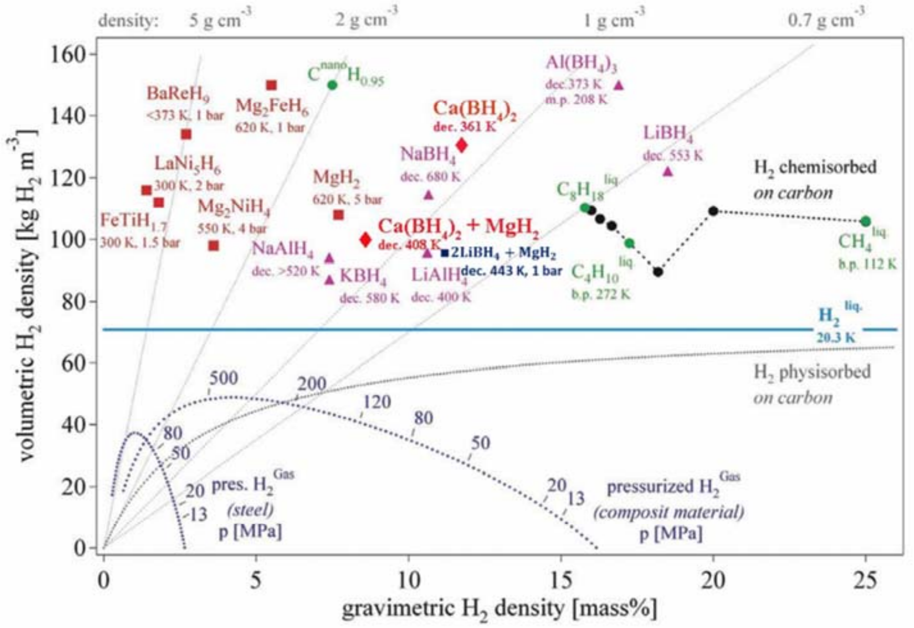

Figure 5. Volumetric and gravimetric capacities of some metal hydrides with liquid, compressed and physisorbed hydrogen (the figure is reproduced from reference[142]).

In addition to their good gravimetric- and volumetric hydrogen capacities, Li-RHC and Ca-RHC possess also moderate theoretical thermodynamic properties. In the following subsections these two RHC systems are introduced in more detail, respectively.

2.6.3.1. Li-RHC system

Reaction enthalpies of $LiBH_4$ and MgH_2 are 67 kJ / mol H_2 [11, 143, 144]and 75 kJ / mol H_2 [7, 49, 145, 146], respectively (see subsections 2.4.4.1, 2.4.1.1). However, the total reaction enthalpy of the hydride composite system ($LiBH_4$-MgH_2) is altered. A theoretical calculation based on DFT calculations, assuming reaction (1), gives a significantly reduced reaction enthalpy value of 46 kJ / mol H_2. Depending on the applied hydrogen backpressure and the final temperature the hydride composite system $LiBH_4$-MgH_2 can have different reaction paths and end products and consequently different desorption enthalpy values.[10, 14] If the applied hydrogen backpressure is lower than 3 bars at 400 °C, the hydride composite system decomposes independently and the possible dehydrogenation products are Mg, LiH, amorphous boron, amorphous/nanocrystallite $Li_2B_{12}H_{12}$, $Li_2B_2H_6$, highly toxic boranes (B_xH_y) and molecular hydrogen (detailed information about $LiBH_4$ is given in subsections 2.4.4.1). In this case reaction enthalpy of the hydride composite system is not altered and it is only partially reversible due to its highly stable decomposition products (amorphous boron, amorphous/nanocrystallite $Li_2B_{12}H_{12}$). By applying hydrogen backpressure greater than 3 bars the desorption products of Li-RHC are MgB_2 and LiH and molecular hydrogen at 400 °C. In the prior case, although MgB_2 is thermodynamically more stable in comparison to Mg, independent decomposition of both hydrides are kinetically more favoured. In the latter case decomposition of $LiBH_4$ is thermodynamically prevented, but not the one of MgH_2. Thus after decomposition of MgH_2 to metallic Mg, $LiBH_4$ can only decompose if it reacts with Mg phase to form MgB_2.[14] These reactions liberate a total theoretical hydrogen capacity of 11.5 wt. %. Moreover, the reaction enthalpy of the composite system is lowered in comparison to pure $LiBH_4$. While the first reaction step in (23) is an endothermic reaction, the second step is an exothermic reaction which leads to an overall reduction of the reaction enthalpy:

$$2LiBH_4 + MgH_2 \rightarrow Mg + 2LiBH_4 + H_2 \;\; (2.9\; wt.\%\; H_2) \qquad (23)$$

$$Mg + 2LiBH_4 \rightarrow 2LiH + MgB_2 \; + 2H_2 \;\; (8.6\; wt.\%\; H_2) \qquad (23.1)$$

Thus, the formation of MgB_2 stabilizes the reaction products of the Li-RHC system. Due to its graphite like layered structure the reverse reaction (hydrogenation of $2LiH+MgB_2$) proceeds under moderate thermodynamic conditions in comparison to hydrogenation of B + Mg + LiH composite system. Therefore, MgB_2 is the key compound to ensure the reversibility of the Li-RHC system.[147] Although thermodynamic and reversibility of $LiBH_4$ could be tuned by the concept of RHC, the de/rehydrogenation reaction kinetics of the system remained slow. In this work the hydrogen sorption kinetics of the composite system could be significantly improved by addition of small amount of TMH. Among them NbF_5 was found to be the most effective additive to enhance the hydrogen sorption properties of Li-RHC. By addition of 10 mol % of NbF_5 to the composite system considerable improvement of the reaction kinetics by an order of magnitude was achieved, in comparison to the pristine $2LiBH_4+MgH_2$ composite system.

2.6.3.2. Ca-RHC system

In this work the concept of the Reactive Hydride Composite is applied to stabilize the decomposition products of $Ca(BH_4)_2$ and to improve its reversible hydrogen storage property.[10, 147] Based on this concept MgH_2 is used to stabilize the desorption products of $Ca(BH_4)_2$. The composite system $Ca(BH_4)_2+MgH_2$ has with ~ 8.4 wt.% H_2 the second highest hydrogen content in the group of RHCs. In contrast to Li-RHC, Ca-RHC can have several decomposition paths and final products. The possible dehydrogenation reaction paths of the Ca-RHC system are listed in the following reactions equations:

$$\begin{gathered} Ca(BH_4)_2 + MgH_2 \leftrightarrow CaH_2 + MgB_2 + 4\, H_2 \\ 8.4\; wt\%\; H_2\, ;\left(46.9 \frac{kJ}{mol\; H_2}\right) \end{gathered} \qquad (24.1)$$

$$\begin{gathered} Ca(BH_4)_2 + MgH_2 \leftrightarrow 2/3\; CaH_2 + 1/3\; CaB_6 + Mg \; + 13/3\; H_2 \\ 9.1\; wt.\%\; H_2\, ;\; \left(45 \frac{kJ}{mol\; H_2}\right) \end{gathered} \qquad (24.2)$$

$$\mathrm{Ca(BH_4)_2 + MgH_2 \leftrightarrow CaH_2 + Mg + 2B + 4H_2} \tag{24.3}$$
$$\mathrm{8.4\ wt.\%\ H_2;\ \left(57.9\,\frac{kJ}{mol\ H_2}\right)}$$

The values for the enthalpy changes in (24.1-3) are given under 1 bar of H_2 pressure and 25 °C, and they are reported by Kim *et. al*.[148] Additionally to above mentioned reaction products $CaB_{12}H_{12}$ can be formed as was recently reported by Minella *et al*.[149] Dodeca-closo- boranes are in general very compact structures and thermodynamically highly stable.[13] Thus $CaB_{12}H_{12}$ is accumulated over the de/rehydrogenation cycles and this leads to limitation of reversible hydrogen storage in the Ca-RHC system. In order to study different decomposition reaction paths and final products of Ca-RCH, the applied experimentally conditions (such as pressure and temperature) are varied upon the dehydrogenation reaction, in this work. Also the kinetical impact of NbF_5 dopant on the Ca-RHC system is investigated, in detail.

2.7. Scattering theory

In the following a general treatment of scattering theory of quantum particles by the matter is given, which follows closely the standard books of Ibach & Lueth, Ch. Kittel, and A. Guinier.[150-152] The theoretical treatments in the following are confined in the frame of kinematical approximation or Born approximation to single- and coherent scattering. A representative scattering event is illustrates in Figure 6. A particle-wave with amplitude A_0 is emitted from the source and scattered at an object at a point P. If the object is located far from the source, than the incoming particle-wave at P can be assumed as a planar wave.

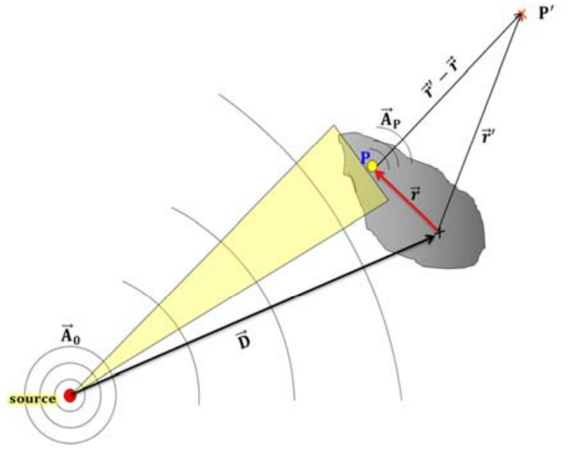

Figure 6. Scattering and detection of an incident wave from a far located source.

The outgoing partial particle-wave has a spherical shape with amplitude A_p which is observed, far from P at point P' (Frauenhofer condition). The amplitude of the scattered particle-wave at the time *t* and at the point *P* can be expressed as:[150]

$$\vec{A}_P = \vec{A}_0 exp(i\vec{k}_0(\vec{D} + \vec{r}) - i\omega t) \tag{25}$$

Here, $\vec{k}_0$ is the wave vector of the incident beam and its value is related with the wavelength ($|\vec{k}_0| = 2\pi/\lambda$). In exception to the laser sources, all other sources have uncorrelated emission phases, hence the detected intensity at the point P' is to be seen as an average over numerous independent diffraction processes. Considering the scattering of the incident particle-wave over all points of the object, each single point of the object initiates a new source of partial spherical particle-wave (Huygens principle). Concerning information about the amplitude and phases of the partial particle-waves relative to the incident particle-beam can be summarized in the scattering density $\varrho(\vec{r})$. The amplitude observed at the point P' in Frauenhofer approximation is thus:

$$\vec{A}_{P'} = \vec{A}_P(t,\vec{r})\varrho(\vec{r})\frac{e^{i\vec{k}(\vec{r}'-\vec{r})}}{(\vec{r}'-\vec{r})_{\vec{r}'\gg\vec{r}}} \approx \vec{A}_0(t,r)\varrho(\vec{r})\frac{e^{i\vec{k}(\vec{r}'-\vec{r})}}{\vec{r}'} \tag{26}$$

Inserting the quantity of $A_P(t,\vec{r})$ in (26) results to:

$$\begin{aligned}\vec{A}_{P'} &= \vec{A}_0 e^{i\vec{k}_0(D+r)-i\omega t}\varrho(\vec{r})\frac{e^{i\vec{k}(\vec{r}'-\vec{r})}}{\vec{r}'} \\ &= \frac{\vec{A}_0 e^{i(\vec{k}_0 D+\vec{k}\vec{r}')}}{\vec{r}'} e^{-i\omega t}\varrho(\vec{r})e^{i(\vec{k}_0-\vec{k})\vec{r}} \\ \vec{A}_{P'} &\sim e^{-i\omega t}\varrho(\vec{r})e^{i(\vec{k}_0-\vec{k})\vec{r}} = e^{-i\omega t}\varrho(\vec{r})e^{i\vec{q}\vec{r}}\end{aligned} \tag{27}$$

Here, we introduced the scattering vector $\vec{q}$ which gives the direction of scattering in the Fourier-space, and its magnitude is given by:

$$|\vec{q}| = \frac{2\pi}{\lambda} sin\theta \tag{28}$$

Here, 2θ is the scattering angle between the incident and scattered particle- wave. The main advantage of introducing the scattering vector is the comparability of results obtained at different sources independent of their incident wavelengths. Integration over the whole scattering object gives the total scattering amplitude observed at P':

$$\vec{A}_{P'} = \vec{A}_0 \int_V \varrho(\vec{r})e^{i\vec{q}\vec{r}} d^3\vec{r} \tag{29}$$

Note that we assumed a time independent scattering density $\varrho(\vec{r})$ (rigid distribution of scattering sources in the object) and therefore we have a constant ω_0 at all times (elastic scattering). In an real experiment, however, not the scattering amplitude $\vec{A}_{P'}$ is measured at the detector but the scattering intensity which is proportional to $\|\vec{A}_{P'}\|^2$. Thus, the measured intensity is:

$$I(\vec{q}) = I_0 \left\| \int_V \varrho(\vec{r}) e^{i\vec{q}\vec{r}} d^3\vec{r} \right\|^2 \tag{30}$$

Equation (30) shows that the scattering intensity is related to the absolute square Fourier transformation of the scattering charge density $\varrho(\vec{r})$. A severe consequence of this fact is the loss of information about the amplitude and phases of the partial particle-waves relative to the incident particle-beam. Therefore, it is not possible to get the spatial distribution of $\varrho(\vec{r})$ by a simple inverse Fourier transformation of equation (30).

2.7.1. Scattering of a monochromatic beam by periodic structures

General characteristics of the scattering density of periodic structures is that they are invariant under a translation: $T = u_1\vec{a}_1 + u_2\vec{a}_2 + u_3\vec{a}_3$. Here, u_i are integers and $\vec{a}_i$ are the Cartesian primitive axes of the periodical structure (crystal).

$$\varrho(\vec{r}) = \varrho(\vec{r} + T) \tag{31}$$

The periodical scattering density with a period a can be expanded in a Fourier series:

$$\varrho(\vec{r}) = \sum_{\vec{G}} \varrho_{\vec{G}} e^{i\vec{G}\vec{r}} \tag{32}$$

Where $\vec{G}$ is a vector of reciprocal space and it has to fulfill the following condition in order to preserve the translation invariance of the periodical scattering density $\varrho(\vec{r})$ of the lattice:

$$\begin{gathered} \vec{G}\,\vec{r} = 2\pi m \ \ ; \ m \in \mathbb{N} \\ \text{with } \vec{G} = h\vec{\mathrm{g}}_1 + k\,\vec{\mathrm{g}}_2 + l\,\vec{\mathrm{g}}_3\,; \ \vec{r} = n_1\vec{\mathrm{a}}_1 + n_2\,\vec{\mathrm{a}}_2 + n_3\,\vec{\mathrm{a}}_3 \end{gathered} \tag{33}$$

This is satisfied only, when the reciprocal axes vectors $\vec{\mathrm{g}}_1, \vec{\mathrm{g}}_2, \vec{\mathrm{g}}_3$ are correlated with their corresponding real space axes vectors as following:

$$\begin{gathered} \vec{\mathrm{g}}_1 = 2\pi \frac{\vec{\mathrm{a}}_2 \times \vec{\mathrm{a}}_3}{\vec{\mathrm{a}}_1(\vec{\mathrm{a}}_2 \times \vec{\mathrm{a}}_3)}, \\ \vec{\mathrm{g}}_2 = 2\pi \frac{\vec{\mathrm{a}}_3 \times \vec{\mathrm{a}}_1}{\vec{\mathrm{a}}_1(\vec{\mathrm{a}}_2 \times \vec{\mathrm{a}}_3)}, \\ \vec{\mathrm{g}}_3 = 2\pi \frac{\vec{\mathrm{a}}_1 \times \vec{\mathrm{a}}_2}{\vec{\mathrm{a}}_1(\vec{\mathrm{a}}_2 \times \vec{\mathrm{a}}_3)} \end{gathered} \tag{34}$$

Thus, all crystal structures have two correlated lattices in real space (marked by integers (a_1, a_2, a_3)), and in reciprocal space (marked by integers (hkl)), respectively.
By substituting the Fourier components of $\varrho(\vec{r})$ into scattering amplitude in (29), we obtain:

$$\vec{A} \sim \int_V \sum_{\vec{G}} \varrho_{\vec{G}} e^{i\vec{G}\vec{r}}\, e^{i\vec{q}\vec{r}} d^3\vec{r} = \sum_{\vec{G}} \varrho_{\vec{G}} \int_V e^{i(\vec{G}-\vec{q})\vec{r}} d^3\vec{r} \tag{35}$$

Note that the integral in (35) is now extended over the volume of a periodical structure. Equation (35) exhibit characteristic extreme points when $\vec{G} = \vec{q}$. One can show that the amplitude has its maxima at these points.[153] Therefore, for each Fourier component at those points $\vec{G} = \vec{q}$ the integral can be approximated (for large scattering volume: abundant identical unit cells) to a delta function:

$$\int_V e^{i(\vec{G}-\vec{q})\vec{r}} d^3\vec{r} = \begin{cases} V & \text{for } \vec{G} = \vec{q} \\ \sim 0 & \text{else} \end{cases} \tag{36}$$

A geometrical insight of the diffraction process can be nicely illustrated by the Ewald-construction as is presented in Figure 7. The condition $\vec{G} = \vec{q} = \vec{k}_0 - \vec{k}$ gives rise to a diffraction signal only when the surface of the sphere touches the reciprocal space points. This means, that neither any arbitrary incident wavelengths nor any arbitrary orientation will lead to a diffraction event by a scattering lattice.

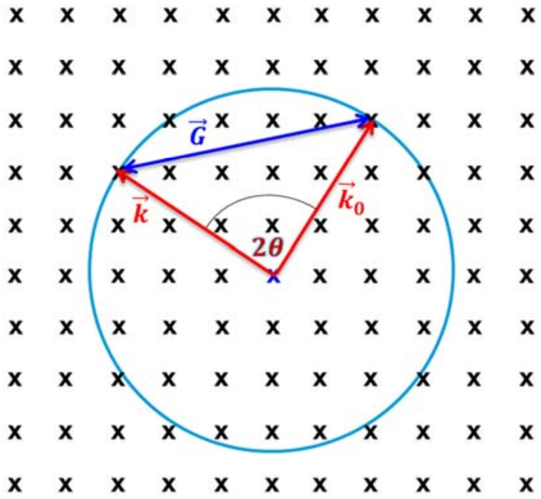

Figure 7 Ewald-construction of the interference effect by an incident beam in a periodic structure.

Taking the square of $\vec{G} = \vec{q} = \vec{k}_0 - \vec{k}$ and using the elastic scattering condition($|\vec{k}_0| = |\vec{k}|$) one obtains:

$$2\vec{k}_0\vec{G} + G^2 = 0 \tag{37}$$

This is the so-called Von Laue-condition and it is the central statement of the elastic scattering of particle-waves by a periodic scattering object. Since $-\vec{G}$ is also an element of the reciprocal space, thus equation (37) can also be rewritten as:

$$2\vec{k}_0\vec{G} = G^2 \tag{38}$$

It can be shown that the spacing between parallel lattice planes is $d(hkl) = 2\pi/\left|\vec{G}\right|$ which are perpendicular to $\vec{G} = h\vec{g}_1 + k\,\vec{g}_2 + l\,\vec{g}_3$. Substituting this fact into equation (38), one obtains:

$$\begin{gathered} 2\vec{k}_0\vec{G} = 2k_0 G\sin\theta = G^2 \;\Rightarrow 2k_0\sin\theta = G \Rightarrow 2(2\pi/\lambda)\sin\theta \\ = 2\pi/d(hkl) \Rightarrow \;\; 2d(hkl)\sin\theta = \lambda \end{gathered} \tag{39}$$

In general the indices have a common factor n in comparison to the scattering crystal plane. Thus, equation (39) can be reduced to common used notation of Bragg-equation:

$$2d\sin\theta = n\lambda \tag{40}$$

The Bragg-equation illustrates the diffraction of particle-waves by reflection of them at the lattice planes into 2θ angle. This phenomenon can be explained by the fact that the lattice planes (hkl) in the real-space are perpendicular situated to the $\vec{G}_{(hkl)}$ vectors in the corresponding reciprocal-space, thus, it gives the impression of mirror reflection of the rays at the (hkl)-plane of the lattice and it gives the origin for the terminology “Bragg-reflection” (this is illustrated in the Figure 8).

2.7.2. **Scattering of a beam by nano structures (Small-angle scattering (SAS))**

In the last chapter the Bragg-law was derived (equation (40)) which describes the scattering of a beam by regular scattering objects with particular spacing. Rearranging the Bragg-law leads to:

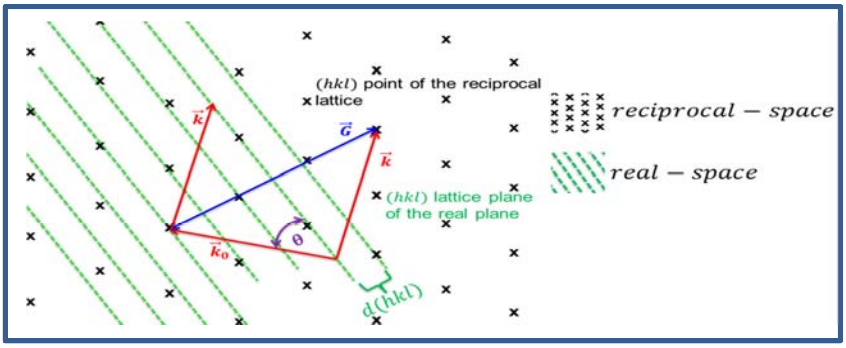

Figure 8. An Illustration of Bragg-reflection at (hkl)-planes of a periodic lattice. For better understanding the reciprocal space is covered by the real space planes.

$$\frac{\lambda}{d} \sim \sin\theta \tag{41}$$

This implies that by a constant wavelength the scattering of an incident beam by structures with large d-spacing will lead to scattering intensities to small angles. So, the bigger the structures the smaller the observation angles of their scattering intensities (by λ = constant!). A. Guinier was the first who observed around the year 1930 and interpreted correctly the scattering of an incident beam from materials at very small angles[154] henceforth this observation was termed as "Small-angle scattering" (SAS). This is not necessarily correct to observe nano structures always at very small angles. One could apply long wavelengths in the same order as the structures increase. This would leave the scattering angle unchanged and the scattering intensities would be observable still at high angles! However, long wavelengths are highly absorbed by matter. Thus, the observed scattered intensities will drastically be decreased hence the measurement times will significantly increase in comparison to short wavelength beams. In addition, sample preparation and detection of low energy scattering beams are very challenging. Therefore, these difficulties give some justification for using frequently the SAS method in order to investigate nano structured materials. As it was described before, the observed intensity of the scattered beam at the detector can be described by the square of $\vec{A}_{sct}(\vec{q})$:

$$\begin{aligned} I(\vec{q}) &= A_{sct}(\vec{q})A_{sct}(\vec{q})^* \\ &= I_0(\vec{q}) \iint\limits_{V1\,V2} \rho(\vec{r}_1)\rho(\vec{r}_2)\ exp(-i\vec{q}(\vec{r}_1 - \vec{r}_2))\, dV_1 dV_2 \end{aligned} \tag{42}$$

Equation (42) describes the Fourier-Transformation (FT) of $\vec{r}_1 - \vec{r}_2$ corresponds to the distances distributed between the couple of $\vec{r}_1$ and $\vec{r}_2$. $I_0(\vec{q})$ is proportional to the scattering intensity of a free electron and is defined as:[155]

$$I_0(\vec{q}(\theta)) = I_p \frac{\tau}{D^2} = \frac{I_p}{D^2} \frac{7.94\ 10^{-26} cm^2 (1 + cos(2\theta))}{2} \tag{43}$$

In (43), I_p is the primary beam intensity, D is the sample-to-detector distance, τ represent the Thomson-factor with the polarization factor of $1/2(1 + \cos(2\theta))$ which can be approximated for small angles ($\theta \leq 5°$) by: $(1/2)(1 + \cos(\theta \approx 0)) \approx 1$. Thus for small-angles:

$$I_0(\vec{q}) \approx I_0 = 3.97\ 10^{-26} I_p \left(\frac{1}{D^2}\right) cm^2 \tag{44}$$

This is the well-known "inverse square power law", which is frequently observed in physics when the distance between source and observer is increased (such as in gravitational -or electromagnetic fields: $\sim\frac{1}{r^2}$). For convenience hereafter I_0 is put to unity. Assuming an isotropic system (particles distributed with random orientation) with no long-range order, than equation (42) can be rewritten as:[156]

$$I(q) = \int 4\pi r^2\, \gamma(r) \frac{\sin(qr)}{qr} dr \tag{45}$$

Where $\gamma(r)$ is an autocorrelation function and is defined as:

$$\gamma(\vec{r}) = \int_{V1} \rho(\vec{r}_1)\rho(\vec{r}_1 - \vec{r}) dV_1 \tag{46}$$

By applying the inverse *FT* of equation (45) it leads to:

$$p(r) = r^2\gamma(r) = \int_0^\infty q^2\, I(q) \frac{\sin(qr)}{qr} dq \tag{47}$$

$p(r)$ is the so called "distance distribution function "(DDF) which describes the frequency of distances *r* between two arbitrary points at the confines of a homogenous particle. In an actual experiment, however, the measured q-range is limited in which the scattering intensities are collected hence the inverse *FT* of (45) is mathematically not straightforward. Therefore, several extrapolation methods were developed in order to determine $p(r)$ of a system directly by measuring its scattering intensities.[157-159] Moreover, if the scattering objects are not monodisperse the DDF does not deliver the right particle sizes hence it cannot be applied for systems with high polydispersity anymore.[160] An alternative approach is to assume a model of scattering objects with certain properties (contrast, degree of polydispersity etc.) and to calculate their scattering intensities by an incident beam. The scattered intensity of a beam by a monodisperse particle system is proportional to its macroscopic differential cross section:[161]

$$I(q) \sim \frac{d\Sigma}{d\Omega} = \frac{N}{V}\frac{d\sigma}{d\Omega} = n_p\ (\Delta\rho)^2\ V_p\ P(q,r)\ S(q) \tag{48}$$

Here $\left(\frac{d\Sigma}{d\Omega}\right)$ and $\left(\frac{d\sigma}{d\Omega}\right)$ are the macroscopic and microscopic differential scattering cross sections, respectively. It is crucial to note that the microscopic differential scattering cross sections represents the cross section of an individual particle and has therefore the unit of an area (cm^2), whereas the macroscopic differential scattering cross sections represents the accumulation of all scattering cross sections of all particles present in a unit volume of a sample, hence, it has the unit of an inverse length (cm^{-1}). Macroscopic differential scattering cross sections can be imagined as the effective scattering cross section of the entire particle system in that unit volume, so to say. N stands for the number of particles present in the volume V of the sample. Thus, n_p is the number density of the particles in the sample and V_p represents the volume of such an individual particle. $\Delta\rho$ stands for the scattering contrast between the scattering particle (ρ_p) and its environment (matrix) (ρ_M). $P(q,r)$ and $S(q)$ represent the form factor and the structure factor of the particles, respectively. The form factor describes the shape of the particle whereas the structure factor describes the interference correlations between particles. For diluted systems $S(q)$ can be approximated by unity. The macroscopic differential cross section for a diluted polydisperse particle system can, therefore, be expressed as:[161]

$$\frac{d\Sigma}{d\Omega} = (\Delta\rho)^2 \int_0^\infty n_p(R) P(r) V_p(r)^2 F(q,r)\, dr \tag{49}$$

Here, $n_p(R)$ represents the size distribution particles in the system. Throughout this work, spherical particles with lognormal distribution are assumed:

$$P(r,q) = 3\,\frac{\sin(qr) - qrcos(qr)}{(qr)^3} \tag{50}$$

$$n_p(R) = \left(\frac{1}{\sqrt{2\pi}\,\sigma r}\right) exp\left[\frac{-\ln\left(\frac{r}{\mu}\right)^2}{2\sigma^2}\right] \tag{51}$$

Here, σ describes the width of the distribution (degree of polydispersity), μ the mean radius parameter and r is the radius of the particle. The as measured scattering intensity in (48) is only proportional to the macroscopic differential scattering cross section which is equalized by multiplying it with proportionality constant, K:

$$I(q) = K\frac{d\Sigma}{d\Omega} \tag{52}$$

The proportionality constant depends, however, directly on several experimental quantities such as incident beam flux Φ, size of the solid-angle $\Delta\Omega$ in which the beam is scattered into, measuring time Δt, sample thickness D, detector property (efficiency) $\varepsilon(\lambda)$, sample transmission T and the area A of the illuminated part of the sample (in other words: the beam size):

$$K = \Phi\ \Delta \mathrm{t}\ \mathrm{T}\ \Delta\Omega\ \mathrm{A}\ \mathrm{D}\ \varepsilon(\lambda) \tag{53}$$

In a real experiment the product Φ Δt can be determined by monitoring the flux over the duration of scattering time (monitor count). After determining the constant K, the macroscopic differential cross section can be obtained by dividing the measured intensity by the constant K. Flux is inverse proportional per unit area in a given time ($1/cm^2$) and the product (AD) in equation (53) is the illuminated volume of the sample (cm^3). The product of these quantities leads to the unit length (cm). Dividing the intensity in equation (52) by the constant K will lead to the inverse length unit (cm^{-1}) for the macroscopic differential scattering cross section $\left(\frac{d\Sigma}{d\Omega}\right)$, which is the right unit for this quantity as was discussed above. Since, in this manner, the arbitrary scattering intensity scale is brought experimentally to the actual scattering property of the measured sample, therefore, the macroscopic differential cross section is also termed as: absolute scattering intensity. A more detailed explanation and derivation on the absolute calibration of small-angle scattering data can be found in the following references.[162-170]

2.7.2.1. Small-Angle X-ray Scattering (SAXS)

In the previous section a general treatment of scattering was given regardless of the nature of the incident beam. In this section some basics of the scattering properties of incident X-rays (photons) by nanostructured material are presented. Photons interact only with charged particles of mater. There are several channels of interaction between photons and charged particles of atoms such as elastic scattering (Rayleigh scattering), inelastic scattering (Compton scattering, Raman scattering, etc.), absorption (photo-electron absorption Beer's-Law) and pair production (nuclear-photo absorption). Details about the respective interactions can be found in the work of J.H. Hubbell *et al.*[171] In the small-angle region and at low energy range ($E < 40$ keV) the coherent elastic scattering cross section is the most dominant portion of the scattering beam. At large large-angles the inelastic part of the scattering cannot be ignored, however, it is incoherent hence it can be removed as a constant background. Since in the scattering experiments the scattering power is visualized by scattering cross sections the scattering density $\rho(\vec{r})$ can be rewritten in terms of scattering lengths:

$$\rho(\vec{r}) = \frac{\sum_j^n \mathrm{b}_{X,j}}{\delta V} \tag{54}$$

Where $\mathrm{b}_{X,j}$ represents the X-rays scattering amplitude of the j^{th} atom of a material included in the small volume δV. Therefore, $\varrho(\vec{r})$ is termed as (spatial) scattering density. In the case of photons the scattering amplitude is given by:

$$\begin{gathered} b_X = r_e(f_0(q) + f'(E) + f''(E)) = b_{O,X}(q) + b_{R,X} \\ \text{Where: } b_{O,X}(q) = r_e f_0(q) \; and \;\; b_{R,X} = r_e(f'(E) + f''(E)) \end{gathered} \tag{55}$$

Here, r_e is the classical Thompson radius of an electron, $f'(E)$ and $f''(E)$ are the anomalous dispersion factors which become prominent when the incident beam approaches an absorption edge of an element. Therefore, the X-ray scattering length is separated (in (55)) in a resonant $b_{R,X}$ and in an off-resonant $b_{O,X}(q)$ scattering length part. The off-resonant scattering length characterizes the scattering power of a specific atom, in its unexcited state, by its scattering form factor $f_0(q)$, which is described by:

$$f_0(q) = \int_{V_a} d^3r\, \varrho_a(\vec{r})\exp(i\vec{q}) \tag{56}$$

This accounts on the fact that the wavelengths of X-rays are comparable to the size of atoms (in the ~Å range), hence the incident X-ray beam doesn't "see" the individual electrons of an atom but rather the entire cloud of electrons (electric charges) distributed around the nucleus. In the small-angle approximation, however, $f_0(q)$ becomes q-independent and equal to the atomic number Z of the element, as can be seen from equation (56). For a typical SAXS experiment the monochromatic energy of the incident photon beam is far away from any absorption edges of any element in the sample. Thus the scattering length of the X-rays for a sample can be written as:

$$b_{SAXS} = b_{O,X}(q) \approx r_e \sum_{i=1}^{n} f_{0,i} = r_e \sum_{i=1}^{n} Z_i \tag{57}$$

With Z_i being the atomic number of the i^{th} element. Therefore, the scattering length density of X-rays in a SAXS experiment can be expressed as (using:$\varrho_{mac} = m/V$, etc.):

$$\rho_{SAXS} = r_e N_A \bar{\varrho}_m \sum_{i=1}^{n} \frac{x_i f_{0,i}}{M_i} \tag{58}$$

Where, N_A represents the Avogadro number, $\bar{\varrho}_m$ the macroscopic average mass density, x_i is the mol fraction of the i^{th} substance, M_i its molecular weight. In a SAXS experiment one is interested in the overall structural information content of the specimen. However, it is not possible to resolve element specific structural information of a sample by applying SAXS method.

2.7.2.2. Anomalous Small-Angle X-ray Scattering (ASAXS)

In cases where it is of special interest to reveal structural properties of specific element containing in a sample, a normal SAXS experiment often is not sufficient. This is due to the fact that all structures and vacancies present in the sample contribute to the total small-angle scattering intensity. In order to extract element specific information on the nanoscopic scale from the entire scattering intensity, alternative methods are needed. To meet these challenges, during 1980-1990's the ASAXS method was developed by H. Stuhrmann and others.[172] The basic idea is to exploit experimentally the resonant $b_{R,X}$ scattering length term of b_X in (55) which is energy dependent:

$$b_{R,X} = r_e(f'(E) + f''(E)) \tag{59}$$

Far away from any absorption edge of an element the scattering length of b_X can be well approximated by $b_{O,X}$, as was stated in the previous section. By varying the energy of the incident beam in the vicinity of an absorption-edge of an element the anomalous dispersion coefficient become significantly larger, hence, the resonant scattering length $b_{R,X}$ can no longer be ignored. The terminology “anomalous” is, however, historically based and is not coherent with the knowledge of today. Behaviours of the dispersion factors are characteristic for all elements, since the atomic levels are generally quantized, thus, absolutely normal. $f''(E)$ is related to the linear absorption coefficient, therefore, it can be experimentally determined:[156]

$$f''(E) = \left(\frac{mcE}{4\pi he^2}\right)\mu(E) \tag{60}$$

$f'(E)$ can be derived by knowing $f''(E)$ because they are correlated over the Kramer-Kronig relation:[155]

$$f'(E) = \left(\frac{2}{\pi}\right)\int_0^\infty \frac{E' f''(E')}{E'^2 - E^2}\,dE' \tag{61}$$

Due to the scattering density $\rho \propto f(E)$, the differential cross section is proportional to $(\Delta\rho)^2 \propto \|\Delta f(E)\|^2$ (see (48)). Thus, if the energy of the incident beam becomes closer to an absorption edge of an element present in the system, its scattering property is affected accordingly. The scattering amplitude of such a system can be divided in contributions of resonant (R) part (particles with $f(E)_p$) and in an off-resonant (O) part (matrix (environment) with $f(E)_M$):

$$A(q,E) = A(q)_O + A(q,E)_R \tag{62}$$

Since, the measured scattering intensity is proportional to the square of the incident beam amplitude and the amplitude is proportional to $(\Delta\rho)^2$, it follows:

$$I(q,E) \propto \left(f(E)_p - f(E)_M\right)\left(f(E)_p - f(E)_M\right)^* \tag{63}$$

Incorporating this information in (42) and reorganizing all terms in resonant and in off-resonant parts leads to the so called “Stuhrmann-equation”:[172]

$$I(q,E) = I_o(q) + 2f'(E)_p I_{oR}(q) + \left({f'(E)_p}^2 + {f''(E)_p}^2\right) I_R(q) \tag{64}$$

Measuring the scattering intensity of a sample at minimum three different energies close (below) to an absorption edge of an element present in the sample, equation (64) allows to separate the resonant scattering contribution ($I_R(q)$) from these total scattering intensities ($I(q,E_i)$; $i = 1,2,3,..$) at different energies.

2.7.2.3. *Small-Angle Neutron Scattering (SANS)*

Dissimilar to photons, neutrons interact with the nuclei of atoms, thus strong forces are involved in their interaction (assuming random spin distribution of nuclei in the sample and neglecting spin function of the electrons, surrounding the nuclei). Since the strong force acting between neutrons and nuclei are highly complex to be described theoretically, in detail, hence a clear link between scattering amplitude and nuclei number similar to photons and atomic number is not straightforward to draw. They show rather complex relationship between their scattering amplitude and the nuclei number of the elements. For instance, neutrons interact strongly with hydrogen whereas they are almost transparent to the X-rays. Moreover, due to their interaction with nuclei, neutrons show a large scattering variation even between isotopes of the same element (*e.g.*: b_{hydrogen}= -3.74 fm and $b_{\mathrm{deuterium}}$= 6.67 fm). Therefore, analogous to ASAXS method, a SANS experiment can be used to perform contrast variation by exchanging isotopes of the same element to reveal element specific structural information in a specimen.

2.8. X-ray Absorption Spectroscopy (XAS)

X-rays interact with matter in various manners such as scattering or absorption, for instance. The absorption of X-rays by an atom can be described as a process of annihilation of the X-ray photon by producing an electron-hole in the shell structure of the atom (exited atom). Depending on the energy of the absorbed photon the exited-electron can be promoted either into a higher unoccupied energy state of the atom or into the continuum state (if the energy of the absorbing photon is greater than the highest bounded state of the absorbing atom). Two kinds of environments for the exited atom (resonant atom) can be considered for the absorption process:

1) The resonant atom is isolated (bare atom)
2) The resonant atom is surrounded by other atoms

Far from any absorption edges of the atom the incident photon-beam is attenuated, in both cases, according to Beer's-Law:

$$I = I_0 exp(-\mu x) \tag{65}$$

Here, I_0 is the attenuated beam after passing through the specimen with a thickness x, and μ is the linear absorption coefficient of the material and its value can be approximated by:

$$\mu \approx \frac{\varrho_{mac} Z^4}{AE^3} \tag{66}$$

Where, ϱ_{mac} is the macroscopic mass density, Z states for atomic number, A represents the atomic mass and E is the energy of the incident beam. However, if the energy of the incident beam approaches any absorption edge of the resonant atom its photo-absorption behaviour changes depend significantly on its local symmetry (environment). Considering case (1) where the resonant atom is isolated, the photo-absorption around its absorption edge reflects the electronic structure of the atom. The photo-electrons are than elevated according to quantum mechanics rules to higher unoccupied energy levels (e.g. in a dipolar approximation only higher energy states with $\Delta l = \pm 1$ are allowed to be occupied). These exited atomic levels retain in femtosecond range and decay subsequently by liberating photons either to the vacuum state (fluorescence radiation) or to promote an electron of the same atom located at a higher energy level into continuum energy state (Auger-Meitner effect). By increasing the energy continuously above the bonding energy of the atom the electrons can be raised to the continuum state. Since there are no other neighbouring atoms the photo-electron can propagate unperturbed through the vacuum state with a kinetic energy of:

$$E_{kin} = h\nu - E_0 \tag{67}$$

Where, $h\nu$ is the energy of the absorbed photon and E_0 is the bonding energy of the absorbing atom. By increasing further the energy of the incident photons more photo-electrons are promoted to the continuum state with higher E_{kin} and the "bare atom" becomes more transparent to the beam. In the latter case (2), where the resonant atom is surrounded by other atoms, the electronic structure of the resonant atom changes. First of all, the coordination symmetry of the resonant atom affects the valence orbitals and their corresponding occupancy. Thus, certain forbidden photo-electric transition becomes accessible and their partial absorption cross sections increase, as a consequence. Due to interaction of the valence electron of the resonant atom with those of the neighbouring atoms the nucleus charge of the resonant atom is less screened. Hence, the core electrons "feel" effectively more positive nuclear charge and they are further attracted toward the electrical potential of the nucleus. Therefore, higher photon-energy is needed to elevate the core-electron into continuum state of the coordinated resonant atom in comparison to "bare atom". Above the ionization energy of a core-level (main absorption edge), the photo-electrons have small kinetic energy and therefore they experience, beside some single scattering (SS) processes, mainly multiple scattering (MS) events. This region roughly ~50-100 eV bellow and ~ 100-150 eV above the main absorption edge, respectively, is the so-called "X-ray Absorption Near Edge Structure" (XANES). The structure of this portion gives information about the chemical state local symmetry of the resonant atom. By increasing the energy of the incident photons above the XANES region, the photo-electrons have higher kinetic energy. Thus, the probability of MS decreases significantly, and the main portion of the photo-electrons experience SS events with the surrounding atoms.[173] Considering the scattered electron as a particle wave, the backscattered electron-wave by neighbouring atoms can be reabsorbed by the exited atom. However, the probability amplitude of reabsorption ($\|\psi\|^2$) at the exited atom is modulated, due to the interference of the backscattered electron-wave with the outgoing electron-wave. Depending on the incident photon energy, $\|\psi\|^2$ can be lowered or increased at that exited atom, contrary to the isolated atom. If the modulation of the reabsorption of the electron-wave at the exited atom gets its maximum, the resonant atom becomes more "visible" to the incident beam and the probability of the photo-absorption increases and vice versa. If one changes the distance of the neighbouring atom, the modulation of the electron-wave changes as well, therefore $\|\psi\|^2$ changes hence the photo-absorption of the resonant atom. By measuring the absorption coefficient of a resonant atom far below the absorption edge (~ -100 eV, 0 eV being the main absorption edge position) up to +1000 eV above the edge (XANES+EXAFS=XAS), and applying the Beer's-Law, one gets the absorption spectrum of the resonant atom:

$$\mu(E) \sim \ln(I_0(E)/I(x,E)) \tag{68}$$

The containing information in the gained spectrum is: coordination symmetry, bond angles, oxidation state and the local environment of the resonant atom. A schematic description of the aforementioned process for the isolated (red line) and for the coordinated atom (black line) is displayed in the Figure 9. The photon absorption of an atom can be described in a quantum mechanical picture using Fermi's Golden rule:

$$\mu(E) \sim \left|\langle\psi_i|H|\psi_f\rangle\right| \tag{69}$$

ψ_i describes the initial quantum state (core-electron, a photon and no photo-electron) and ψ_f represents the final stat of the system (core-hole, no photon and a photo-electron). Due to closely bonded core-electrons, their initial states are not significantly affected by the neighbouring atoms.

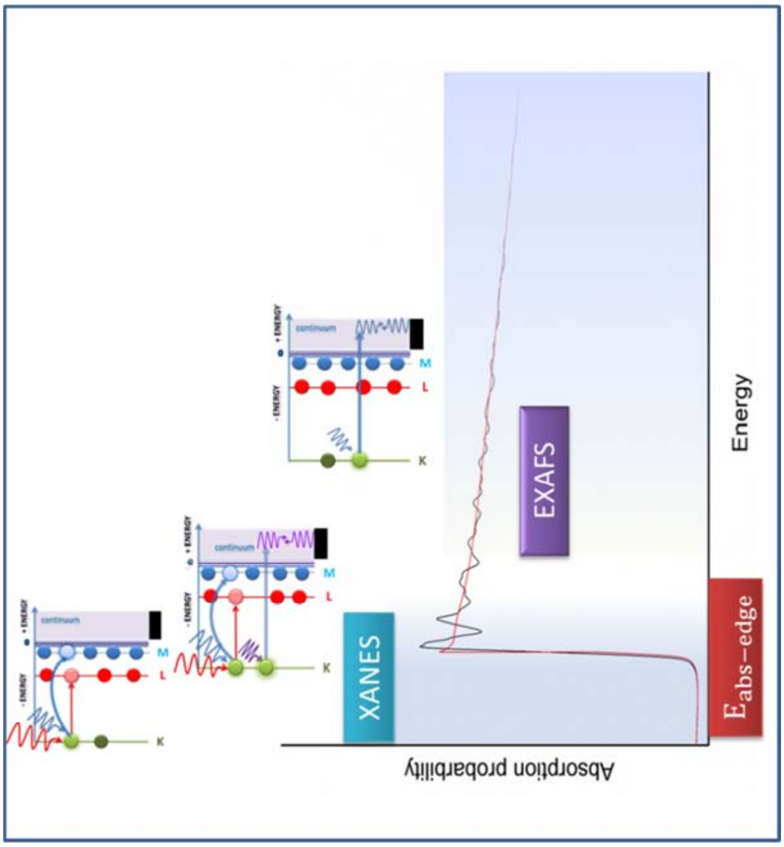

Figure 9 Superposition of outgoing and backscattering photo-electron at the resonant atom.

The final state, in contrast, is considerably altered by the surrounding atoms due to the interaction of photo-electron and the surrounded atoms. However, if one assumes the final stat of a superposition of the exited isolated atom ψ_0 and a perturbed part $\Delta\psi_f$ of the wave-function $\psi_f = \psi_0 + \Delta\psi_f$, than (69) can be rewritten as:

$$\mu(E) \sim |\langle\psi_i|H|\psi_0\rangle|^2 \left[1 + \langle\psi_i|H|\Delta\psi_f\rangle \frac{\langle\psi_0|H|\psi_i\rangle^*}{|\langle\psi_i|H|\psi_0\rangle|^2} + c.c.\right] \qquad (70)$$

Here, the last term (c.c.) represents the complex conjugated portion of the expression. The first term represents the absorption process of a "bare atom" $\mu_0 \sim |\langle\psi_i|H|\psi_0\rangle|^2$, where the isolated atom transformed from the initial state ψ_i to an exited state ψ_0 at a higher energy-level, by annihilation of a field photon. On the other hand one can see the interference of the initial state and the perturbation of the final state. Hence, the structure information is curbed in $\chi(E) \sim \langle\psi_i|H|\Delta\psi_f\rangle$, the so-called "fine-structure" function. Including these notations in equation (70) it results to:

$$\mu(E) \sim \mu_0\,(E)[1 + \chi(E)] \qquad (71)$$

The result of the fine-structure function is given by:[174]

$$\chi(E) = \sum_j \frac{N_j\, e^{-2k^2\sigma_j^2}\, e^{-2R_j/\lambda(k)}\, f_j(k)}{kR_j^2} \sin[2kR_j + \delta_j(k)] \qquad (72)$$

This is the so called EXAFS-equation and contains all relevant structural information concerning the local environment of an absorber atom, such as coordination number (N_j), distances of the neighbouring atom (R_j) their mean-square-displacements (σ_j^2). The information regarding the scattering neighbouring atoms are contained in the atom scattering factor $f_j(k)$ and the phase shift $\delta_j(k)$ of the backscattered photo-electron, respectively. $f_j(k)$ and $\delta_j(k)$ are typically calculated by computer programs such as FFEF8, EXCURVE or GNXAS and provided for the fitting procedure of EXAFS equation.

3. Experimental

3.1. Material and sample preparation

All material investigated in this work are listed in Table 2 with their physical and chemical properties.

Table 2- Investigated materials with their physical and chemical properties and additional information.

Initial material	Company	Purity	Chemical formula	Aggregate / Crystal structure at room Temp.	Mass density [g/cm^3]	Melting point [°C]
Magnesium hydride	Alfa aeser	98 %	MgH_2	Solid/	1.45	327
Lithium borohydride	Sigma Aldrich	95 %	$LiBH_4$	Solid/	0.666	275
Calcium borohydrid	Sigma Aldrich	98 %	$Ca(BH_4)_2$	Solid/		--
Niobium (VI) fluoride	Alfa aeser	99.9 %	NbF_5	Solid/	3.293	79

3.1.1. High energy ball milling

All samples in this work were ball-milled in a high energy Spex 8000 mill/shaker. The Spex 8000 mill/shaker was placed in a glove box (BRAUN, company). The atmosphere (slightly higher than 1bar) in the glove box consisted of argon gas with less than 10 ppm oxygen and moisture, respectively. The glove box was kept under continuously purified argon atmosphere by a circulation system combined with a series of filters. The Spex 8000 mill/shaker was equipped with only one milling vial station. During the milling operation the vial follows a chain of motions which can be visualized with the shape of the number 8, when following the ends of the vial. It shakes the sample vial with a frequency of 60 Hz and amplitude of approximately 5 cm. The sample vial was made of stainless steel with a volume of ~ 194 cm^3. The vial was closed by screwing a cup on it. The cup was sealed with an elastic rubber O-ring to avoid any sample loss during the milling procedure. The amount of powder to be milled was kept always between 1g and 2g in the milling vial. The milling balls were made of stainless steel, as well. The ball-to-powder ratio was kept always at roughly 10:1.

3.1.2. Hydrogen de/absorption measurements

Volumetric measurements were performed by using HERA (designed by Hydro Quebec, Canada)[175] and PCTpro2000 (designed by Setaram company, France) systems, respectively, in order to study the dehydrogenation/hydrogenation properties of the composite systems and to prepare cycled samples for further investigation methods. In both measuring systems the absorbing gas volumes are pre calibrated. However, the principle how the amount and rate of desorbed/absorbed hydrogen gas is determined differs in the respective systems. PCTpro2000 system has only one sample holder and measures therefore the absolute pressure change in the entire volume (reservoir) with respect to initial pressure and time, respectively. Therefore, prior to each measurement the entire volume needs to be calibrated. HERA system is equipped with two pre calibrated sample holders (one serves as a reference holder and the other one contains the sample which is to be measured). Here, the measuring quantity is the change in differential pressure between the reference and sample side with respect to time. The HERA system has the advantage of being insensitive to slight reservoir temperature variations since it affects, both, reference and sample side hence it is cancelled in the differential pressure whereas it has big effect in PCTpro2000 on the absolute pressure. The disadvantage of HERA system is its complicated design (with two sample holders) and it can't measure the Pressure-Composition-Isotherms whereas PCTpro2000 is designed for such measurements, as well.

3.2. Material characterization

3.2.1. Coupled volumetric-DSC measurements and MS-measurements

Coupled manometric-calorimetric measurements were performed by connecting a PCTPro-2000 instrument (Setaram &Hy-Energy, France) with a Sensys high-pressure DSC (Setaram, France). Desorption measurements were performed by heating the samples (about 30 mg) from room temperature up to 500 °C at 3 °C/min under vacuum. For determination of the activation energy (E_a) measurements were performed with pure and doped samples under the same conditions by heating at 1, 3, 7 and 10 °C/min. Mass spectrometry (MS) measurements were performed by using the HPR-20 Q/C apparatus (Hiden-Analytical Ltd., UK).

3.2.2. SEM, EDS- and TEM-measurements

The material morphology and material local composition were characterized by SEM, using an EvoMA10 (Zeiss, Germany) microscope equipped with a LaB_6 filament. The composition of the samples was determined by EDS, using an INCA Energy 350 X Max detector from Oxford Instruments, equipped with a Be window. A cobalt standard was used for calibration of quantitative elementary analysis. To avoid oxidation during material handling, a special custom-made sample holder was used. The sample was loaded into the sample holder in a glove box and afterwards vacuum was generated inside the holder to transport the sample to the SEM. To further elucidate the nanoscopic structures and composition of the material, TEM was performed on a JEOL 3000F FEG TEM at an operating voltage of 300 kV. Samples were suspended in toluene then ultrasonicated before dropping onto 200 mesh holey carbon coated copper grids. Samples were shortly exposed to air (up to a minute) before they were inserted into the TEM column.

3.2.3. *In situ* SR-PXD-measurements

In-situ SR-PXD measurements were carried out at the powder diffraction beamline D3 at the DORIS III synchrotron storage ring (at DESY in Hamburg, Germany) and at the diffraction beamline I711 at MAXLAB (in Lund, Sweden). The samples were loaded into single crystal sapphire tubes in an argon glove box. The sapphire tubes were subsequently mounted in a gas pressure cell and exposed to a monochromatic synchrotron beam. A picture and a schematic description of the in situ XRD cell are displayed in the following figure. All details of the gas pressure cell and experimental set up are given in two works published by Bösenberg *et. al.* [1,176]. The diffracted intensities were at both beamlines collected by a MarCCD-165 area detector. The incident photon wavelengths were set to about 1 Å and 0.5 Å at I711and D3, respectively. Sample-to-detector distances were set roughly to about 80 mm at I711 and 125 mm at D3.

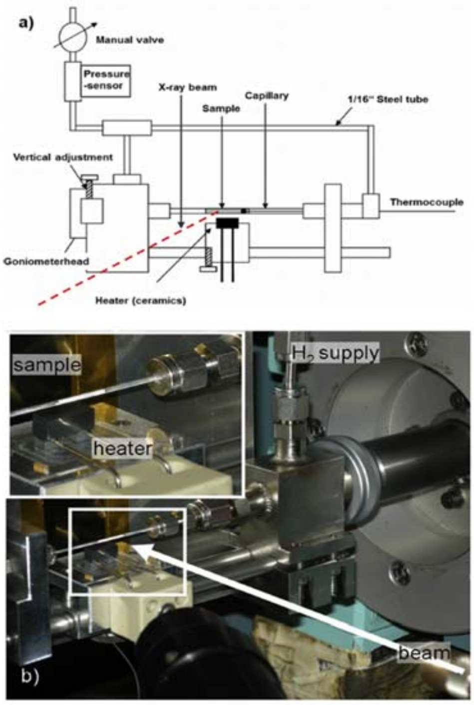

Figure 10. (a) Schematic description of the in situ XRD cell, and (b) Picture of the in situ cell is depicted mounted at the D3 beamline at DESY. In the inset figure a magnification of the sample in the capillary placed on the top of the heater is shown.[1, 2]

The sample was heated up by a ceramic oven placed underneath the capillary while the sample temperature was measured by a thermocouple positioned close to the sample in the capillary and controlled *via* a PID regulator. The temperature and pressure parameters were chosen close to volumetric measurements. The acquired 2D-patterns were further processed and integrated to a 1D curve using the program Fit2D[177] and the program FindIt (ICSD-database) [178] was used for phase identification.

3.2.4. **XAS-measurements**

X-ray absorption spectroscopy (XAS) measurements were performed at the C-beamline at DORIS III. The ideal amount of powder to be used for measurements was calculated by the program “XAFSMASS”.[179] The samples were then mixed with dry cellulose (~50 mg) in a mortar and pressed (5 bar) into pellets of 10 mm diameter. The pellets were placed in an aluminum sample holder and sealed with Kapton tape (55 μm in thickness) to avoid oxidation of the samples. Transition metals in their metallic state, in their fluorinated state and as borides were measured as reference materials. All measurements were recorded in transmission mode at the K-edge of transition metals. A schematic sketch of a XAS beamline is depicted in Figure 11. After passing the beamline optic the photons reach the XAS experimental station. The experimental station consists of three ionisation chambers (ICs) and two sample environments. Between the first and second ICs the sample was mounted and between the third and fourth IC a corresponding metallic reference foil was fixed in order to calibrate the energy axis. All ICs were filled with Argon gas and the ideal gas pressure in the respective ICs was calculated by using the software XAFSMASS and other software provided by the beamline.[179] Data acquisition was initiated at 200 eV prior to the K-absorption edge. The step width was chosen to be 2 eV (acquisition time of 60 s) up to 200 eV above the K-absorption edge, in order to have a high resolution of the X-ray absorption near edge structure (XANES). After the XANES-range the step width was increased to 5 eV (acquisition time of 180 s) up to 500 eV above the edge. Thereafter, the step width was once again increased to 7 eV (acquisition time of 300 s).

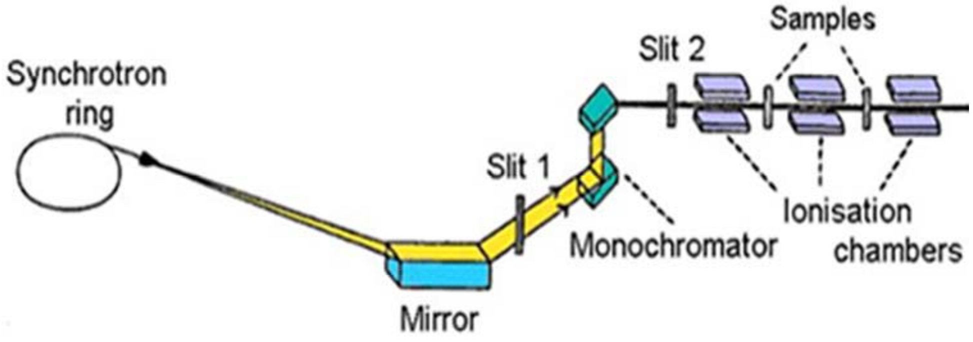

Figure 11. Schematic depiction of a XAS beamline at a synchrotron ring in HASYLAB (at DESY, Hamburg).[4]

Data acquisition was terminated at 1300 eV above the K-absorption edge, in order to have the maximum available information about the extended absorption fine structure (EXAFS) part of the XAS-spectra. For each sample three XAS-spectra were acquired. After removing their spikes these spectra were than aligned, and subsequently averaged in order to improve the data quality. XAS data processing and analysis were conducted by using the “IFEFFIT” software package.[180]

3.2.5. **ASAXS-measurements**

Anomalous small-angle X-ray scattering (ASAXS) measurements were performed at the beamline B1 at DORIS III (DESY in Hamburg, Germany). A detailed construction of the B1 ASAXS beamline is depicted in the Figure 12. The double crystal monochromator was made of a Si (311) with a wavelength resolution of $\Delta\lambda/\lambda < 10^{-4}$.
Instead of the multiwire detector (as is displayed in the Figure), a Pilatus 300 k detector was used, in the measurements conducted for this work. All measurements were carried out near the K absorption edge of niobium (18.99 keV), in order to characterize the Nb containing structures upon de/rehydrogenation cycles. The samples were mounted in an aluminium sample-holder with a circular hole of 5 mm in diameter and 0.25 mm in thickness. All samples were sealed with Kapton tape to avoid any oxidation of the material.

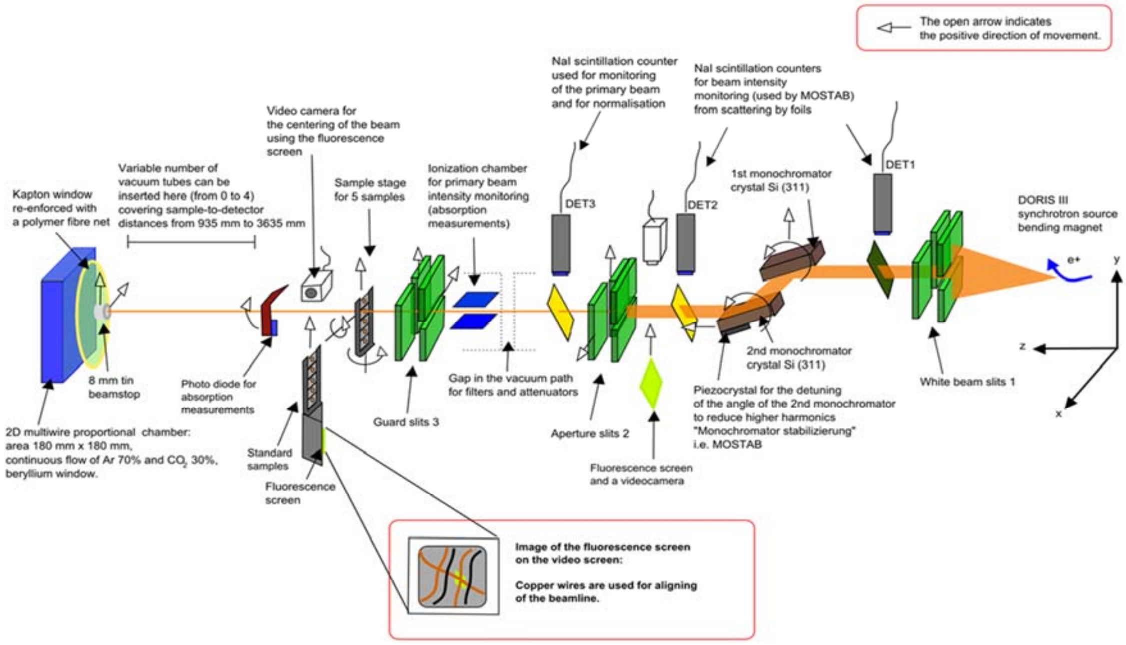

Figure 12 .Schematic outline of the ASAXS beamline B1 (DORIS III, DESY, Hamburg, Germany).

The ASAXS patterns were acquired at two sample-to-detector distances (D_{min}= 885 mm and D_{max}= 3585 mm) to cover the maximum available q-range and at four different energies, respectively. Here, q is the magnitude of the scattering vector: $q = (4\pi/\lambda)\,sin\,\theta$, where λ is the incident X-ray wavelength and 2θ is their respective scattering angle. All selected energies with their corresponding anomalous dispersion factors are listed in Table 3 (the dispersion factors are calculated based on the theory developed by Cromer & Lieberman).[181]

Table 3. Selected energies for the ASAXS-measurements at the K-edge of Nb and the corresponding anomalous dispersion factors.[5]

Ei	**Energy [eV]**	***f'***	***f''***
E1	18522	-3.095	0.557
E2	18822	-4.074	0.541
E3	18924	-5.027	0.535
E4	18926	-5.940	0.533

3.2.6. SANS/USANS-measurements

Small-Angle Neutron Scattering (SANS) measurements were performed at the SANS-1 station at FRM-II of Heinz Maier-Leibnitz Zentrum (MLZ, Bavaria, Germany). A schematic image of the beamline is shown in the following figure.

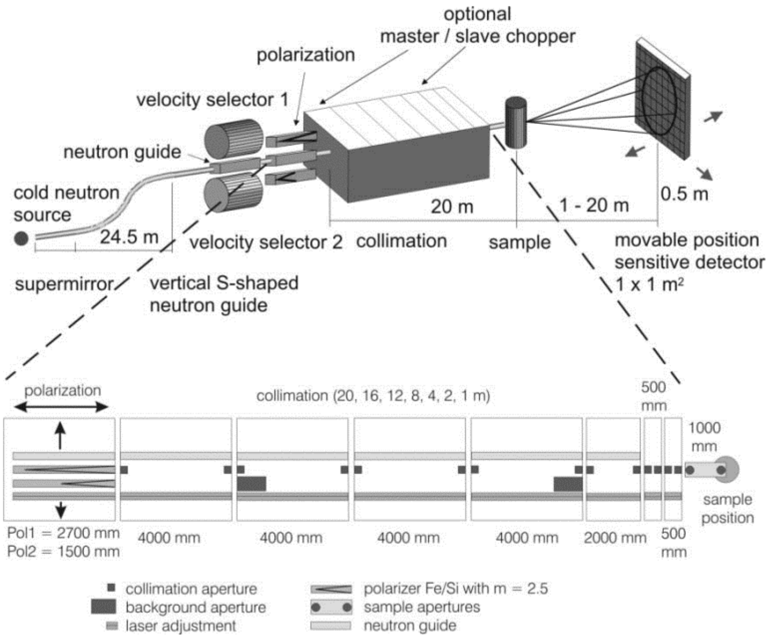

Figure 13. SANS-1 schematic set-up at the FRM-II in MLZ, Garching.[8]

The thermal neurons are delivered from the source with a maximum flux of $8x10^{14}$ n cm^{-2} s^{-1}. The incident neutron wavelength can be monochromated in the range of 3.4 Å – 30 Å by applying an array of two mechanical velocity selectors with wavelength resolution of 10 % and 6 %, respectively. The sample to detector distance can be set in the range 1.1 – 21 m with a maximum *q*-range of 0.001 $Å^{-1}$ - 2 $Å^{-1}$. For the performed experiments in this work three sample to detector distances (1.6, 8, 20 m) and two wavelengths (6, 12 Å) were applied, respectively, to cover the maximum *q*-range available at the high *q* values and to cover a reasonable *q*-range in the low *q* region in order to have a good overlapping with the USANS measurements. For the "short" sample to detector distance (1.6, 8 m) 6 Å was applied whereas for longest distance (20 m) 12 Å was selected. The scattering intensities were measured by using a 128 ^{3}He proportional counter detector with an area of 1000x1020 mm^2 with a count rate of 1 MHz. Silverbehenate (AgBe) was measured at short distance (1.6 m) to calibrate the *q*-axis. A water standard was measured in order to set the scattering intensities onto an absolute scale. All SANS data were processed by BerSANS software.[182] In addition to SANS measurements USANS measurements were carried out to evaluate the larger structures present in the samples. USANS measurements were performed at the BT5-Instrument at the National Institute of Standard and Technology (NIST) in Gaithersburg (Maryland, USA). A schematic description of the instrument is shown in the following figure.

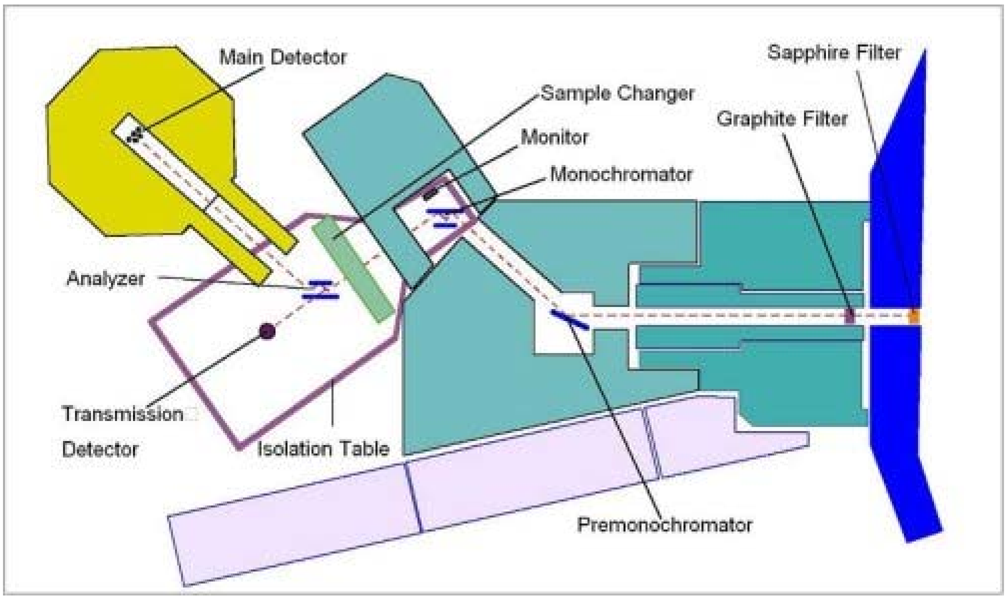

Figure 14. Sketch of the BT5-USANS instrument at NIST in Gaithersburg (Maryland, USA)[3] [2]

The instrument was equipped with a perfect crystal diffractometer (PCD) in order to have ultra-high resolution USANS data. The flux at the sample was > 17000 n cm^{-2} s^{-1} and the incident neutron wavelength was about 2.4 Å. The accessible q-range was 0.00003 $Å^{-1}$-0.01 $Å^{-1}$. The so observed 2D USANS data were subsequently reduced to 1D scattering curves by using a program designed by Scott *et al.*[183] After desmearing and correction for multiple scattering (a procedure described by Staron & Bellmann in detail[184]) the final USANS scattering curves were obtained and subsequently merged with the SANS curves.

3.2.7. NMR-measurements

^{11}B Solid State NMR measurements were carried out on a 500MHz (^{11}B frequency: 160.46 MHz) Bruker Avance III HD NMR spectrometer equipped with a Bruker 4 mm BB/1H-19F probe. Rotation speeds between 8 kHz and 12 kHz were used and due to the high ^{11}B background of the probe all measurements were performed employing the zgbs sequence. The repetition times were chosen in such a way that the sample was fully relaxed. Chemical shift values were measured relative to BF_3Et_2O using a 0.1M H_3BO_3 solution as a secondary standard at 19.6 ppm.

3.2.8. BET-measurements

BET stands for Brunauer Stephen, Emmett, H. Paul and Teller, Edward who were the developer of this method. BET is an analysing method for determination of (specific) surface area of porous material *via* inert gas adsorption. BET measurements were performed with a micromeritics ASAP 2020 Surface Area and Powder Analyser using N_2 as adsorbent gas at a sample temperature of liquid nitrogen. Prior to the BET-measurements, all samples have been outgassed for 24 hours under vacuum at a temperature of 100°C to remove impurities adsorbed to the surface. Both the doped and undoped samples were measured after milling procedure as well as after first dehydrogenation. The highest possible sample amount (1.5 grams) together with a filler rod was used to ensure a minimal dead volume inside the sample holder for higher measurement accuracy.

4. Results and discussion of Li-RHC

4.1. Effect of additives on the hydrogen de/absorption kinetics of the $LiBH_4$-MgH_2 hydride composite systems

4.1.1. Volumetric measurements

All kinetic curves were collected at a heating rate of 3 K / min to a maximum temperature of about 390 °C at 4 bar of hydrogen backpressure for dehydrogenation and 50 bar and 350 °C for rehydrogenation, respectively. In order to enhance the reaction kinetics of the pure Li-RHC system several transition metal halide and oxide additives ($ScCl_3$, Sc_2O_3, $TiCl_3$, TiF_3, TiO_2, VCl_3, V_2O_5 NbF_5, and Nb_2O_5) were used. Among them, NbF_5 showed the best performance regarding the de/rehydrogenation reaction kinetics. Therefore, in this work only the effect of NbF_5 on the Li-RHC was further investigated in detail. The first dehydrogenation reaction of pure and doped (with $0.1NbF_5$) Li-RHC are presented in Figure 15. The normalized converted fraction of desorbed hydrogen is plotted over the corresponding elapsed time in hours. As one can see, the overall dehydrogenation reaction process of undoped Li-RHC takes place in approximately 45 h. This dehydrogenation process proceeds in two distinct reaction steps separated by a plateau phase. The first reaction step is accomplished after 0.75 h followed by a plateau phase which extents nearly up to 18 h, before the second reaction step occurs. The subsequent last reaction step takes roughly 20 h. The dehydrogenation reaction of the Li-RHC with additive shows significantly improved kinetics in comparison to the system without additive (pure system) (see Figure 15).

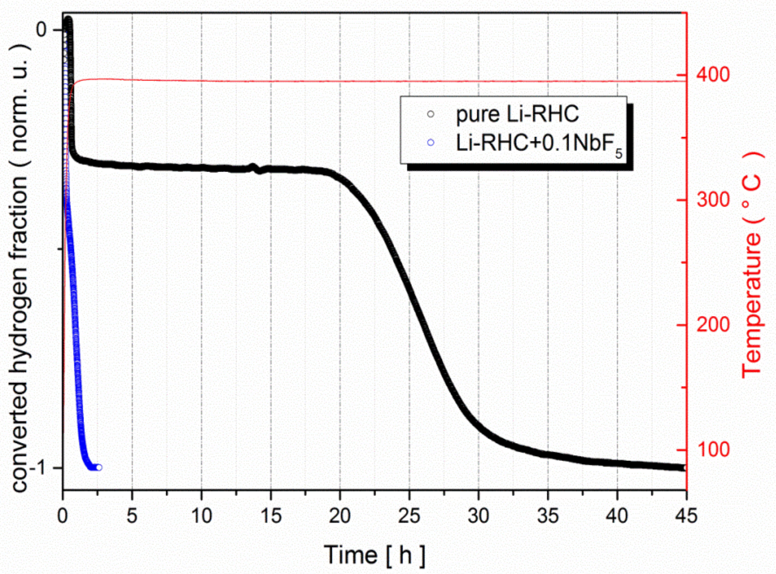

Figure 15. Dehydrogenation reaction kinetics of pure and doped Li-RHC under 4 bar of hydrogen backpressure. The samples were heated up (3 K/min) to about 390 °C and were kept isothermal for the rest of the measurement (measured at HZG).

The two dehydrogenation reaction steps, however, remain unchanged. In contrary to the dehydrogenation reaction of pure Li-RHC, there is no incubation period observed in the doped system. The overall reaction kinetics of the first desorption is improved by a factor of ~ 20 relative to that of the pure Li-RHC system. The reaction kinetics of the first step for both systems is approximately the same and is completed roughly after 0.25 h. The second reaction step of the doped system proceeds for ~ 1.65 h, which is significantly (about ~20 times faster) faster than the corresponding value (20 h) of the pure Li-RHC. In order to demonstrate the reversibility of the system, a second dehydrogenation cycle at the aforementioned conditions was done.

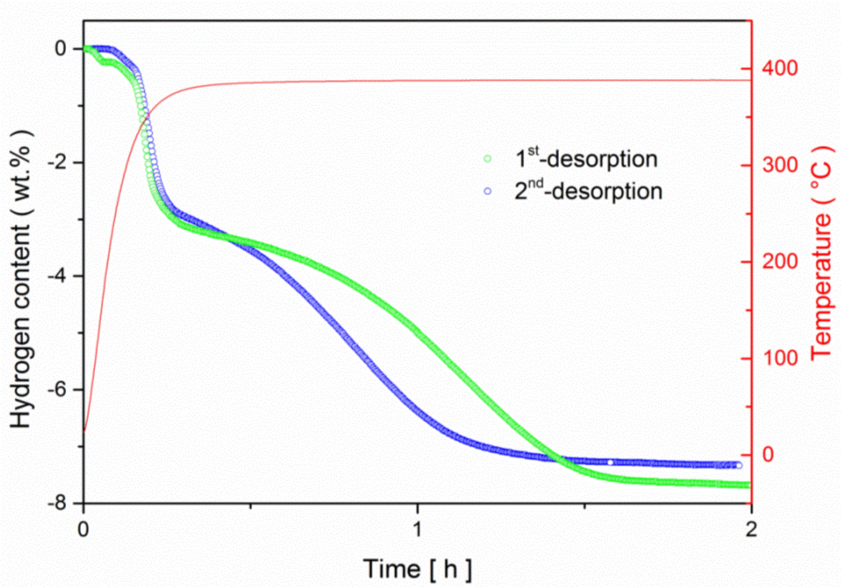

Figure 16. First and second dehydrogenation reaction of Li-RHC+0.1NBF$_5$.
The red curve shows the temperature evolution with time (measured at HZG).

As can be seen in Figure 16, the doped system shows good reversibility over the dehydrogenation cycle. The second dehydrogenation reaction is improved in comparison to the first one by roughly 20 %. Over the second dehydrogenation process the system releases lower (7.2 wt. % H_2) hydrogen content in comparison to the corresponding value (7.6 wt. % H_2) for the first dehydrogenation reaction, which means a hydrogen capacity loss of about 5 %. According to volumetric measurements, the theoretical capacity of the Li-RHC+0.1NbF$_5$ sample is not reached, if the following chemical reaction is assumed:

$$2\mathrm{LiBH_4} + \mathrm{MgH_2} + 0.1\mathrm{NbF_5} \leftrightarrow 2\mathrm{LiH} + \mathrm{MgB_2} + 0.1\mathrm{NbF_5} + 4\mathrm{H_2} \qquad (73)$$

$$(9.0\ \mathrm{wt.\%\ H_2})$$

A possible explanation may be that the additive has reacted during the ball milling procedure with the surrounding hydride matrix. In order to clarify this conjecture, an experimental confirmation of the phases is important. Also for the evolution and transformation of all existing phases with respect to temperature and time it is crucial to follow the kinetics of different reaction steps. For this reason *in situ* SR-XPD experiment were carried out, and the results are presented in the following subsection.

4.1.2. In situ SR-XPD-measurements

By means of *in situ*-SR-XPD the reaction paths of Li-RHC+0.1NbF_5 were investigated. The results are presented in Figure 17 and Figure 18, respectively. In both figures the intensities of the diffracted beam are plotted over temperature and 2-theta diffraction angle. As it can be seen from Figure 17, the crystalline phases after milling consist of MgH_2, orthorhombic $LiBH_4$ (*o*-$LiBH_4$) and LiF. However, no diffraction peaks of any Nb-containing phases are detected. The temperature is raised from room temperature up to a maximum temperature of 390 °C and kept isothermal for one hour. The reaction paths in the range of the temperature ramp up to 390 °C are presented in Figure 18. Here, with increasing temperature the diffraction patterns are narrowing and they shifted toward lower diffraction angles.

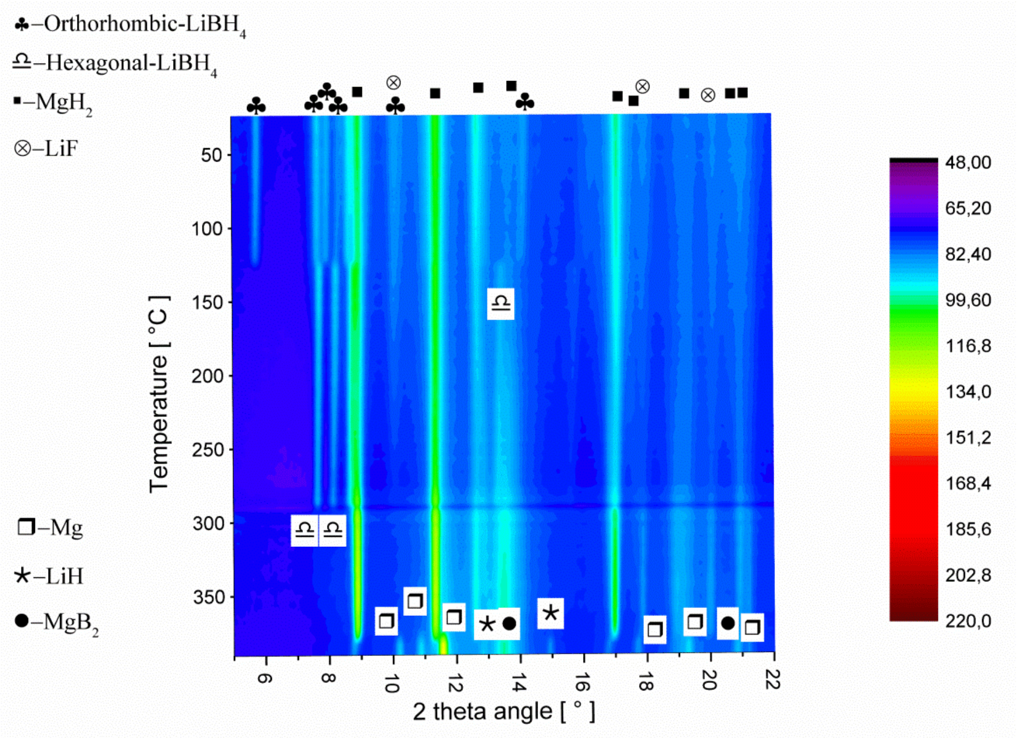

Figure 17. In situ SR-XPD plot of first desorption of Li-RHC+0.NbF_5 with a temperature ramp of 3 K/min up to 390 °C. (measured with $\lambda = 0.5$ Å at HASYLAB, DESY, Hamburg)

The prior mentioned case indicates a higher degree of ordering in the material, which was previously partially destroyed by the high-energy ball milling procedure. The later mentioned case is due to the expansion of the unit cells of the crystalline phases with increasing temperatures. The first change in diffraction patterns occurs at about 120 °C which can be assigned to the structural phase transformation from orthorhombic *o*-$LiBH_4$ (space group *Pnma*)[185] to hexagonal *h*-$LiBH_4$ (space group $P6_3mc$).[186] Around 270 °C the diffraction peaks of *h*-$LiBH_4$ disappear, which can be assigned to liquefaction of *h*-$LiBH_4$. Around 370 °C, the Bragg-peaks of MgH_2 starts to diminish and diffraction peaks of metallic Mg appear, which can be correlated with the decomposition of MgH_2. Simultaneously to metallic Mg, also Bragg-peaks of MgB_2 and LiH appear. The plateau phase, which occurs in the dehydrogenation reaction of pure Li-RHC, is not observed here. Moreover, after decomposition of MgH_2 immediate appearance of MgB_2 is detected. This is in good agreement with the volumetric measurements presented in subsection 4.1.1. These phases grow with time at isothermal conditions as is displayed in Figure 18. As the diffraction intensities of the metallic Mg-phase decreases, an increase of diffraction intensities of MgB_2 and LiH is observed, which implies a mutual reaction between metallic Mg and $LiBH_4$ (decomposition of $LiBH_4$ is not observable *via* XRD here due to its liquid state at the applied temperatures).

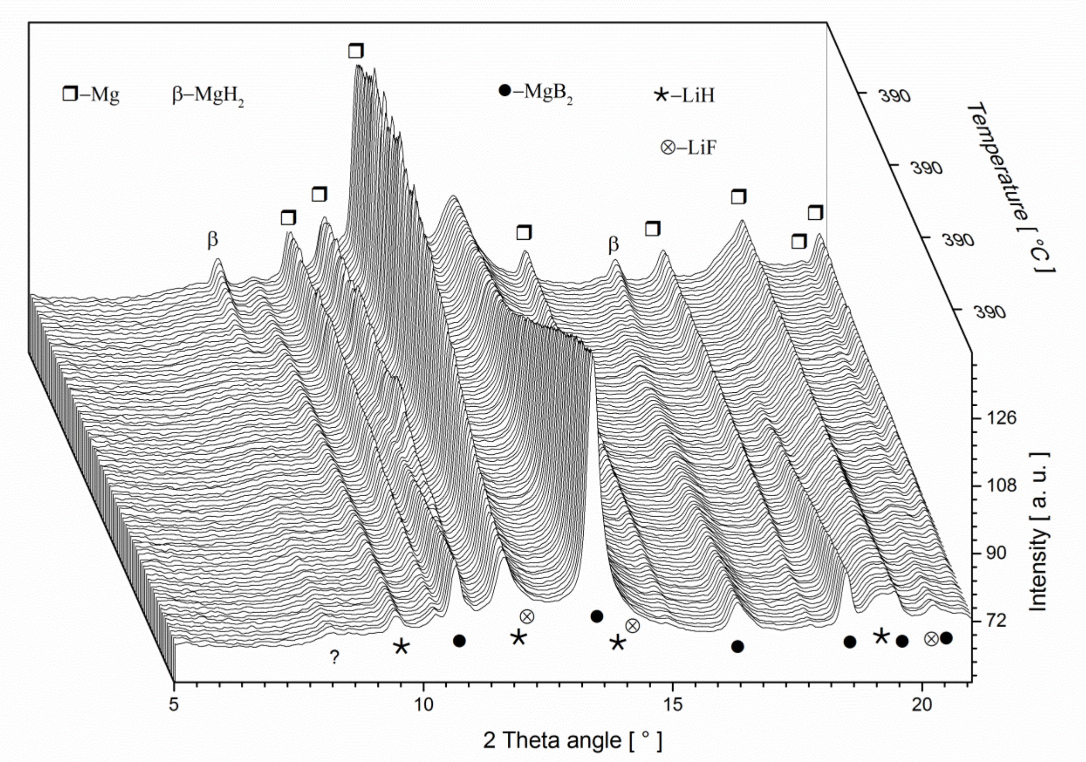

Figure 18. In situ SR-XPD plot of first desorption of Li-RHC+0.NbF_5 at isothermal condition, and 4 bar of hydrogen backpressure (measured with λ = 0.5 Å at HASYLAB, DESY, Hamburg).

Since no Nb-containing phases could be detected by *in situ* SR-XPD measurements, X-ray Absorption Spectroscopy (XAS) measurements were carried out to determine the chemical state and the local environment of Nb in the Li-RHC matrix.

4.1.3. EXAFS/XANES measurements

Near Edge Structure of the XAS-spectra (XANES) were performed to determine the valance states of niobium in the Li-RHC at different hydrogenation states. Several reference compounds such as NbF_5 and NbB_2 were measured to compare them to the valance states of niobium in the hydride matrix. The first derivatives of the XANES region of sample and references were built to emphasize the XANES structures. The results of these measurements are displayed in Figure 19.

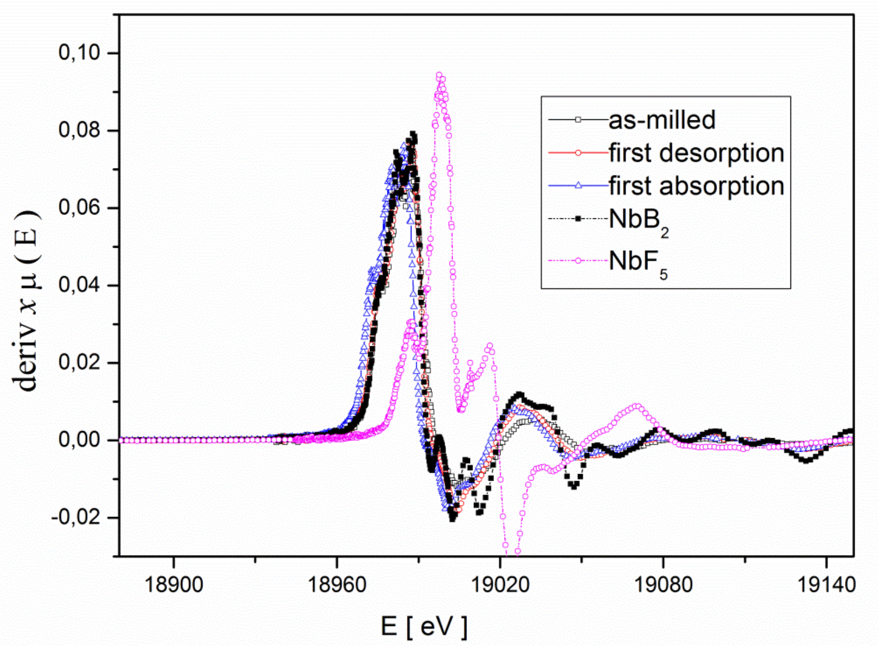

Figure 19. XANES derivative of samples and references (measured at the beamline C1 at the DORIS III synchrotron storage ring at HASYLAB (DESY, Hamburg, Germany)).

A comparison between the XANES spectra of Li-RHC+0.1NbF_5 samples shows that Nb has approximately the same oxidation state in the milled and in the cycled states, respectively. However, a comparison between the XANES spectra of samples and reference compounds indicate a change of oxidation number of niobium from Nb^{5+} to Nb^{2+}. In order to study the fluctuations of the nearest neighbours (NNs) of Nb in the hydride matrix at different hydrogenation states, the EXAFS regions of the XAS spectra of the samples together with NbB_2 and NbF_5 reference spectra were extracted and plotted in un-weighted $\chi(k)$ against k in the k-range of [2-12] $Å^{-1}$ (see Figure 20). The local environment of Nb in the Li-RHC shows considerable changes after the ball milling process in comparison to NNs of Nb in the NbF_5 lattice. These positional shifts hint to a removal of flour atoms and their substitution by other atoms. Also, the decrease in oscillation strength shows that the long-range order is substantially decreased, which indicates a higher degree of disorder/dispersion of Nb-containing phase(s).

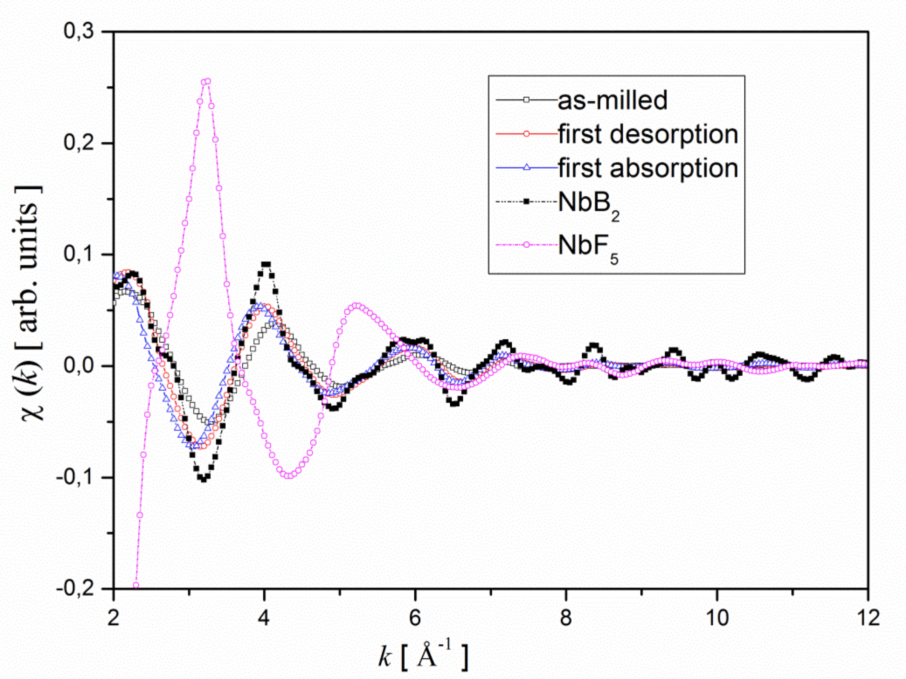

Figure 20. Unweighted EXAFS of samples and references in the K-range between 2 and 12(measured at the beamline C1 at the DORIS III synchrotron storage ring at HASYLAB (DESY, Hamburg, Germany).

After the first dehydrogenation, the EXAFS-amplitudes are increased and they remain stable upon further de/rehydrogenation process. This hints to a higher degree of ordering and/or growing of Nb-containing structures relative to the ball milled sample. Furthermore, a comparison of the Li-RHC+0.1NbF_5 sample at different hydrogenation states with the reference spectrum of NbB_2 shows that the spectra match excellently, indicating a F-B atom exchange in the nearest neighbourhood (NN) of the central Nb-atom. However, the spectrum of the as-milled sample, in particular, is not perfectly in phase with those of the cycled samples. This indicates that a minor portion of NbF_5 remained unreacted in the hydride matrix after the milling process. To reveal the local environment around the Nb-atom, the data (presented above) were Fourier transformed and displayed in Figure 21. It shows the radial distribution (RD) of atoms around the resonant atom (Nb being the resonant atom) situated at the origin of the coordinate system. The first peak in RD curves of as-milled and cycled samples are shifted towards higher distances relative to the first peak of NbF_5 reference but they coincide rather well with the first peak of the NbB_2 reference. It should be noted, that the RD of as-milled sample does not match perfectly with the curves of cycled samples and reference sample. A linear combination fitting procedure gave a relative content of 18 % NbF_5 and 82 % NbB_2 in the as-milled Li-RHC sample, whereas in all cycled samples the content of NbF_5 was determined to be 0 %. To verify the F-B exchange and the formation of NbB_2 in the Li-RHC+0.1NbF_5 samples, *ab initio* calculations were carried out using the FEFF6-program,[180] and the results are presented in Figure 22**.**

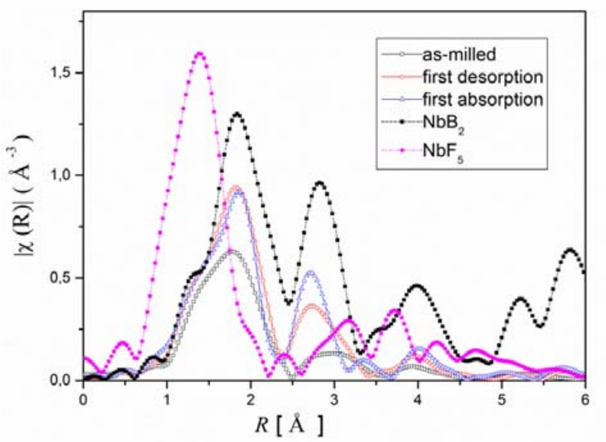

Figure 21. EXAFS signals of samples and references plotted in the R-space (measured at the beamline C1 at the DORIS III synchrotron storage ring at HASYLAB (DESY, Hamburg, Germany).

In the calculation the magnitudes of scattering amplitudes were not corrected for electron relaxation processes, since only the existence of the mentioned phases were the centre of interest. FEFF- calculations were performed assuming F to be in the crystalline state of NbF_5 (Space Group *C12/M1*; Cryst. Sys. monoclinic (ICSD #26647)) and B in the crystalline state of NbB_2 (Space Group *P6/MMM*; Cryst. Sys. hexagonal (ICSD #30328)). The calculations identify the first peak of NbF_5 as the fluorine backscattering amplitude and the first and second peak of the NbB_2 reference were addressed to the boron and Nb backscattering amplitudes, respectively.

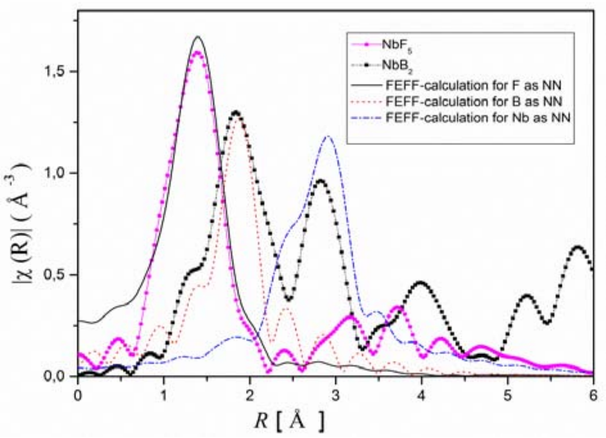

Figure 22. RD - functions of the samples and their corresponding FEFF-calculated backscattering amplitude for the Nearest-Neighbour (NN) (measured at the beamline C1 at the DORIS III synchrotron storage ring at HASYLAB (DESY, Hamburg, Germany).

This clarifies the removal of fluorine atoms and shows the presence of niobium boride phase (NbB_2) in the milled Li-RHC+0.1NbF_5, which remains stable upon further dehydrogenation and rehydrogenation cycling procedure. Since the effectiveness of the applied additive is very much related to their size and distribution in the host material, the size distribution of NbB_2 in doped Li-RHC was investigated and the results are presented in the following subsection.

4.1.4. **ASAXS measurements**

The size distribution of NbB_2 particles in the hydride matrix at different hydrogenation states was determined using the ASAXS method. In Figure 23 exemplary curves of ASAXS for Li-RHC+0.1NbF_5 system after the first absorption are shown. Figure 24 shows the ASAXS curves after correction for scatterings effects described in the following. The peak in the region of 4-5 nm^{-1} belongs to scattering of the Kapton foil, which was used to seal the sample. In the inset figure, the resonant behaviour of the sample at changing wavelengths of the incident beam is demonstrated. As the energy of the incident photons approaches the K-edge of the resonant atom (niobium) the intensities of the scattering curves in the range of large q-values (Porod-region) increase considerably (see Figure 23). This is due to the fluorescence and inelastic Raman-scattering which leads to an energy dependent constant shift of the scattering intensities.[187]

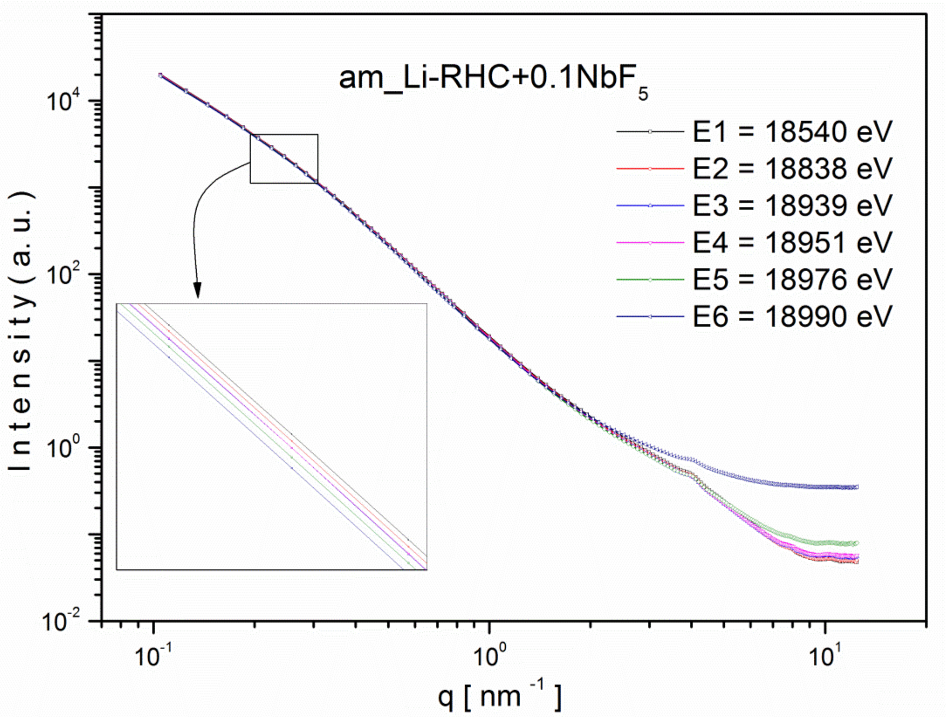

Figure 23. ASAXS curve collected at 6 energies below the K-edge of Nb. At the high q-values the inelastic scattering in dependency of energy is visible (measured at the beamline B1 at the DORIS III synchrotron storage ring at HASYLAB (DESY, Hamburg, Germany).

This constant is found and removed here by fitting a power law curve with an energy dependent constant to the tail of each scattering curve at different energies:

$$B_i(q, E_i) = q^{\alpha} + c(E_i) \tag{74}$$

Figure 24 shows the background corrected scattering intensities for the same sample as shown above. All other scattering curves have similar scattering behaviour and are shown in appendix. The shape of the scattering curve in Figure 24 gives the evidence of two preferred structures in the sample (see inset figures, both figures were magnified with a common factor). At the large q-values around 4 nm^{-1} the structures are rather resonant and they can be estimated to be approximately 2 nm in size (using the rule of thumb: $d \approx 2\pi/q$).

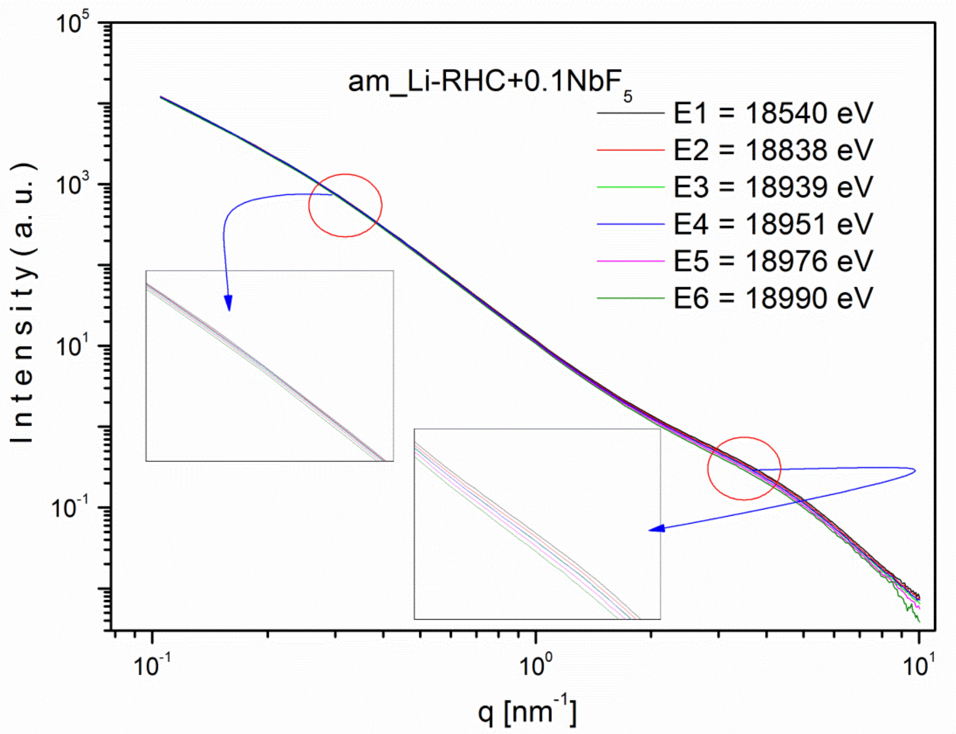

Figure 24. ASAXS curves as shown in Figure 23, each scattering curve subtracted by an energy dependent constant value (measured at the beamline B1 at the DORIS III synchrotron storage ring at HASYLAB (DESY, Hamburg, Germany).

The structures that are located about 0.3 nm^{-1} are relatively less resonant in comparison to the structures at large q-values and their size can be estimated to be roughly 10 nm. The resonant scattering contribution of the total intensity was extracted by using the method described by Goerigk *et al.*[188] (see subsection 2.7.2.2). In Figure 25, the resonant scattering curve together with its total and mixed resonant scattering curve with their corresponding fits of the as-milled sample is presented, exemplary. All curves were fitted by assuming surface scattering from much bigger particles (out of experimental accessible q-range) and two spherical like particle distributions. The form factor of a sphere can be found in subsection 2.7.2.2 or in.[189] The fitting procedure was carried out using the program SASfit.[190] As can be seen from Figure 25 the intensities in the Guinier region (see section 2.7.2) are increasing which implies the existence of bigger structures in the total and mixed resonant scattering (see section 2.7.2.2) curves, whereas the resonant scattering curve shows a plateau in the Guinier region, which shows that there are most likely no bigger resonant structures in the sample. As an example, fitting procedure of the Guinier region for all three curves were performed and their size distributions were calculated.

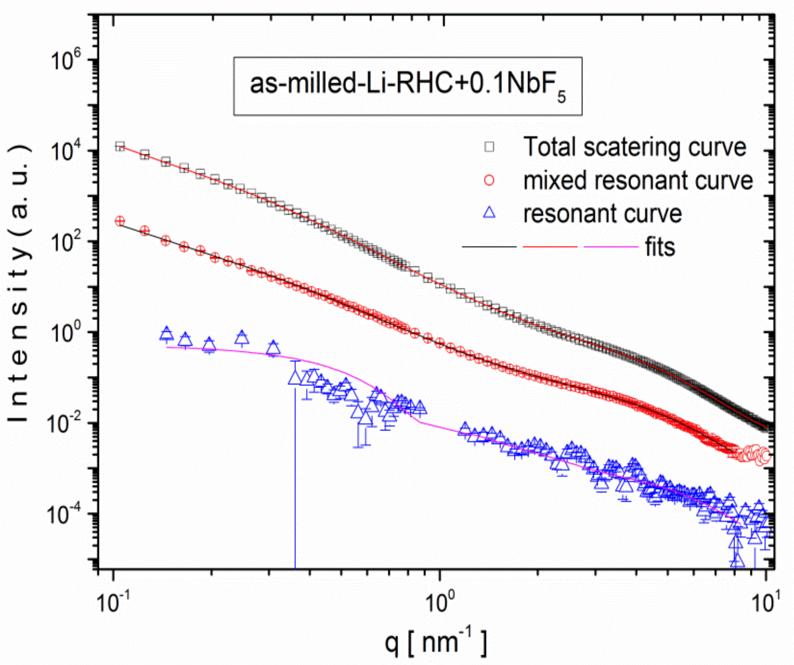

Figure 25. Resonant scattering curve together with total and mixed resonant curve with their corresponding fits (measured at the beamline B1 at the DORIS III synchrotron storage ring at HASYLAB (DESY, Hamburg, Germany).

The results of the size distributions are shown in Figure 26. The size-distributions functions were normalized by the integrals below the curves. The maximum structures obtained from the total scattering curve are significantly bigger in amount and size in comparison to mixed resonant and especially to pure resonant structures which is a reasonable result, considering the addition of small amounts of NbF_5 in the hydride matrix. However, the polydispersity and amount of the pure resonant structures in the sample is considerably smaller in comparison to the corresponding value for mixed resonant structures. As can be seen in Figure 25, the statistics of the resonant curve is rather poor; however, it gives very useful information on the range of sizes present in the samples. As a compromise for having relatively good statistics and being very close to the resonant curve the difference curves were chosen for a new fitting approach. Here, it is assumed that the mixed resonant structures are very big and therefore their contribution in the difference curve can be considered as a power-law contribution with some marginal background. We can assume spherical shapes for small and large resonant particles. The result of this procedure is presented in Figure 27.

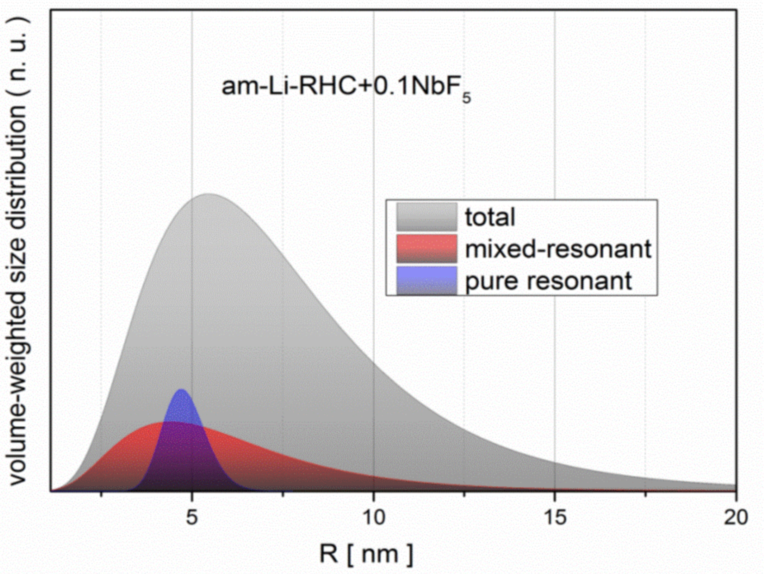

Figure 26. Volume weighted size distribution of the total sample, mixed resonant structures and the pure resonant structures.

There it is clearly visible that big resonant particles have much smaller resonant scattering contribution to difference-scattering curve in comparison to small resonant particles, relative to mixed-resonant matrix structures. The result of the calculated size distribution for the big resonant particles using the aforementioned procedure is shown in Figure 28.

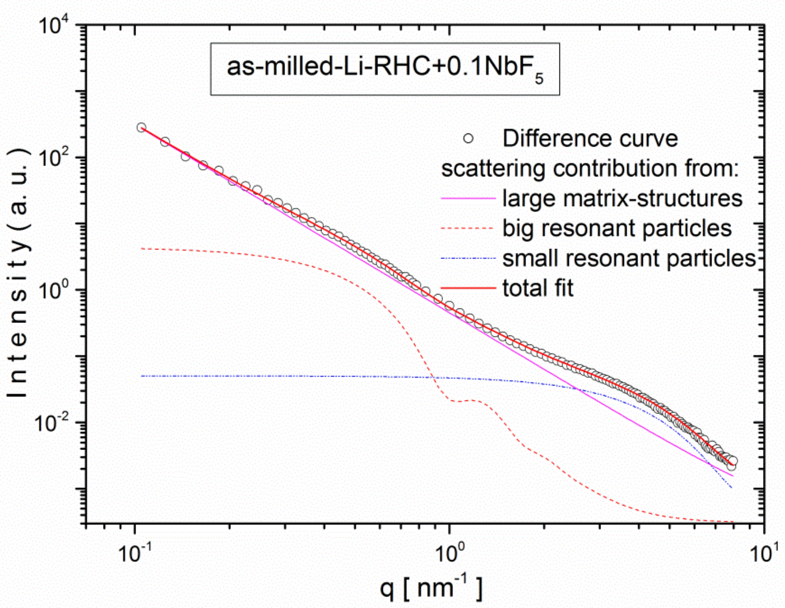

Figure 27. Contribution of different structures to the difference scattering curve of the as-milled Li-RHC+0.1NbF$_5$ with its corresponding total fit.

To follow the size evolution of the resonant structure upon the de/rehydrogenation process the cycled samples were measured and the pure resonant scattering contributions were extracted and the corresponding size distributions were calculated which are displayed in Figure 29.

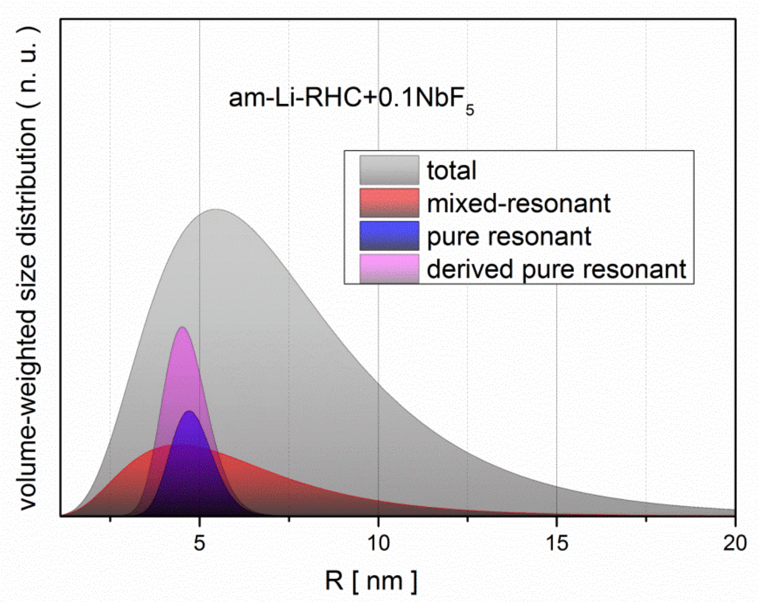

Figure 28. Volume weighted size distribution as shown in Figure 26 with addition of the size distribution of derived pure resonant method.

As can be seen, the resonant scattering structures have two distinct size distributions. One distribution lies in the range of 1nm and the other one at about 10 nm in size, as was estimated before. However, the amount of particles distributed in the range of 1 nm is significantly higher than those in the range of 10 nm. Concerning the larger resonant structures, their mean size increases over the cycle from about 10 nm to 13 nm (see Figure 29 b). The average sizes of the small distribution shifts from around 2 nm to about 1 nm (see Figure 29 a). It should be noted that the dynamics of size distributions over the cycle is mutual. The amount of small resonant structures in the as-milled sample is far bigger than those present in the de/rehydrogenated samples, respectively, whereas it is *vice versa* in the case of size distributions of the larger resonant particles. It is also visible from Figure 29 (a) that after the dehydrogenation process the sizes of the average resonant structures remains stable. However, their amount increases after the rehydrogenation process. Although these results are described technically well by the fits to the scattering curves, there are still remaining questions about the statistical distribution of niobium containing particles in the hydride matrix.

It is not clear, why niobium particles should be distributed in distinct size regions during the milling procedure, which is a highly random process, and why the resonant scattering behaviours of the two distributions are significantly different?

To make an attempt to answer these open questions, a series of Li-RHC samples with different content of NbF_5 additive (Li-RHC+$x$$NbF_5$, with $x = 0, 0.01, 0.025, 0.05$ and 0.1) was prepared (all samples were milled for 5 hours under the same conditions) and measured in SAXS setup. The results of these measurements are displayed in Figure 30. First of all, in Figure 30 it is visible that all scattering curves of the samples obey two different q^{α} behaviours (power-law) in the low and in the high q-region, respectively. In the low q-region the power law exponent is between 3.2 and 3.5. This indicates fractal structures with a dense core and small fractal units on the surface. The exponent in the high q-region for all scattering curves is about 2, which suggests open fractal structures ("mass fractal") consisting of small units building large mass fractal aggregates [161]. Since the particles consist essentially of grains and grain boundaries, the open fractal structures at the high q-region can be attributed to grain boundaries, where atoms are almost randomly distributed around the grain surfaces in the high q-region, with typical sizes of 1-3 nm for grain boundaries, and the dense particles in the core with fractal structures can be correlated with the grains themselves. By portion wise addition of NbF_5 in the Li-RHC, an impact on both, the low as well as the high q-region of the scattering curves is observed.

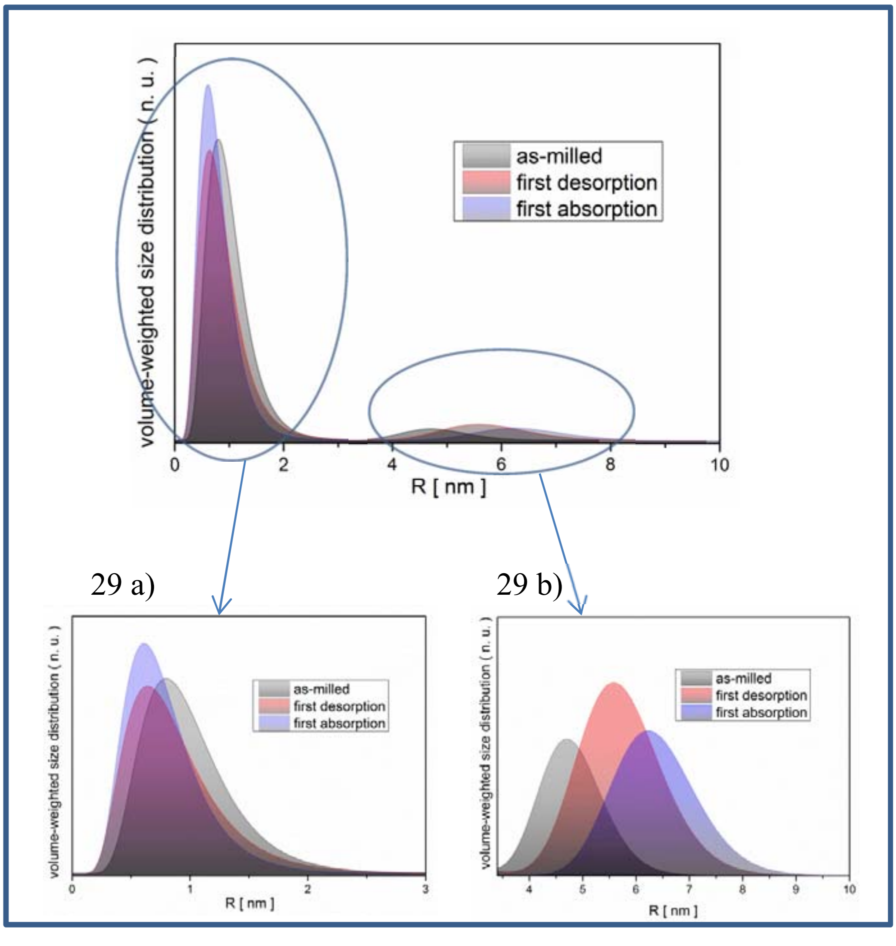

29 a)

29 b)

Figure 29. Volume-weighted size distribution of the Li-RHC+0.1NbF_5 sample cycled once. Figure 29 a) and b) display the magnification of small and large size distributions, for the sake of clarity.

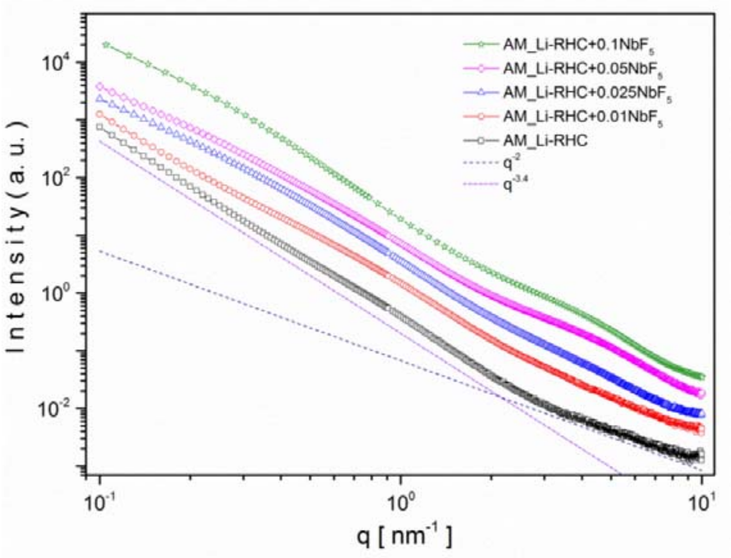

Figure 30. SAXS curves of Li-RHC + xNbF$_5$ samples with x being 0, 0.01, 0.025, 0.05 and 0.1. Additionally two power law lines are shown which indicate a division of structures in two fractal fractions (measured at the beamline B1 at the DORIS III synchrotron storage ring at HASYLAB (DESY, Hamburg, Germany).

The scattering curve of the sample without any addition of NbF$_5$ follows almost perfectly the power law in the high q-region. However, in the low q-region the scattering curve deviates slightly from the power law in the range of 0.4 - 2 nm^{-1}, corresponding to preferred structures (which are most likely grains) between 10 - 15 nm in size. Interestingly, the bigger resonant structure appears rather prominent with small amount of additive, whereas the signal at high q-range becomes clearly visible only after addition of 0.05NbF$_5$. By increasing the content of the additive the structures in the high q-region start to build preferential sizes which are distributed around 1 - 1.5 nm. Thus these structures can be attributed to Nb-containing structures as observed in Figure 24. The signal of the structures centred at about 1 nm^{-1} in the undoped sample increases with higher content of the additive. Furthermore, in contrast to structures in the high q-region, the centre of these signals also shifts toward lower q-values. This indicates a growth of the structures located in the low q-region with increasing amount of additive. This behaviour contradicts the results of ball milling procedure, in which the provided energy is transferred to the powder to refine its grain and particle sizes. This contradiction can be solved if one assumes that the structures at low and high q-range are not entirely independent but they are rather interrelated. Assuming smaller structures to be NbB$_2$ nanoparticles (distributed in flat fractal structures at the grain boundaries) and the bigger structures (at the low q-range) to be grains (with dense core surrounded by small NbB$_2$-nanoparticles distributed in fractal structures on their surfaces), would explain the resonant behaviour of both structures. Due to high Nb content in NbB$_2$ nanoparticles, they “respond” more “sensitive” to the resonant incident photon, whereas the bigger particles have only a small fraction of Nb in comparison to their volume on their surfaces and they react, accordingly, less sensitive to the resonant incident beam. These argumentations can basically be condensed in a simplified spherical core-shell model, where the core consists of a spherical grain and the shell is made of NbB$_2$. The scattering intensity and the form factor of a spherical core-shell particle are given by:

$$I_{core-shell}(q,R,\Delta R,\Delta\eta_1,\Delta\eta_2) = [F(q,R+\Delta R,\Delta\eta_2) - F(q,R,\Delta\eta_2-\Delta\eta_1)]^{\,2}$$
$$wehre\colon F(q,R,\Delta\eta_i) \;= \frac{4}{3}\pi\Delta\eta_i\, R^3\, \frac{3[\sin(qR) - qRcos(qR)]}{(qR)^3} \qquad (75)$$

Where, q is the scattering vector, R the core radius, ΔR the thickness of the shell and $\Delta\eta_{i=1,2}$ contrast between core and shell. By applying this model only one polydisperse size distribution was needed to fit the entire scattering curve. The resulting fit for the as-milled sample is shown in Figure 31, and all the other fits can be found in the appendix. For the as-milled sample the calculated size distribution gives an average core size of 12-15 nm with shell thickness of 1-1.5 nm (see Figure 32), which is in good agreement with results obtained with previous models. The fit result is not perfect, particularly in the middle and for very small q-values, due to the very simplified model of a grain and its boundaries assumed for fitting the experimental curve.

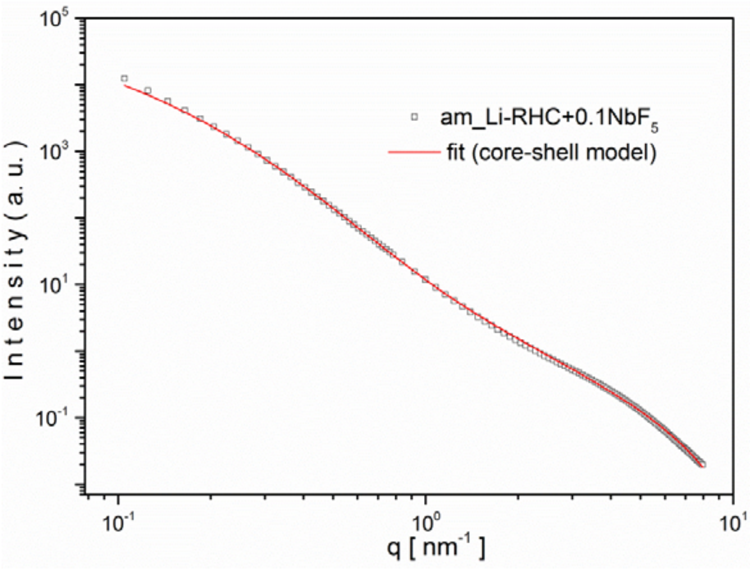

Figure 31. Total scattering curve of the as-milled Li-RHC+0.1NbF$_5$ sample with its corresponding fit assuming a spherical core-shell model (measured at the beamline B1 at the DORIS III synchrotron storage ring at HASYLAB (DESY, Hamburg, Germany).

Of course, the grains are most likely not that spherical and they are not fully covered with a shell consisting of only the additive. Therefore, this model should be taken as a first approximation to reality, where the grains can have all kinds of shapes and their boundaries have highly complex two dimensional fractal structures. However, this basic model already gives a useful and profound insight into the distribution of the additive inside the hydride matrix.

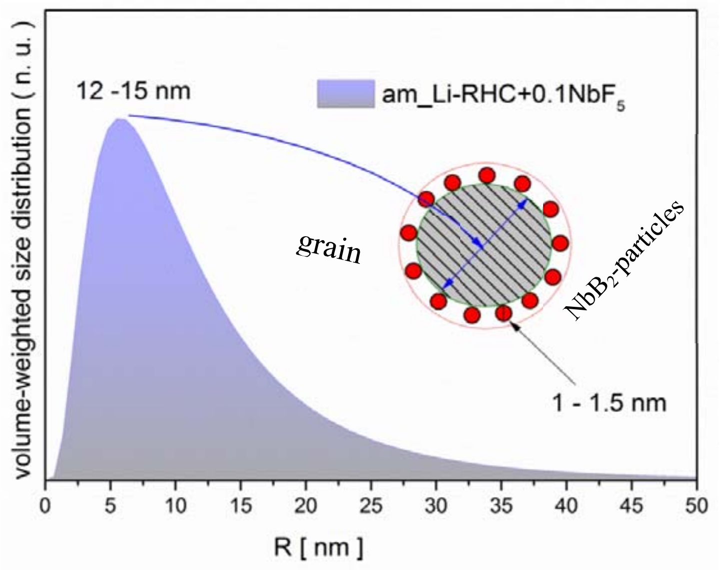

Figure 32. Size distribution of Nb containing particles in the hydride matrix assuming core-shell model for the fitting procedure.

4.1.5. SANS/USANS measurements

Small-Angle/Ultra Small-Angle Neutron Scattering (SANS/USANS) measurements were performed to reveal the structural effects of the additives on the surrounding hydride matrix. For this purpose, samples with and without additive, at different hydrogenation states, were investigated using SANS/USANS for a comparative structural study. In order to determine the composition differences between the particles of pure Li-RHC and Li-RHC+0.1NbF$_5$ samples after the first dehydrogenation process, Li-RHCs with different lithium and boron isotopes were used as starting materials, as listed in the following table.

Table 4-List of different isotope containing Li-RHC samples for SANS/USANS measurements.

Sample state/sample composition	**Pure Li-RHC**	**Li-RHC+0.1NbF$_5$**
as-milled	$2LiBH_4$+MgH_2	$2LiBH_4$+MgH_2+0.1NbF_5
	$2Li^{(11)}BH_4$+MgH_2	$2Li^{(11)}BH_4$+MgH_2+0.1NbF_5
	$2^{(7)}Li^{(11)}BH_4$+MgH_2	$2^{(7)}Li^{(11)}BH_4$+MgH_2+0.1NbF_5
1st-desorption	2LiH+MgB_2	2LiH+MgB_2+0.1NbF_5+0.1NbF_5
	2LiH+$Mg^{(11)}B_2$	2LiH+$Mg^{(11)}B_2$+0.1NbF_5
	$2^{(7)}$LiH+$Mg^{(11)}B_2$	$2^{(7)}$LiH+$Mg^{(11)}B_2$+0.1NbF_5

SANS measurements were performed at three sample-to-detector distances (SDD). In an exemplary SANS scattering curve plotted in double logarithmic scale is shown. All other SANS scattering curves can be found in the appendix. At the very high q-values (Porod-region) the scattering curve shows a flat scattering region, which corresponds to the incoherent scattering of the sample (see Figure 33). In the region $0.1\ \mathrm{nm}^{-1} \leq q \leq 1\ \mathrm{nm}^{-1}$ a clear scattering signal from nano structures is observed. At the very low q-values the scattering curve obeys a power law ($\sim q^{-x}$), which indicates scattering contribution from much larger structures present in the sample.

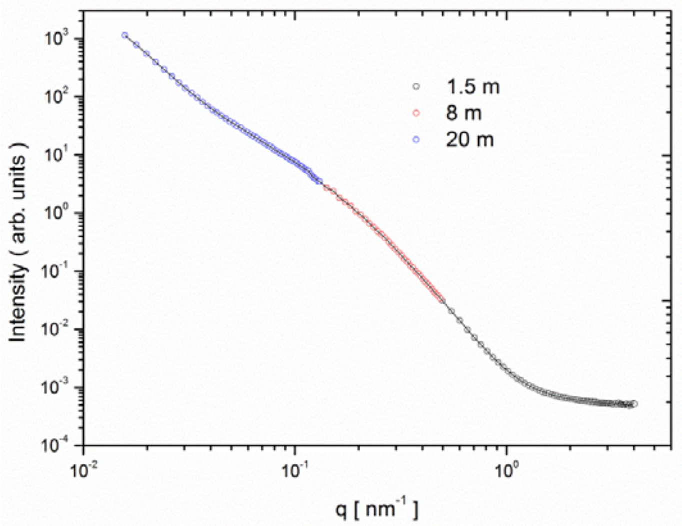

Figure 33. SANS scattering curve of Li-RHC+0.1NbF$_5$ after the first desorption (measured at the SANS-1 instrument at FRM II Neutron Source (MLZ, Munich, Germany).

In order to reveal the largest structures in the sample USANS measurements were performed. The measurement and details of processing of the USANS scattering data can be found in experimental section (3.2.6). The result of the USANS scattering curve of the aforementioned sample is displayed in the Figure 34. All other USANS curves are gathered in the appendix. As can be seen there at the very low q-values (Guinier region) the scattering curve approaches a plateau, which indicates the size of the maximum structures present in the sample.
At high q-values scattering hump in the region $0.002\ \text{nm}^{-1} \leq q \leq 0.01\ \text{nm}^{-1}$ is observed, which corresponds to structures in the size range of ~ 1 μm. SANS and USANS curves were merged subsequently to characterise all structures ranging from nano- to micrometre size (see Figure 35, and section 2.7.2).

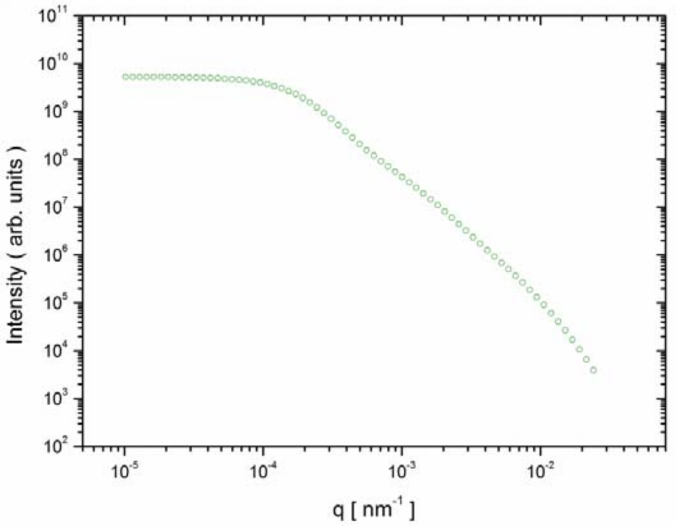

Figure 34. USANS scattering curve of Li-RHC+0.1NbF$_5$ after the first desorption (measured at the BT5-USANS instrument at NIST Centre for Neutron Research (Gaithersburg, USA).

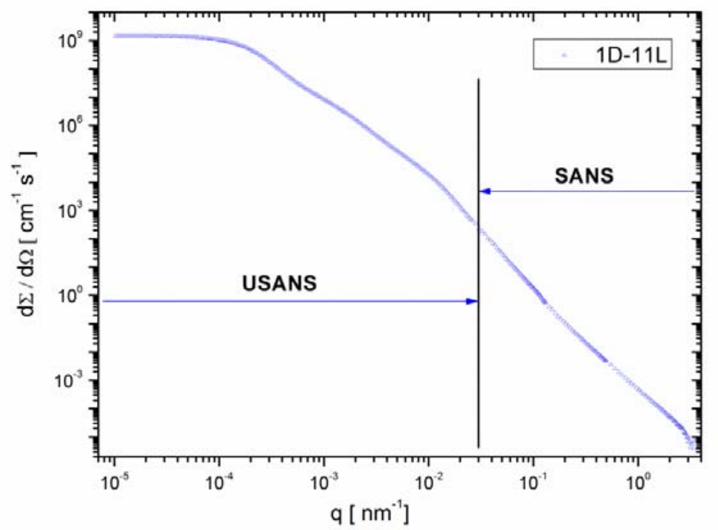

Figure 35. Merged SANS/USANS curve of $2Li^{(11)}BH_4$+MgH_2 after the first desorption.

A comparison between the SANS/USANS curves in Figure 35 and Figure 36 reveals that the scattering curve of the doped sample after the first dehydrogenation process contains more structural features than the corresponding curve of the pure Li-RHC system. In order to reveal the structural features depending only on the isotopes, SANS/USANS scattering curves of different isotopes for the doped and undoped samples, respectively, were fitted simultaneously. Since contrast and number density of the particles are correlated in a SANS/USANS measurement, therefore, only the number density was varied in the fitting procedure to pronounce the structural effects of the isotopes. The obtained size distributions for the pure and doped Li-RHC after the first desorption are displayed in Figure 37a and Figure 37b, respectively. The figures are plotted in a double logarithmic scale, where the *x*-axis represents the radii of spheres and the *y*-axis represents the volume weighted number density of particles. As can be seen in Figure 37a, the size distributions of the pure Li-RHC samples with different isotopes vary in their number densities, which can be attributed to different scattering properties of the isotopes in the samples. This allows the following first qualitative interpretation of the structures present in the Li-RHC samples: Because of the higher coherent scattering and lower absorption cross section of ^{7}Li and ^{11}B in the $^{(7)}LiH$-$Mg^{(11)}B_2$ and LiH-$Mg^{(11)}B_2$ samples, in comparison to LiH-MgB_2, the scattering intensities - with this also the number density of the scattering structures in the corresponding size range- of the first two samples should be comparable, if the $^{(7)}Li$-isotope is not located in structures that scatter in this region.

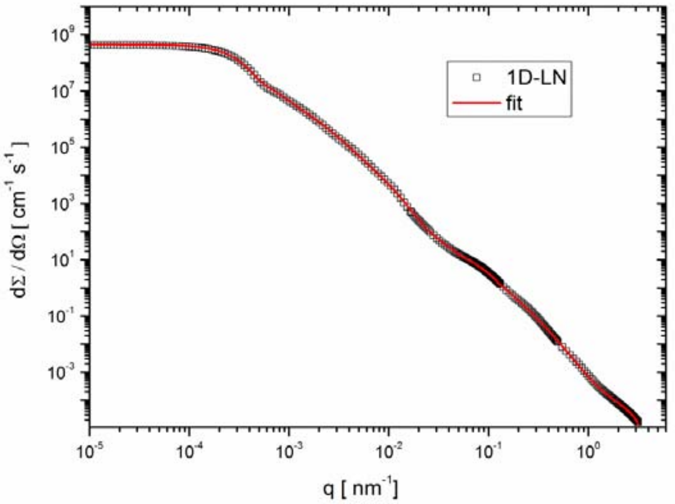

Figure 36. SANS/USANS curve of $2LiBH_4$+MgH_2+0.1NbF_5
after the first desorption with its corresponding fit.

In contrast, the number density of the scattering structures of the first sample should be higher in this size region than that of the third sample without ^{7}Li and ^{11}B. This is exactly the case in the size region around 334 nm. Therefore, this region can be assigned to consist predominantly of boron containing structures. In the region around 1300 nm the number densities of the LiH-Mg$^{(11)}$B$_2$ and LiH-MgB$_2$ samples are similar, but smaller than the one of $^{(7)}$LiH-Mg$^{(11)}$B$_2$. This behaviour shows that the structures in this size range contain no boron, since the LiH-Mg$^{(11)}$B$_2$ and $^{(7)}$LiH-Mg$^{(11)}$B$_2$ samples have the same boron isotope. Therefore it can be deduced that these structures predominantly contain lithium. Likewise, it can be concluded that the structures in the size region of 4700 nm are boron rich. However, in the region at about 10500 nm, none of the size distribution curves cover each other. Consequently, it can be deduced that the structures with sizes in this range contain both lithium and boron. The size distributions of the doped Li-RHC systems with different isotopes show a different behaviour (see Figure 37b): The largest structures are much smaller in comparison to those found in the pure Li-RHC system. Structures with sizes around 250 nm are predominantly lithium containing, whereas structures at about 450 nm and 1150 nm are mostly boron rich. In the size range between 2300 nm and 7400 nm the structures are lithium and boron containing, for the same reasons as mentioned before.

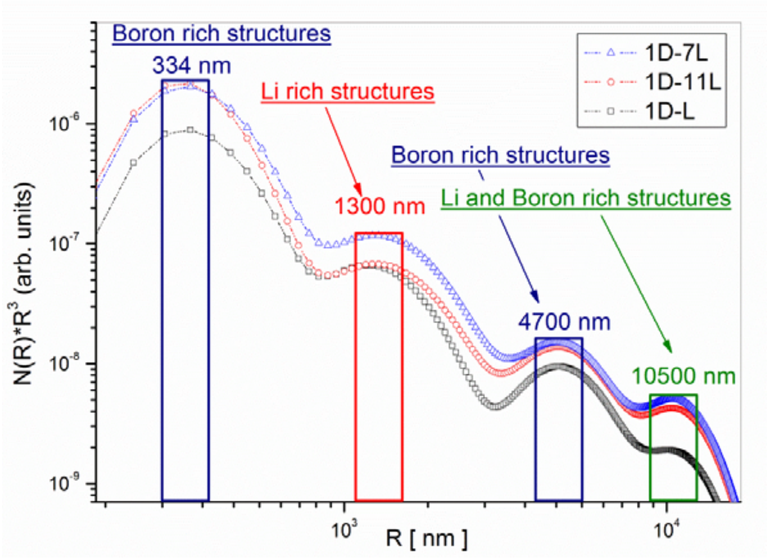

Figure 37a. Size distribution of pure Li-RHC with different isotopes after the first dehydrogenation reaction.

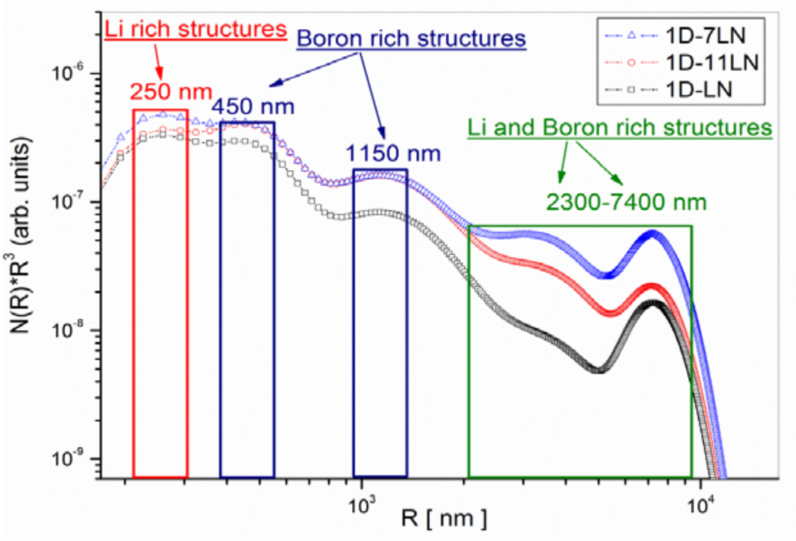

Figure 37b. Size distribution of doped Li-RHC with different isotopes after the first dehydrogenation reaction.

4.2. Discussion of the results of Li-RHC composite system

Volumetric measurements of the $LiBH_4$-MgH_2 composite system have shown that the sample doped with NbF_5 has significantly faster dehydrogenation kinetics in comparison to the undoped sample (see Figure 15). However, its dehydrogenation capacity is reduced in comparison to the undoped system. This indicates that the dopant might have reacted with the hydride matrix during the ball milling or first dehydrogenation process. An indirect hint for this perception was observed via the results of the in situ SR-PXD measurement (Figure 17), which showed the existence of LiF phase in the starting material. Furthermore, a chemical reaction between NbF_5 and MgH_2 can be excluded according to *in situ* SR-PXD results since this reaction would have led to formation of Mg metallic, MgB_2 or MgF_2 (which are not detected by XRD method). Also the chemical state of niobium couldn't be detected directly by means of XRD method. Thus XAS measurements were conducted and the results showed that NbB_2 was formed after the milling procedure and remained chemically stable over the cycling process. Therefore, the reaction paths can be written as:

$$\begin{aligned}
2\mathrm{LiBH_4} + \mathrm{MgH_2} + 0.1\mathrm{NbF_5} &\xrightarrow{\text{milling}} 1.5\mathrm{LiBH_4} + \mathrm{MgH_2} + 0.5\mathrm{LiF} \\
&+ 0.1\mathrm{NbB_2} + 0.3\mathrm{B} + \mathrm{H_2} \xleftrightarrow{1^{st} desorption} \\
1.5\mathrm{LiH} + 0.75\mathrm{MgB_2} &+ 0.5\mathrm{LiF} + 0.1\mathrm{NbB_2} + 0.3\mathrm{B} + 0.25\mathrm{Mg} + 3.25\mathrm{H_2}
\end{aligned} \tag{76}$$

A theoretical calculation based on the reaction (76) predicts a hydrogen release of 7.28 wt. % H_2, which is in very good agreement with the capacity value observed after the second desorption reaction. However, this prediction misses the capacity value observed after the first dehydrogenation process. During the milling procedure the following alternative reaction between $LiBH_4$ and NbF_5 can take place, as well:

$$\begin{aligned}
2\mathrm{LiBH_4} + \mathrm{MgH_2} + 0.1\mathrm{NbF_5} &\xrightarrow{\text{milling}} 1.8\mathrm{LiBH_4} + \mathrm{MgH_2} + 0.2\mathrm{LiF} \\
&+ 0.1\mathrm{NbB_2} + 0.3\mathrm{HF} + 0.25\mathrm{H_2} \\
&\xrightarrow{1st-step} 1.8\mathrm{LiBH_4} + \mathrm{Mg} + 0.2\mathrm{LiF} + 0.1\mathrm{NbB_2} + \mathrm{H_2} \\
\xrightarrow{2nd-step} 1.8\mathrm{LiH} &+ 0.9\mathrm{MgB_2} + 0.2\mathrm{LiF} + 0.1\mathrm{NbB_2} + 0.1\mathrm{Mg} + 3.7\mathrm{H_2}
\end{aligned} \tag{77}$$

This reaction path gives a desorption capacity of 8.73 wt. %, which exceeds the observed capacities of the first and second dehydrogenation reaction, respectively. Since the reaction between $LiBH_4$ and NbF_5 during the milling process occurs randomly, the reaction is concluded to be a superposition of reactions (76) and (77). This is also further supported by the results obtained from XAS for the as-milled sample (see: 4.1.3), which states an incomplete conversion of NbF_5 in to NbB_2 phase. Thus, the reaction after the ball milling procedure and a subsequent dehydrogenation can be rewritten in a more general form as:

$$\begin{aligned}
2\mathrm{LiBH_4} + \mathrm{MgH_2} + 0.1\mathrm{NbF_5} &\xrightarrow{\text{milling}} (2-5x)\mathrm{LiBH_4} + \mathrm{MgH_2} \\
&+ (0.1-x)\mathrm{NbF_5} + \delta(x)\mathrm{HF} + 5x\mathrm{LiF} + \xi(x)\mathrm{B} + x\mathrm{NbB_2} \\
&+ \left(\frac{25x-0.5}{2}\right)\mathrm{H_2} \xrightarrow{1^{st}-step} (2-5x)\mathrm{LiBH_4} + \mathrm{Mg} \\
&+ (0.1-x)\mathrm{NbF_5} + 5x\mathrm{LiF} + \xi(x)\mathrm{B} + x\mathrm{NbB_2} + \mathrm{H_2} \\
&\xrightarrow{2^{nd}-step} (2-5x)\mathrm{LiH} + (1-2.5x)\mathrm{MgB_2} + 5x\mathrm{LiF} + \xi'(x)\mathrm{B} + 2.5x\mathrm{Mg} + \\
&x\mathrm{NbB_2} + (6-15x)/2\mathrm{H_2} \\
&\qquad here\ is: 0 \le x \le 0.1 \\
&\delta(x) = \xi(x) = 0\ ;\ \text{ for } x = 0 \text{ and } x = 0.1,\ \textit{else unknown.}
\end{aligned} \tag{78}$$

In (78), the hydrogen fluoride gas release and formation of boron during the milling procedure is assumed in order to balance the chemical equation. Their formation during the milling process is a function of x which is only known at the limits of the variable x. Depending on the "conversion parameter"(x), thus, the hydrogen release of the system can vary between 8.73 wt. % H_2 and 7.28 wt. % H_2. The capacity loss over the cycles is also likely to be due to evaporation of Mg under the applied conditions, as was reported by

Bodanovič *et. al.* [191], or phase separation between $LiBH_4$ and MgH_2, which will lead -over the dehydrogenation process- to highly stable $Li_2B_{12}H_{12}$ and amorphous boron phases.[148, 192-194] Furthermore, inaccuracies in the weighting process and phase agglomeration at balls and vials during the milling procedure of the samples can cause additional molar disproportion between $2LiBH_4$ and MgH_2, which would lead to a reduction of the theoretical maximum hydrogen storage capacity of the system as well. EXAFS results showed also significantly improved signals of NbB_2 after the first dehydrogenation process, which supports the reaction equation given above. ASAXS results (subsection 4.1.4), showed that the NbB_2 particles are -dispersed in the hydride matrix- in the nano-metric range (1-1.5 nm), which explains the absence of its diffraction peaks in the *in situ* SR-PXD patterns. The model that was assumed to describe the observed data was such that the NbB_2 particles in the range 1-1.5 nm are distributed around the grains of the matrix. It should be noted that this is not the only possibility to describe the experimental data. Other three options are presented in Figure 38 which are equivalent to the model presented in section 4.1.4. Spherical particles with rough surface (in Figure 38 (a)), smooth spherical particles with prismatic dislocation loops (b), or spherical particles with rough surface with prismatic dislocation loops (c) are possible models, as well. The formation of such structures is likely during the ball milling process, since the crystallization process does not occur under controlled conditions, as it is the case for classical crystallization methods such as cooling or evaporating crystallization methods. Characterization

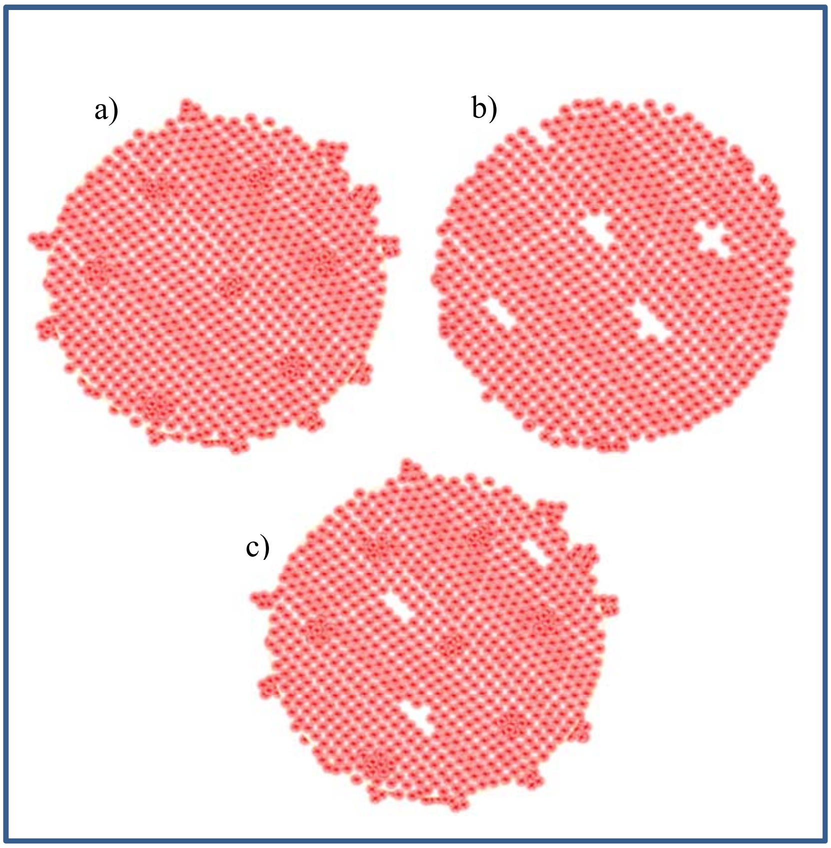

Figure 38. Different models of NbB_2 particles. a) Spherical NbB_2 particle with rough surface, b) with smooth surface but prismatic dislocation loops in the particles, c) with rough surface and prismatic dislocation loops in the bulk.

Due to Babinet's principle, the scattering curves of prismatic dislocation loops in the NbB_2 particles would produce the same characteristic as if there would be NbB_2 discs. Following these argumentations, the final and most likely model should be the model of spherical particles with rough surfaces, including some prismatic dislocation loops. This model, however, should also justify the results obtained by varying the amount of additive in the hydride composite as well (see Figure 30, section 4.1.4). Interestingly, the less resonant structures located in the low q-range appear first evidently in comparison to those structures laying at the high q-range, when a small amount of additive is added. This can be explained by the fact that the scattering intensities of objects are proportional to their number and square of their volume:

$$I(q) \propto NV^2 \xrightarrow{sphere} \sim NR^6 \qquad (79)$$

On the other hand, the scattering intensities of the objects are also proportional to square of their scattering length densities:

$$I(q) \propto \Delta\varrho^2 = (\varrho_{\mathrm{Nb-structure}} - \varrho_{\mathrm{environment}})^2 \qquad (80)$$

Now, the model of spherical particles with rough surfaces, and with possible prismatic dislocation loops (SPRD) can explain the abovementioned results in the following way:
With a few SPRD there are more small structures (on the surface of the particles and defects in the particle), however, the volume of the particle is decisive over the number of small particles (see equation (79)). For instance, if we assume a monodisperse system of SPRD, and we further assume that each particle has 10 smaller substructure units (SSU), then we have a linear relationship between the amount of SPRD (additive) and the amount of their SSU. On the other hand, their environment has to be considered to be different. Since the SPRD are "seen" from the "view" of the incident beam to be in the matrix, whereas the SSU are "seen" in the range of grain boundaries. This situation is illustrated in Figure 39, using the SAXS curve of as-milled sample. Therefore not only the number density of SSU plays a role but also their contrast becomes significant by increasing the amount of the additive in the hydride matrix. As a consequence, the signal of SSU becomes more pronounced at the high q-range of the scattering curve. This model has to be seen still as a very first approximation to the reality. Of course, the autonomic existence of small particles in the range of 1-2 nm cannot be excluded entirely. Nevertheless, their existence will not violate the proposed model here, since they can be assumed to be distributed also in the grain boundaries of the hydride matrix as was discussed above. It should be pointed out that the spherical shape assumed here is an approximation to reality, as well.

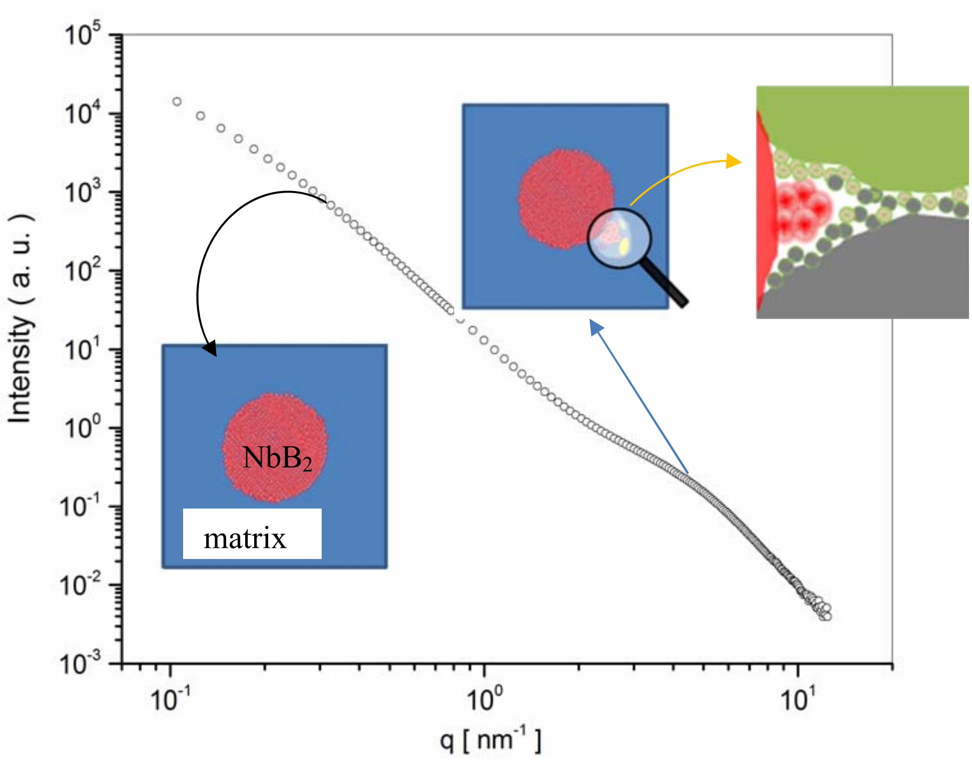

Figure 39. Visualization of contrast variation between NbB_2 particles and matrix at different scales (measured at the beamline B1 at the DORIS III synchrotron storage ring at HASYLAB (DESY, Hamburg, Germany).

Before starting to draw a correlation (or function) between NbB_2 nano particles and hydrogen sorption kinetics of the Li-RHC, it is necessary to understand the problematic hidden behind the long incubation period in the dehydrogenation process of $2LiBH_4$+MgH_2 composite system (see: Figure 15.),in some detail. After decomposition of MgH_2, the metallic magnesium (Mg) remains in the liquid $LiBH_4$ matrix. Formation of the new phase by reaction between these two phases occurs randomly by formation of a small heterogeneous nuclei and further growth process of this phase on those nuclei. However, the formation of these nuclei requires certain amount of energy, which is to be delivered by the system in order to initiate the nucleation and growth of the new phase. For spherical nuclei this (Gibbs free) energy is determined by the classical nucleation theory:[195]

$$\Delta G_n = \left[-\left(\frac{4}{3}\right)\pi \Delta g_{v,n} r^3 + 4\pi r^2 \gamma_{a,n}\right] S(\theta) \qquad (81)$$

Here, $\Delta g_{v,n}$ stands for the energy per unit volume, $\gamma_{a,n}$ represents the interfacial energy consumed per unit area between the nucleus and the matrix, r represents the radius of the nucleus and $S(\theta)$ is the shape factor of the nucleus, which describes the wetting angle between the nucleus and its environment. For the simplicity the shape factor is set to be one in further calculations. This relation and its two contributors are illustrated in the following figure.

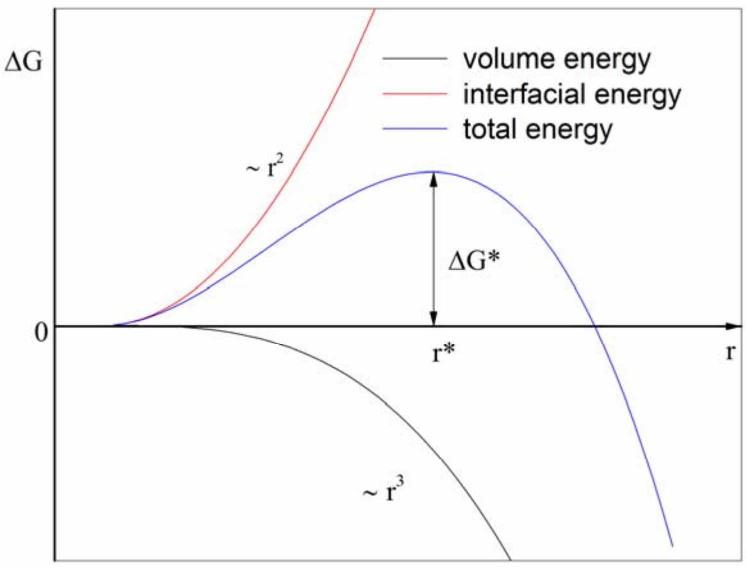

Figure 40. The change of Gibbs free-energy required for a spherical nuclei.

As can be seen in Figure 40, the Gibbs free-energy rises by the formation of a nucleus. In the beginning the nucleus has more atoms on its surface presented as in its volume, therefore, its surface characteristics dominates its bulk properties. Due to proportionality of the interfacial energy to square of the radius of the nucleus, the free energy increases correspondingly. After the growth of the nucleus to a certain size the ratio between surface and volume atoms becomes smaller, and the volume or bulk properties of the nucleus shine through and start to determine the properties of the nucleus. Since, the volume free energy is cubical proportional to the radius of the nucleus, thus, the free energy decreases accordingly. At certain nucleus size both effects balance each other and the nucleus size at this point is assigned to so-called "critical nucleus size". The corresponding free energy is termed as critical free energy or activation energy. The critical radius (r^*) is determined by determining the maximum of Gibbs free-energy function (inflection point of the first derivative) in equation (82):

$$r^* = \frac{2\gamma_{a,n}}{\Delta g_{v,n}} \tag{82}$$

Thus, nuclei smaller than r^* which are formed will be unstable and the probability is high that it will decompose for they cannot overcome the energy barrier ΔG^* (quantum mechanical tunnelling process is neglected here), whereas nuclei greater than r^* possess enough energy to pass the barrier hence it is most likely that they remain stable (since they reduce the overall free energy) and provide nucleation centres for further growth of the new phase. To get a rough idea about the scale range of the nuclei in the Li-RHC system, an attempt is made to calculate a numerical value for r^*. For doing so, numerous simplifications have to be drawn in order to be able to calculate an approximated value for r^* in this highly complicated system. First of all, the precipitation from the matrix has two phases LiH, and MgB_2, hence two interfacial energy terms are to be included in equation (82). The first simplification is by using an average value $\overline{\gamma_{a,n}}$ for both interfacial energy and treating this approximated value for the all interfacial energies, which is a reasonable assumption since the surface energies of ceramic materials are relatively high in comparison to all other phases which are present in the sample.[196-198] Since nucleation occurs preferably at the grain boundaries, and there in turn at places (or planes) with highest surface tension, we assume a hierarchy of structures at the grain boundaries of magnesium for nucleation of the new phase. This hierarchy is coded in Figure 41 by dark colour at the top layer with the highest probability for nucleation and decreases to brighter colour as the probability for nucleation decreases. In this picture Mg has to be seen as a weighted-substrate for nucleation of MgB_2 from molten $LiBH_4$ phase.

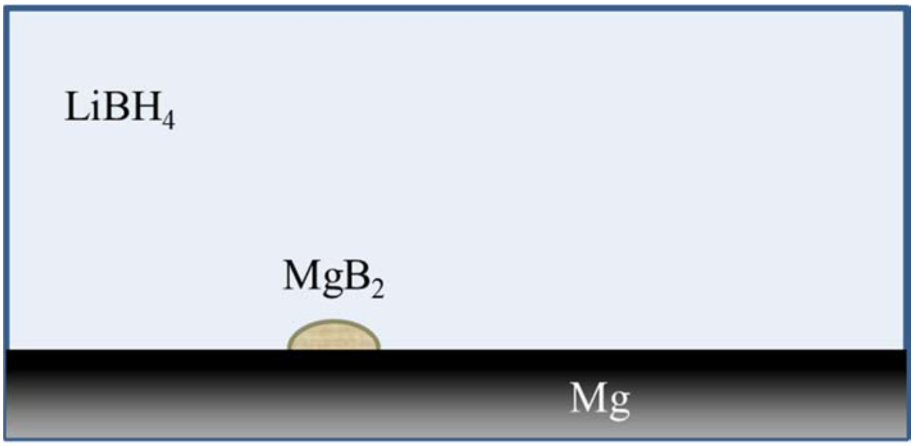

Figure 41. Simplified model for nucleation and growth of MgB_2 phase from the $LiBH_4$ molten phase on the Mg substrate.

Despite the presence of Mg substrate we treat the nucleation process here for calculation of the critical radius to be homogenous ($S(\theta) = 1$). This approximation is sensible, because the shape factor $S(\theta)$ in the heterogeneous nucleation process only affects the energy barrier for nucleation but not the critical radius of the nuclei. Also the hydrogen in the gaseous phase (4 bar backpressure and 3 moles of H_2) is neglected here, which can have some effects on the nucleation and growth processes.[199] The thermodynamic calculations were performed based on the following reaction:

$$2(\mathrm{LiBH_4})_l + (\mathrm{Mg})_s \rightarrow 2(\mathrm{LiH})_s + (\mathrm{MgB_2})_s + 3(\mathrm{H_2})_g \qquad (83)$$

The driving force for the reaction above is divided to form the three final products, thus its value has to be divided as well for the formation of only MgB_2. The thermodynamic values used for calculating the critical radius are gathered in the following table. Typical surface energy values for metal hydrides and ceramic materials range between 0.3 kJ/m² to 2.5 kJ/m².[195-198, 200] Taking the minimum and maximum of the aforementioned surface energy values one obtains critical radii ranging roughly from 1 nm to 3.5 nm. Assuming an average critical radius of 2 nm, leads to a nucleus volume of 33.5 nm^3. For creating such a nucleus size in the pure Li-RHC, approximately $850 \cdot 10^3$ MgB_2 molecules are required. Thus this many reactions have to take place, in the vicinity of each other, in order to form a stable nucleus.

Table 5. Thermodynamic values for the elements and compound used in the calculation for critical radius of a nucleus. Values were taken from: a,[201, 202] , b[11], and c[203].

Substance/parameter	**$LiBH_4$**	**Mg**	**LiH**	**MgB_2**	**H_2**
$H^{(of)}$ [kJ/mol]	-194.5[a]	0	-90.63[b]	-92[c]	0
S° [kJ/mol K]	0.076[a]	0.0326[c]	0.0203[b]	0.0359[c]	0.1305[c]
$H^{(l)}$ [kJ/mol]	-180.17				
$S^{(l)}$ [kJ/mol K]	0.1085				

However, the reaction between $2LiBH_4$ and Mg takes place randomly in space and time hence the reacted MgB_2 particles are separated correspondingly. Therefore, they need diffusion time/or existing time on the surface of Mg substrate in order to adjoin and to build a MgB_2 clusters and end up in a stable nucleus. There is a finite probability for each reaction that MgB_2 particles evaporate from the Mg substrate in to the molten $LiBH_4$ matrix and re-react there and scatter around in the matrix, which eventually can be recaptured (recombined) on the Mg surface or by other MgB_2 particles in the matrix or on other MgB_2 particles, which are placed on the Mg substrate. Owing to very high curvatures of the MgB_2 particles at the beginning of the nucleation these particles are highly instable. This is due to the so-called "Gibbs-Thomsen-Effect":[195]

$$\Delta P = \frac{2\gamma}{r};\ with\ a\ free - energy\ increase\ of:\ \Delta G = \frac{2\gamma V_n}{r} \qquad (84)$$

Where, ΔP represent the pressure created by the surface of the nucleus on the matrix, γ is the interfacial energy between the matrix and the nucleus, V_n and r are volume and radius of the nucleus, respectively. The instability of the nucleus grows as the radius of the nucleus drops since the Gibbs free-energy of the nucleus increases. After certain radius size the structure as such is energetically not favourable anymore and decomposes in many parts. This can happen only if the rate of growth of the nucleus is much smaller in comparison to corresponding value of decomposition. There are also a probability of chemical decomposition of MgB_2 clusters back in to matrix along the following possible paths:

$$\mathrm{MgB_2 + 2LiH + 4H_2 \leftrightarrow Mg + 2LiBH_4}$$

$$\mathrm{MgB_2 + 3H_2 + 2LiH \rightarrow Mg + B_2H_6 + 2LiH \rightarrow Mg + 2LiBH_4}\ ^{204} \qquad (85)$$

$$\mathrm{MgB_2 + 4H_2 + 2LiH \rightarrow Mg(BH_4)_2 + 2LiH \rightarrow Mg + 2LiBH_4}\ ^{205}$$

These processes can occur either on the Mg substrate or in the matrix. The MgB_2 clusters which decompose along either aforementioned paths back on to the substrate surface as Mg clusters which do not possess -due to their significantly different coordination number hence altered binding properties- the same properties of the surface atoms of Mg substrate. These clusters, which are separated by a distance, can agglomerate by surface diffusion in order to minimize their surface energies. The abovementioned processes are all illustrated in the following figure.

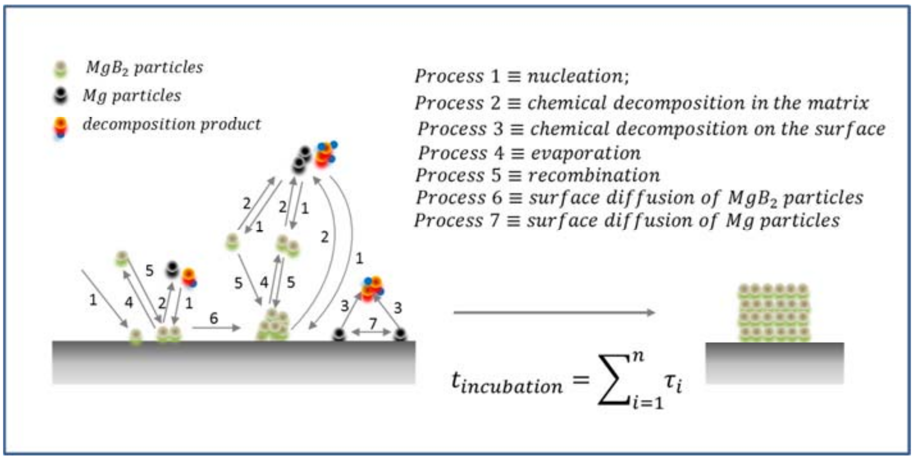

Figure 42. Nucleation, decomposition and growth processes of MgB_2 nuclei along various reaction processes and paths.

The time consumed for all these processes is projected in the plateau period (incubation time) of desorption curve of the pristine Li-RHC (Figure 15). However, the experiments show that if the samples are equally prepared and desorbed under the same conditions, the incubation times of these samples are rather similar and do not behave really randomly. This indicates that the nucleation and growth processes have to be governed by one of the aforementioned events and, therefore, it determines the time being consumed for the plateau period (see Figure 42). It is assumed here that the decomposed Mg atoms are distributed randomly on the surface of Mg substrate and they differ considerably from Mg surface atoms (as aforementioned). Hence, they can diffuse on the surface of the substrate and an accumulation of these Mg atoms can occur (clustering) to reduce their surface energies. After a given time (incubation period) the size of these agglomerated particles approaches the critical nucleus size, which after the chemical reaction with the matrix remains as a stable MgB_2 nucleus for further growth of this phase (see Figure 43).

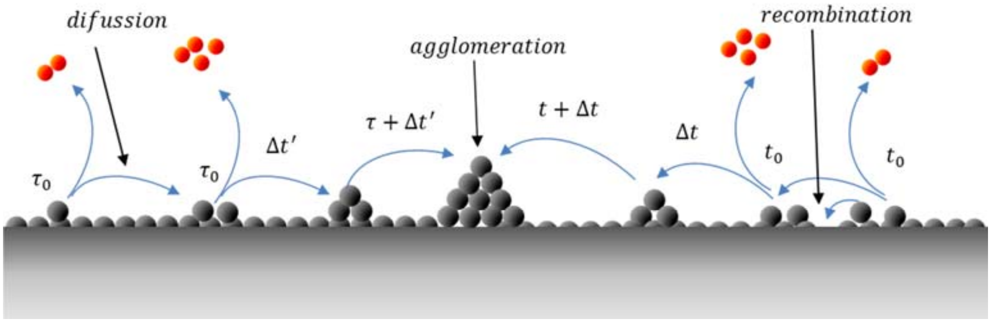

Figure 43. Agglomeration of Mg clusters by surface diffusion on the Mg substrate.

Therefore, the surface diffusion of Mg atoms on the Mg substrate is proposed to be most likely the rate limiting step which determines the incubation time over the first dehydrogenation process of an as-milled pure Li-RHC sample. In Figure 44 a qualitative evolution of MgB_2 nucleus with respect to time is illustrated which corresponds to all possible creation and decay processes of MgB_2 nucleus that are displayed in Figure 42 and Figure 43 in real space. After nucleation of stable MgB_2 seeds the growth process of this phase is further investigated in the following by using kinetic models introduced by A. N. Kolmogorov, W. A.

Johnson, R. F. Mehl and M. Avrami (KJMA-model) and further improved by others which describe the rate-limiting step of a reaction.[206-218] All models used for fitting the transformed fraction $\alpha(t)$ of the desorption process with time are gathered in the following table.

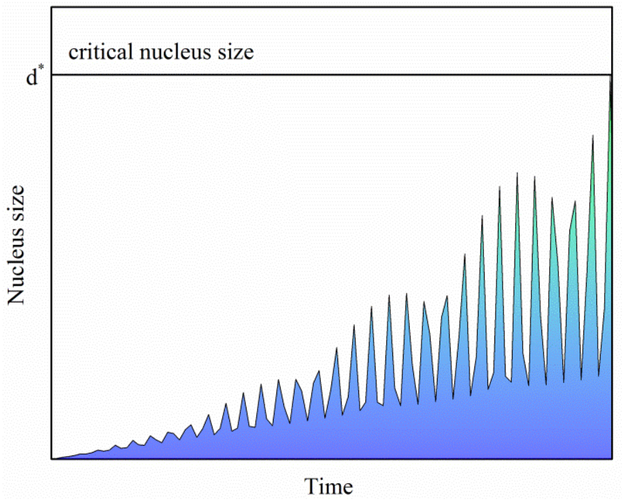

Figure 44. A qualitative description of the oscillation of nucleation and decomposition process of MgB_2/Mg with time in the pure Li-RHC system.

Table 6. The used kinetic models to fit the experimental data and their corresponding descriptions. The equations were taken from [208-211]

Equation of the model	**Model description**
$\boldsymbol{\alpha(t) = kt}$	Chemisorption/recombination on the particle surface is the rate-limiting step.
$\boldsymbol{[-\ln(1-\alpha(t)]^{1/2} = kt}$	2-dimensional growth of existing nuclei with constant interface velocity (2D-KJMA).
$\boldsymbol{[-\ln(1-\alpha(t)]^{1/3} = kt}$	3-dimensional growth of existing nuclei with constant interface velocity (3D-KJMA).
$\boldsymbol{[-\ln(1-\alpha(t)]^{2/3} = kt}$	Diffusion controlled 3-dimensional growth of existing nuclei with decreasing interface velocity (DC: 3D-KJMA).
$\boldsymbol{1-(1-\alpha(t))^{1/2} = kt}$	2-dimensional growth of contracting volume with constant interface velocity (2D-CV).
$\boldsymbol{1-(1-\alpha(t))^{1/3} = kt}$	3-dimensional growth of contracting volume with constant interface velocity (3D-CV).
$\boldsymbol{1-(\frac{2\alpha(t)}{3})-(1-\alpha(t))^{2/3} = kt}$	Diffusion controlled 3-dimensional growth of contracting volume with constant interface velocity (DC: 3D-CV).

For the fitting procedure of the kinetic data the second step of the first dehydrogenation process of pure and doped Li-RHC system was taken, respectively. The used models (Table 6) have been adapted and applied for binary hydrides, and further used in RHCs by Bösenberg *et al.*[219] as an approximate description to reality. Hence, the fit results obtained here have to be considered as an indication toward a definite growth mechanism of the MgB_2 phase. For the fitting procedure only a transformed fraction of maximum 0.6 was chosen in order not to overstress the limits of the used models. The results of the transformed fraction $\alpha(t)$ of the pure Li-RHC system fitted by the models from the Table 6 are shown in Figure 45.

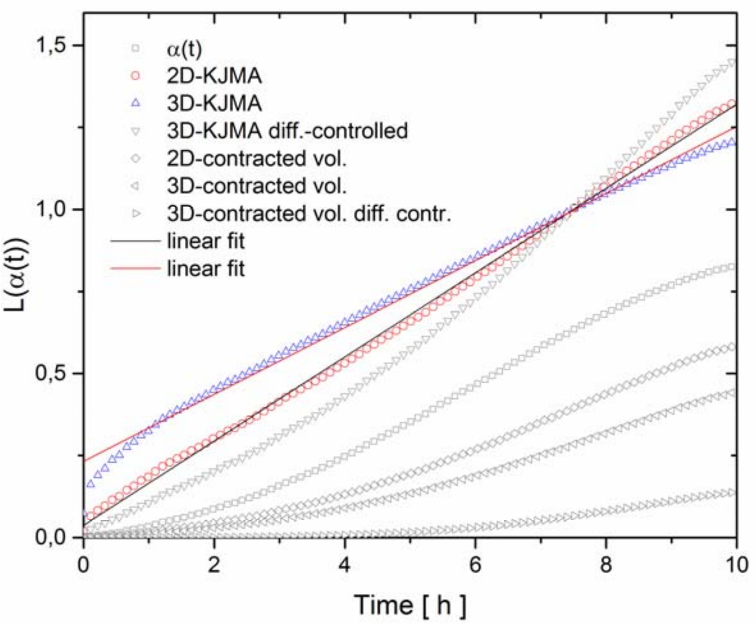

Figure 45. Kinetic models for the first desorption of pure Li-RHC with the corresponding best fits.

As can be seen, the best fit result suggest the two dimensional growth of MgB_2 with constant interface velocity of existing nuclei and the second best fit, which starts to converges the curve after one hour of delay and diverges roughly two hours before the final state of the curve, result is obtained by three dimensional growth of MgB_2 with constant interface velocity of existing nuclei. Since the two dimensional growth of MgB_2 seems to describe the experimental data well over the entire observation reaction time, it is likely that at the early stages of the growth process it proceeds in two dimensions as in a plate-like manner in two favourite direction along the grain boundaries and after an elapsed time the additional three dimensional growth process starts toward the grain centre, as is illustrated in Figure 46. This is also in good agreement with the heterogeneous nucleation of MgB_2 phase on the Mg substrate as it was discussed above.

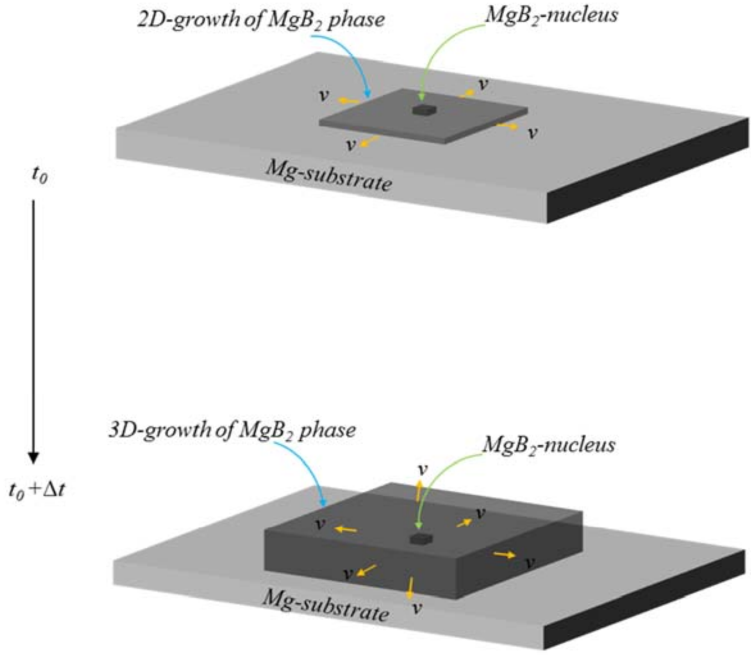

Figure 46. Illustration of two and three dimensional growth of MgB_2 phase during the second step desorption of Li-RHC system.

A possible mechanism might be the interfacial tension between incoherent interfaces of MgB_2 and Mg which is created by MgB_2 layers on the surface of Mg substrate. After reaching a certain size, the MgB_2 layers are removed (peeled off)/tilted from the Mg surface to minimize the interfacial energy between the two phases which in turn provides fresh Mg layers for further growth of MgB_2 phase. Consequently, the repetition of this process will lead to the growth of MgB_2 phase toward the magnesium grain centre. The results of the kinetic models for the doped system (Li-RHC+0.1NbF_5) are shown in Figure 47. The models which describe the doped Li-RHC the best corresponds to those of the pure Li-RHC. Therefore, it can be concluded that the growth mechanism of MgB_2 in both systems are most likely the same. However, in the doped Li-RHC system the same converted fraction of MgB_2 phase is achieved in significantly shorter amount of time (a factor of ~ 10) in comparison to the pure Li-RHC system (see Figure 45 and Figure 47). The present NbB_2 nanoparticles not only eliminate the incubation period of Li-RHC, but also enhance the growth process of the newly formed MgB_2 phase. It is well known that two crystals with low lattice mismatch can provide mutually nucleation sites for each other and thereby lowering the wetting angle hence promoting the formation and growth of the new phase.[220] This, indeed, would explain the effect of NbB_2 nanoparticles on discarding the incubation time of the first dehydrogenation reaction of the doped Li-RHC and its enhanced kinetics of formation of MgB_2 during the second reaction step of dehydrogenation. Regarding the incubation period, NbB_2 possesses the same hexagonal crystal structure as MgB_2.

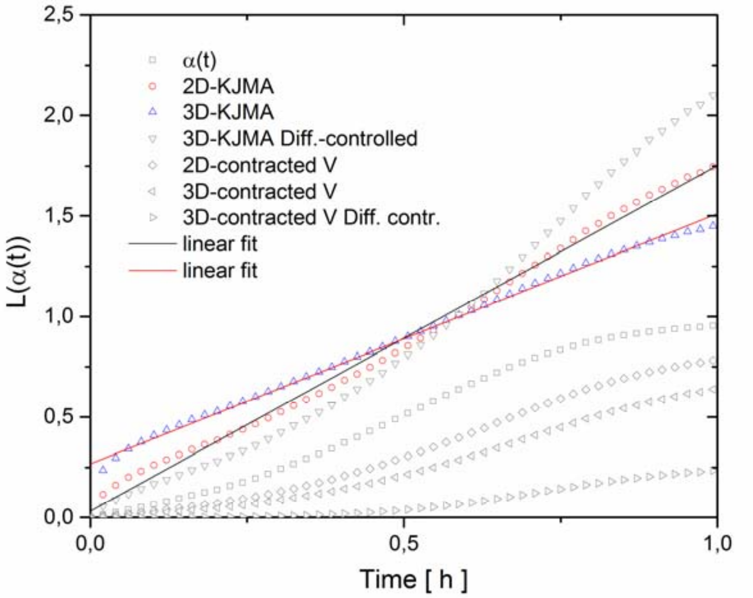

Figure 47. Kinetic models for the first desorption of Li-RHC doped with NbF_5 with the corresponding best fits.

Furthermore, it has two possible matching planes with MgB_2: MgB_2 {1011}|| NbB_2 {1011} and MgB_2 {1010} || NbB_2 {1010} with *d*-mismatch values of 2.3 % and 0.7 %, respectively. These *d*-mismatch values are well below the critical value of 6 %[195, 221-224] which leads to low lattice strain at the interface between the seed and MgB_2, hence minimizing their interfacial energy to provide beneficial conditions for stable growth of the new phase on the surface of the seed. The results obtained here are in good agreement with results obtained by Bösenberg *et al.* and Deprez *et al.*[219, 225-227] for ZrB_2 and TiB_2, respectively. It should be noted here that also Mg provides a possible nucleation plane for MgB_2 with an appropriate misfit of 3.7 % (MgB_2 {0001} || Mg {0001}), however, its directional misfit in the altitude ⟨0001⟩ of the hexagonal unit cell amounts to about 48 %.[219] Taking into account that nucleation favourably does not occur on flat surfaces but on ledges, this huge misfit (48 %) would hinder a nucleation significantly. On the other hand the corresponding misfit value for NbB_2 is only 5 %. Even if a nucleation of MgB_2 on Mg starts, despite these structural obstacles, than the discussion (above) about the critical nucleus size is again true and would lead to an incubation time for nucleation of MgB_2 in the pure system! In contrary to the pure Li-RHC system, in the doped hydride composite there are already stable nucleation seeds with suitable nucleation sites and sizes (the size distribution of NbB_2 nanoparticles (see Figure 32) covers the entire size range of the estimated critical MgB_2 nuclei). This explains the absence of an incubation period in the doped Li-RHC system. Concerning the kinetics of growth of MgB_2 in both system (where the kinetic of the doped system is enhanced by a factor of ~10 in comparison to the pure Li-RHC system), it is most likely that the amount of nucleation centres built in the pure Li-RHC system are significantly lower hence inhomogeneously distributed in the matrix in comparison to the doped system, where a high amount of nucleation centres already homogeneously are distributed in the hydride matrix. This would lead with time to much faster reaction kinetics in favour of the doped system. A graphic description of this process is illustrated in Figure 48. At the top panel of the figure initial nucleation state at a given time for pure and doped system is shown, respectively, and in the lower panel the same systems are sketched after an elapsed time. Indeed, this would explain the considerably smaller structures and well mixed final phases in the particles in the doped system in comparison to those in the pure Li-RHC system which were observed by SANS/USANS measurements (see Figure 37a,

Figure 37b). These fine structures in turn create significantly larger reaction surface areas and noticeably shorter diffusion paths in the doped Li-RHC in comparison to the pure system. Consequently, the rehydrogenation reaction kinetics is improved by a factor of 10. An additional effect of NbB_2 nanoparticles might be to prevent the grain growth under the applied conditions by Zener pinning.[228, 229] NbB_2 is also known for being one of the hardest ceramic material (2130 (Knoop hardness)) with a relatively high melting point (3050 °C)[230] and can therefore act also as a grain refiner during the milling- and de/rehydrogenation process. Possible chemical activities of NbB_2 nanoparticles during the dehydrogenation process cannot be entirely excluded. Recently a catalytic effect of $LiTiO_4$ additive on the Li^+ ion conductivity in complex hydrides was reported.[231] Similarly a very thin layer of $LiNbO_3$ can be formed due to oxygen impurities in the hydride composite system and/or oxygen impurities in the gaseous hydrogen atmosphere (which cannot be detected *via* XAS, due to their very insignificant amount) and promote the Li^+ ion conductivity in the interfacial area. However, this needs to be experimentally further investigated in detail which exceeds the scope of this thesis.

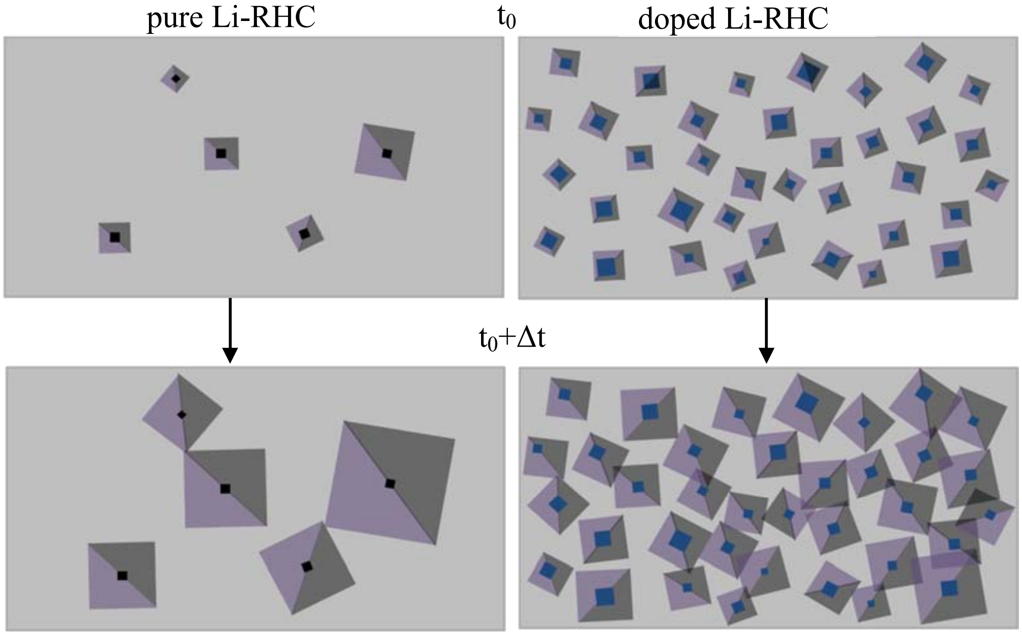

Figure 48. Kinetic illustration of phase growth of the second dehydrogenation step of pure and doped Li-RHC systems, respectively (the small dark squares in the pure system represents MgB_2 seeds and the blue small squares in the doped system represents NbB_2 nanoparticles).

4.3. Conclusions

In this work the structural and kinetical effects of NbF_5 additive on the Li-RHC have been investigated using several experimental methods such as: volumetric measurements, *in situ* SR-PXD, XAS, ASAXS and SANS/USANS. The volumetric measurements showed a hydrogen capacity drop relative to theoretical capacity value of the system, which could be retraced to a reaction between the additive and the hydride matrix. The reaction products were determined (by XRD and EXAFS methods) to be LiF and NbB_2. Both are highly stable under the applied conditions for de/rehydrogenation processes, hence, they do not participate in the cycling process. However, by the presence of an additive the kinetics of Li-RHC was significantly improved. At the first place, the kinetics of pure Li-RHC system suffered under the long incubation plateau, which was proposed to be due to nucleation of MgB_2 phase. The critical nucleation radius of MgB_2 under the applied conditions was calculated to be about 4 nm in size. The main obstacle for the formation of the MgB_2 nucleus was suggested to be the surface diffusion of Mg atoms on Mg substrate in the pure Li-RHC system. In the doped system, however, no incubation plateau was observed. This fact led to the conclusion that NbB_2 might act as nucleation seeds for MgB_2 phase. Indeed, MgB_2 and NbB_2 possess the same hexagonal crystal structure. Moreover, NbB_2 has two possible crystallographic planes which are very similar to those of MgB_2, namely: MgB_2 {1011} || NbB_2 {1011} and MgB_2 {1010} || NbB_2 {1010} with dissimilarities in their *d*-spacing values of 2.3 % and 0.7 %, respectively, which is reasonable small in comparison to the critical value of 6 %. Also the size distribution of NbB_2 (determined *via* ASAXS measurements) covers well the aforementioned average critical nucleus size of MgB_2. Moreover, it was revealed that these nanoparticles possess internal structures and show rough surfaces, which in turn can provide manifold nucleation sites for the MgB_2 phase. Thus, the presence of NbB_2 nanoparticles in the doped system overcomes already the energy barrier, which is correlated with nucleation of MgB_2 seeds in the pure system. It was also found that the growth process of MgB_2 in pure and doped systems was very similar (by fitting different kinetical models to the observed kinetic curves) and follows a two dimensional growth process controlled by diffusion. This model of homogeneously distributed NbB_2 nanoparticle seeds for MgB_2 phase in the hydride matrix could also explain the much smaller matrix structures in the doped system after the first dehydrogenation process (observed by SANS/USANS measurements) in comparison to those in the dehydrogenated pure Li-RHC.

5. Results and discussions of the Ca-RHC system

5.1. Effect of additives on the $Ca(BH_4)_2$-MgH_2 composite system

Among all applied additives, NbF_5 showed the best performance considering the dehydrogenation kinetics of the $Ca(BH_4)_2$+MgH_2 hydride composite system. Moreover, Bonatto Minella *et al.* [133] showed that using NbF_5 as an additive improves even the reversibility of the single $Ca(BH_4)_2$ complex hydride. However, up to date no satisfactory explanation for these effects was given. Therefore, in the following the effect of NbF_5 additive on the hydride matrix, its chemical state in the hydride matrix as well as its size distribution in the matrix is investigated in detail to shed some light on the mechanism concealed behind the positive performance of this additive in the Ca-RHC system.

5.1.1. Coupled DSC-manometric and mass spectrometric measurements

Coupled manometric-calorimetric measurements were performed on both the doped and the undoped samples by connecting a PCTPro-2000 instrument (Setaram &Hy-Energy, France) with a Sensys high-pressure DSC (Setaram, France). Desorption measurements were performed by heating the samples (about 30 mg) from room temperature up to 500 °C at 3 °C/min under vacuum. For determination of the activation energy (E_a) DSC measurements were performed on the undoped and the doped samples under the same pressure conditions by heating at 1, 3, 7 and 10 °C/min. Mass spectrometric (MS) measurements were conducted by using the HPR-20 Q/C apparatus (Hiden-Analytical Ltd., UK). After the ball milling procedure, the milling vial was connected to a MS to measure the atmosphere inside the vial. Results of the MS are presented in semi-log scale in Figure 49.

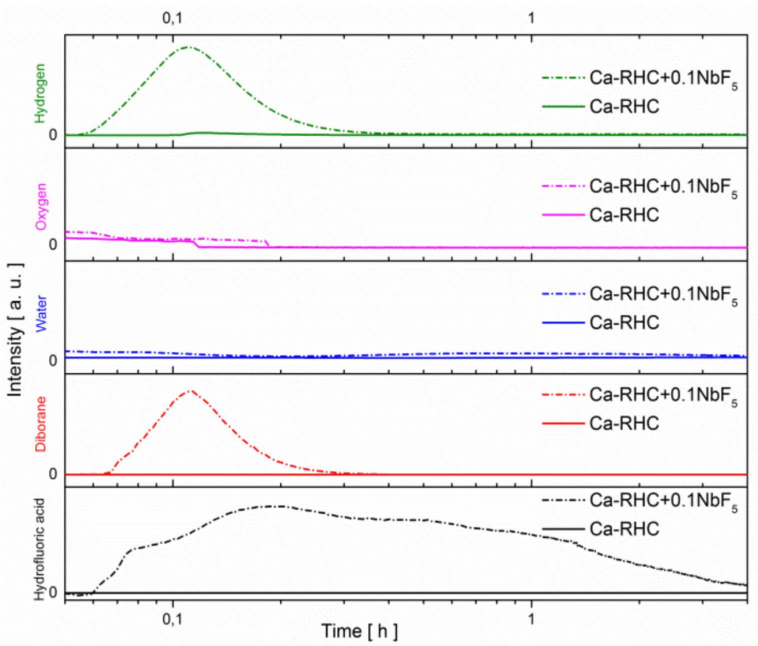

Figure 49. Mass-spectroscopy of the gases measured in the milling vial directly after the milling procedure of pure Ca-RHC and Ca-RHC+0.1NbF_5.

The signals observed from the pure Ca-RHC are displayed by solid lines and those from Ca-RHC+0.1NbF_5 are presented by dashed lines, in all panels. In contrast to the as-milled pure

Ca-RHC sample, the MS of the doped sample reveals an atmosphere consisting of hydrofluoric acid (HF), diborane (B_2H_6) and hydrogen (H_2). In both samples, neither humidity nor oxygen is observed. Coupled manometric-calorimetric measurements performed on the undoped and doped samples are displayed in Figure 50. The manometric curve of pure Ca-RHC shows hydrogen release starting from ~350 °C, with an increase in desorption rate at about 360 °C, which is correlated to a H_2 release of more than 6 wt % in about 20 °C range. Along with this process, the calorimetric curve shows an endothermic peak with an onset temperature of 357 °C. The dehydrogenation reaction enthalpy (42 kJ/mol H_2) of the pure Ca-RHC was calculated by taking the amount of hydrogen released under the main endothermic peak. The small endothermic peak at 160 °C (onset T = 155 °C) is not associated to any mass decrease and can be attributed to the phase transition from α and γ-$Ca(BH_4)_2$ to β-$Ca(BH_4)_2$, as was reported in the literature.[232] Regarding the as-milled NbF_5 doped sample (see Figure 50 b), this endothermic peak at 160 °C is absent, indicating that the α and γ-$Ca(BH_4)_2$ polymorphs have disappeared or at most is present in a negligible amounts in the as-milled Ca-RHC+0.1NbF_5 sample. The hydrogen release starts at approximately 250 °C, as it is evident in the manometric curve and in the calorimetric profile (the onset temperature of the endothermic peak is 301 °C). This means that there is a significant decrease (~ 100 °C) in the desorption onset temperature. The desorption enthalpy, of the doped system was determined to be 37 kJ/mol H_2. The apparent activation energy E_a of the overall desorption process for the undoped and the doped systems were evaluated by the Kissinger method [233] after performing the calorimetric measurements at four different heating rates (1, 3, 7 and 10 °C/min, respectively; see Figure 51).

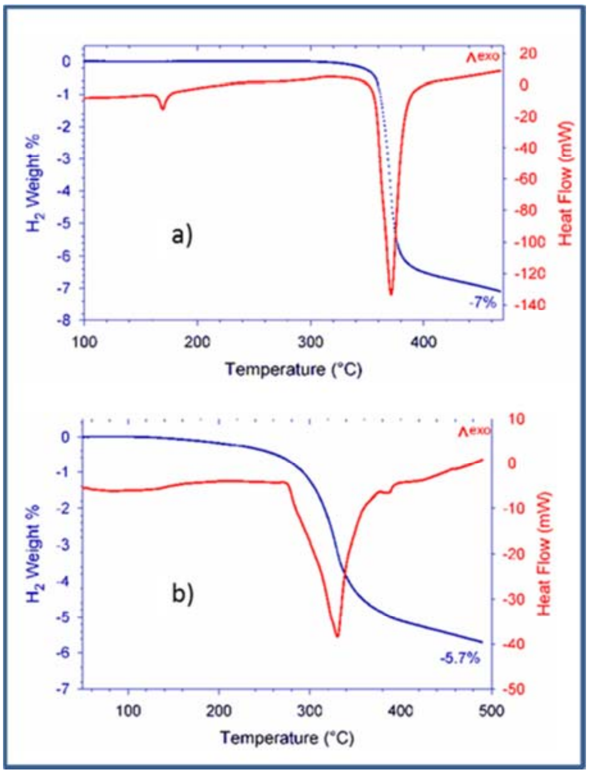

Figure 50. Coupled DSC-manometric curves of Ca-RHC and Ca-RHC+0.1NbF_5 with 3 K/min under vacuum condition

For the undoped systems a value of 217 kJ/mol H_2 was obtained, and for the NbF_5 doped system a value of 198 kJ/mol H_2. In order to determine the reaction mechanism and final products of the pure and doped Ca-RHC *in situ* SR-PXD were carried which are presented in the following subsection.

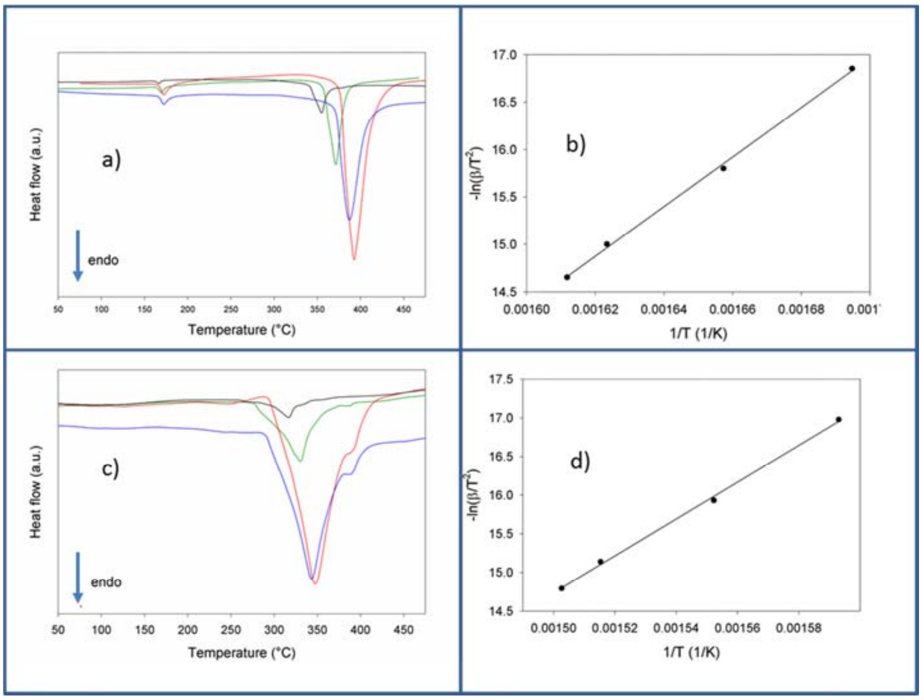

Figure 51. Calorimetric profiles and related Kissinger plot of the undoped (a, b) and the doped (c, d) samples heated from room temperature up to 500 °C at 1 (black line), 3 (green line), 7 (blue line) and 10 (red line) °C/min in vacuum.

5.1.2. In situ SR-PXD-measurements

The dehydrogenation reaction paths of the as-milled pure Ca-RHC and Ca-RHC+0.1NbF_5 were investigated using *in-situ* SR-PXD. In Figure 52 the *in-situ* SR-PXRD pattern of Ca-RHC and Ca-RHC+0.1NbF_5 are shown. The diffractograms peaks corresponding to the starting material, intermediate state and final desorption products are denoted by symbols.

One dimensional diffraction patterns are plotted as a function of temperature and diffraction angle (T, 2θ) 3D and 2D plots in Figure 52 (a). In the case of pure Ca-RHC, the starting material is composed of α, β and γ polymorphs of $Ca(BH_4)_2$ and MgH_2. With increasing temperature all phases remain stable up to 140 °C. Thereafter the phase transformation from α and γ to β-$Ca(BH_4)_2$ occurs, while the intensities of MgH_2 remain unchanged. Subsequently an intermediate $Ca_4Mg_3H_{14}$ phase temporarily appears. The $Ca_4Mg_3H_{14}$ phase is formed by the chemical reaction of CaH_2 and MgH_2 phases, [234] with CaH_2 being a decomposition product of $Ca(BH_4)_2$. Then, $Ca_4Mg_3H_{14}$ decomposes at about 365 °C, leading to the formation of CaH_2 and Mg phases. After the decomposition of $Ca(BH_4)_2$, no boron containing phases are detected in the XRD pattern, neither among the intermediate phases nor in the final products. This indicates the amorphous and/or nano-crystalline nature of boron compound(s) among the decomposition products of the Ca-RHC sample. Indeed the broad hump in the 2θ region between 7° and 17° hints at an amorphous phase present in the desorbed Ca-RHC sample. Possible amorphous/nanocrystalline products, CaB_6, amorphous boron or amorphous sub-stoichiometric $CaB_{12}H_{12-x}$ compounds may be formed, as well, as it was observed recently for

$Li_2B_{12}H_{12}$ in the $LiBH_4$ system [193] Figure 52 (b) shows the *in-situ* SR-PXD of the dehydrogenation paths of Ca-RHC+0.1NbF_5. The starting material consists of MgH_2, CaF_2, β-$Ca(BH_4)_2$ and a low amount of the α and γ-polymorphs of $Ca(BH_4)_2$. In this case, the decomposition of β-$Ca(BH_4)_2$ starts around 250 °C, in accordance with the coupled manometric-calorimetric measurements (Figure 50 (b)).

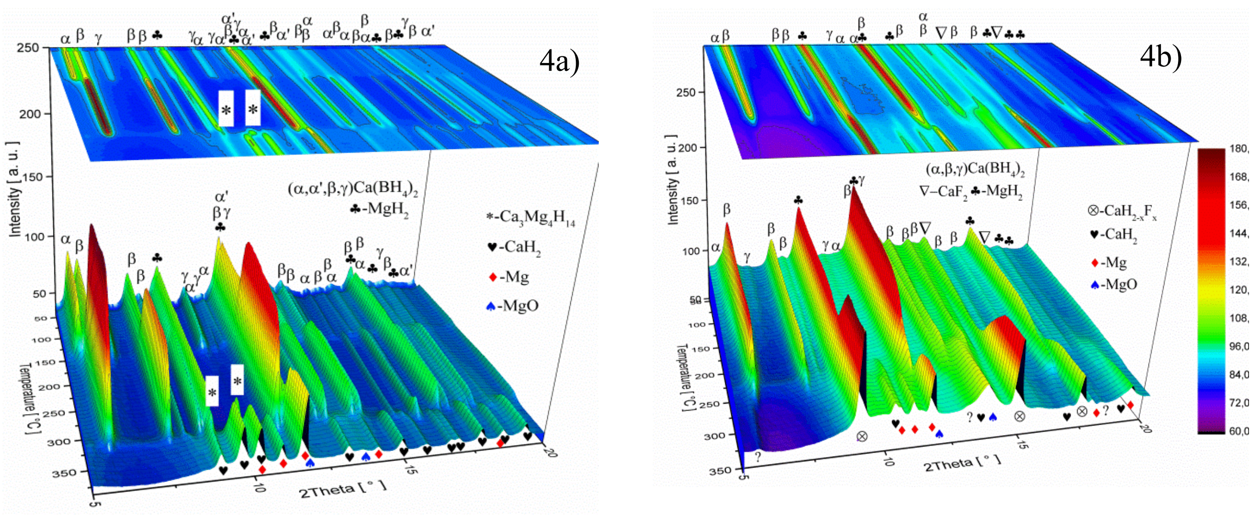

Figure 52. In-situ SR-PXD measurement of Ca-RHC (a) and Ca-RHC+0.1NbF_5 (b) under static vacuum. The samples were heated up from RT up to 400 °C with a heating rate of 3 K/ min (measured at the diffraction beamline D3 with $\lambda = 0.5$ Å at the DORIS III synchrotron storage ring at HASYLAB (DESY, Hamburg, Germany).

Furthermore, in contrast to pure Ca-RHC, neither the intermediate phase ($Ca_4Mg_3H_{14}$) nor CaH_2 peaks are observed after dehydrogenation of $Ca(BH_4)_2$ and MgH_2. Instead, after the decomposition of $Ca(BH_4)_2$, the peak intensities of a CaF_2-like structure arises which can be assigned to the formation of a solid solution phase $CaF_{2-x}H_x$ as has been is reported in the literature. [235-237] Magnesium, MgO and a minor unknown phase are observed as final products of the desorbed Ca-RHC+0.1NbF_5. The formation of MgO could not be avoided in both measurements. This could be due to either impurities present in the starting materials, which has been an issue for other studies on $Ca(BH_4)_2$ [238] and/or a small undetected leakage in the sample holder system. A broad hump (in the region ~ 7° to 17°) is also observed in the XRD-pattern of dehydrogenated Ca-RHC+0.1NbF_5 is also observed which is more pronounced than that of pure dehydrogenated Ca-RHC. In a similar way as for the pure Ca-RHC, this hump might be due the presence of a portion of the sample in amorphous and/or nano-crystalline state. This suggests the presence of a higher amount of nanocrystalline/amorphous material in the dehydrogenated doped sample in comparison to desorbed pure Ca-RHC. Neither NbF_5 nor any other known Nb-containing phases are observed *via* SR-PXD in the starting material or desorbed sample. Also, the state of boron is unknown. Thus, to reveal the state of Nb and other amorphous/nanocrystallite Ca-B-H containing phases in the composite system, solid state ^{11}B MAS NMR measurements were conducted.

5.1.3. NMR measurements

Solid-state ^{11}B MAS NMR was applied to investigate the possible presence of amorphous/nanocrystalline boron containing phases on both the ball-milled samples and after the first dehydrogenation process. Results of these measurements are shown in the Figure 53. In the top and middle panels the spectra of desorbed Ca-RHC+0.1NbF$_5$ / Ca-RHC and as-milled Ca-RHC+0.1NbF$_5$ / Ca-RHC are presented, respectively. In the inset figure of the middle panel, a magnification of a weak signal of the ^{11}B NMR-spectrum of the as-milled Ca-RHC+0.1NbF$_5$ is shown, which is not present in the NMR-pattern of the as-milled pure Ca-RHC. The NMR-spectra of reference compounds are presented in the bottom panel. Side bands are marked by asterisks and peaks are pronounced by a vertical line. No significant differences are visible between the ^{11}B NMR spectra of the as-milled pure Ca-RHC and Ca-RHC+0.1NbF$_5$. At -30 ppm and at -32 ppm the signals of, respectively, α-Ca(BH$_4$)$_2$ and β-Ca(BH$_4$)$_2$ polymorphs[232] are observed. [149] In addition, a closer look at the spectrum of Ca-RHC+0.1NbF$_5$ shows a weak signal at ~ +15 ppm which is not present in the spectrum of pure Ca-RHC and it can be attributed to the signal of CaB$_6$. [133] No trace of any Ca(BF$_4$)$_2$ or Ca(BF$_{4-x}$H$_x$)$_2$ species can be observed which is in agreement with the results obtained by Grove *et al.* [239]

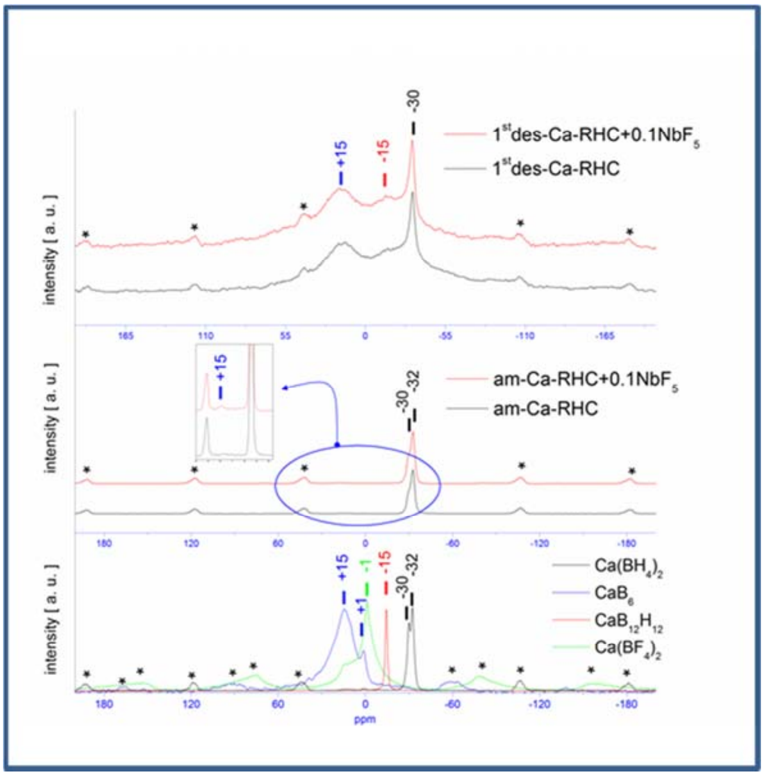

Figure 53. ^{11}B MAS NMR-pattern of once desorbed Ca-RHC/Ca-RHC+0.1NbF$_5$ (top) and as-milled Ca-RHC/Ca-RHC+0.1NbF$_5$ (middle) samples with the pattern of references (bottom). These measurements were carried out at HZG.

The spectra of the dehydrogenated samples (pure and doped Ca-RHC) show peaks at matching positions, suggesting the same boron containing decomposition products. The signals at +15 ppm, -15.5 ppm and -32 ppm, respectively, correspond to CaB$_6$, CaB$_{12}$H$_{12}$ and to residual β-Ca(BH$_4$)$_2$ phases.[133] However, the chemical state of the niobium-containing phases in the hydride matrix could not be detected using the ^{11}B MAS NMR method. This might be due to the presence of nanoscopic Nb-containing structures in the samples. Because they produce very broad NMR-signals, their distinguishable detection is not straightforward. Therefore, these issues are addressed in the following subsection by the XAS technique which is a powerful method for probing the chemical state and the local environment of a nanoparticulate system.

5.1.4. EXAFS/XANES measurements

To determine the oxidation state of niobium in the Ca-RHC+0.1NbF$_5$ after both ball milling and dehydrogenation, XANES measurements on these samples were carried out. Several Nb-based compounds (metallic Nb, Nb$_2$O$_5$, NbF$_5$ and NbB$_2$) were measured as well, for comparison with the near edge structures of niobium in the samples. Derivatives of the XANES spectra were built in order to emphasis the similarities or differences of the near edge structures. The results of this aforementioned procedure are displayed in Figure 54.

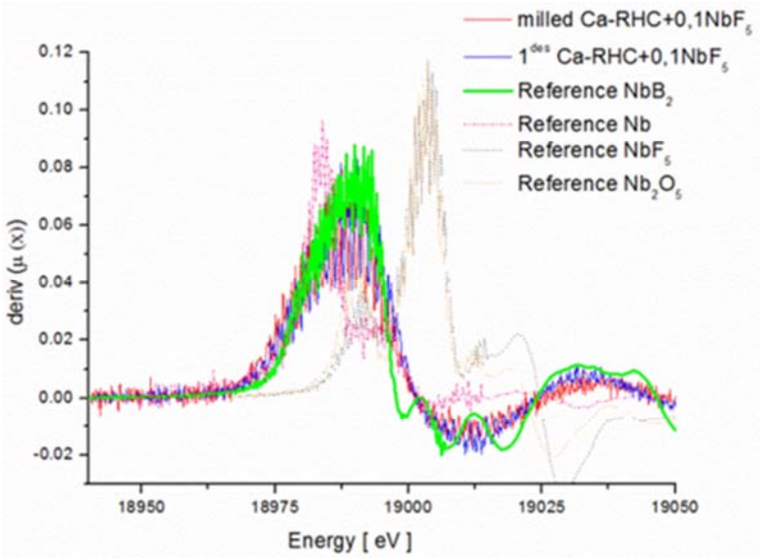

Figure 54. Derivative of XANES structures of the samples and the main references (measured at the beamline C1 at the DORIS III synchrotron storage ring at HASYLAB (DESY, Hamburg, Germany).

Both Ca-RHC+0.1NbF$_5$ samples show similar XANES structures indicating that all Nb atoms have the same chemical state after the milling procedure as well as after the first dehydrogenation step. A comparison between the XANES of the Ca-RHC+0.1NbF$_5$ samples and the Nb-based reference compounds shows a good agreement between the XANES of the NbB$_2$-reference curve and those of the Ca-RHC+0.1NbF$_5$ samples. Therefore, the oxidation state of niobium after milling in the Ca-RHC matrix can be estimated to be +2 which is stable upon hydrogen cycling. The local environment of the niobium atoms was revealed by using the Extended X-ray Absorption Fine Structure (EXAFS) region of the measured XAS-spectra. The extracted EXAFS region of the samples and references were Fourier transformed to display the radial distribution of the atoms around the resonant Nb atoms (Figure 55).

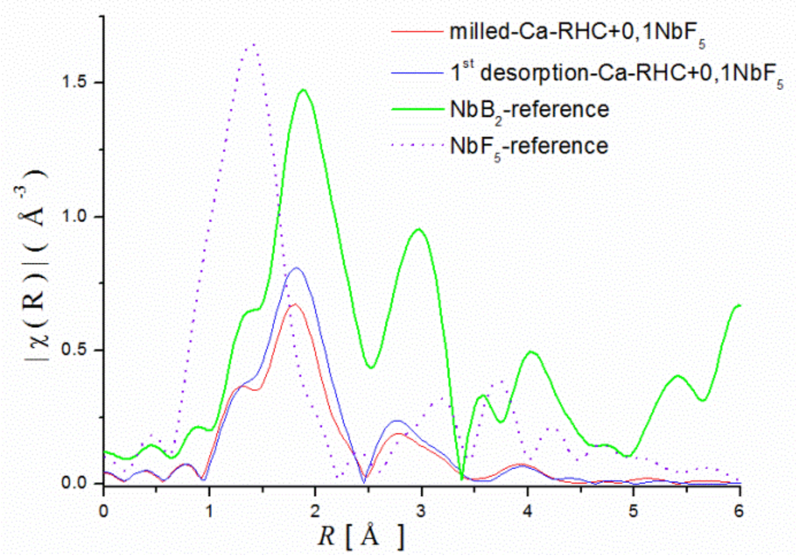

Figure 55. Radial distribution functions (FT-of EXAFS-spectra) of the samples and references (measured at the beamline C1 at the DORIS III synchrotron storage ring at HASYLAB (DESY, Hamburg, Germany)..

By comparing the radial distribution functions (RDFs) of the samples shown in Figure 55 with that of the NbF$_5$ reference, the absence of fluorine atoms in the first shell of the samples is obvious. Higher order shells also show significant differences in RDFs to the NbF$_5$ reference, which indicates the removal of fluorine atoms from the environment of Nb atoms. A further comparison of the RDFs of the samples with that of the NbB$_2$ reference exhibits high similarity up to the second shell. The amplitude of the milled sample shows the lowest RDF magnitude and grows after the dehydrogenation process. This is an indication of a higher degree of ordering/growing of Nb containing structures with hydrogen cycling. Due to the absence of higher order amplitudes in the RDFs of the samples and the lack of any diffraction peaks of NbB$_2$ in the *in-situ* SR-PXD measurements or a well-defined signal in the ^{11}B NMR spectra of Ca-RHC+0.1NbF$_5$ samples (see Figure 52, Figure 53), the formation of nanocrystalline NbB$_2$ can be assumed. This indicates the presence of well-dispersed and unsegregated NbB$_2$ in the Ca-RHC matrix. To verify the presence of the NbB$_2$ species in Ca-RHC+0.1NbF$_5$ samples the EXAFS data of the dehydrogenated Ca-RHC+0.1NbF$_5$ sample was fitted by assuming a hexagonal NbB$_2$ crystal structure model with the space group *P6/mmm*, and the result is displayed in Figure 56.The fit parameters are summarized in Table 7. The fitting procedures were carried out simultaneously from 1 to 3 *k*-weighted range in R-space.

Table 7. Fitting parameters for the desorbed-Ca-RHC+0.1NbF$_5$ sample.in R-space (1.3 - 6) Å and (2.0 - 8.0) Å^{-1} in the k-space with a $S_0^2 = 0.78$, $\Delta E = 7.97$ eV and a R-factor = 0.018.

Modell	**Shell**	***N***	**ΔR[Å]**	**σ[Å]**
NbB$_2$ Hexagonal-*P6/mmm*	Nb-B1	12	0.0348	0.0149
	Nb-Nb1	8	0.0246	0.0141
	Nb-B1-B1	24	0.0696	0.1234
	Nb-B2	12	0.1267	0.0298

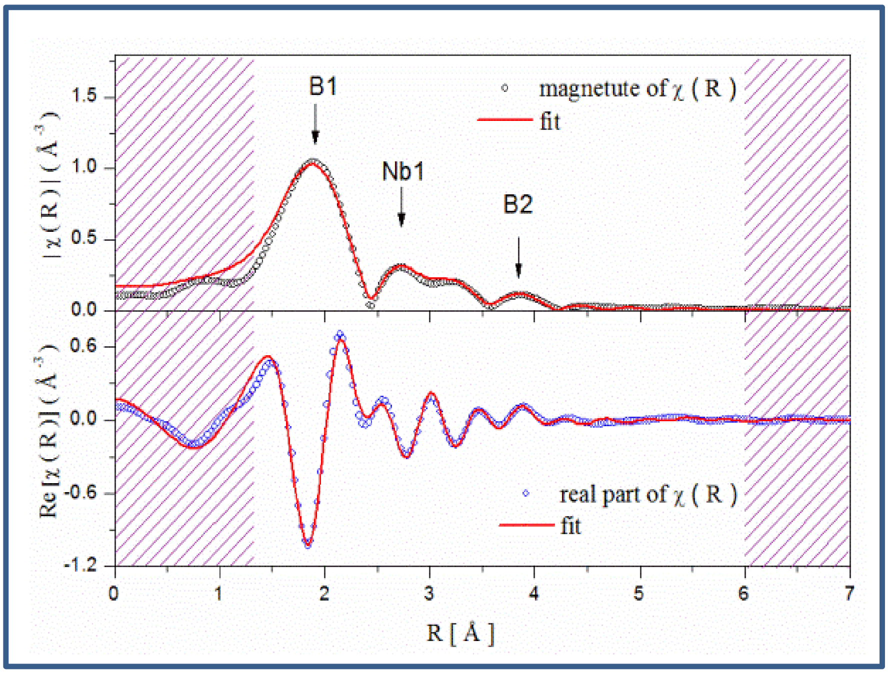

Figure 56. The magnitude (top) and the real part (bottom) of the EXAFS-spectrum of the desorbed Ca-RHC+0.1NbF_5 sample in R-space with their corresponding fits (measured at the beamline C1 at the DORIS III synchrotron storage ring at HASYLAB (DESY, Hamburg, Germany).

These results are in excellent accordance with the results observed by other authors,[102, 130, 240, 241] who also reported the formation of transmission metal (TM)-diborides during ball milling of complex borohydrides with TM-fluorides, chlorides and isopropoxides in other RHC systems. Taking into account the additional information gained by NMR and XAS further insight and a more reliable attribution of Bragg reflections can now be obtained by refinement of the diffraction profiles using the Rietveld method.[242] MAUD software[243] was used for the Rietveld refinement of the SR-PXD patterns. The SR-PXD patterns of as-milled Ca-RHC and Ca-RHC+0.1NbF_5 at room temperature (RT) is displayed in Figure 57 (a) and (c), respectively. The ratio between the polymorphs of calcium borohydride in the doped systems is altered in comparison to the pure system. The relative change in mass fraction of the α, β and γ-$Ca(BH_4)_2$ polymorph is 0.10, 0.86, and 0.04 , respectively, for the NbF_5- doped system in comparison to the respective values 0.18, 0.72, 0.10 of the pure Ca-RHC system. The microstructure of the compounds in Ca-RHC+0.1NbF_5 is also strongly refined in comparison to undoped Ca-RHC. It was found that the overall crystallite sizes in doped Ca-RHC were roughly 50% smaller and the microstrain values were approximately doubled compared to the undoped sample, as a consequence of the combined use of additive and ball milling action. In the high temperature (HT) state, metallic magnesium, amorphous calcium hexaboride and crystalline calcium hydride phases were produced in Ca-RHC. However, in the corresponding doped system in addition to CaB_6 a calcium- fluoride- hydride solid solution was formed instead of the equivalent metal hydride phase (Figure 57 (b), and (d)). Diffractograms, taken at RT and dehydrogenated material at HT, of doped and undoped Ca-RHC were refined and their quantitative results were compared. The comparison between the refinements of the diffraction patterns collected at RT (Figure 57 (*a*), (*c*)) revealed different composition and crystallinity of the Nb-doped systems. It is worth mentioning that the diffraction patterns were fitted with a high degree of confidence ($R_w < 3\%$) only if the nanocrystalline/amorphous phases were included in the refinement model. Examples of similar approaches can be found in the literature.[244] As a result of the refinement, $CaF_{2-x}H_x$ is supposed to contain less of hydride anions than the maximum value (x = 1.07 rather than x_{max} = 1.24).[235] The results suggest that $CaF_{2-x}H_x$ can play an active role in the dehydrogenation reaction by exchange of the fluoride and hydride ions in the hydrogen concentration range of $0 < x \leq 1.24$. The sizes of the NbB_2 grains, calculated by the Rietveld refinement, were determined to be in the range of 7-10 nm. However, the presence of at least two different nanocrystalline components (CaB_6, $CaB_{12}H_{12}$) in a system with such rich phase composition raised problems in the accuracy of the numerical result due to correlations between the two phases. Hence, the size distribution of NbB_2 phase was further evaluated by ASAXS measurements which are presented in the following subsection.

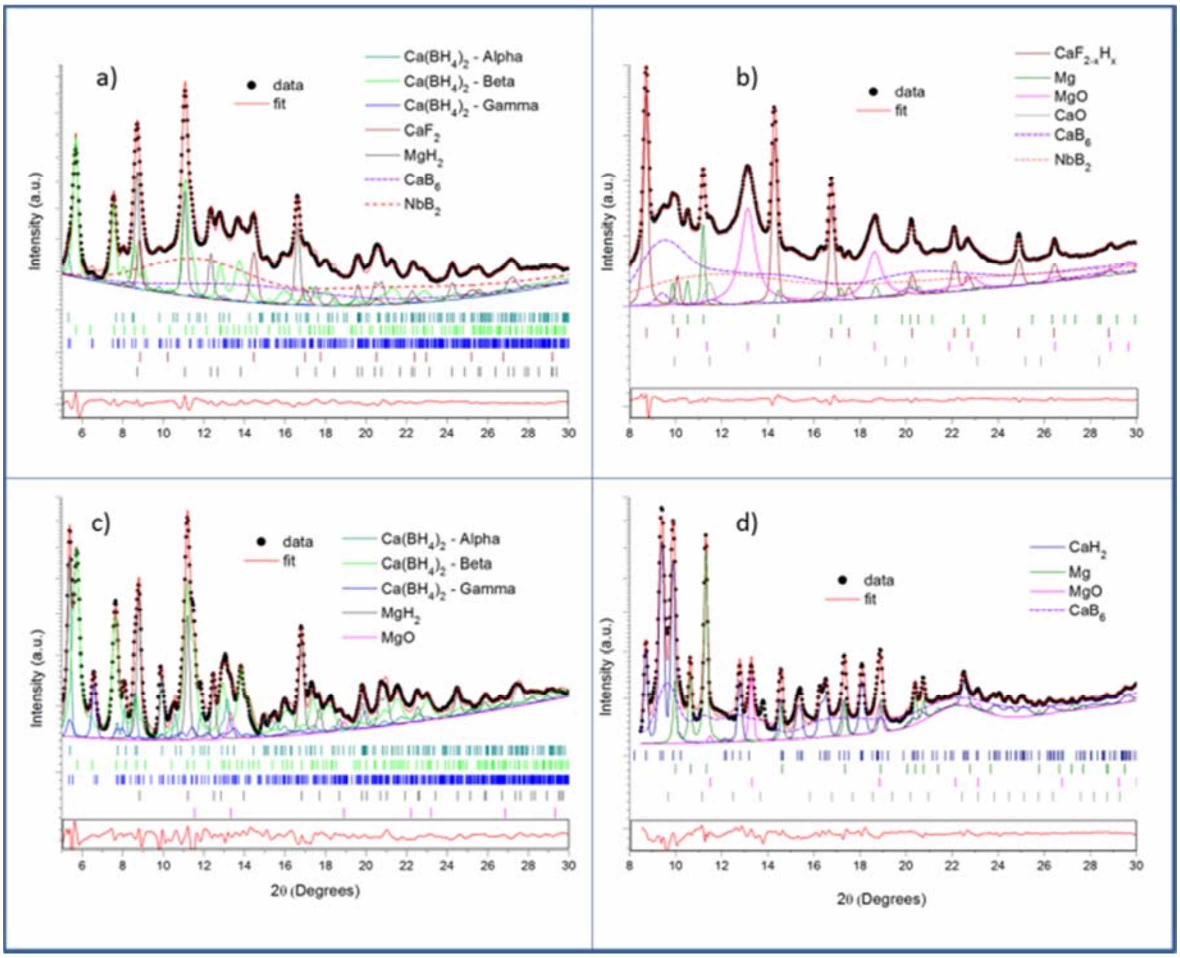

Figure 57. SR-PXD pattern (black dots) collected at room temperature and high temperature respectively for doped - (a) , (b) , and undoped - (c), (d) - Ca-RHC, and the corresponding simulated profiles. The contribution of each phase with the corresponding Bragg reflections (marked ticks) and the residuals function (red line in the box) are also reported. Only structural models from ICSD database were used (measured at the diffraction beamline D3 with $\lambda = 0.5$ Å at the DORIS III synchrotron storage ring at HASYLAB (DESY, Hamburg, Germany).

5.1.5. **ASAXS measurements**

ASAXS measurements were carried out at the calcium and at the niobium K-edge, respectively, in order to determine the impact of the additive on the calcium containing structures of the hydride matrix and to characterize the size distribution of niobium containing structures. Calcium-ASAXS measurements were performed at the 7T-MPW-SAXS beamline at BESSY (Berlin, Germany). The samples were put into a circular hole (5 mm in diameter and 0.2 mm thick) of an aluminum sample holder and sealed with Kapton tapes to avoid any oxidation of the samples. Two sample-to-detector distances (D_{min}= 400 mm and D_{max}= 3345 mm) were chosen in order to cover the maximal q-range accessible. The SAXS measurements were taken at four distinct energies at the calcium K-edge (Table 8). The SAXS data was collected on a Multi-Wire-Proportional-Counter (MWPC) gas filled area detector with a pixel size of 207 μm. During the measurements, the samples were kept under continuous vacuum (10^{-4} mbar) conditions to minimize parasitic scattering. The measured intensities were corrected for background (scattering contribution of the beam without sample)), for detector dead time, for detector sensitivity by measuring a scandium foil, and also for transmission and flux. 90 μm thick glassy carbon standards were used for obtaining the scattering cross section in absolute units. Also silver behenate standard was measured to calibrate the q-axis.

Table 8. Selected energies for the Ca-ASAXS measurements at the K-edge of Ca at the ASAXS beamline (BESSY, Berlin) and the corresponding theoretical anomalous dispersion factors (ADF).[5]

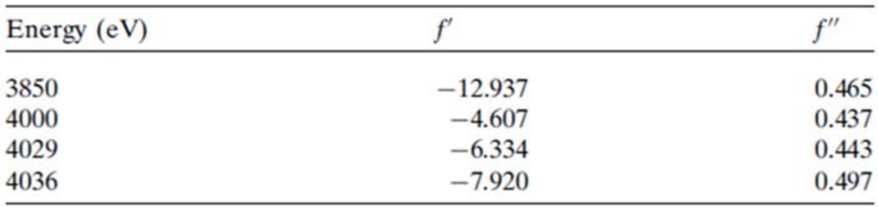

Energy (eV)	f'	f''
3850	−12.937	0.465
4000	−4.607	0.437
4029	−6.334	0.443
4036	−7.920	0.497

The Nb-ASAXS measurements were carried out at the beamline B1 at the DORIS III synchrotron ring (DESY, Hamburg, Germany). The samples were mounted in aluminum sample holders with a circular hole of 5 mm in diameter and 1 mm in thickness. All samples were sealed with Kapton tapes to avoid any change in the oxidation state of Nb-containing phases. To avoid possible sample oxidation over the measurement time and air scattering the measurements were performed under continuous vacuum (10^{-4} mbar). The SAXS patterns were acquired at four distinct energies (Table 9) below the Nb K-edge at two distances (D_{min}= 885 mm and D_{max}= 3585 mm) to cover the maximum available q-range. The SAXS measurements were collected with a 2-dimensional single photon counting Pilatus 1M detector. The measured intensities were corrected for background (scattering contribution of the beam without sample), sample absorption, and incoming flux, and were put onto absolute intensity units by measuring a glassy carbon reference. Both beamlines were equipped with a double crystal Si-monochromator with the wavelength resolution of $\Delta\lambda / \lambda \approx 10^{-4}$. Handling and preparing of the samples were carried out in purified Argon glove box (H_2O and O_2 levels were kept below 10 ppm).

Table 9. Selected energies for the ASAXS-measurements at the K-edge of Nb at the B1-beamline (DESY) and the corresponding theoretical ADF.[5]

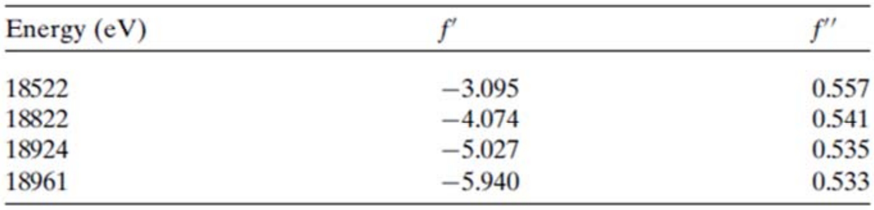

Energy (eV)	f'	f''
18522	−3.095	0.557
18822	−4.074	0.541
18924	−5.027	0.535
18961	−5.940	0.533

All the as-collected 2D-ASAXS data were integrated over the polar variables (R, 2π) and reduced to 1D-scattering curves. Subsequently, the ASAXS curves were subtracted by an energy dependent background, which is caused by inelastic resonant Raman scattering (RRS) and fluorescence at the high q-values [245, 246]. The energy dependent background is removed as described in [247]) before further analysis. All ASAXS curves were fitted by using SASfit[248] assuming a polydisperse spherical particle model. Since the crystal growth processes usually yield a lognormal distribution of the particle dimensions (Bergmann & Bill, 2008), a lognormal distribution was used. The average size parameter (μ) and the width parameter (σ) of the distribution were varied to obtain the best fit to the experimental data. The resonant scattering curves of the Ca-containing phase were separated by using the method described by Goerigk *et al.* [249] Figure 58 shows, exemplarily, the resonant scattering curves and their corresponding fit curves for pure Ca-RHC and Ca- RHC+0.1 NbF_5 samples in the desorbed state. All resulting size distributions of the Ca-containing structures from the fits were normalized by their area and are presented in Figure 58. A comparison of the curves of the samples with and without additive, respectively, shows that the calcium structures in the desorbed and absorbed doped samples are much finer. Also the degree of polydispersity in the desorbed and absorbed samples is also considerably lower than the corresponding pure Ca-RHC samples.

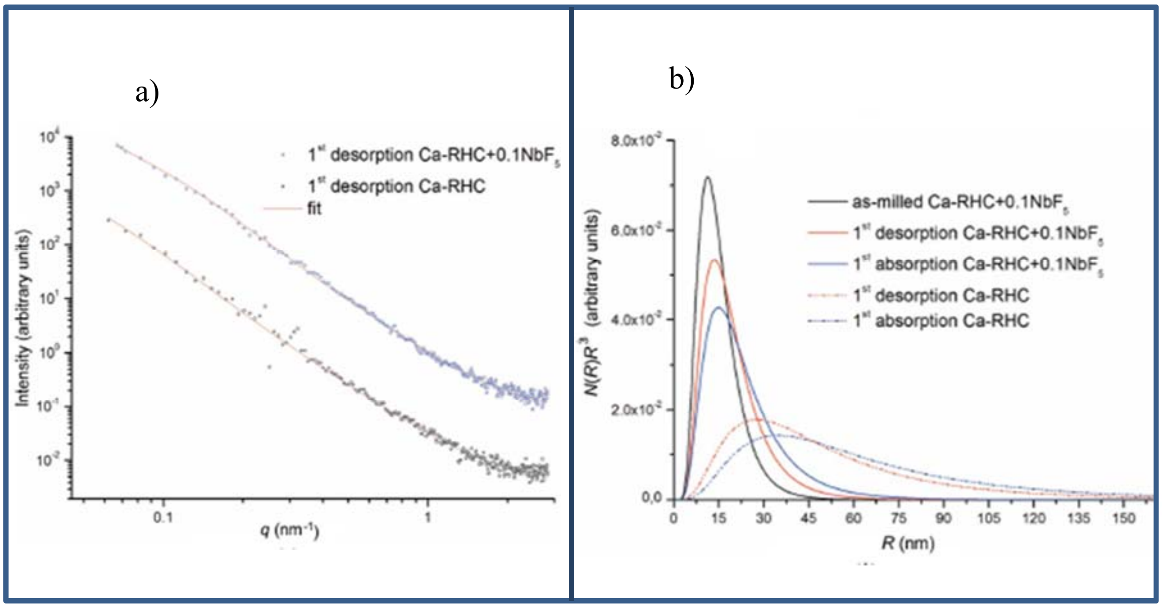

Figure 58. (a) Calcium resonant scattering curves of pure Ca-RHC and Ca- RHC+0.1NbF_5 samples after the first desorption and their corresponding fits. (b) Volume-weighted size distribution functions of calcium structures in pure Ca-RHC and Ca-RHC+0.1NbF_5 samples. Measurements were carried out at the 7T-MPW-SAXS beamline at the BESSY synchrotron storage ring (Berlin, Germany).

The mean sizes of calcium-containing structures after desorption and absorption in the pure Ca-RHC is approximately 54 and 68 nm, respectively. This corresponds to a relative coarsening of the mean size of Ca-containing particles by 26% in comparison to the desorbed state. The maximum size of the Ca structures after the first desorption and the first absorption of the pure Ca-RHC remains roughly stable and their sizes amount to ~500 nm. Likewise the degree of polydispersity of the absorbed pure Ca-RHC sample increases slightly from σ_{des} = 0.653 to σ_{abs} = 0.655. The average sizes in the as-milled Ca-RHC+0.1NbF_5 are about 22 nm, which grow after first desorption and first absorption, respectively, to about 27 and 30 nm. This corresponds to an average size growth of 18% after the first desorption and 10% after the first absorption. The maximum structures presented in the as-milled Ca- RHC+0.1NbF_5 sample are ~80 nm, which coarsen after the first desorption and first absorption to 100 and

140 nm, respectively. This relates to coarsening degrees of 20 and 28% after the first desorption and first absorption, respectively. Also an increasing degree of polydispersity with the sorption cycle is observed for the Ca-RHC+0.1NbF$_5$ samples (σ_{am} = 0.447 → σ_{des} = 0.492 → σ_{abs} = 0.541). The result of Nb-containing structures in the surrounding hydride matrix is presented in Figure 59. The SAXS scattering curve shows two scattering features at a low q value centred at about 0.25 nm^{-1} and a broad hump extended over the q-interval of 1.5-7 nm^{-1}. The inset plots show in more detail the strong scattering region (0.1 nm^{-1} < q < 0.6 nm^{-1}), and the less pronounced scattering region at the higher q values. These resonant scattering regions can be attributed to two distinct niobium nano particle distributions.

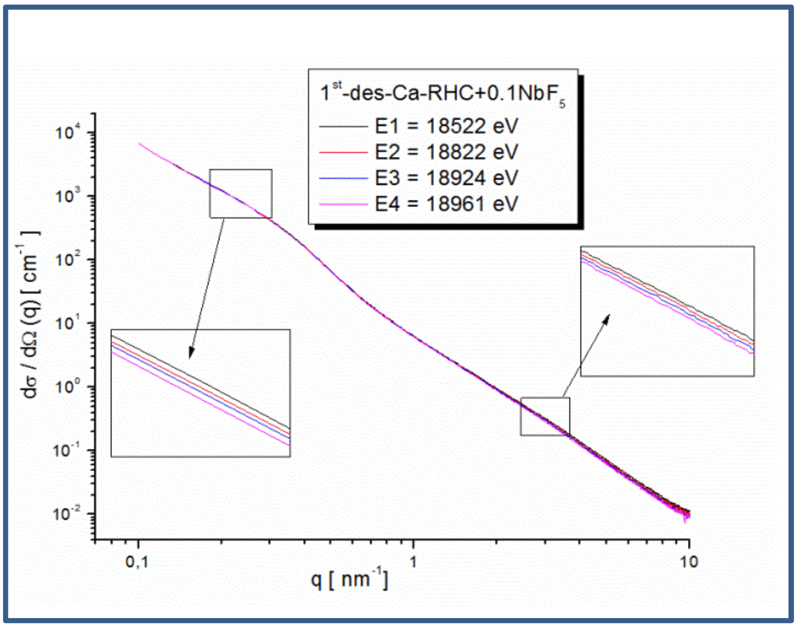

Figure 59. ASAXS curves of Ca-RHC+0.1NbF$_5$ sample after the first desorption. In the inset figures the resonance effect of Nb containing structure in the sample illustrated (measured at the beamline B1 at the DORIS III synchrotron storage ring at HASYLAB (DESY, Hamburg, Germany).

Hence, two sets (j = 1,2) of polydisperse spherical Nb containing particles were simultaneously fitted to the ASAXS data measured at four different X-ray energies (E_i; i=1, 2 , 3, 4*; see* Tabale.1) by the following theoretical intensities:[250,251]

$$I(q,E_i) = \sum_{j=1}^{2} \Delta\rho_j^2(E_i) \int N(r,\sigma_j,R_j) V^2(r) F_j(r,q) dr + B(q,E_i) \qquad (86)$$

The energy-dependent contrast of the j^{th} scattering contribution is represented by $\Delta\rho_j^2$. To account for the polydispersity of the Nb- containing particles in the hydride matrix, a normalized log-normal size distribution of the nano-particles was included:

$$N(r,\sigma_j,R_j) = \frac{1}{\sqrt{2\pi}\sigma r} exp[-\frac{\ln\left({}^{r}/_{R_j}\right)^2}{2\sigma_j^2}] \qquad (87)$$

With σ_j being the standard deviation of the distribution and R_j the mean radius parameter of the j^{th} constituent and r denote the radius of the spherical particles. $V(r)$ and $F(r,q)$ represent, respectively, the volume and the form factor of spherical particles (see section 2.7.2). A non-constant background $B(q,E_i) = q^{-\alpha(E_i)} + C(E_i)$ was included to account for the scattering of large particles (out of experimental accessible q-range) and the energy dependent fluorescence and resonant-Raman scattering. For the fitting procedure, the program SASfit[248] was used. The calculated volume-weighted size distribution from the fit for the dehydrogenated Ca-RHC+0.1NbF$_5$ sample is presented in Figure 60.

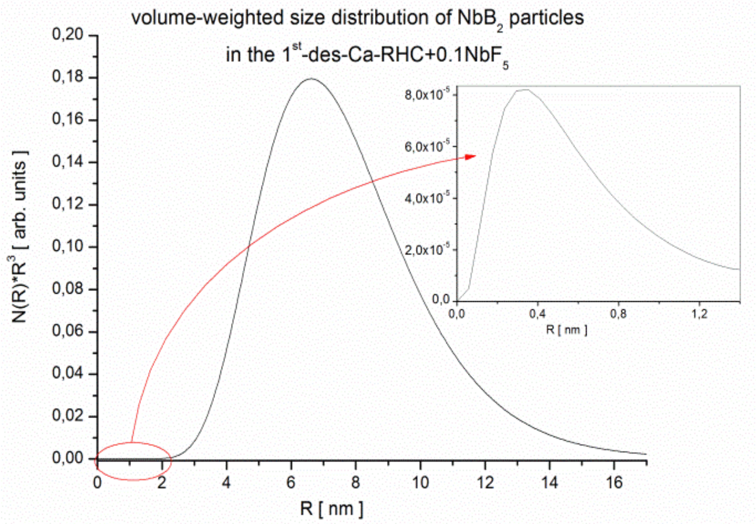

Figure 60. Volume-weighted size distribution of NbB$_2$ particles in the Ca-RHC+0.1NbF$_5$ hydride composite sample after the first desorption. In the inset figure size distribution of smallest particles are observed in the very high q-values.

The mean particle sizes, related to the broad hump located at high q values, are around ~ 0.8 nm on average and maximum sizes are about 1.5 nm (inset Figure 60). However, their volume fraction is negligible small in comparison to the Nb-containing particles due to the pronounced hump at lower q values. Therefore, the most frequent NbB$_2$ particle sizes present in dehydrogenated Ca-RHC+0.1NbF$_5$ sample are about 14 nm. This result is in good agreement with observation carried out on additive size distributions in complex hydrides and hydride composite systems.[102, 241, 252] SEM and HR-TEM investigations were undertaken to further investigate the local nanostructure of the Ca-RHC and Ca-RHC+0.1NbF$_5$ samples.

5.1.6. **TEM/SEM measurements**

SEM investigations on the as-prepared Ca-RHC and Ca-RHC+0.1NbF$_5$ samples showed the presence of agglomerates with sharp borders and sizes between 5 and 50 µm. The same morphology is preserved in the desorbed samples. By EDS analysis, a map of the distribution of the different elements in the doped as-milled sample and the same sample after desorption was obtained. For both samples the Ca-containing phases appeared to be distributed homogeneously, as is evident in Figure 61, which shows the elemental mapping of the doped sample after the first desorption. The Mg-containing phases exist in regions that have aggregated in larger agglomerates lying on the Ca-phases. The F and Nb containing phases are highly distributed in the hydride matrix (see the overlapping maps for Nb and F).

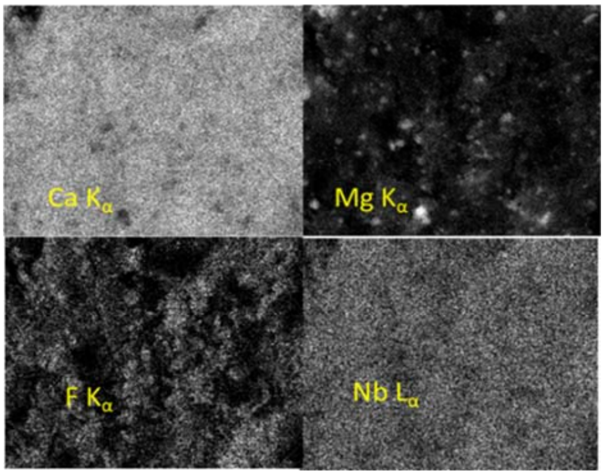

Figure 61. Elemental maps obtained by EDS for the NbF_5 doped Ca-RHC sample after desorption (the measurements were performed at the university of Pavia (Italy) in collaboration with Prof. Dr. C. Milanese).

A further insight into the nanoscopic scale was undertaken by using TEM to reveal the local structure of the hydride matrix and the Nb-based additive in the hydride matrix. TEM investigations showed that after desorption, both, Ca-RHC and Ca-RHC+0.1NbF_5, samples consisted of large aggregates (typically > 10 μm) that had a composite morphology of nanoscopic domains (~ 5 - 10 nm) as shown in Figure 62. The nano-composite morphology was observed in all regions of, both, the Ca-RHC and Ca-RHC+0.1NbF_5 samples, but interestingly some regions appeared less crystalline than others (see Figure 62B and C). The highly crystalline regions in Ca-RHC could be indexed by high resolution TEM (HR-TEM) to the reaction products as seen by SR-PXD, NMR and EXAFS results and are displayed in Figure 64. Points (1) and (2) indicate the amorphous region in the Ca-RHC, surrounded by nanocrystalline lattice planes. The amorphous region can be assumed to contain the recently mentioned $CaB_{12}H_{12}$ and/or residual β-$Ca(BH_4)_2$ reaction products (subsection 3.3). Although, the presence of β-$Ca(BH_4)_2$ could be tentatively assigned to some crystalline regions of the desorbed Ca-RHC sample, however, the phase did not appear to be stable under the electron beam. The decomposition of metal hydride phase under the electron beam was also observed by Deprez *et al.*[225] All single phase identifications are made difficult due to a significant overlap of *d*-spacing values between phases, within resolution. Some of the reliable measured lattice planes can be assigned to the following phases: (A) 2.49 Å (011) *hkl* reflection of Mg; (B) and (C) 2.8 Å (011) *hkl* reflection of CaB_6 (D) 1.98 Å (011) *hkl* reflection of CaB_6 (E) and (F) 2.49 Å, Mg.

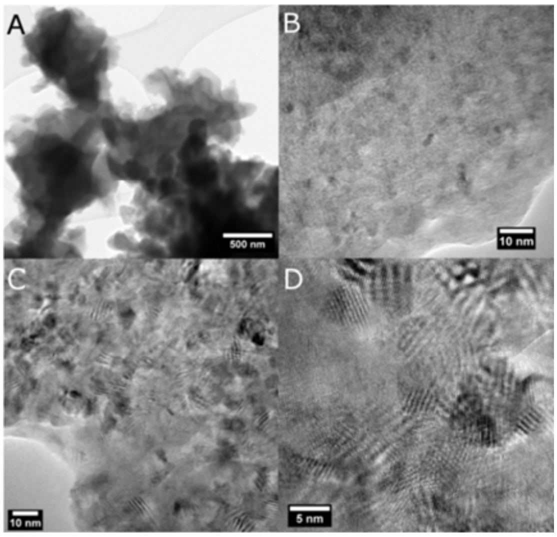

Figure 62. TEM micrographs of Ca-RHC after the first desorption displaying A) large aggregates of smaller particles, B) multiphase regions of low crystallinity C) and D) multiphase region of high crystallinity (the measurements were performed at the Curtin University (Perth, Australia) in collaboration with Dr. M. Paskevicius).

The directional contact of the CaB_6 phases on the Mg nanocrystallites found here indicates that Mg might provide nucleation sites for the CaB_6 phase, therefore inducing further growth of this phase as the reaction proceeds. This behaviour was also observed in other studies,[223] and is an indication that Mg indeed provides a catalytic driving force for the formation of nanocrystalline CaB_6. Further HR-TEM-images were taken to reveal the niobium containing particles in the hydride matrix of the dehydrogenated Ca-RHC+0.1NbF_5 and the results are presented in Figure 63. Due to the low concentration of the additive in the Ca-RHC+0.1NbF_5 sample it was not possible to find many Nb-rich regions. Figure 63B presents a dark-field image of a crystalline Nb-rich region where the lattice planes could be reliably measured. By Fast-Fourier Transformation (FFT) of the aforementioned region, the crystal structure could be assigned to NbB_2. The environment surrounding NbB_2 was investigated to determine which phases were in close contact with this additive. In numerous cases, the NbB_2 was only surrounded by the non-crystalline, amorphous material presumably of Ca-B-H ternary composition (see Figure 63D). Hence, HR-TEM micrograph analysis failed to reveal the crystalline interfaces of the NbB_2 with the surrounding matrix in the present work. The most frequent NbB_2 particle sizes were determined to be ~ 10 nm. These results are in fair agreement with the results obtained by XAS and ASAXS methods.

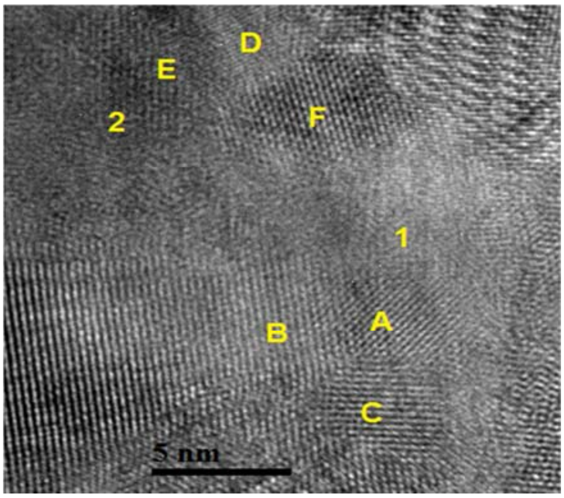

Figure 64. TEM micrographs of Ca-RHC+0.1NbF_5 after the first desorption displaying A) a dark-field where bright regions indicate Nb-rich areas, B) a dark-field of a large Nb-rich region where lattice planes are evident, C) the FFT of a Nb-rich region identifying single crystal NbB_2, and D) a filtered image demonstrating the amorphous structure surrounding NbB_2 (the measurements were performed at the Curtin University (Perth, Australia) in collaboration with Dr. M. Paskevicius).

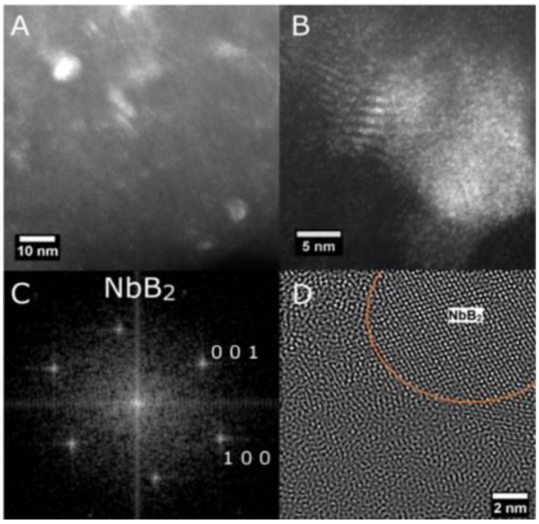

Figure 63. Micrograph indicating localised amorphous regions (1) and (2). Attributed phases for the lattice spacing present include: (A) (011) Mg; (B) and (C) (011) CaB_6; (D) 1.98 Å (011) *hkl* reflection CaB_6 (E) and (F) 2.49 Å, Mg (the measurements were performed at the Curtin University (Perth, Australia) in collaboration with Dr. M. Paskevicius).

5.1.7. Discussion

The significant impact of the NbF_5 additive on decreasing the desorption temperature of the Ca-RHC was evident from the DSC and manometric measurements (Figure 1a, b). The additive reacts during the milling with the Ca-RHC producing hydrofluoric acid; diborane and hydrogen, which was observed via mass spectrometry (see Figure 49). From the DSC curves, the E_a for the dehydrogenation process for the undoped and doped Ca-RHC system was determined (Figure 51). The E_a values for Ca-RHC: (217 kJ/mol H_2) and Ca-RHC+0.1NbF_5 (198 kJ/mol H_2) indicate that the additive reduce activation barrier of the Ca-RHC system during the dehydrogenation process noticeably. Another significant influence of NbF_5 on the Ca-RHC system is its effect on the dehydrogenation reaction path of the system. In-situ SR-PXD analysis (see Figure 52) clearly shows different desorption reaction paths and end products for the pure Ca-RHC and Ca-RHC+0.1NbF_5. According to the in-situ SR-PXD measurements and all the previous analysis of the results, the following dehydrogenation reaction path for the pure Ca-RHC can be proposed:

$$
\begin{aligned}
&(\alpha,\beta,\gamma)\mathrm{Ca(BH_4)_2} + \mathrm{MgH_2} \xrightarrow{160\ ^\circ\mathrm{C}} (\beta)\mathrm{Ca(BH_4)_2} + \mathrm{MgH_2} \xrightarrow{350^\circ\mathrm{C}} \\
&\xrightarrow{350^\circ\mathrm{C}} \text{amorph/nano crys}(x[(\alpha)\mathrm{Ca(BH_4)_2}] + y\mathrm{CaB_6} + z\mathrm{CaB_{12}H_{12}}) - \text{phases} \\
&\quad + \ w\,\mathrm{CaH_2} + \mathrm{MgH_2} + j\mathrm{H_2}
\end{aligned} \tag{88 a}
$$

$$
4\ \mathrm{CaH_2} + 3\mathrm{MgH_2} \xrightarrow{350\ ^\circ\mathrm{C}} \mathrm{Ca_4Mg_3H_{14}} \xrightarrow{365\ ^\circ\mathrm{C}} 4\mathrm{CaH_2} + 3\mathrm{Mg} + 3\mathrm{H_2}\uparrow \tag{89 b}
$$

$$
\begin{aligned}
&\xrightarrow{365\ ^\circ\mathrm{C}} \text{amorph/nano crys.}\,(p(\beta)\mathrm{Ca(BH_4)_2} + x\mathrm{CaB_6} + y\mathrm{CaB_{12}H_{12}}) - \text{phases} \\
&\quad + \ z\mathrm{CaH_2} + \mathrm{Mg} + v\mathrm{H_2}\uparrow
\end{aligned} \tag{89 c}
$$

Thee crystalline phase CaB_2H_x reported by Riktor *et al* [253] is not observed under the conditions applied here. In pure Ca-RHC the intermediate $Ca_4Mg_3H_{14}$ phase is observed Figure 52 (a) although the formation of $Ca_4Mg_3H_{14}$ is not a necessary reaction step as it was pointed out by Bonatto Minella *et al.* [223] By mixing $Ca(BH_4)_2$ and MgH_2, the intermediate phase ($Ca_4Mg_3H_{14}$) was not observed by these authors, upon dehydrogenation, in contrast to the high energy ball milled $Ca(BH_4)_2$+MgH_2 sample. Therefore, they concluded that the production of $Ca_4Mg_3H_{14}$ is correlated with the microstructure of the as-prepared material. In the present work, both samples (Ca-RHC and Ca-RHC+0.1NbF_5) were high energy ball milled under the same conditions (as described in section 2.1). Unlike to pure Ca-RHC, no Bragg peaks of $Ca_4Mg_3H_{14}$ phase are observed during the dehydrogenation reaction of Ca-RHC+0.1NbF_5 (in the *in-situ* SR-PXD measurements, see Figure 52 (b)). The formation of the intermediate phase *via*: $4CaH_2+3MgH_2 \rightarrow Ca_4Mg_3H_{14}$ was already predicted by first principle calculations to be more likely due to its negative Helmholtz free energy (ΔF = -7.9 kJ at 350 °C). [148] Since the solid solution $CaF_{2-x}H_x$ is formed, during the decomposition reaction of $Ca(BH_4)_2$ in the Ca-RHC+0.1NbF_5 sample, the Helmholtz free energy of a reaction involving $4CaF_{2-x}H_x+3MgH_2$ might be more favourable than $4CaH_2+3MgH_2$. This would explain the independent dehydrogenation reaction of MgH_2 in the Ca-RHC+0.1NbF_5 system and the reaction of $4CaH_2+3MgH_2$ in the pure Ca-RHC. In the pure Ca-RHC, CaH_2 reacts with MgH_2 to form $Ca_4Mg_3H_{14}$. Subsequently, upon the dehydrogenation of the ternary hydride a simultaneous formation of metallic Mg and CaH_2 can be observed. However, in the presence of $CaF_{2-x}H_x$, the formation of $Ca_4Mg_3H_{14}$ does not take place. Hence, the diffraction peaks of Mg appear after those of $CaF_{2-x}H_x$ upon the slightly delayed decomposition of MgH_2. Regarding the XAFS-results, NbF_5 reacts with $Ca(BH_4)_2$ during high energy ball milling to form CaF_2 and NbB_2 (Figure 54-57). No trace of MgF_2 is observed in the milled Ca-RHC+0.1NbF_5 sample *via* SR-PXD which is in agreement with the results obtained by [254] Assuming a complete reaction between 0.1NbF_5 and $Ca(BH_4)_2$ during the milling procedure, the following initial educts, reaction pathways and reaction products for Ca-RHC+0.1NbF_5 can be proposed:

$$(\alpha,\beta,\gamma)\mathrm{Ca(BH_4)_2} + \mathrm{MgH_2} + 0.1\mathrm{NbF_5} \xrightarrow{\text{ball milling}} j(\alpha,\beta,\gamma)\mathrm{Ca(BH_4)_2} + \mathrm{MgH_2} + l\mathrm{CaF_2} + m\mathrm{B_2H_6}\uparrow + n\mathrm{HF} \tag{89 a}$$

$$\uparrow + \text{amorph/nano crys.}\,(p\mathrm{CaB_6} + 0.1\mathrm{NbB_2}) + q\mathrm{H_2}\uparrow \xrightarrow{250°\mathrm{C}}$$

$$\text{amorph/nano crys.}\,(a[(\beta)\mathrm{Ca(BH_4)_2}] + b\mathrm{CaH_2} + c\mathrm{CaB_6} + d\mathrm{CaB_{12}H_{12}} + {} + 0.1\mathrm{NbB_2}) - \text{phases} + e\mathrm{CaF_{2-x}H_x} + \mathrm{Mg} + e\mathrm{H_2}\uparrow \tag{90 b}$$

The dehydrogenation of the sample doped with $0.1NbF_5$ starts, in accordance with the manometric measurements, at much lower temperatures in comparison to the pure Ca-RHC sample. After the desorption process of Ca-RHC and Ca-RHC+$0.1NbF_5$, no SR-XPD signals of $Ca(BH_4)_2$ can be detected, suggesting the complete decomposition of this phase (Figure 52 and Figure 57). By means of NMR (Figure 53), nevertheless, a trace of residual β-$Ca(BH_4)_2$ polymorph is detectable in both samples. It was concluded that the remnant β-$Ca(BH_4)_2$ is present for the same reasons in both samples. During the desorption process the residual β-$Ca(BH_4)_2$ might be covered with the decomposition products of the composite system. This effect could hinder the decomposition of this residual borohydride phase. The main difference concerning reaction (90) and (91) is the formation of the $CaF_{2\text{-}x}H_x$ solid solution between CaF_2 and CaH_2 in the doped sample, as was also observed by Pistidda *at el.* and Suarez-Alcantara *at el.*[255, 256] The value of x is determined to be 1.07, using the Rietveld method. These results also explains the change of desorption enthalpy values 42 ± 2 kJ/mol H_2 and 37 ± 1 kJ/mol H_2 for the Ca-RHC system and Ca-RHC+$0.1NbF_5$, respectively (DSC-measurements-subsection 3.1). Additionally, no phase transformation of α and γ-$Ca(BH_4)_2$ to the β-$Ca(BH_4)_2$ polymorph was found in the DSC pattern of the Ca-RHC+$0.1NbF_5$ sample. Rietveld refinement of the room temperature SR-XPD pattern of pure and doped Ca-RHC revealed only a relative reduction of the mass fraction of the α, β and γ-$Ca(BH_4)_2$ polymorphs from 18 % ,72 % ,10 % in the as-milled pure Ca-RHC changed to 10 % , 86 % , 4 % in the NbF_5 doped Ca-RHC system, respectively (see Figure 57). This contradiction between DSC and SR-XPD can be inferred to the detection limit of DSC-apparatus itself. The absence of the α and γ-$Ca(BH_4)_2$ polymorph in the XRD pattern after high energy ball milling with TMF-additives was reported by other authors[133, 236], as well. However, they attributed the absence of the α-$Ca(BH_4)_2$ polymorph to the high energy involved during the milling process able to drive phase transition. As mentioned previously, in this study Ca-RHC and Ca-RHC+$0.1NbF_5$ samples were ball milled under the same conditions, respectively. Hence, it is concluded that the NbF_5 additive might initiate the α and γ to β-$Ca(BH_4)_2$phase transition during the milling process of the Ca-RHC+$0.1NbF_5$ sample. According to [257] the maximum temperature achieved during ball-milling is dependent on the materials being milled. In the SPEX 8000 under the same milling conditions, an Al-Mg mixture would reach a maximum temperature of 120 °C, [258] whereas a mixture of Fe with an addition of 1.2 wt.% C could reach 300 °C. [259] In the present study, the milling procedure causes a chemical reaction between NbF_5 and $Ca(BH_4)_2$ in the Ca-RHC+$0.1NbF_5$ sample as was shown by EXAFS analyses (Figure 55). The heat released by the reaction might local reach temperatures needed for the phase transition (from α and γ to β-$Ca(BH_4)_2$) of about 160 °C which could explain the lowered amount of the α and γ-$Ca(BH_4)_2$ polymorph in the as-milled Ca-RHC+$0.1NbF_5$ sample. However, a phase transformation based only on structural deformation by the additional NbB_2 during ball milling of the Ca-RHC+$0.1NbF_5$ sample cannot be excluded entirely (e.g. the formation β-MgH_2 phase upon milling procedure).[260] Since NbB_2 is known as a hard and inert material, [261-263] it can act during the milling procedure as a grain refiner in the hydride matrix.[264-266] According to, both, theoretical [267] and experimental [268] studies the phase transition in nano crystalline materials is mainly dependent on the grain size. This feature is about twice finer distributed in Ca-RHC+$0.1NbF_5$ samples in comparison to pure Ca-RHC samples, as it was shown *via* Rietveld-refinement in section 3.4. In contrast to the as-milled pure Ca-RHC, ^{11}B NMR-measurements of as-milled Ca-RHC+$0.1NbF_5$ showed a trace of nanocrystalline CaB_6 (since no sharp Bragg-peaks of CaB_6 in the SR-XPD of the as-milled Ca-RHC+$0.1NbF_5$ was detectable). Since, the *d*-value mismatch between crystallographic planes of Mg/CaB_6 is less than 6%,[223, 219, 222, 269] this nanoparticulated CaB_6 phase provides nucleation centres for new CaB_6 and Mg phases during the dehydrogenation process. Moreover, XAS, ASAXS and TEM analyses revealed the presence of finely distributed NbB_2 nanoparticles in the Ca-RHC+$0.1NbF_5$ samples (Figure 61-Figure 63). Based on the Edge-to-edge matching model calculation of the *d*-value mismatch of the planes {1011} CaB_6 / {1011} NbB_2 and {111} CaB_6 / {1010} NbB_2 are, respectively, equal to 2.9 % and 2.8 %.[223] Therefore, NbB_2 provides in additional to existing nanoparticulated CaB_6, two more possible crystallographic planes for heterogeneous nucleation and growth of the CaB_6 phase in the Ca-RHC+$0.1NbF_5$ composite system. Hence, upon the desorption reaction of Ca-RHC+$0.1NbF_5$, a heterogeneous nucleation and growth of CaB_6 on NbB_2 nanoparticles is expected which consequently enhances the reaction kinetics of doped Ca-RHC in comparison to the undoped hydride composite system. As a consequence of the heterogeneous nucleation and growth the particle sizes in the doped sample should be reduced. Indeed, the BET results of the doped sample after the first dehydrogenation process shows 55 % smaller average particle sizes in comparison to the first dehydrogenated pure Ca-RHC. However, the shape of a single particle can be more complex than the assumed spherical-model used for calculation of average particle sizes according to subsection 3.7. In that sense, an increased SSA can additionally also be referred to a change of the particle shape and increase of surface area originating from the emergence of cracks and defects during dehydrogenation. [270] Also the as-milled Ca-RHC+$0.1NbF_5$ sample shows approximately 40 % larger SSA relative to the undoped as-milled sample. This points towards lower diffusion paths, higher reaction surfaces and smaller structure for fast hydrogen recombination processes. The crucial role of small structures, high reaction surface area and reaction contact area of the metal hydrides and hydride composite systems on their de/rehydrogenation behaviour was also pointed out in detail by Dornheim *et al.*, Pistidda *et al.* and others. [54, 271, 272] An additional effect of the NbB_2 particles might also be an increase in the material strain at the grain boundaries. This hinders the crystallite growth and ensures the stability of the matrix structure. In fact, the strain of doped Ca-RHC was determined *via* the Rietveld method to be approximately twice larger than that found in the pure Ca-RHC sample. Using NbF_5 as an additive shows great improvement on the kinetic of the Ca-RHC, however, the problem with long term reversibility remains yet unsolved. This is due to partial exclusion of stable calcium and boron containing compounds from the hydrogenation cycles during each dehydrogenation process. This notion is sketched in the Figure 65 for the first hydrogenation cycle (a) and after long term hydrogenation cycling (b).

The hydrogenation cycle is subdivided in boron containing and non-boron (ternary hydride) containing cycles. Upon cycling the stable boron/calcium containing compounds are extracted and accumulated gradually out of the hydrogenation cycles and the capacity of boron containing cycle is reduced, whereas the one of the ternary hydride cycle is increased. Eventually, this would lead to vanishing of the boron containing cycle, hence to a constant hydrogen capacity, which is based on the ternary hydride containing cycle. This is also true if one starts with the possible desorbed states of the Ca-RHC system. Thus it is mandatory to stabilize the decomposition of boron in such a way to make the system reversible.

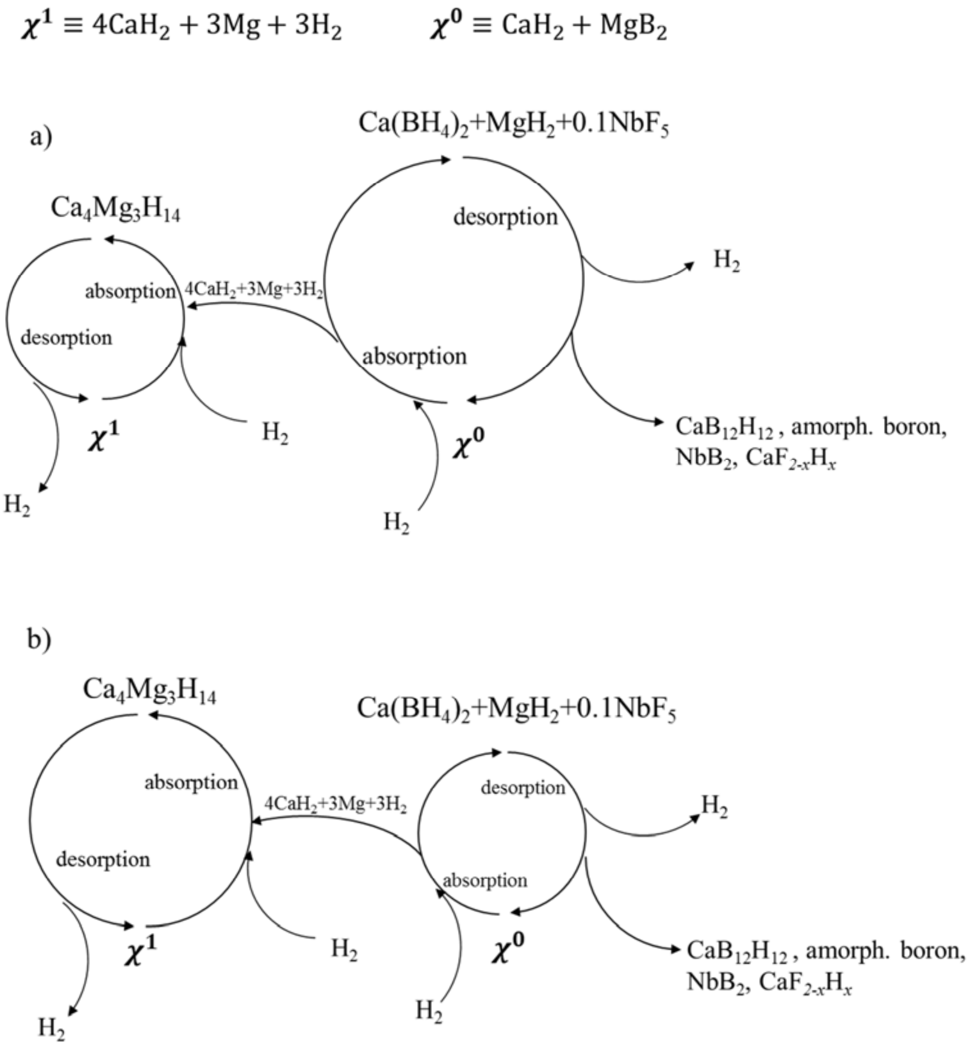

Figure 65. Hydrogenation cycles of the doped Ca-RHC in the first cycle (a) and after long term cycling (b)

5.2. Stabilization of decomposition products of $Ca(BH_4)_2$ by concept of RHC

As it was already mentioned in the subsection (2.6.3.2), $Ca(BH_4)_2$+MgH_2 can theoretically decompose through different dehydrogenation reaction paths to different decomposition products. In this section a detailed study of dehydrogenation reaction paths and products of the $Ca(BH_4)_2$-MgH_2 composite system in dependency on the thermodynamic parameters such as temperature (T) and hydrogen backpressure pressure (P) is conducted. Lastly an alternative destabilization agent is proposed to stabilize the decomposition products of $Ca(BH_4)_2$, which is key issue for the reversibility of complex hydride.

5.2.1. Effect of hydrogen pressure and temperature variation on the decomposition products of $Ca(BH_4)_2$-MgH_2 composite system

For the variation of temperature and hydrogen backpressure as parameters during the dehydrogenation process of the Ca-RHC system the following values were selected: T = (350, 375, 400, and 450) °C and p = (0, 1, 5, 10, and 20) bar H_2. Using these parameters, volumetric measurements were carried out to observe the dehydrogenation kinetics and the final hydrogen capacities of the Ca-RHC with respect to the applied conditions. Results of these measurements are presented in Figure 66.

In case of dehydrogenation carried out at 350 °C, the reaction of the sample desorbed under static vacuum conditions proceeds with the fastest kinetics. The kinetic rate drops with increasing pressure until the reaction stops at a hydrogen backpressure of about 20 bar. Interestingly, with increasing hydrogen backpressure also the total hydrogen capacity of the composite system drops, as well. Concerning the capacity drop and decrement of the reaction kinetics with respect to hydrogen backpressure, the dehydrogenation reaction of the samples measured at 375 °C, 400 °C (not shown here), and at 450 °C show similar behaviour as the one at 350 °C. These dependencies of the hydride composite with respect to temperature and pressure are condensed and visualized in Figure 66 (d). The decomposition reaction seems to proceed in one step at 350 °C and at 375 °C, whereas the desorption reaction of the hydride composite at 450 °C appears to proceeds in three steps. To investigate these aspects of the hydride composite system, in more detail, coupled volumetric-calorimetric measurements

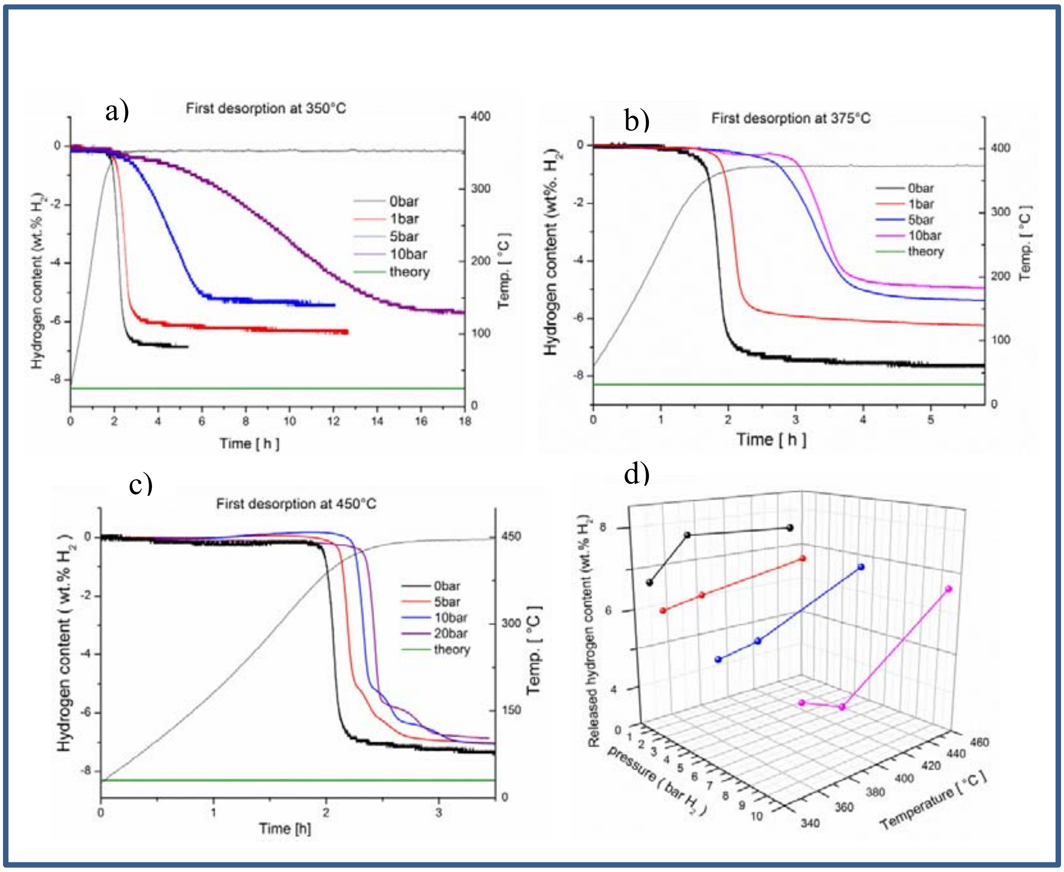

Figure 66. Dehydrogenation reaction kinetics observed under various hydrogen backpressures (0, 1, 5, 10 and 20) bar at 350 °C (a), at 375 °C (b) and at 450 °C (c) (these measurements were conducted at HZG (at the HERA apparatus).

were performed and the results are presented in Figure 67. The *x*-axis and the left side *y*-axis represent the temperature and the released hydrogen content, respectively, whereas the right *y*-axis represents the released or absorbed heat from the samples. By increasing the temperature (3 K/min), all show an endothermic peak at about 160 °C which is independent of the applied backpressure. This small endothermic reaction with an onset temperature of roughly 155 °C is not related to any hydrogen release as can be seen from the coupled volumetric curves and can be attributed β-$Ca(BH_4)_2$.

The next endothermic peak is the most pronounced peak over the entire observed temperature range of the measurement, carried out under different hydrogen backpressures. This second peak is accompanied by a significant release of hydrogen, as is evident from the coupled volumetric measurements. The onset temperature and the peak temperature of this endothermic peak are shifted toward higher temperatures with increasing hydrogen backpressure. A third endothermic peak at ~ 420 °C appears only after applying a hydrogen backpressure of 5 bar or more. The peak position of this peak transfers to 435 °C and 450 °C by applying hydrogen backpressures of 10 bar and 20 bar, respectively. A forth endothermic peak is revealed at about 420 °C by applying 20 bar hydrogen backpressure. This shows that the dehydrogenation reaction of the system does not proceed in one step but rather in at least three steps, which are submerged (parallel reactions) by one broad endothermic peak under vacuum condition. In order to reveal these reaction mechanisms of the system under various hydrogen backpressures, *in situ* SR-PXD measurements under 0, 10 and 20 bar H_2 b were carried out and the results are presented in Figure 68, Figure 69, and Figure 70, respectively.

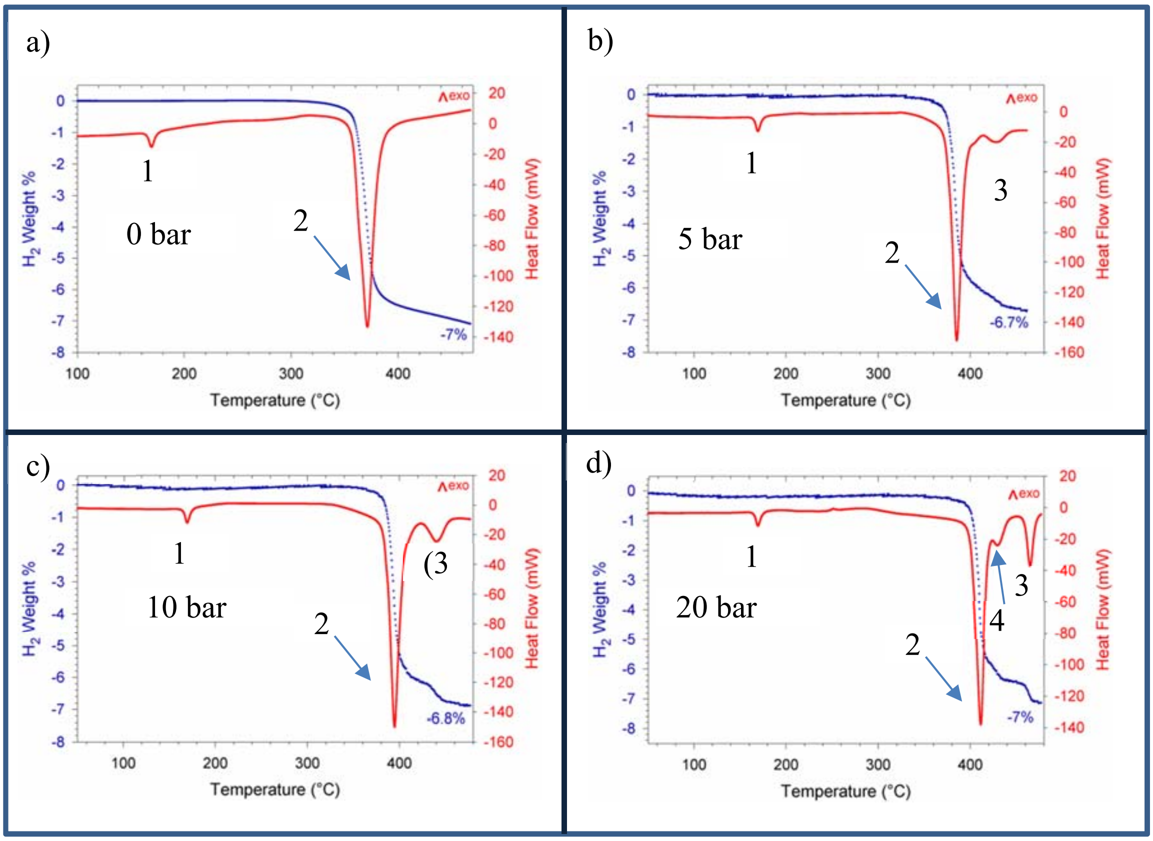

Figure 67. Coupled volumetric-colorimetric dehydrogenation reaction kinetic measurements observed under 0 bar H_2 backpressure (a), 5 bar H_2 backpressure (b), 10 bar H_2 backpressure (c), and 20 bar H_2 backpressure (d) (the measurements were carried out at the university of Pavia (Italy) in collaboration with Prof. Dr. C. Milanese).

The *z*-axis is assigned to scan number and the scan numbers are translated into temperature. At about 150 °C in all *in situ*-diffraction pattern of the $Ca(BH_4)_2$+MgH_2 system under different H_2 backpressures a first change occurs (green colored) which is due to a structural transformation of α-$Ca(BH_4)_2$ and γ-$Ca(BH_4)_2$ low temperature polymorphs to β-$Ca(BH_4)_2$. This corresponds to the first endothermic peak in the DSC-patterns in Figure 67. The temperature at which the second alteration of the diffraction peaks takes place depends on the applied backpressure. In the sample under 0 bar this reaction takes place at about 350 °C, under 10 bar H_2 backpressure it starts approximately at 390 °C, and under 20 bar H_2 backpressure the reaction starts at temperatures about 400 °C.

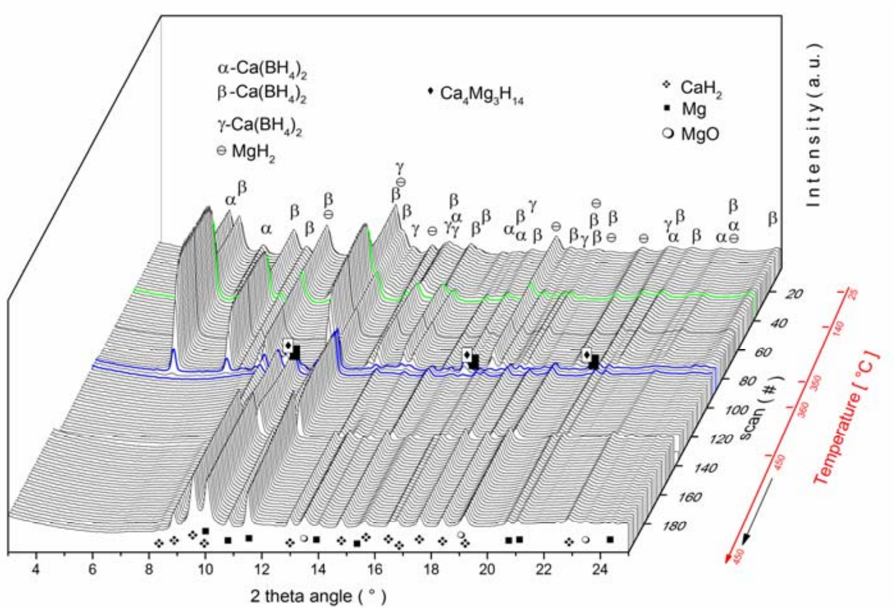

Figure 68. *In situ* SR-PXD measurements of Ca-RHC under 0 bar H_2 backpressure. The sample was heated up to a maximum temperature of 450 °C with a temperature increment of 3 K/min (this measurement and the two following measurements were carried out at the diffraction beamline 711 with $\lambda = 0.5$ Å at MAXLAB-II synchrotron storage ring (Lund, Sweden).

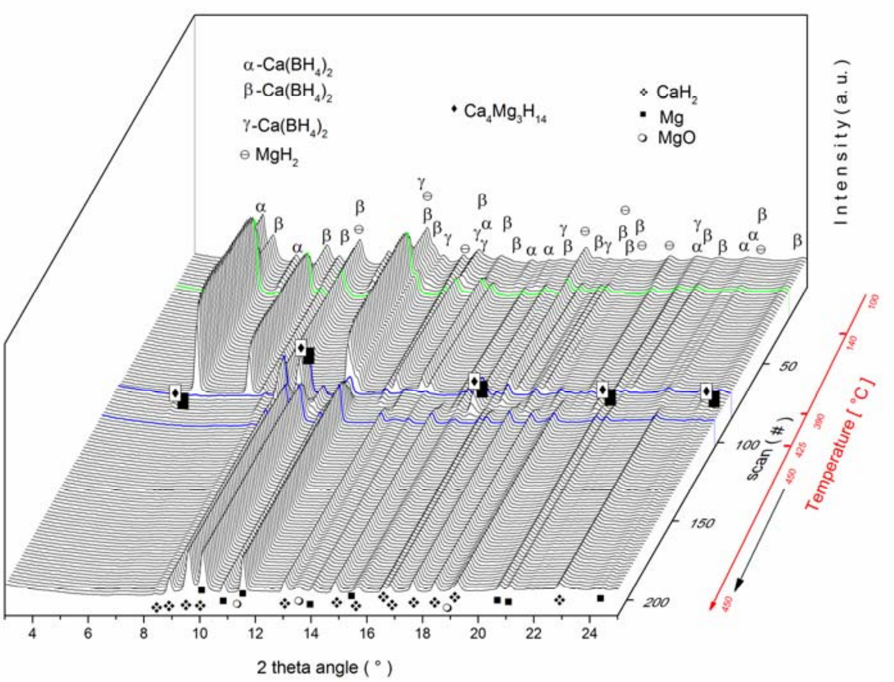

Figure 69. *In situ* SR-PXD measurements of Ca-RHC under 10 bar H_2 backpressure. The sample was heated up to a maximum temperature of 450 °C with a temperature increment of 3 K/min.

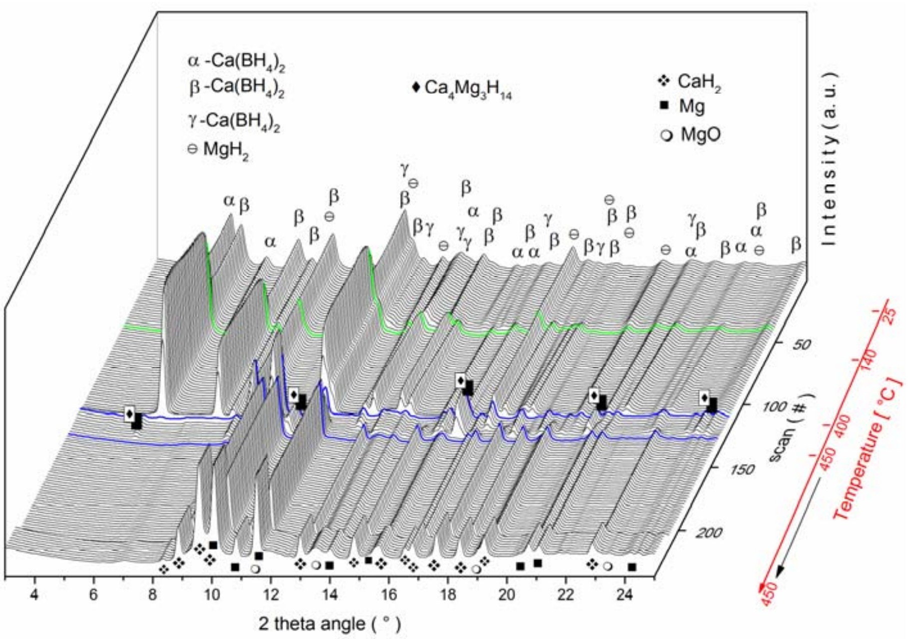

Figure 70. *In situ* SR-PXD measurements of Ca-RHC under 20 bar H_2 backpressure. The sample was heated up to a maximum temperature of 450 °C with a temperature increment of 3 K/min.

These changes can certainly be assigned to the decomposition of β-Ca(BH$_4$)$_2$ in all samples, however, not to the one of MgH$_2$. As can be seen in the sample under 0 bar H$_2$ (Figure 68) after decomposition of β-Ca(BH$_4$)$_2$ an immediate appearance of the ternary metal hydride phase Ca$_4$Mg$_3$H$_{14}$ is observed which hints towards a decomposition of MgH$_2$ by reacting with CaH$_2$ to form the ternary hydride phase. This fact becomes clearly visible after applying hydrogen backpressures of 10 or even 20 bar. At a backpressure of 10 bar H$_2$ the ternary phase stays longer stable in comparison to the sample under 0 bar of H$_2$ backpressure. This effect is furthermore emphasised in the *in situ* XRD measurement of the sample under 20 bar H$_2$. After decomposition of β-Ca(BH$_4$)$_2$, the Bragg peaks of MgH$_2$ are still present and they decrease gradually with appearance and increasing of the Ca$_4$Mg$_3$H$_{14}$ phase. At backpressures of 10 bar and 20 bar H$_2$, the ternary phase remains stable up to higher temperatures compared to the sample kept under 0 bar of H$_2$. Ca$_4$Mg$_3$H$_{14}$ decomposes at temperatures of about 430 °C under 10 bar H$_2$ backpressure and at 450 °C under 20 bar H$_2$. These decomposition reactions can be assigned to the third endothermic peak of the DSC-curves presented in Figure 67 (c, d). Three events of the coupled volumetric-calorimetric measurements could be assigned to the corresponding events in the *in situ* SR-PXD measurements. However, the fourth endothermic peak at ~ 420 °C under 20 bar H$_2$ could not be assigned to any crystalline phase by XRD method. Thus it can be assumed that this reaction step with hydrogen release is due to decomposition of nano-crystalline or/and amorphous phase(s) presented in the samples but not detectable by diffraction methods. Since boron containing phases are not detected in any diffraction pattern of dehydrogenated Ca-RHC, ^{11}B MAS NMR measurements were conducted to determine the state of boron after the dehydrogenation process of the hydride composite system under different hydrogen backpressure conditions. Results of these measurements are plotted in Figure 71.

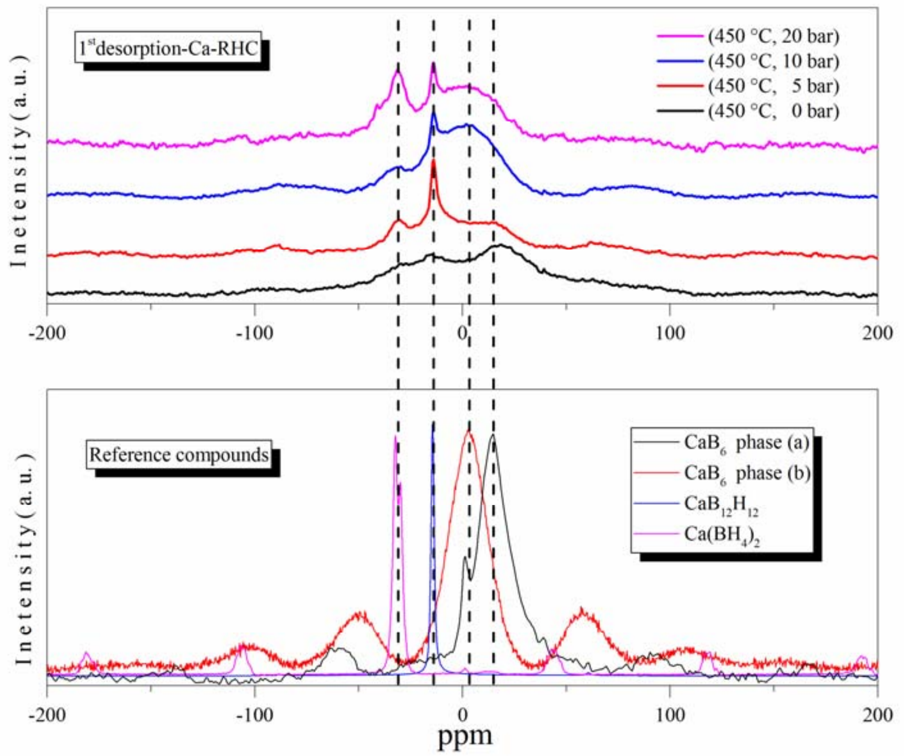

Figure 71. 11B MAS NMR spectra of Ca-RHC after the first desorption process under different conditions (top panel), and those of the reference spectra (bottom panel) (measurements performed at HZG in collaboration with Dr. T. Emmler).

The upper panel of the figure shows spectra of the dehydrogenated Ca-RHC under variation of hydrogen backpressure pressure at 450 °C (the applied conditions correspond to those used in Figure 67). The lower panel displays the spectra of the reference compounds. It should be noted that two phases of CaB_6 were measured (which were available as powder) and the spectra are distinguished (a) and (b), respectively. As can be seen in the upper panel of Figure 71 the sample heated up to 450 °C under static vacuum, still shows some signal from residual hydrogen containing compound such as $Ca(BH_4)_2$, $CaB_{12}H_{12}$, and the only non-hydrogen containing boron compound signal is from CaB_6. By increasing the hydrogen backpressure to 5 bar, the amount of phase (a) of CaB_6 seems to be reduced. An increase of the phase (b) of CaB_6 or amorphous boron is detected. It should be noted that amorphous boron also has a broad ^{11}B MAS NMR main peak at about 0 ppm which might be overlapped with the phase (b) of CaB_6 here, and therefore undistinguishable. Also signals of $CaB_{12}H_{12}$ and $Ca(BH_4)_2$ are clearly pronounced in comparison to the sample measured under 0 bar H_2. By further increment of hydrogen backpressure, the dehydrogenation paths of the system are more deflected toward hydrogen containing phases ($Ca(BH_4)_2$, $CaB_{12}H_{12}$). Under these conditions, $Ca(BH_4)_2$ is stabilized by the hydrogen backpressure, and its ratio increases, relative to the $CaB_{12}H_{12}$ phase. On the other hand, also the formation of CaB_6 is deflected toward amorphous boron or its phase (b). However, this assumption is rather speculative since resolution of the NMR patterns does not allow making accurate statements. Nevertheless the NMR signal of amorphous boron is also expected to be around 0 ppm (in the top panel of Figure 71). To clarify this issue the following experiments were carried out. Since, amorphous boron is well known for its high degree of stability against the hydrogenation reaction to form complex borohydrides under mild conditions and CaB_6 for its reversibility under mild conditions,[148, 273 274, 275] it is reasonable to expect an accumulation and clear detection of amorphous boron upon cycling in the hydrogenated state of the Ca-RHC, in comparison to the signal of CaB_6. Thus, ^{11}B MAS NMR measurements were conducted on hydrogenated samples of Ca-RHC cycled once and twice, respectively, and the corresponding references. The results of these measurements are displayed in Figure 72. NMR spectra of the hydrogenated samples are displayed in the lower panel of the Figure 72, and those of the references are depicted in the top panel. Dehydrogenation of the samples was carried out under 0 bar (black coloured) and 20 bar (red coloured) of hydrogen backpressure at 450°C, respectively. As could be projected (see Figure 72) the spectrum of the first hydrogenated sample (dehydrogenation at: (450 °C, 0 bar)) shows the signal of $Ca(BH_4)_2$ and it has almost no signal around 0 ppm where the signal of amorphous boron is expected. Only a minor signal of CaB_6 phase but a clear signal of $CaB_{12}H_{12}$ phase is observed, respectively. The same sample after the second hydrogenation cycle shows clearly the signal of CaB_6 phase (a) which is superimposed by a signal centred around 0 ppm. Mainly this signal makes it possible to reveal the second small side band of CaB_6 (phase (a)). Also the signal from $CaB_{12}H_{12}$ is significantly increased in comparison to the first hydrogenated sample (also the signal of $Ca(BH_4)_2$ is identified, as expected). NMR spectrum of the first hydrogenated sample after dehydrogenation under 20 bar H_2 backpressure at 450 °C does not show any clear signal from CaB_6 phase (see Figure 72, (red solid line)). Though, a broad signal is observable around zero ppm, which is also detected in the dehydrogenated state of the same sample (see Figure 71).

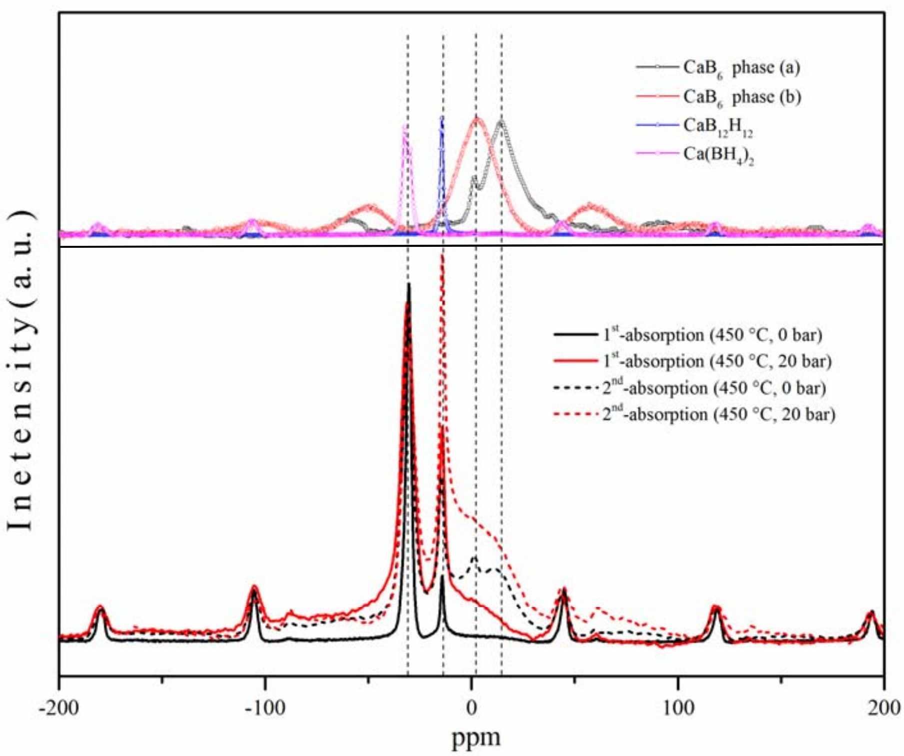

Figure 72. ^{11}B MAS NMR pattern of cycled hydrogenated Ca-RHC samples hydrogenated under 130 bar H_2 at 400 °C. Dehydrogenation of the samples were carried out at 20 bar H_2 and 0 bar H_2, respectively, at 450 °C (measurements performed at HZG in collaboration with Dr. T. Emmler).

Also the NMR signal from $CaB_{12}H_{12}$ is considerably amplified in comparison to the corresponding spectrum of the sample dehydrogenated under vacuum conditions and at 450 °C (see Figure 72). The sample was dehydrogenated under the same conditions as aforementioned (20 bar, 450 °C) and rehydrogenated for the second time .The ^{11}B MAS NMR spectrum of this sample shows a huge broad hump approximately in the matching position (about 0 ppm), similar to the firstly hydrogenated sample. However, no clear signal of CaB_6 is detected as it was the case for the corresponding sample desorbed under 0 bar hydrogen backpressure and at 450 °C. Thus, the broad signal around zero ppm can be assigned to the amorphous boron phase. Nonetheless, the existence of phase (b) of CaB_6 as is depicted in the top panel of Figure 72 cannot be excluded entirely. The amorphous boron phase and the one of $CaB_{12}H_{12}$ are increased significantly in comparison to the first hydrogenation cycle (as can be seen by a comparison between the red dashed and red solid lines). As a matter of fact, ^{11}B MAS NMR measurements reveal that even after dehydrogenation process the samples contain residual hydrogen containing compounds such as $Ca(BH_4)_2$ and $CaB_{12}H_{12}$, for instance. Thus, it was assumed that these hydrogen containing phases were for yet unknown reasons "deactivated" for dehydrogenation. Therefore, another Ca-RHC sample (desorbed under 0 bar H_2 at 450°C) was prepared. In order to "reactivate" the sample it was removed from the sample holder and it was further milled in a SPEX-mill. Furthermore, a sample was taken for volumetric measurement after 1 hour of milling and another one after 10 hours of milling time. The results of these measurements are displayed in Figure 73. The first dehydrogenation reaction of the Ca-RHC system liberates approximately 6.5 wt. % H_2.

After post milling this sample for one hour it, indeed, releases further about 0.5 wt. % H_2. After post milling the sample for ten hours, unexpectedly, it released about 2 wt. % H_2.

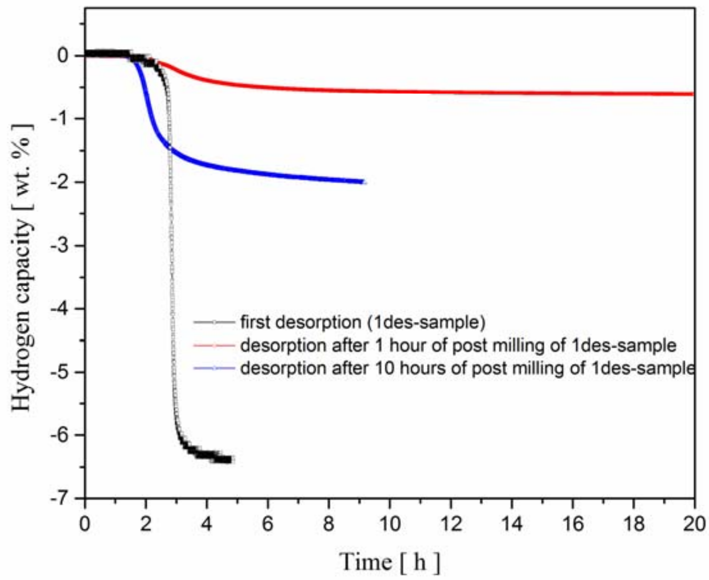

Figure 73. Dehydrogenation reaction of Ca-RHC (1des-sample), 1 h post milled 1des-sample, and 10 h post milled 1des-sample at 450 °C under static vacuum conditions (measured at HZG (at the HERA apparatus).

To further investigate the desorption products of these samples they were investigated *via* XRD and ^{11}B MAS NMR methods to reveal their crystalline and amorphous phases, respectively. The XRD results did not show any new crystalline phases of desorption products beside CaH_2 and metallic Mg. Therefore, NMR measurements were conducted to gain some insights into the amorphous desorption products of the samples. The results of these measurements are presented in Figure 74. As can be seen there the spectrum of the first desorbed sample (at 450 °C and 0 bar) shows still residual signals from $Ca(BH_4)_2$ and $CaB_{12}H_{12}$. The spectrum of the desorbed sample after one hour of post milling shows signal from residual $Ca(BH_4)_2$ and $CaB_{12}H_{12}$, respectively. A clear signal of the spectrum is concentrated around the signal of (b) phase of CaB_6. However, the presence of amorphous boron in this sample cannot be excluded certainly, as was discussed before.

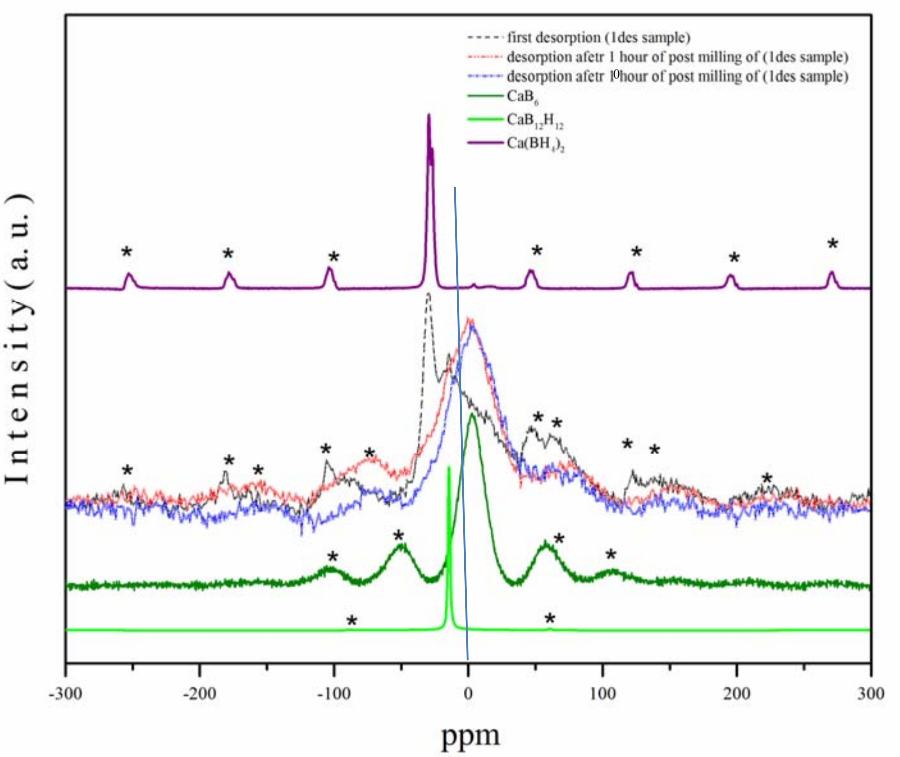

Figure 74. ^{11}B MAS NMR spectra of the sample measured in Figure 73 with the spectra of the standards (measurements performed at HZG in collaboration with Dr. T. Emmler).

The spectrum of the desorbed sample after 10 hour of post milling shows no longer any residual signals from $Ca(BH_4)_2$ or $CaB_{12}H_{12}$. This becomes also clear if one compares the spectrum of 10 hours post milled sample with the spectrum of one hour post milled samples. The width of the main signal of 10 hours post milled sample cantered about CaB_6 reference sample is much more narrowed (almost the same width as the reference signal) in comparison to the corresponding signal of the one hour post milled sample, showing that there are no hydrogen containing phases anymore in the sample which correlates nicely with the observed hydrogen capacity obtained by volumetric measurements (see Figure 73). However, the presence of amorphous boron cannot be excluded, entirely, hence the signal could be from CaB_6, and/or amorphous boron. The above presented results clearly show that MgH_2 does not destabilize $Ca(BH_4)_2$. Consequently, MgH_2 has to be destabilized in order to stabilize the decomposition products of $Ca(BH_4)_2$ such as amorphous boron which is hardly reversible (under mild conditions) and to avoid the formation of $CaB_{12}H_{12}$ structures. These stable compounds are accumulated over the de/rehydrogenation cycles until the storage material becomes "inactive", as was discussed in section 5.1.7. Therefor destabilized MgH_2 compounds, such as Mg_2NiH_4, Mg_2FeH_6, Mg_2CoH_5 (which are well known since 1960's) can be used, for instance. In this work, Mg_2NiH_4 was chosen to stabilize the desorption products of $Ca(BH_4)_2$ because it is basically the only candidate which can form several ternary boride phases such as, $MgNi_{2.5}B_2$, $MgNi_3B_2$, $MgNi_7B_3$, etc. The molar ratio between $Ca(BH_4)_2$ and Mg_2NiH_4 was chosen such, that the resulting ternary boride phase should lead to the formation of $MgNi_{2.5}B_2$. The as-milled $Ca(BH_4)_2$-Mg_2NiH_4 composite sample was measured by means of *in situ* SR-PXD to follow its reaction paths and final desorption products and the result of this measurement is shown (from two different perspectives) in Figure 75. The starting materials consist of α and γ polymorph of $Ca(BH_4)_2$, Mg_2NiH_4, residual Ni, NiO, and a trace of $MgNi_2H_{3.2}$.which shows that the synthesis of Mg_2NiH_4 was not synthesized perfectly. The sample was heated up with a heating rate of 3 K/min to a maximum temperature of 390 °C. Upon heating a phase transformation from α and γ polymorph to high temperature β polymorph of $Ca(BH_4)_2$ is observed at around 150 °C. Further heating leads to depleting and fading out of the metallic nickel and $MgNi_2H_{3.2}$ phases, while concurrently the diffraction peaks of Mg_2NiH_4 increase. This hints toward a reaction between $MgNi_2H_{3.2}$ and Ni to form Mg_2NiH_4. At around 250 °C, the phase transformation of Mg_2NiH_4.from monoclinic low temperature (LT) phase to HT cubic phase is observed. Around 280 °C the diffraction peaks of $MgNi_2$ is visible. Further growth of the $MgNi_2$ phase leads to an immediate decay of the Mg_2NiH_4 diffraction peaks which in turn leads to formation of new unknown phase. By further heating this unknown phase further decomposes into $MgNi_{2.5}B_2$ and CaH_2, as final products. Also MgO and NiO are detected as final products, which were formed either during the ball milling process or during sample preparation for *in situ* SR-PXD in the glove box. Nevertheless these phases are highly stable and do not affect the reaction paths of the hydride composite system.

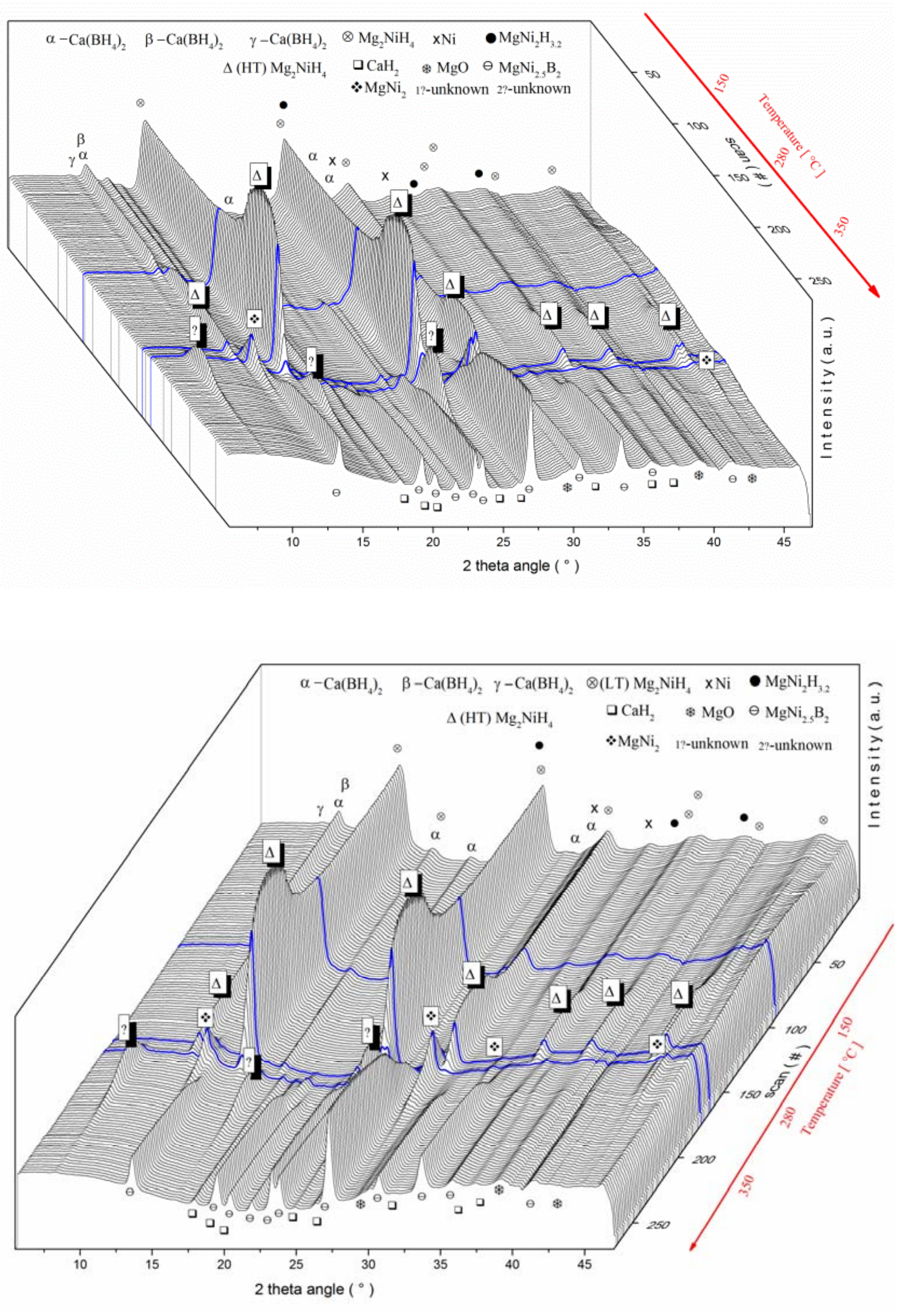

Figure 75. *In situ* SR-PXD dehydrogenation reaction of $Ca(BH_4)_2$-Mg_2NiH_4 under static vacuum condition. The sample was heated with 3 K/min to a maximum temperature of 390 °C (this measurement and the two following measurements were carried out at the diffraction beamline 711 with $\lambda = 0.5$ Å at MAXLAB-II synchrotron storage ring (Lund, Sweden).

This result clearly shows that the decomposition products of $Ca(BH_4)_2$ can be stabilized by using Mg_2NiH_4 as a destabilization agent. Therefore the system is now in principle reversible and the detailed investigation of this system is left for further studies to be come.

5.2.2. **Discussion**

The effect of pressure and temperature variation on the dehydrogenation reaction pathway of Ca-RHC is clearly observed at (10, 20) bar H_2 backpressure and 450 °C (see Figure 66 (c)). Using calorimetric-volumetric measurements by applying static vacuum showed that the 2nd endothermic (large) peak is correlated with hydrogen release (see Figure 66 and Figure 67 (a)). If one compares the width of the second endothermic peak of the sample measured under static vacuum with those measured with higher hydrogen backpressures (see Figure 67 (b-d)), an interesting observation can be made. Namely, the FWHM of the second endothermic peak decreases as the hydrogen backpressure increases (from 1.0 (normalized value) for the sample measured under static vacuum conditions to 0.77 after applying 5 bar H_2, to 0.72 at 10 bar H_2 and 0.70 after applying 20 bar of H_2 backpressure). This fact indicates that the dehydrogenation reaction steps of the Ca-RHC system occur concurrently under static vacuum, which are separated (due to different hydrogen equilibrium pressure of the compounds involved in these dehydrogenation reaction steps) by applying different hydrogen backpressures. The results of *in situ* SR-XPD measurements showed that the 3rd dehydrogenation reaction step in Figure 67 (c) corresponds to decomposition of the ternary hydride ($Ca_4Mg_3H_{14}$). The 4th endothermic peak could not be correlated to any crystalline phases. Thus ^{11}B NMR measurements were carried out. ^{11}B NMR measurements revealed that the applied hydrogen backpressure promotes the formation of amorphous boron instead of CaB_6. The results obtained by ^{11}B MAS NMR, however, contradict the results obtained for hydrogen capacities measured by volumetric method (see Figure 67). All samples release a hydrogen content that is roughly 7 wt. %. However, Figure 71 (top panel) predicts lower hydrogen release by increasing hydrogen backpressure. Since ^{11}B MAS NMR is a highly sensitive method (detecting phases even in the ppm range), it can be assumed that the discrepancy between these results are due to measurements inaccuracy of the volumetric method. Thus, the reaction mechanism of the Ca-RHC in dependency of pressure and temperature can concluded as following:

$$\begin{aligned}\mathrm{Ca(BH_4)_2} + \mathrm{MgH_2} &\xrightarrow{\text{0 bar, 350–450 °C}} \mathrm{aCaH_2} + b\mathrm{Mg} + c\mathrm{CaB_6} \\ &+ d[amorph.\,\mathrm{Ca(BH_4)_2}] + e\mathrm{CaB_{12}H_{12}} + f\mathrm{H_2}\end{aligned} \tag{92 a}$$

$$\begin{aligned}\mathrm{Ca(BH_4)_2} + \mathrm{MgH_2} &\xrightarrow{\text{5–10 bar, 350 °C}} a\mathrm{Ca_4Mg_3H_{14}} + b\mathrm{CaH_2} + c\mathrm{Mg} \\ &+ d\mathrm{CaB_{12}H_{12}} + e[amorph.\,\mathrm{Ca(BH_4)_2}] + f\mathrm{B} + g\mathrm{CaB_6} \\ &+ h\mathrm{H_2}\end{aligned} \tag{92 b}$$

$$\begin{aligned}\mathrm{Ca(BH_4)_2} + \mathrm{MgH_2} &\xrightarrow{\text{10–20 bar, 450 °C}} a\mathrm{CaH_2} + b\mathrm{Mg} + c\mathrm{CaB_{12}H_{12}} \\ &+ d[amorph.\,\mathrm{Ca(BH_4)_2}] + e\mathrm{B} + f\mathrm{H_2}\end{aligned} \tag{92 c}$$

Where, all molar factors are a function of applied pressure and temperature. The results discussed above strongly suggest that not MgH_2 destabilizes $Ca(BH_4)_2$ upon its decomposition but rather $Ca(BH_4)_2$ upon its decomposition product CaH_2 which in turn destabilizes MgH_2 to form $Ca_4Mg_3H_{14}$.

Interestingly, unreacted amorphous $Ca(BH_4)_2$ is observed among the decomposition products under all experimental conditions. The term "amorphous" is somehow confusing and might be even inaccurate. This terminology is, nevertheless, justified by the results obtained by Kim *et al.*[276], where they show, *via* cross-polarization NMR method (^{11}B CP MAS-NMR) that the boron in this Ca-B unit (around -30 ppm) is bonded to hydrogen atoms. Yet, it is not indeed understandable why even an amorphous $Ca(BH_4)_2$ does not decomposes under the conditions where a crystallite $Ca(BH_4)_2$ does decompose. Recently, Yan *et al.*[277] have reported the formation of CaB_2H_6 during the dehydrogenation reaction of $Ca(BH_4)_2$ but only at temperatures between 320-350 °C. Yet, they couldn't observe this phase at temperature in the range of 400-450 °C. This is in good agreement with the NMR results (subsection 5.1.3) obtained here. However, this phase was reported to be an intermediate phase which decomposes to CaH_2, CaB_6 by releasing H_2 gas. A work published recently by Kee-Bum Kim *et al.*[278], reported the drop of dehydrogenation capacity of the $4LiBH_4+YH_3$ is over the cycles. They could show that this capacity loss was due to inclusion of the borohydride phase in the shell of $Li_2B_{12}H_{12}$ structure which prevents the decomposition of the included phase. In the light of these results this model can be transferred also to Ca-RHC system. The Ca-B-H units can be thought as covered by layers of $CaB_{12}H_{12}$ phase. These layers may prevent the decomposition of the inner phase. Therefore the Ca-B-H phase remains stable inside this shell even at high temperatures. This model would also explain the hydrogen release of the post-milled dehydrogenated Ca-RHC system (see Figure 73). The $CaB_{12}H_{12}$ layers (shells) are cracked during the ball-milling procedure and the surface/contact area of the interfaces are significantly increased hence the post-milled desorbed sample releases additional hydrogen. Moreover, in the range of the pressure and temperature, applied in this work, the results do not lead to the favoured reaction path:

$$\mathrm{Ca(BH_4)_2 + MgH_2 \xrightarrow{0-20\ bar,\ \ 350-450\ °C} \neq CaH_2 + MgB_2 + 4H_2} \qquad (93)$$

Which according to Barkhordarian *et al.*[279] is entirely reversible. Kim *et al.* [148] calculated (based on DFT) the reaction enthalpies for (92 a) a), (92 a) b) (without counting amorphous $Ca(BH_4)_2$ and $CaB_{12}H_{12}$) and (93) to be about -45 kJ/mol H_2 , 58 kJ/mol H_2 and -47 kJ/mol H_2, respectively. These enthalpy values are very close to each other, especially, if considering that DFT calculation can only predict these quantities with an accuracy of roughly ± 10 kJ/mol H_2.[6 280] Also experimentally determined values for metal borides are very rough and do scatter widely.[281, 282] Thus it can be assumed that the dehydrogenation reaction paths of Ca-RHC are not driven by its thermodynamical properties, under different experimental conditions, but most likely by its kinetical properties. The fact that the Ca-RHC system does not react upon dehydrogenation to CaH_2-MgB_2 (upon an exothermic reaction to form MgB_2) suggests, as one possibility, that the activation barrier between $Ca(BH_4)_2$-MgH_2 and CaH_2-MgB_2 might be relatively high, hence forbidding a mutual reaction of these compounds (independent of applied hydrogen backpressure and temperature) in comparison to other possible dehydrogenation routs. On the other hand the activation barriers of reactions (92 a-c) seem to be not independent of the applied hydrogen backpressure. At 0 bar H_2 and 350-450 °C the reaction (92 (a)) is favoured, whereas at 20 bar H_2 and 450 °C the Ca-RHC system preferably takes the reaction rout (92 (c)). This implies that the activation barrier for (92 (c)) increases with hydrogen backpressure while it behaves *vice versa* for (92 (a)). These notions are illustrated qualitatively in the following diagram.

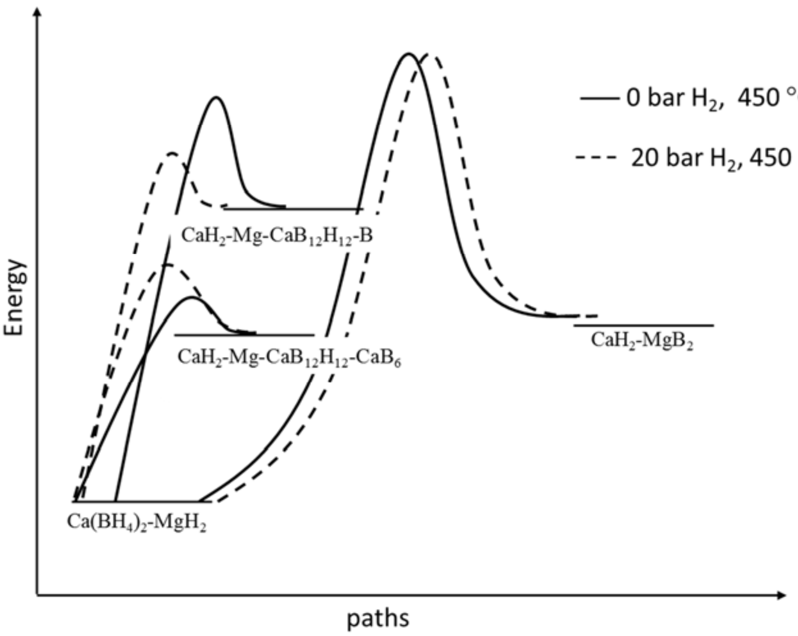

Figure 76. Schematic representation of energy barriers of different dehydrogenation reaction paths of Ca-RHC with dependency of hydrogen backpressure.

In order to alter the thermodynamic of the system Mg_2NiH_4 was chosen to stabilize boron after decomposition of $Ca(BH_4)_2$. The thermodynamic alteration of $Ca(BH_4)_2$-Mg_2NiH_4 in comparison to $Ca(BH_4)_2$-MgH_2 is illustrated in Figure 77. The values for enthalpy of $Ca(BH_4)_2$ or CaH_2 are constant for $Ca(BH_4)_2$-Mg_2NiH_4 and $Ca(BH_4)_2$-MgH_2, respectively, and do not affect the following consideration, hence the corresponding qualitative enthalpy evaluation of these compounds are omitted in the diagram. Using Mg_2NiH_4 as a destabilization agent leads to decomposition of Mg_2NiH_4 (to Mg_2Ni) prior to decomposition of $Ca(BH_4)_2$. Subsequently, Mg_2Ni destabilizes $Ca(BH_4)_2$ to form $MgNi_{2.5}B_2$ which has a higher thermodynamical stability in comparison to Mg_2Ni and MgB_2, respectively.[144, 283]

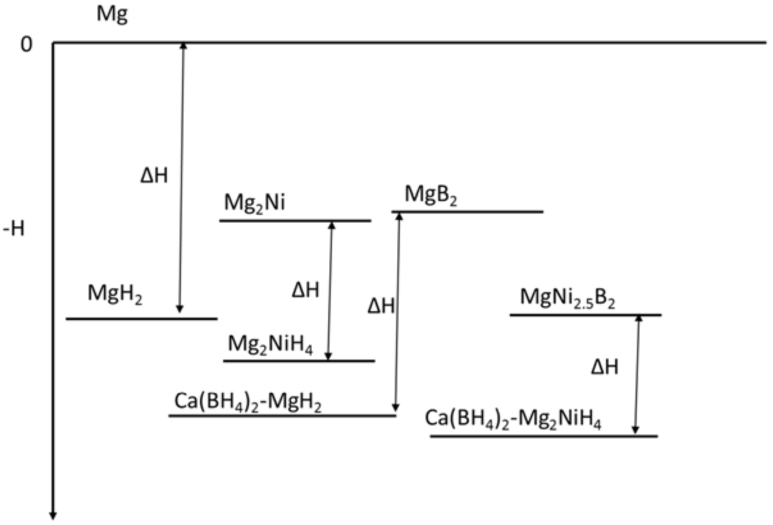

Figure 77. Qualitative enthalpy diagram of $Ca(BH_4)_2$-MgH_2 and $Ca(BH_4)_2$-Mg_2NiH_4.

5.2.3. **Conclusion**

In the last part of this work, the effect of NbF_5 on the Ca-RHC system, its reaction paths with respect to temperature and hydrogen backpressure and the possibility of stabilization of its decomposition products were studied in detail. For the investigation of the effect of NbF_5 on the Ca-RHC system, two sets of samples ($Ca(BH_4)_2$+MgH_2 and $Ca(BH_4)_2$+MgH_2+0.1NbF_5) were prepared for comparative studies. It was found that the NbF_5 additive noticeably decreases the desorption-temperature of Ca-RHC from 350 °C to 250 °C. By means of DSC measurements, it was shown that the dehydrogenation enthalpy value of NbF_5-doped Ca-RHC was lowered (37 kJ/mol H_2) in comparison to pure Ca-RHC (42 kJ/mol H_2). The activation energy for dehydrogenation process of the doped systems was found to be smaller (198 kJ/mol H_2) in comparison to the corresponding value of the undoped system (217 kJ/mol H_2). This suggests that the addition of NbF_5 has a catalytic effect on the Ca-RHC system. Also, the dehydrogenation reaction paths and final products of Ca-RHC system doped with 0.1NbF_5 are altered compared to those of pure Ca-RHC. While the desorption reaction pathway of pure Ca-RHC proceeds with the formation of an intermediate ternary alkaline earth hydride phase ($Ca_4Mg_3H_{14}$), the dehydrogenation of the doped sample proceeds through the formation of the solid solution phase $CaF_{2-x}H_x$ by releasing hydrogen. Therefore, the first major effect of NbF_5 on the Ca-RHC system is the alteration of its dehydrogenation reaction pathway. An analysis of the microstructural characteristics of the doped material showed that the overall particle and crystallite structures in the doped system were approximately ~ 50 % finer in comparison to the pure Ca-RHC system. This suggests that the additive considerably enhances the surface areas of the composite system, which leads effectively to higher contact points between the reaction partners. The refined microstructure of the doped material also significantly decreases the diffusion paths and consequently the mass transport takes place in much shorter times compared to the undoped sample. Hence, the second major impact of NbF_5 is on the microstructural characteristics of the Ca-RHC system. Furthermore, NMR results revealed a trace of CaB_6 nanoparticles in the as-milled Ca-RHC+0.1NbF_5, in contrary to pure as-milled Ca-RHC. It is concluded that during the dehydrogenation process CaB_6 nanoparticles provide seed crystals for the growth of CaB_6. SEM results indicated a fine distribution of the additive in the hydride matrix. XAS measurements showed a change in the chemical state of Nb during the milling procedure from NbF_5 to more stable NbB_2 phase. The mean NbB_2 particle sizes were determined to be around 14 nm, using ASAXS method. HR-TEM confirmed XAS and ASAXS results. Furthermore, NbB_2 nanoparticles also provide two additional crystallographic planes aside the aforementioned CaB_6 nanoparticles for nucleation and growth of the new CaB_6 phase upon the decomposition process of the Ca-RHC+0.1NbF_5 composite system. Therefore, it is concluded that the third effect of the additive is to provide numerous heterogeneous nucleation centres for CaB_6 in the doped hydride composite matrix, so that the formation of new CaB_6 takes place faster in comparison to pure Ca-RHC.

The variation of applied experimental conditions on the dehydrogenation process of pure Ca-RHC showed notable effects on its reaction pathways and its final decomposition products. In the temperature range of 350 - 450 °C and at 0 bar hydrogen backpressure the composite system tends to form more CaB_6 and less amorphous boron and $CaB_{12}H_{12}$. Applying middle pressures in the range of 5 - 10 bar and low temperatures in the range of 350 - 370 °C the system decomposes, in addition to CaH_2 and metallic Mg, into the ternary metal hydride $Ca_4Mg_3H_{14}$ and some residual amorphous $Ca(BH_4)_2$ like structures. In the high temperature and high hydrogen backpressure range (400 - 450 °C and 10 - 20 bar) the composite system tends to form more amorphous boron and $CaB_{12}H_{12}$. In this high temperature and H_2 pressure range, CaB_6 is not detected among the decomposition products of pure Ca-RHC. It should be noted that in the entire range of the applied conditions the formation of MgB_2 is not observed (which is one of the key compound for the reversibility of the Ca-RHC system). One of the reasons why the decomposition reaction pathway of the Ca-RHC system doesn't tend to form MgB_2 is most likely the kinetics of the system. Another reason is based on the thermodynamical properties of the system which is discussed in subsection 6 in more detail. Mg_2NiH_4 was used instead of MgH_2 as destabilization agent for $Ca(BH_4)_2$ which indeed led to stabilization of boron by formation of $MgNi_{2.5}B_2$. The dehydrogenation state of this hydride composite consists of CaH_2-$MgNi_{2.5}B_2$ in analogy to CaH_2-MgB_2.

6. Concluding discussion on RHC systems

In this chapter, thermodynamical, kinetical, and structural properties of the Li-RHC and the Ca-RHC systems are compared and discussed, in more detail. To draw a general picture about the RHCs, the Na-RHC ($NaBH_4$-MgH_2) composite system, which is the last interesting member of the light weight RHCs, is included in these discussions, as well (though it was not the subject of investigation in this work). In particular, differences and analogies of these systems are discussed. This approach will allow elucidating these composite systems in a broader context and will lead to a deeper understanding of their thermodynamical and kinetical, and structural properties.

The results obtained in this work on both investigated composite systems ($LiBH_4$-MgH_2 and $Ca(BH_4)_2$-MgH_2) do not show a mutually destabilization of the constituent hydrides. The $LiBH_4$-MgH_2 composite system decomposes (at 4 bar of H_2 and at 400 °C) in two reaction steps. In the first step MgH_2 decomposes by releasing hydrogen into metallic Mg which subsequently reacts with $LiBH_4$ to form MgB_2, therefore, not the hydrides are mutually reacting but the metal (Mg) and the hydride ($LiBH_4$) phases. In the case of $Ca(BH_4)_2$-MgH_2, both hydrides decompose independently and parallel in one step in to CaH_2, Mg, amorphous B and $Ca(BH_4)_2$, CaB_6, and $CaB_{12}H_{12}$ (at 350 - 450 °C in the hydrogen backpressure range of 0 - 20 bar), thus under these conditions it is questionable to name it a RHC but rather a hydride composite (HC) system or a hydride mixture. The next light weight borohydride-hydride composite system $NaBH_4$-MgH_2 decomposes even in three steps ($NaBH_4+MgH_2 \rightarrow NaBH_4+Mg \rightarrow (2x\text{NaH-}(1-2x)\text{NaBH}_4)_{\text{molten phase}}+(1-x)\text{Mg}+x\text{MgB}_2 \rightarrow \text{NaH}+\text{MgB}_2$).[284] Hence, the terminology of RHC has to be further refined in order to satisfy the various behaviours of different hydride composite systems. Thus, it proposed to subdivided the RHC systems further in the class of "mutually Reactive Hydride Composites" (m-RHCs), where the two constituent hydrides mutually react and destabilize the reaction, and the class of "single (or: simple) Reactive Hydride Composites" (s-RHCs), where the first dehydrogenation occurs independently and only in the second (or further) reaction step (s) its dehydrogenation product reacts with the other hydride constituent to destabilize the reaction.

It should be noted that also $LiBH_4$-MgH_2 decomposes at 400 °C independently and parallel in one reaction step in to LiH, Mg, B, and $Li_2B_{12}H_{12}$, if applying dynamic vacuum condition or even at 1 bar of H_2 backpressure during the dehydrogenation process.[14, 285-287]

The reason why the mutual destabilization reaction of both hydrides in the composite systems does not take place is based on the thermodynamics and kinetics of the respective composite systems. This distinction between the aforementioned systems in m-RHC and s-RHC are further discussed in the following, in detail.

By comparing the dehydrogenation reactions of $LiBH_4$-MgH_2 (at 4 bar H_2, 400 °C), $Ca(BH_4)_2$-MgH_2, and $NaBH_4$-MgH_2, the dehydrogenation behaviour of $Ca(BH_4)_2$-MgH_2 distinctly differs from the other aforementioned hydride composite (HC) systems. The main difference is the lack of formation of the MgB_2 phase among the desorption products under all applied conditions. In contrary to that, in $LiBH_4$-MgH_2 and in $NaBH_4$-MgH_2 the formation of

MgB_2 as a dehydrogenation product was observed by several groups.[10, 111, 288-291] Furthermore, $LiBH_4$-MgH_2, and $NaBH_4$-MgH_2 release hydrogen in their first dehydrogenation reaction step by decomposition of MgH_2 into Mg and H_2, and subsequently the borohydrides build a solid-liquid interface with the metallic Mg $((LiBH_4)_{(l)}/Mg_{(s)}$ and $(NaH/NaBH_4)_{(l)}$ $/Mg_{(s)})$. In $Ca(BH_4)_2$-MgH_2 composite system, however, the borohydride phase initially decomposes and CaH_2 reacts subsequently with MgH_2 to form the ternary metal hydride $Ca_4Mg_3H_{14}$. Although $LiBH_4$-MgH_2 and in $NaBH_4$-MgH_2 behave similarly to each other in their dehydrogenation performances, their initial conditions and their respective thermodynamical properties are considerably different. The $LiBH_4$-MgH_2 HC system is kept at a minimum hydrogen backpressure of ~ 4 bar and it is heated up to 400 °C, whereas the $NaBH_4$-MgH_2 HC system is kept at ~ 0-1 bar H_2 and it is heated up to a maximum temperature of 450 °C (it should be noted that also in the $NaBH_4$-MgH_2 HC system a maximum temperature of 400 °C would lead to the same final products, however, with far lower reaction kinetics, and therefore the maximum temperatures of both systems can be assumed to be ~ 400 °C for further consideration). The $LiBH_4$-MgH_2 HC system has a theoretical equilibrium pressure higher than MgH_2 and $LiBH_4$, respectively (in the temperature range of 300-650 K) (see Figure 78). This is a sufficient condition for the system to be termed as m-RHC system, theoretically. This, however, is not true in the case of $NaBH_4$-MgH_2 composite system.

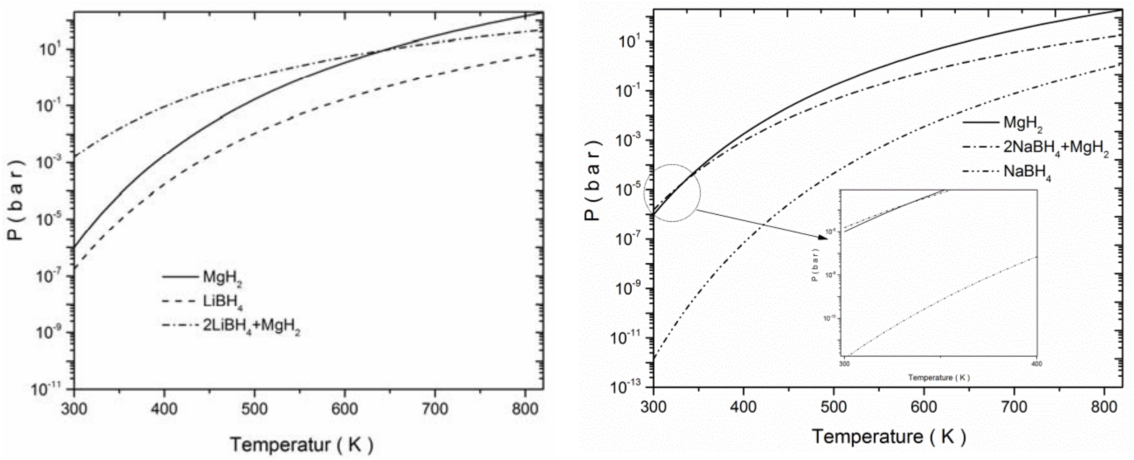

Figure 78. Phase diagram of MgH_2, $LiBH_4$, $2LiBH_4$+MgH_2 (left) and MgH_2, $NaBH_4$, $2NaBH_4$+MgH_2 (right), the thermodynamical values for the compound and for the hydride composites were taken from[7 9 10 14 12].

Although, the $NaBH_4$-MgH_2 HC system has a higher equilibrium pressure in comparison to $NaBH_4$, nevertheless, it has a lower equilibrium pressure in comparison to MgH_2 in the interested temperature range. Only in the nearby of room temperature the composite system has slightly higher equilibrium pressure in comparison to MgH_2 (see inset figure in the Figure 78). In the $LiBH_4$-MgH_2 HC system, in principle, it is thermodynamically favourable to react in one step to form LiH-MgB_2, whereas in the $NaBH_4$-MgH_2 HC system, it is thermodynamically favourable (enforced) to react in two steps ($NaBH_4$-MgH_2 → $NaBH_4$-Mg) to form NaH-MgB_2. Thus, the $NaBH_4$-MgH_2 HC system does not fulfil the condition for being a m-RHC and it should be termed as s-RHC system. Dissimilar to the two aforementioned HC systems, dehydrogenation of the $Ca(BH_4)_2$-MgH_2 composite system can, theoretically, occur along several reaction paths (see 2.6.3.2). Furthermore, this composite system (including all destabilized reaction pathways) and its individual hydride compounds have lower equilibrium pressure in comparison to pristine $Ca(BH_4)_2$, respectively (see Figure 80). In this special case the complex hydride decomposes at lower temperatures relative to the composite system (including all its reaction paths (hatched area in Figure 80)) or MgH_2. Therefore, this system does not fulfil the conditions for neither m-RHC system nor for s-RHC system. Therefore, it is debatable to term this HC system as a RHC, in general. Consequently, MgH_2 is not an appropriate metal hydride, theoretically and experimentally (as was shown in this work), to stabilize the decomposition products of $Ca(BH_4)_2$. The case is even reversed here! After decomposition of $Ca(BH_4)_2$ to CaH_2 and other species, CaH_2 further destabilizes MgH_2 (as is predicted by theory (see Figure 80)), and is measured experimentally (see Figure 66, Figure 67, and Figure 70) to form the ternary metal hydride phase $Ca_4Mg_3H_{14}$. This result is rather analogous to the $NaBH_4$-MgH_2 composite system, where the ternary metal hydride compound $NaMgH_3$ is formed during the rehydrogenation reaction between NaH and MgH_2 [292,293,294]. Pistidda *et al.* [272, 295] could show that the formation of the ternary hydride $NaMgH_3$ was only possible if MgH_2 was involved in the reaction (but not metallic Mg). Such a ternary metal hydride was not observed in the $LiBH_4$-MgH_2 composite system. Thus, in this work MgH_2 was substituted by its destabilized compound Mg_2NiH_4 to shift the equilibrium pressure of the composite system to higher values in comparison to $Ca(BH_4)_2$. If one assumes a mutual reaction of both hydride compounds to occur by the formation of $MgNi_{2.5}B_2$, than this can lead to a composite system with a higher equilibrium pressure (in the interested temperature range) in comparison to its respective single hydride compounds (see Figure 79).

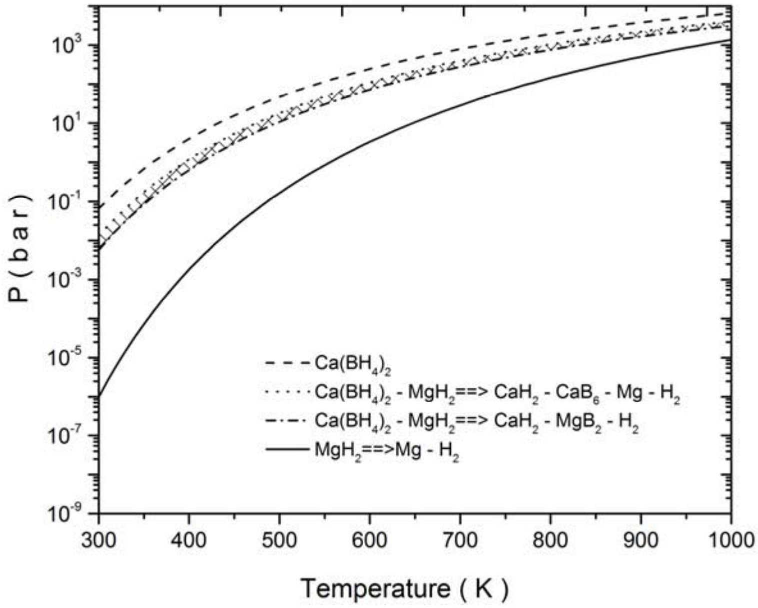

Figure 80. Phase diagram of MgH_2, $Ca(BH_4)_2$, and $Ca(BH_4)_2$-MgH_2 with its different reaction paths (hatched area). The thermodynamical values for the compounds and for the hydride composites were taken from[7 6 12].

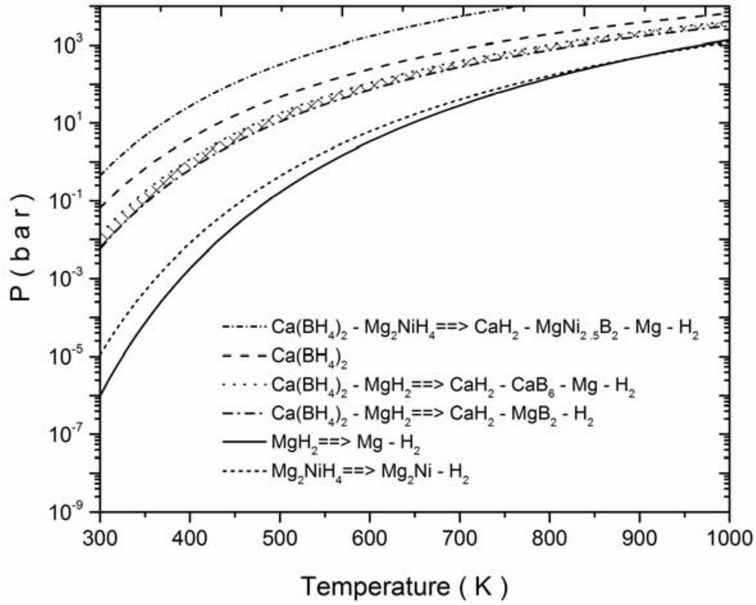

Figure 79. Phase diagram of MgH_2, Mg_2NiH_4, $Ca(BH_4)_2$, and $Ca(BH_4)_2$-MgH_2 with its different reaction paths(hatched area), and $Ca(BH_4)_2$-Mg_2NiH_4. The values for enthalpy and entropy for the compounds and for the hydride composites were taken from[6 12 7, 13].

Based on this calculation, this composite system theoretically fulfils the sufficient thermodynamical condition for being m-RHC system. Indeed, the formation of a ternary boride $MgNi_{2.5}B_2$ compound was experimentally observed, in this work (see subsection 5.2), after dehydrogenation process of the $Ca(BH_4)_2$-Mg_2NiH_4 composite system. The reaction occurred, similarly to $LiBH_4$-MgH_2 composite system, in two steps. In the first step Mg_2NiH_4 decomposes to Mg_2Ni which reacts in the second reaction step with $Ca(BH_4)_2$ to form $MgNi_{2.5}B_2$ and CaH_2. Hence the decomposition products of $Ca(BH_4)_2$ are stabilized by

Mg_2NiH_4. This is the first time, to the knowledge of the author, that the desorption product of $Ca(BH_4)_2$ is stabilized according to the original idea of the concept of RHCs.

Summarizing the discussion above, the question still remains open why the $LiBH_4$-MgH_2 system does not react in one step (under 1 bar of H_2) to form LiH-MgB_2, despite showing the favourable thermodynamical conditions for a mutual reaction between the constituent hydrides. However, as mentioned above, the constituents of the $LiBH_4$-MgH_2 system decompose at 400 °C and at pressures below 1 bar H_2 independently and parallel in one step to form LiH, amorphous boron, and $Li_2B_{12}H_{12}$, and Mg, whereas MgB_2 is not formed. Thus, the reason must be based on kinetical restrictions of the $LiBH_4$-MgH_2 system.

The kinetical obstacles in this system can be deduced mainly to its microstructure. During the high energy ball milling procedure of the $LiBH_4$-MgH_2 composite system, not only both phases are well mixed, respectively, but also their individual crystalline structures are refined. However, the crystallite sizes of the respective phases are still in the range of 50-200 nm. Assuming that the phases in the HC systems contain in average about 10-100 mono crystals, this will lead to a phase size of roughly 1-10 μm, as was shown in this work and this assumptions are in good agreement with the works carried out by other researchers.[225, 227, 296, 297] This naturally leads to relatively large mass diffusion paths in both phases in comparison to their respective unite cell sizes, which are typically in the Å range. Therefore, it is kinetically favourable for boron and magnesium to react with their neighbouring atoms. A further consequence of the large phases of the respective composite systems is their small reaction surface area which may lead to a low interfacial contact area between the two phases in the composite system. Moreover, the first few layers of the surface areas of different phases can be contaminated (typically oxides) which can act as an additional diffusion barrier at the interfacial areas (inactivation)[298 96, 299](see Figure 81).

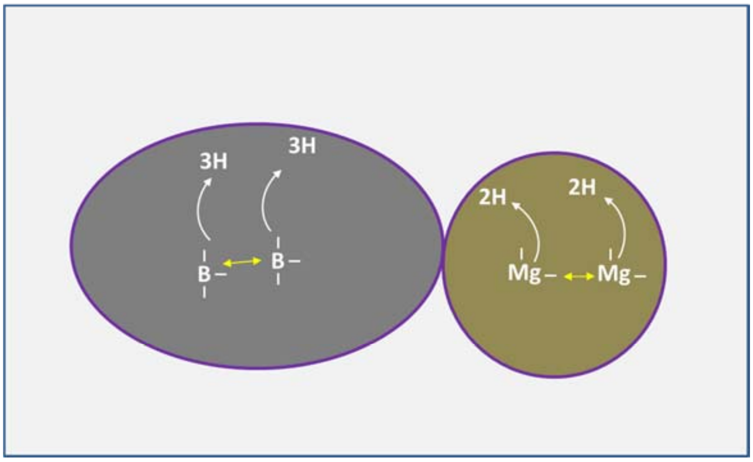

Figure 81. A sketch of the diffusion paths of boron and Mg in a borohydride-magnesium hydride composite system. The purple lines at the circumferences of the particles illustrate the oxide layers.

The importance of the interfacial contact area was shown in the $NaBH_4$-MgH_2 composite system by Pistidda *et al.* [288]. In this study, the as-milled $NaBH_4$-MgH_2 composite system was heated up with 3 K/min to 450 °C under vacuum condition. Although, they kept the system at isothermal condition for roughly 14 hours only the decomposition of MgH_2 to Mg and H_2 could be observed whereas $NaBH_4$ remained stable. However, the $NaBH_4$-MgH_2 composite system liberated its entire theoretical hydrogen content (NaH-MgB_2-H_2 being the desorption products) after they kept the milled composite system under humidity for certain time, and subsequent drying. They found indeed NaH/MgB_2 as final decomposition products, using

XRD and NMR methods. The authors postulated as a possible reason the significantly improved interfacial contact area between $NaBH_4$ and MgH_2. Due to the solubility of $NaBH_4$ in water the physical property of the system is changed from solid-solid to solid-liquid, hence $NaBH_4$ is wetting (covering) the MgH_2 phase. MgH_2, however, is not affected by the moisture because $NaBH_4$ occupies the major volume fraction of the composite system therefore it protects the MgH_2 phase by covering it. After drying the composite system possesses, therefore, a significantly enhanced interfacial contact area of the constituents. After decomposition of MgH_2 (which is thermodynamically enforced, as was discussed above) to Mg and H_2, Mg finds a much larger contact area with $NaBH_4$, in comparison to untreated sample, so that the nucleation and growth of MgB_2 between the two phases can take place. Similar to moisturizing of $NaBH_4$ in the $NaBH_4$-MgH_2 system, $LiBH_4$ has the possibility for wetting the MgH_2 phase on its surface area. In this work experiments were carried out, using a Sievert type apparatus, where the $LiBH_4$-MgH_2 HC system was kept under a hydrogen backpressure of 50 bar and was heated up to 300 °C which is above the melting point of $LiBH_4$ (~ 270 °C) and below the decomposition temperature of MgH_2 (450 °C, at 50 bar). After cooling down the sample to room temperature, a large interfacial contact area was expected. Subsequently the sample was heated up to 250 °C (which is below the dehydrogenation temperature of MgH_2 and $LiBH_4$, respectively) under static vacuum condition. However, no dehydrogenation reaction could be observed, even after waiting for 40 hours. For the molten $LiBH_4$ phase to wet out the MgH_2 phase, it has to be optimal adhesive to its surface area. The mechanism for adhesion can be assumed as mechanical (infiltration of pours and voids) as well as chemical at the solid/liquid interface. Recently, Zeng *et al.*[300] have investigated the interaction between $LiBH_4$ and MgH_2 before their individual decomposition reactions, by substituting hydrogen with deuterium (MgH_2/MgD_2). They could observe, using *in-situ* FT-IR method, already at 200 °C the appearance of B-D stretching mode in addition to B-H stretching mode. At this temperature (200 °C) neither MgH_2 nor $LiBH_4$ are decomposing and $LiBH_4$ is in the solid-state. The B-D stretching mode becomes more pronounced with increasing temperature and after the melting point of $LiBH_4$ phase it reaches its maximum. This implies the exchange of hydrogen with deuterium at the solid/liquid interface of MgH_2 and $LiBH_4$. By using mass spectroscopy (MS), the authors showed that by dehydrogenation of MgH_2 and $LiBH_4$ compounds HD molecules are released, respectively. This shows clearly the mutual diffusion of hydrogen across the phases upon the heating process (see Figure 82).

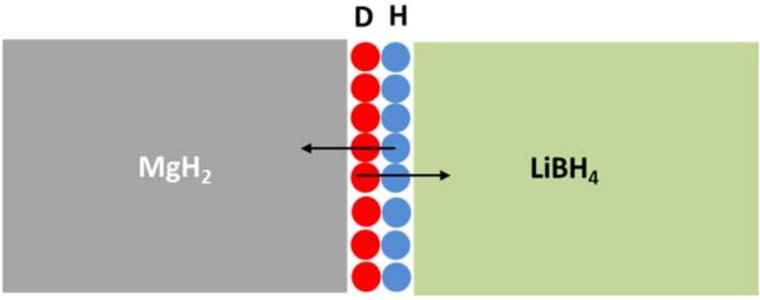

Figure 82. A sketch of the interfacial area between MgH_2 and $LiBH_4$.

It is worth mentioning that the H-D exchange is not limited to the $LiBH_4$-MgH_2 system. Recently Pottmaier *et al.* [301] reported an H-D exchange in the $NaBH_4$ - $MgFe_2D_6$ HC system during the milling procedure. This finding suggests a general scheme of the HC systems with respect to hydrogen exchange at their interfacial boundaries during the heating procedure. Following these facts, it can be assumed that, during the mutual hydrogen-deuterium diffusion between the two phases at a given time, the interfacial areas of both phases are separated by layers of hydrogen. Thus the chemical interaction between the two phases can be assumed to be dominated by hydrogen-bonding forces, at a given time, which are much weaker in comparison to ionic or covalent bonding forces. Therefore, the chemical adhesion between the two phases can be expected to be relatively weak. Moreover, this hydrogen layer at the interfacial area of both phases may act as a diffusional barrier for a mutual reaction between boron and magnesium. An additional diffusional barrier may exist due to presence of some oxygen atoms (which cannot be avoided entirely) at the surfaces of both phases. Nonetheless, there is always a finite probability for MgH_2 or $LiBH_4$ to pass the diffusional barrier at the interfacial area by tunnelling effect. However, these species need to build first a seed greater than a critical nucleus size in order to be stable (as was discussed in chapter 4.2). This might be the second reason for the absence of a mutual reaction between the hydrides. Another possible pitfall is the formation of dodecaborate $Li_2B_{12}H_{12}$ during the dehydrogenation process. Although, the equilibrium pressure of the decomposition of $LiBH_4 \rightarrow Li_2B_{12}H_{12}$-LiH-$H_2$ is lower in comparison to the equilibrium pressure of $LiBH_4$-$MgH_2 \rightarrow$ LiH-MgB_2-H_2, $LiBH_4 \rightarrow$ LiH-B-H_2, respectively, it can be formed if the applied temperature is high enough (~450 K) at a very low H_2 backpressure (~ 10^{-3} bar) (see Figure 83). Despite, the $LiBH_4$-MgH_2 composite system having a higher equilibrium pressure than $Li_2B_{12}H_{12} \rightarrow$ LiH-B-H_2 and $LiBH_4 \rightarrow$ LiH-B-H_2, respectively, it suffers by other large kinetical barriers to form LiH-MgB_2 in the m-RHC phase region (as was pointed out before). Therefore, in the m-RHC phase region of low H_2-backpressure (< 10^{-3} bar) and high temperature (> 450 K) (blue marked area in Figure 83), $Li_2B_{12}H_{12}$ would be formed. Due to the small diffusion paths and the low mass transports in $LiBH_4$, in comparison to the $LiBH_4$-MgH_2 composite system, the formation of $Li_2B_{12}H_{12}$ has lower kinetical barriers. Since the equilibrium pressure of $Li_2B_{12}H_{12}$ is considerably lower in comparison to the entire phase region of RHC, consequently, the $Li_2B_{12}H_{12}$ phase remains stable located at the interfacial areas[192, 302] between $LiBH_4$ and MgH_2. Recently, it was reported [303] that no interaction between a mixture of $Li_2B_{12}H_{12}$+6MgH_2 was observed until 400 °C. Therefore, $Li_2B_{12}H_{12}$ seems to build another diffusional/contact barrier at the interfacial area of $LiBH_4$/MgH_2 in the m-RHC phase region and hinders a mutual reaction between the two hydrides. This conclusion is also supported by observations made by Shim *et al.*[287] in $LiBH_4$-MH_x (x=2, 3; M=Ca, Ce, Y) composite systems and Kim *et al.*[304], who investigated the dehydrogenation reaction pathway of the $LiBH_4$-MgH_2 composite system under Argon and various hydrogen backpressures. It should be noted also that in the phase region of m-RHC the temperature (200-270 °C) is still below the melting point of $LiBH_4$, hence, the mobility of the $[BH_4]^{-1}$ unit is highly limited to overcome the apparent diffusional barrier.

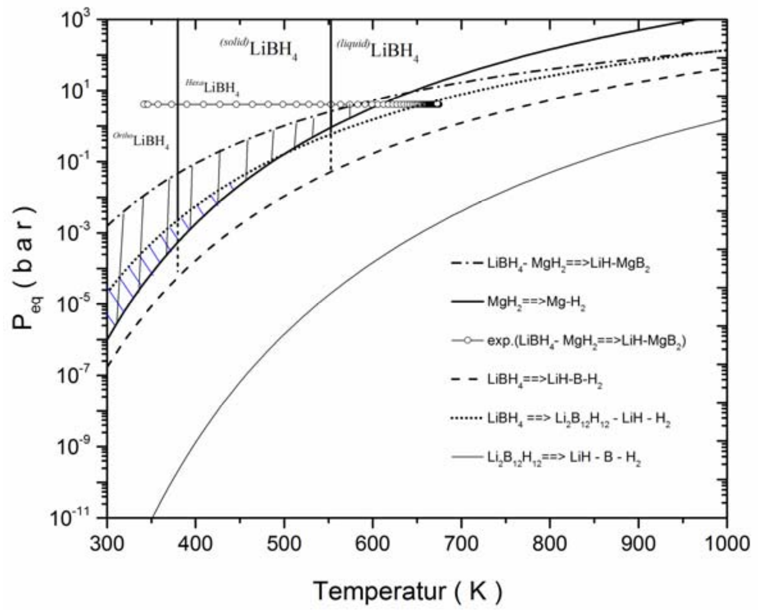

Figure 83. Phase diagram of orthogonal $LiBH_4$, hexagonal $LiBH_4$, liquefied $LiBH_4$, $Li_2B_{12}H_{12}$, MgH_2, and $LiBH_4$-MgH_2 and $LiBH_4$ with its different reaction paths. As an illustration, a volumetric desorption measurement of an as-milled $LiBH_4$-MgH_2 sample is shown. The hatched area display the RHC phase. The values for enthalpy and entropy for the compounds and for the hydride composites were taken from[7 11 14 12, 13.15]

To overcome these kinetical restrictions a hydrogen backpressure higher than 3 bar was proposed by Pinkerton *et al.* [14] A major advantage of this procedure is the liquid state of $LiBH_4$ in this phase region, which results in a high mobility for $[BH_4]^{-1}$ units. However, this approach has two obstacles. The first one is the increase of the equilibrium temperature of the composite system along its phase boundaries (~ 300 °C). The second drawback is the confined operating conditions inside the m-RHC phase region (between $^{(liquid)}LiBH_4$ phase and the equilibrium point of the composite system and MgH_2 phase). Since the composite system suffers under high kinetical barriers, the system needs to be operated far from its equilibrium temperature (to increase the driving forces). Therefore the operating temperature has to be shifted outside the narrow m-RHC phase region which, in turn, is below the equilibrium pressure of MgH_2 and consequently the entire composite system is transferred in s-RHC phase region ($LiBH_4$/Mg). In this region it is favourable for $LiBH_4$ to remain in its liquid phase, however, it is thermodynamically beneficial for the composite system ($LiBH_4$/Mg) to move to the LiH-MgB_2-H_2 phase region by a mutual reaction. An experimental result, obtained by volumetric measurement, is included in Figure 83 to demonstrate the kinetical hindrance and destabilization of $LiBH_4$ (this dynamical measurement is included in the phase diagram only as an illustration). As can be seen the decomposition of the composite system occurs experimentally below the equilibrium pressure of the $Li_2B_{12}H_{12}$ phase, which might create a problem for the reversibility of the system after long cycles. These kinetical constraints enforce the $LiBH_4$-MgH_2 composite system to behave as $NaBH_4$-MgH_2 behaves thermodynamically (as was discussed above). This analogous behaviour is illustrated with a desorption reaction of moisturized $NaBH_4$-MgH_2 sample in Figure 84. As can be seen, the composite system $NaBH_4$-MgH_2 decomposes in its corresponding phase region, where $NaBH_4$ has considerably lower equilibrium pressure.

Therefore, $NaBH_4$ is destabilized by the Mg phase. It should be noted that MgH_2 starts to decompose far behind its equilibrium pressure which indicates its kinetical barriers.

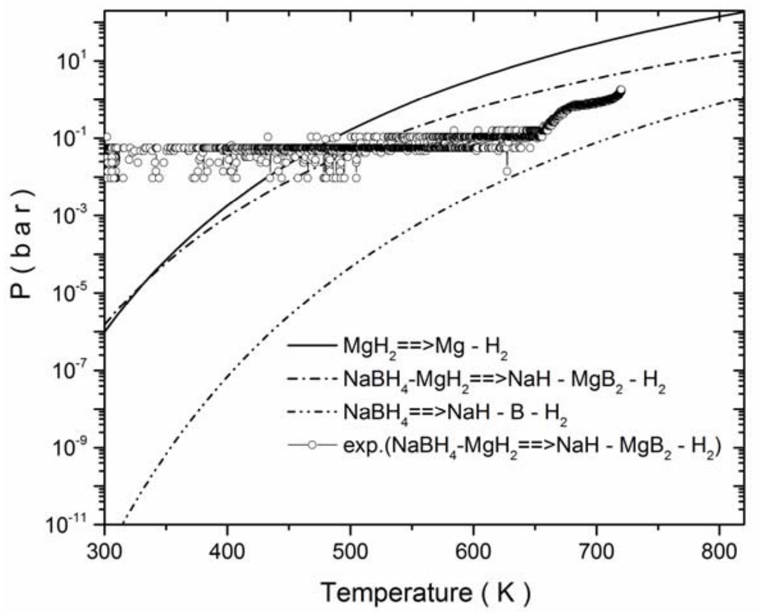

Figure 84. Phase diagram of MgH_2, and $NaBH_4$-MgH_2 and $NaBH_4$ with its different reaction paths. As an illustration, a volumetric desorption measurement of moisturized $NaBH_4$-MgH_2 sample (The volumetric measurement was included in with kind permission of Dr. C. Pistidda). The values for enthalpy and entropy for the compounds and for the hydride composites were taken from[7] [9] [12]

In contrary to $LiBH_4$-MgH_2, where the system needs to be operated out of the m-RHC phase region in to due to s-RHC phase region due to its kinetical limitations, interestingly, the $NaBH_4$-MgH_2 system is shifted in to s-RHC phase region because of its kinetical limitations.

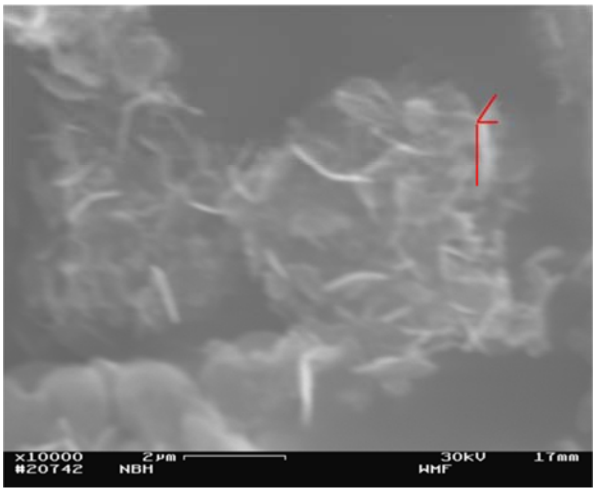

Figure 85. TEM micrograph of dehydrogenated moisturized $NaBH_4$-MgH_2 sample (kindly provided by C. Pistidda). The edges of the MgB_2 plates are marked by bright stripes (as an eye guidance, red lines are drawn at the edges of a MgB_2 plate).

Although, MgH_2 remains stable far in the phase region of s-RHC (NaH-MgB_2-H_2), it does not react with $NaBH_4$ to form MgB_2, in one step. Therefore, the second reaction step of

$LiBH_4$/Mg and $NaBH_4$/Mg composite systems are to build MgB_2 *via* nucleation and growth process, as was discussed in subsection 4.2. Pistidda *et al* [297] reported the nucleation and growth of MgB_2 to occur in the $NaBH_4$/Mg composite system in plate like structures (see Figure 85). This is in excellent agreement with the results obtained in this work (see subsection 4.2.) and with the results obtained by Bösenberg *et al.*[219] However, no incubation period in the moisturized $NaBH_4$-MgH_2 is observed, in contrary to the $LiBH_4$-MgH_2 composite system. In the $LiBH_4$-MgH_2 system, without any dopant, a clear incubation period is observed. After adding small amount of NbF_5 as additive, the incubation period vanishes entirely. It was shown in this work (see subsection 4.1.3) that the chemical state of NbF_5 is changed to NbB_2, after milling with the composite system, and NbB_2 provides two crystallographic nucleation sites for the MgB_2 phase to grow on it. Therefore, it can be assumed that in the moisturized $NaBH_4$-MgH_2 sample this might be due to formation of some nanosized impurities (additives) during the moisturizing- and drying process of the sample, which may act as nucleation centres for MgB_2. However, no experimental evidence of such nucleation agents has been reported so far.

Dissimilar to these both hydride composite systems no MgB_2 phase is formed during the dehydrogenation process of $Ca(BH_4)_2$-MgH_2. Nevertheless, an addition of NbF_5 has a significant effect on the dehydrogenation temperature of the $Ca(BH_4)_2$-MgH_2 composite systems. By addition of $0.1NbF_5$ to the $Ca(BH_4)_2$-MgH_2 composite system its dehydrogenation temperature is reduced by roughly 100 °C (subsection 5.1.1). This is the highest temperature reduction reported so far in this system in comparison with other applied additives (e.g. $TiCl_3$, TiF_4, VF_5). EXAFS investigations showed the formation of NbB_2 after the milling procedure of $Ca(BH_4)_2/MgH_2/0.1NbF_5$ mixture, which remains stable over the cycles (subsection 5.1.4). These results are in accordance with EXAFS results obtained for the $2LiBH_4+MgH_2+0.1NbF_5$ composite system (subsection 4.1.3). ASAXS results showed that the size distributions of NbB_2 nano particles, in both composite systems, are in the range of 5-10 nm. SEM and TEM measurements showed that these particles are finely distributed in the hydride matrix. The function of NbB_2 in both systems ($Ca(BH_4)_2$-MgH_2 and $LiBH_4$-MgH_2) is very similar, but its impact on the respective hydride composite system is rather different. It plays the role of a nucleation agent in both systems. In the $LiBH_4$-MgH_2 composite system, NbB_2 provides two possible crystallographic planes for the nucleation of the MgB_2 phase: MgB_2 {1011}|| NbB_2 {1011} and MgB_2 {1010} || NbB_2 {1010} with the respective *d*-mismatch values of 2.3 % and 0.7 %. These values are well below the critical *d*-mismatch value of 6%.[223, 219, 222, 269] As it was mentioned before, no MgB_2 is formed during the dehydrogenation process of the $Ca(BH_4)_2$-MgH_2 composite systems, but CaB_6. The formation of MgB_2 is the key compound for being a reversible system at moderate temperatures and low pressures. According to the edge-to-edge matching model, the two crystallographic planes {1011} CaB_6 / {1011} NbB_2 and {111} CaB_6 / {1010} NbB_2 show *d*-value mismatches of 2.9 % and 2.8 %, respectively. These two crystallographic planes of NbB_2 provide, therefore, potential nucleation sites for CaB_6 phase. Thus the role of NbB_2 in both systems is to provide nucleation sites for MgB_2 (in the $LiBH_4$-MgH_2 system) and CaB_6 (in the $Ca(BH_4)_2$-MgH_2 system), respectively. The impact of NbB_2 nano particles on the $LiBH_4$-MgH_2 composite system is the reduction (elimination) of the incubation time of MgB_2, whereas NbB_2 nano particles accelerate the formation of CaB_6 during the decomposition reaction of $Ca(BH_4)_2$ in the $Ca(BH_4)_2$-MgH_2 composite system, which leads to a reduction of the dehydrogenation temperature of the system. Also the nucleation process of the respective phases, without additive, proceeds differently in both systems. In the $LiBH_4$-MgH_2 system, the nucleation includes two elements from two distinct phases, namely boron from the $LiBH_4$ phase and Mg from the metallic Mg phase to form MgB_2. This is associated with large mass transports and long diffusion paths. The nucleation process of CaB_6, in contrary, includes only the $Ca(BH_4)_2$

phase, hence, the mass transport and the diffusion paths are significantly smaller in comparison to the $LiBH_4$-MgH_2 system. NbB_2 as nucleation agent would also explain the structural impact on both hydride matrices. The USANS/SANS results showed that the matrix structures in the doped $LiBH_4$-MgH_2 system are significantly smaller in comparison to the pure system. Similarly, Ca-ASAXS results revealed the presence of much finer calcium containing structures in the doped $Ca(BH_4)_2$-MgH_2 system in comparison to the pure composite system. This structural effect of NbB_2 nano particles on the hydride composite system is schematically illustrated in the following figure.

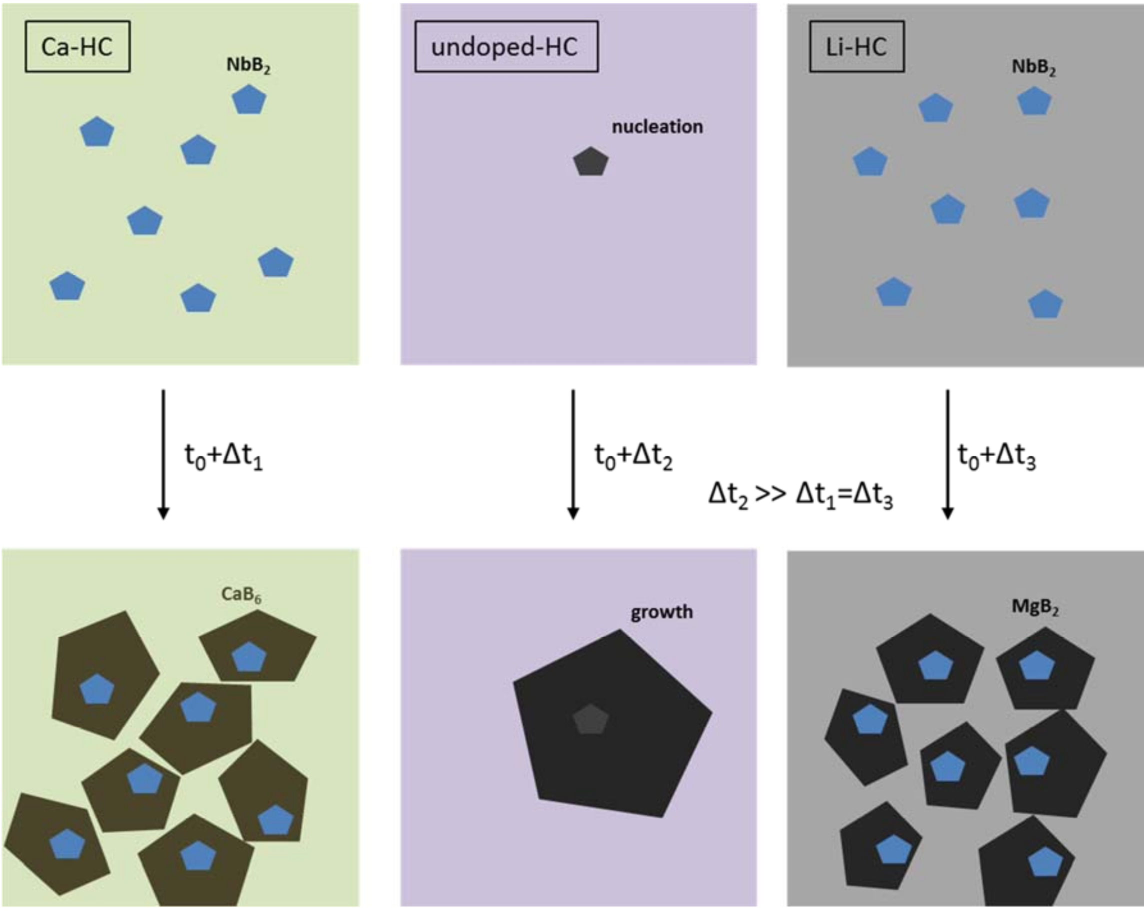

Figure 86. Illustration of nucleation and growth effect of a new phase during the dehydrogenation process of a pure hydride composite system and the doped hydride composite systems ($t_1 = t_3 << t_2$).

The addition of NbF_5 leads also to formation of other by-products in addition to NbB_2, already during the milling procedure. The results of *in situ* XRD measurements exhibited (subsections 4.1.2 and 5.1.2) the formation of LiF and CaF_2 phases after the milling procedure in the doped $LiBH_4$-MgH_2 and $C(BH_4)_2$-MgH_2 composite systems, respectively. In the case of the doped $LiBH_4$-MgH_2, LiF remains stable and inactive over the entire dehydrogenation process. However, CaF_2 does interact with CaH_2, during the dehydrogenation process of $Ca(BH_4)_2$-MgH_2, to form the solid-solution $CaF_{2-x}H_x$. This solid-solution does not have any positive effect on the kinetics of the doped $Ca(BH_4)_2$-MgH_2 composite system.[256] In conclusion, the fundamental difference between $Ca(BH_4)_2$-MgH_2 and $LiBH_4$-MgH_2 composite systems is the lack of formation of MgB_2 during the dehydrogenation process of the $Ca(BH_4)_2$-MgH_2 composite system. This, however, is not only due to kinetical limitations of the system but also due to its thermodynamical properties, as was discussed above. This becomes more obvious by considering the applied hydrogen backpressure on the $LiBH_4$-

MgH_2 and $Ca(BH_4)_2$-MgH_2 composite systems, respectively. As was observed in this work, the hydrogen backpressure tends to change the dehydrogenation reaction path of the system towards more $CaB_{12}H_{12}$, amorphous boron and amorphous $Ca(BH_4)_2$ like structures, which cannot be rehydrogenated under milled conditions,[274 101 305] and less CaB_6, which can be rehydrogenated at low temperatures and pressures.[148 306] Whereas, the hydrogen backpressure, applied during the dehydrogenation process of $LiBH_4$-MgH_2 (or in general MH_2; with M=Ce, Ca)), leads to formation of more MgB_2, less $Li_2B_{12}H_{12}$ and less amorphous boron.[307-310 311]

7. Summary and outlook of the work

In the framework of this thesis, the two most important members of the borohydride based "Reactive Hydride Composite" (RHC) systems were investigated as possible solid-state hydrogen storage systems; namely: $LiBH_4$-MgH_2 (with a gravimetric capacity of ~ 11 wt. % H_2) and $Ca(BH_4)_2$-MgH_2 (with a gravimetric capacity of ~ 8 wt. % H_2). The aim of this work was to characterize the structural effects of additives on these RHCs, determination of the chemical state and size distribution of the applied additives in the hydride matrix, to determine the relationship between the structures of the hydride matrix and chemical state, size distribution of the additives (in the hydride matrix) and the kinetical behaviour of the respective systems. Several experimental methods were applied, such as *in situ* SR-XPD, EXAFS, ASAXS, SANS/USANS, NMR, MS-DSC, microscopy, BET, Sievert's type device and high-energy mill, to achieve the objectives of this research project.

Volumetric measurements of the undoped $LiBH_4$-MgH_2 composite system showed a two-step dehydrogenation reaction at ~ 400 °C and 4 bar H_2 in accordance with previous measurements. The reaction steps were separated by an incubation period of roughly ~ 6 hours. *In situ* SR-PXD measurements (subsection 4.1.2) revealed the first dehydrogenation reaction to be $MgH_2 \rightarrow Mg + H_2$. In the second dehydrogenation reaction step Mg reacts with $LiBH_4$ to form MgB_2 and LiH. Several transition-metal halides were used as additive to improve the kinetical properties of the system. Among them NbF_5 showed the best performance. By adding $0.1NbF_5$ in the $2LiBH_4+MgH_2$ system, the incubation period could be removed and the overall dehydrogenation reaction kinetics was enhanced by a factor of about 10. However, the two-step reaction during the dehydrogenation process remained unchanged. XANES measurements showed that the oxidation state of NbF_5 has changed during the milling procedure from Nb^{+5} to Nb^{+2}. The chemical state of Nb was determined to be NbB_2 by modelling the EXAFS spectra (subsection 4.1.3). The size distribution of NbB_2 particles was determined using ASAXS method. The mean size of these particles in the hydride matrix was determined to be roughly around 10 nm (subsection 4.1.4). In addition, the size distribution of the hydride matrix was determined by using SANS/USANS measurements (subsection 4.1.5). Here, the isotopic contrast variation was used to determine phase specific size distributions of the hydride matrix. The results of these measurements showed that the matrix structures presented in the doped composite system is considerably finer distributed in comparison to the pure composite system. Furthermore, the phase mixture in the particles of the doped system was considerably greater in comparison to the pure system. The results (subsection 4.2) suggest the function of NbB_2 to be a nucleation agent for MgB_2 during the dehydrogenation reaction. Since NbB_2 nano particles are finely distributed in the hydride matrix, they provide significantly higher number of heterogeneous nucleation sites for MgB_2 in comparison to the pure Li-RHC system. Kinetics modelling (subsection 4.2) showed that the new formed MgB_2 phase grows in plate-like structures, which supports the idea of heterogeneous nucleation at the ledges of a substrate (Mg).

Similar to $LiBH_4$-MgH_2, the addition of 0.1NbF_5 to the $Ca(BH_4)_2$-MgH_2 composite system showed the best kinetical performance among other applied transition-metal halides. The chemical state of NbF_5 is transformed after the milling process into NbB_2 and remained stable over the de/absorption process, as was the case for the $LiBH_4$-MgH_2 composite system. The size distribution of NbB_2 and its effect on the hydride matrix are also analogous to those of $LiBH_4$-MgH_2 composite system. Here, for the first time to the best knowledge of the author, successful Ca-ASAXS measurements were performed. Despite, the similar positive effect of NbB_2 on the kinetics of both composite systems, its function in these systems is considerably different. During the dehydrogenation process of the $LiBH_4$-MgH_2 composite system it acts in the interfacial area of $^{(solid)}Mg/^{(liquid)}LiBH_4$ as nucleation agent for MgB_2 which is formed by mutual reaction of both phases (by liberation of hydrogen) on the NbB_2 particles (substrate). In this process, large mass transports from both phases over far distances are involved which leads to elimination of the incubation period of the $LiBH_4$-MgH_2 composite system. Thereby, the overall dehydrogenation time is reduced; however, the additive does not change the dehydrogenation temperature of the composite system significantly. In contrary to the $LiBH_4$-MgH_2 system, there is no incubation period in the undoped $Ca(BH_4)_2$-MgH_2 composite system. NbB_2 acts in this system as a nucleation agent for CaB_6 and depletes the activation barrier for the formation of this phase. Hence, it decreases the dehydrogenation temperature (subsection 5.1). Moreover, in this process only one solid-phase ($Ca(BH_4)_2$) is involved and, therefore, less mass transport and shorter diffusion paths are involved.

In subsection 6, RHCs were discussed in a broader context. For this sake, in the discussions the $NaBH_4$-MgH_2 composite system was included, as well. Difference and analogies between these composites was elucidated. Here, the RHCs were subdivided in to “mutual-Reactive Hydride Composites” (m-RHC) and in “single-Reactive Hydride Composites” (s-RHC). In the case of m-RHCs, the two constituent hydrides mutually react and destabilize the overall reaction, and in the case of s-RHCs, the first dehydrogenation of the composite occurs independently and only in the second (or further) reaction step (s) the dehydrogenated product reacts with the remaining hydride phase to destabilize the entire reaction. This classification helps describing the individual and differentiating between thermodynamical properties of the respective systems. The $LiBH_4$-MgH_2 composite system possesses a higher equilibrium pressure in comparison to $LiBH_4$ and MgH_2, respectively. Therefore the system fulfils the theoretical condition for being m-RHC. Due to the lack of experimental results (carried out in this work and by others) of one step reaction ($2LiBH_4+MgH_2 \leftrightarrow 2LiH+MgB_2$) the system does not show the behaviour of a m-RHCs system. Therefore, this behaviour can be addressed clearly to the poor kinetical properties of the system which forces to operate it in the phase region of s-RHCs (in this way the $LiBH_4$-MgH_2 composite system is indeed a RHC (which includes, both, m-RHCs and s-RHCs)). In the case of $NaBH_4$-MgH_2, the composite system has a higher equilibrium pressure in comparison to $NaBH_4$; however, it has a lower equilibrium pressure in comparison to MgH_2. Therefore, the $NaBH_4$-MgH_2 composite system enforced to react in two steps ($NaBH_4$-$MgH_2 \rightarrow NaBH_4$-Mg) to form NaH-MgB_2. Thus, the $NaBH_4$-MgH_2 composite system falls in the class of s-RHC (it is a member of RHC; however, it will never be a member of m-RHCs!). On the other hand, the $Ca(BH_4)_2$-MgH_2 composite system has a lower equilibrium pressure in comparison to $Ca(BH_4)_2$, however, it has a higher equilibrium pressure in comparison to MgH_2. Based on the concept of RHC (which aims to destabilize the complex hydride with a metal hydride), the $Ca(BH_4)_2$-MgH_2 composite system does not fulfil this condition, hence, it does not fall neither in the class of m-RHCs nor in that of s-RHCs. For instance, the $NaBH_4$-MgH_2 system has to be distinguished from the $Ca(BH_4)_2$-MgH_2 system, based on their thermodynamical behaviour. In the $Ca(BH_4)_2$-MgH_2 composite system, MgH_2 can “only” be seen as an additive. Therefore, this class of RHCs can be termed as additive- RHCs (a-RHC). Thus, a hierarchy or desirability of RHCs can be created in the order of m-RHC > s-RHC > a-RHC. In order to promote $Ca(BH_4)_2$-MgH_2 composite system into m-RHC, it was mandatory to find a hydride compound, which increases the equilibrium pressure of the composite system in such a way to fulfil the condition for a m-RHC system. A possible route, which was followed in this work, was to destabilize MgH_2 to Mg_2NiH_4:

$$2\mathrm{Ca(BH_4)_2} + 5\mathrm{Mg_2NiH_4} \rightarrow 2\mathrm{CaH_2} + 2\mathrm{MgNi_{2.5}B_2} + 8\mathrm{Mg} + 16\mathrm{H_2}$$

The stabilization of decomposition products of $Ca(BH_4)_2$ by the formation of $MgNi_{2.5}B_2$ was also observed experimentally in this work. This is the first time, to the knowledge of the author, that the decomposition of $Ca(BH_4)_2$ is stabilized by the original method of RHC. Thus, $Ca(BH_4)_2$-Mg_2NiH_4 belongs to the class of m-RHC, in contrary to $Ca(BH_4)_2$-MgH_2.

Several questions arise from this work, which exceeded its scope to be answered in detail, but should be important for the future research in this field:

1) Is it possible to synthesize transition-metal boride nano-particles in a required size range and use them directly as additives in order to optimize the hydrogen capacity of the system?
2) Can the nucleation and growth process of MgB_2 -during the dehydrogenation of $LiBH_4$-MgH_2 system- be shown, experimentally, by direct observation?
3) Do the $LiBH_4$-MgH_2 and $Ca(BH_4)_2$-MgH_2 composite systems have potential for reversible hydrogen storage applications?

In the following some suggestions are made as an outlook for the abovementioned open questions. Regarding the first question, transition-metal borides are formed upon the milling procedure together with the borohydrides. Therefore, MgH_2 is not needed for their formation. One promising approach is to mix transition-metal chlorides (MCl_x) and $NaBH_4$ in a proper molar ratio and ball-mill them for ~ 5 hours. After the ball-milling procedure, NaCl and MB_2 can be expected as final products. The final milled powder is to be dissolved in water (1 g in ~ 1 L). Since NaCl is soluble in water, only MB_2 will precipitate, as ceramic nano particles, in the aqueous solution. These nano particles can be removed by various well known techniques (e.g.: by washing). Due to the high stability of the MB_2 (ceramics) compound, the chemical state can be expected to be stable in the aqueous solution, hence the reaction route can be resembled as:

$$2\mathrm{NaBH_4} + \mathrm{MCl}_x \rightarrow 2\mathrm{NaCl} + (\mathrm{MB_2})^{nano-particles} + (x-2)\mathrm{HCl}\uparrow + \left(\frac{10-x}{2}\right)\mathrm{H_2}\uparrow$$

If one desires to avoid the hydrochloric acid gas in the atmosphere, the addition of NaH to the initial educts may help to bind the residual Cl atoms during the milling procedure and to form NaCl by releasing hydrogen:

$$2\mathrm{NaBH_4} + \mathrm{MCl}_x + (x-2)\mathrm{NaH} \rightarrow x\mathrm{NaCl} + (\mathrm{MB_2})^{nano-particles} + \left(\frac{6+x}{2}\right)\mathrm{H_2}\uparrow$$

Some preliminary results seem to confirm these assumptions made above. As a first example $TiCl_3$ was ball-milled with $NaBH_4$ for five hours. As can be seen in Figure 87 (a), the XRD pattern of the milled sample shows only Bragg-peaks of NaCl. No trace of any other Cl-containing species is detected. Figure 87 (b) shows the XRD pattern of the sample after the washing process. As can be seen, there are no diffraction peaks observed at all.

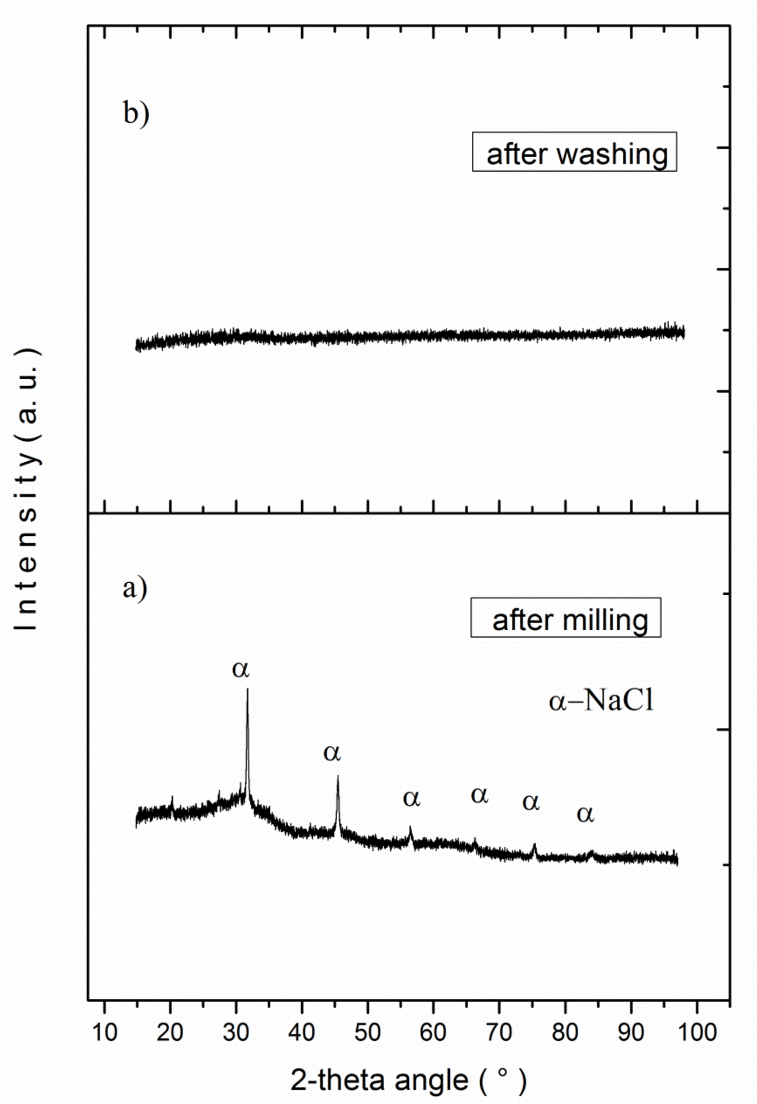

Figure 87. XRD patterns (λ = 1.54 Å) of $NaBH_4$-$TiCl_3$ after milling (a) and after washing process (b).

This suggests the removal of NaCl from the powder by the washing process and hints toward the presence of nano sized powder particles. In order to determine the chemical state of the powder XANES measurements were carried out and the result is shown in Figure 88.

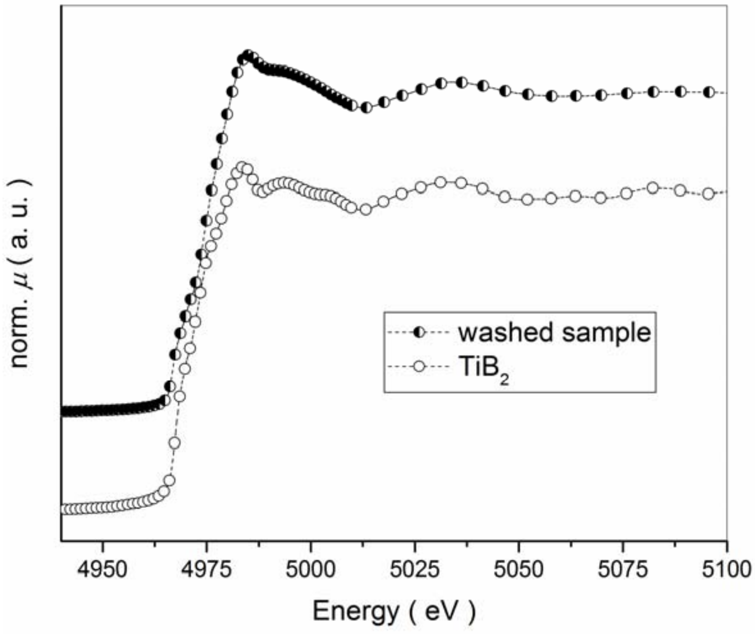

Figure 88. XANES spectra of the washed sample and the TiB_2 reference.

The lower curve in the figure is the XANES spectrum of TiB_2 and the upper curve is the spectrum of the washed sample. A comparison of these two spectra shows a great agreement between their respective features. This suggests the presence of TiB_2 in the washed sample. In order to determine the size distribution of TiB_2 in this sample, SAXS measurement needs to be carried out. *In situ*-SAXS measurements on the sample from the time the powder being introduced into the water until the precipitation of the diboride nano particles should be carried out in order to follow the agglomeration of the diboride nano particles. Furthermore, temperature and pH value of the aqueous solution might be the two crucial experimental parameters which could have some effect on the size distribution and chemical state of the nano particles.

Regarding question 2): Being able to synthesize e.g. NbB_2 nano particles, a model experiment can be performed as shown in Figure 89. A magnesium thin film could be deposited on a substrate (Si, for instance) using a deposition method such as epitaxy or sputtering. The thin film (including the substrate) should be transferred into a HR-TEM apparatus and should be kept under 3 bar of hydrogen. Thereafter, a few hundred NbB_2 nano particles should be distributed homogenously on the Mg thin film. Subsequently, a small amount of $LiBH_4$ powder should be dispersed on the thin film containing NbB_2 nano particles.

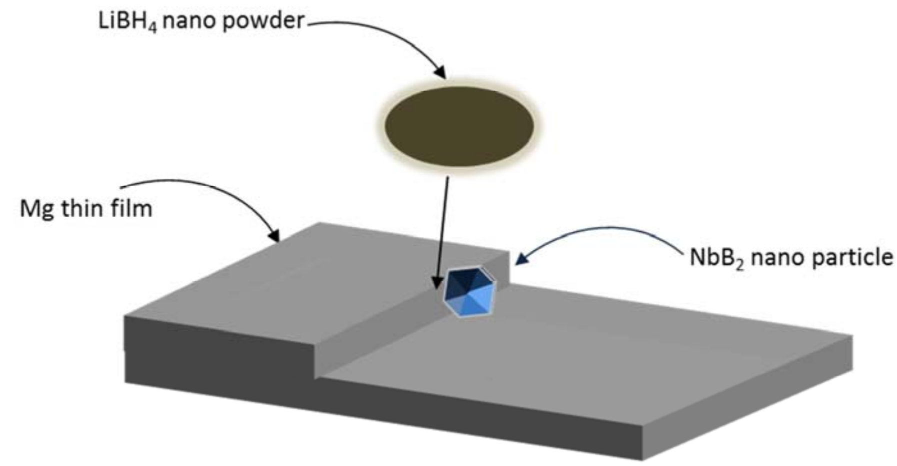

Figure 89. A sketch of an *in situ* HR-TEM thought experiment.

One spot of interest should be found where the three phases are in contact with each other, before slowly increasing the temperature. With this approach it is expected to observe, *in situ*, in the process of nucleation and growth of MgB_2 and the postulated role of NbB_2 in the $LiBH_4$-MgH_2 composite system. The same experiment can be performed without any additive, which might be even better for *in situ* observations, due to the high nucleation barrier for the formation of MgB_2.

Regarding question 3): The potential of the $LiBH_4$-MgH_2 and $Ca(BH_4)_2$-MgH_2 composite systems for possible applications as reversible hydrogen storage systems, a solution of the problem of the degradation of the hydrogen storage capacity in both systems, due to the formation of highly stable phases (such as $CaB_{12}H_{12}$, $Li_2B_{12}H_{12}$, and amorphous boron) and possible phase separations for up-scaled storage systems, needs to be issued. A new approach would be the building of a storage tank system with two nested cylindrical tanks, where the inner tank is rotatable and contains the possible composite system with stainless steel balls (see Figure 90). After the system storage capacity level is dropped below a certain value, the milling process of the system can be initiated. This opens the possibility to reactivate the storage material (breaking the core-shell structures of $M_xB_{12}H_{12}$ and remixing up the separated phases) and it can be recharged to the maximum theoretical capacity.

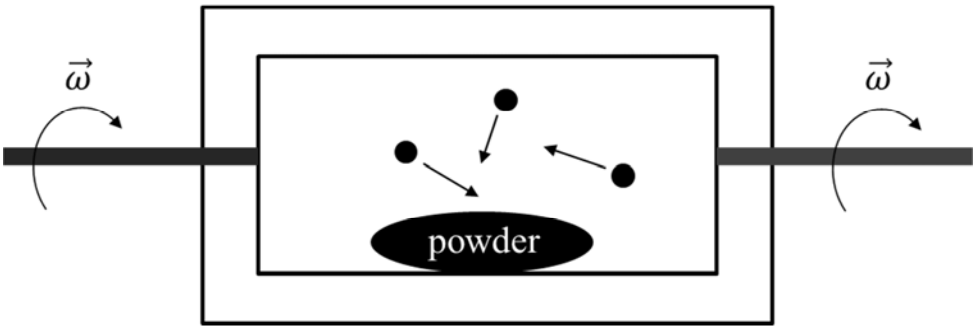

Figure 90. Rotational-milling storage tank system with two nested tanks.

Another possibility is to exchange the tank with a new tank and discharge the inactive material from the used tank and reactivate the material as described above.

For application of these composite systems in large scales, it is also necessary to produce large amounts of complex borohydrides. Therefore, it is mandatory to keep the production costs as low as possible. Here, a new synthesis path with boric acid is proposed to produce complex borohydrides in an economical way and in large scales. The light alkaline and earth alkaline metal hydrides (LiH, NaH, and CaH_2) should be mixed with the boric acid and metallic magnesium or MgH_2 and should be ball milled (under hydrogen pressure, if it improves the reaction rate) for certain times. The most stable compounds are expected to be $M(BH_4)_x$ and MgO.

$$2\mathrm{LiH} + 2\mathrm{H_3BO_3} + 6\mathrm{Mg}/6\mathrm{MgH_2} \xrightarrow{\text{ball-milling}} 2\mathrm{LiBH_4} + 6\mathrm{MgO}$$

$$2\mathrm{NaH} + 2\mathrm{H_3BO_3} + 6\mathrm{Mg}/6\mathrm{MgH_2} \xrightarrow{\text{ball-milling}} 2\mathrm{NaBH_4} + 6\mathrm{MgO}$$

$$\mathrm{CaH_2} + 2\mathrm{H_3BO_3} + 6\mathrm{Mg}/6\mathrm{MgH_2} \xrightarrow{\text{ball-milling}} \mathrm{Ca(BH_4)_2} + 6\mathrm{MgO}$$

The borohydrides can be dissolved by appropriate solvents (such as tetrahydrofuran (THF) or diethylether for the both compounds $LiBH_4$ and $Ca(BH_4)_2$ and water for $NaBH_4$) and MgO can be separated from the solution by filtration. Subsequently, the solvent can be removed and the pure borohydride is obtained after the drying procedure.

In conclusion, the results of this work showed that the addition of $0.1NbF_5$ can lead to significant kinetical enhancement of dehydrogenation/rehydrogenation process in the $LiBH_4$-MgH_2 and $Ca(BH_4)_2$-MgH_2 composite systems, respectively. Based on the results obtained in this work, using USANS/SANS, ASAXS and EXAFS methods, these kinetical improvements could be explained and related to the structural properties of the respective composite systems. Furthermore, the decomposition products of $Ca(BH_4)_2$ could be stabilized, for the first time, using Mg_2NiH_4 as destabilisation agent. The combination of experimental methods at large scale research facilities (synchrotron radiation facilities and neutron research reactor facilities) and apparatus at the lab scale (DSC, TEM, SEM, and NMR) was the key approach to accomplish the characterization of such complex systems which were investigated in this work.

Although the dehydrogenation kinetics of the composite systems are considerably improved within the frame of this research, using NbF_5 as an additive, their dehydrogenation temperatures ($LiBH_4$-MgH_2 (390 °C) and $Ca(BH_4)_2$-MgH_2 (250 °C)) are still too high to be used as hydrogen storage systems for practical mobile applications, due to operating temperature of proton exchange membrane (PEM) fuel cells (~100 °C), at present. Therefore, additional strategies/investigations are needed to further reduce the dehydrogenation temperatures of these composite systems. One strategy might be the nanoconfinement of these composite systems in nano-structured graphene -or mesoporous carbon based materials.

The knowledge gained by this work will lead to better and deeper understanding of structural, kinetical and thermodynamical effects of transitional metal halide additives on metal hydride and hydride composite systems. Consequently, it will help to further optimise the solid-state hydrogen storage systems for possible applications in the near future.

Appendix 1 ASAXS curves

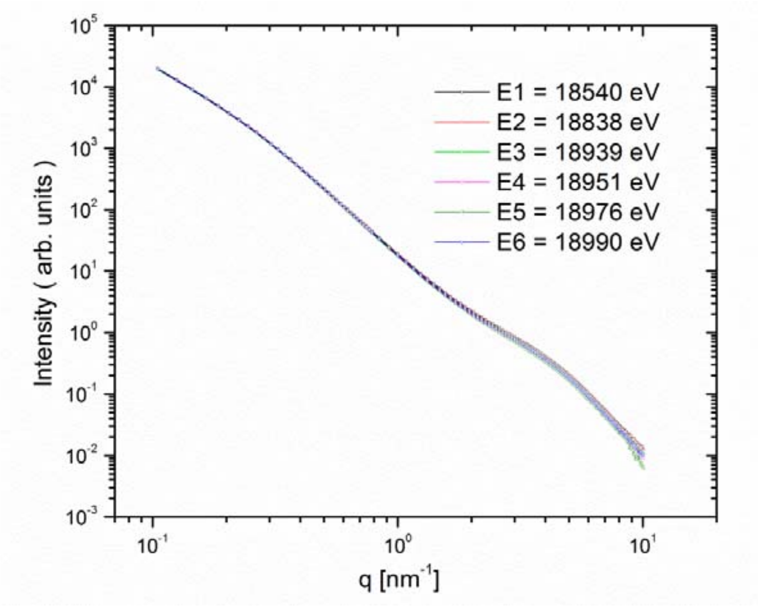

Figure 91. ASAXS curve of 1st dehydrogenated Li-RHC+0.1NbF$_5$

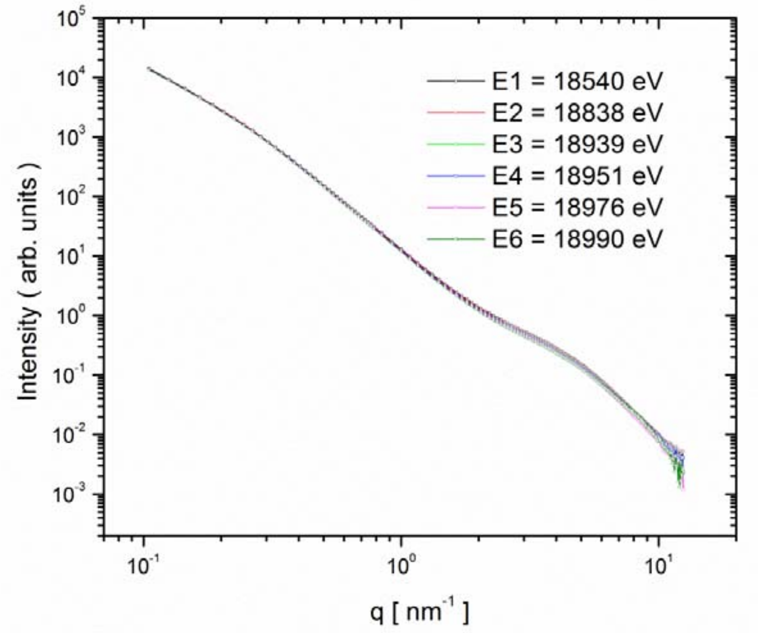

Figure 92. ASAXS curve of 1st rehydrogenated Li-RHC+0.1NbF$_5$

Appendix 2 SANS/USANS curves

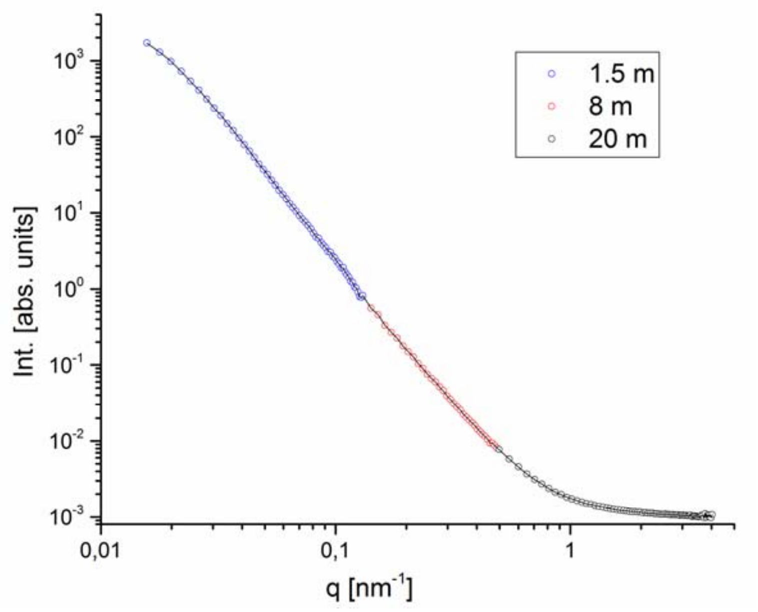

Figure 93. SANS curve of 1st dehydrogenated $LiBH_4$-MgH_2 sample.

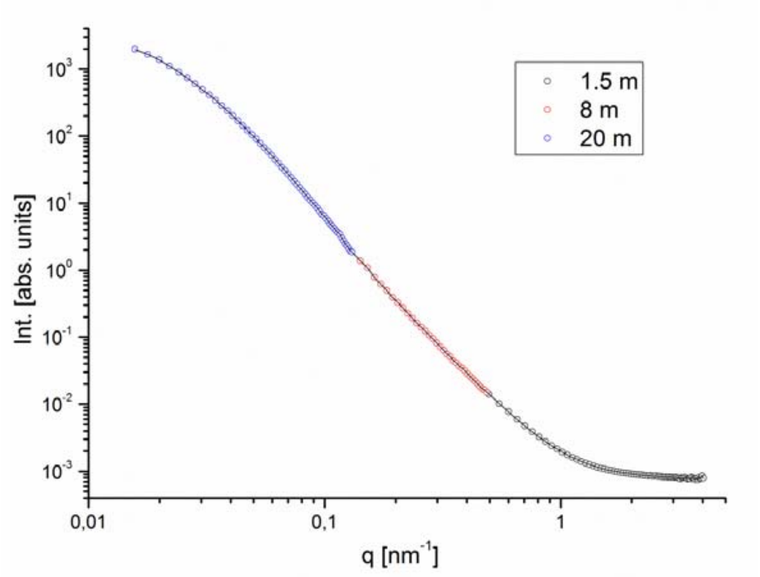

Figure 94. SANS curve of 1st dehydrogenated $Li^{11}BH_4$-MgH_2 sample.

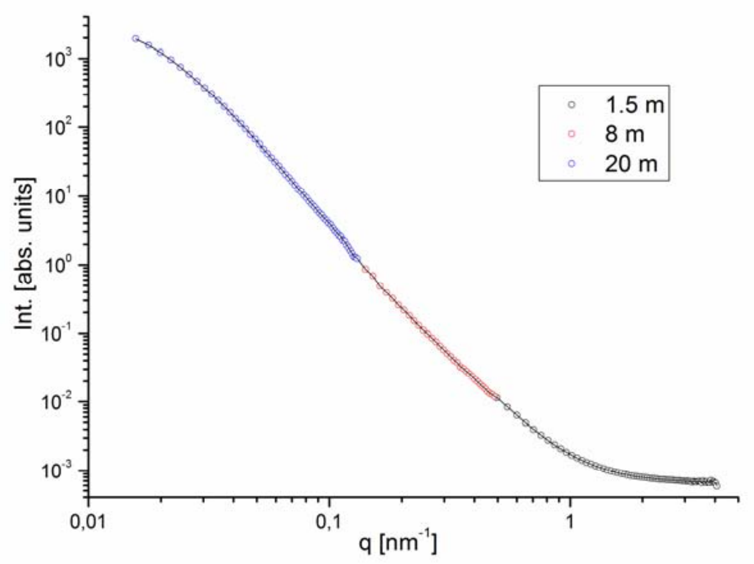

Figure 95. SANS curve of 1st dehydrogenated $^7Li^{11}BH_4$-MgH_2 sample.

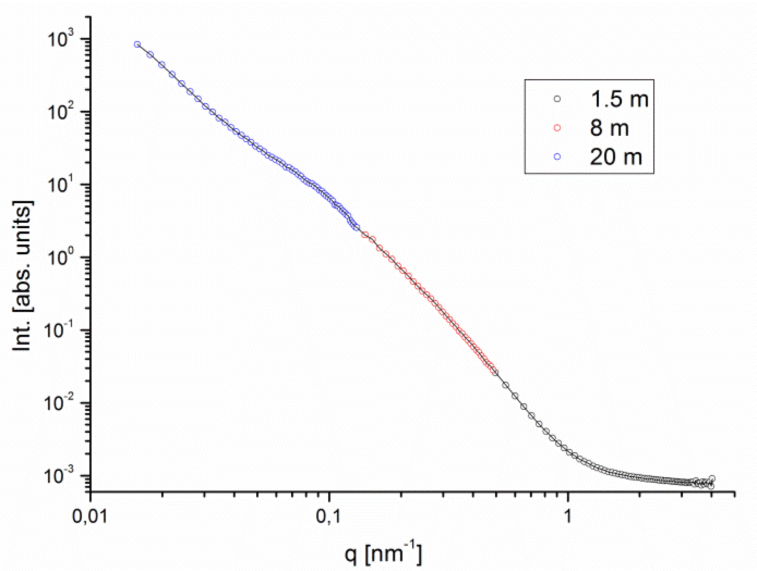

Figure 96. SANS curve of 1st dehydrogenated $LiBH_4$-MgH_2+$0.1NbF_5$ sample.

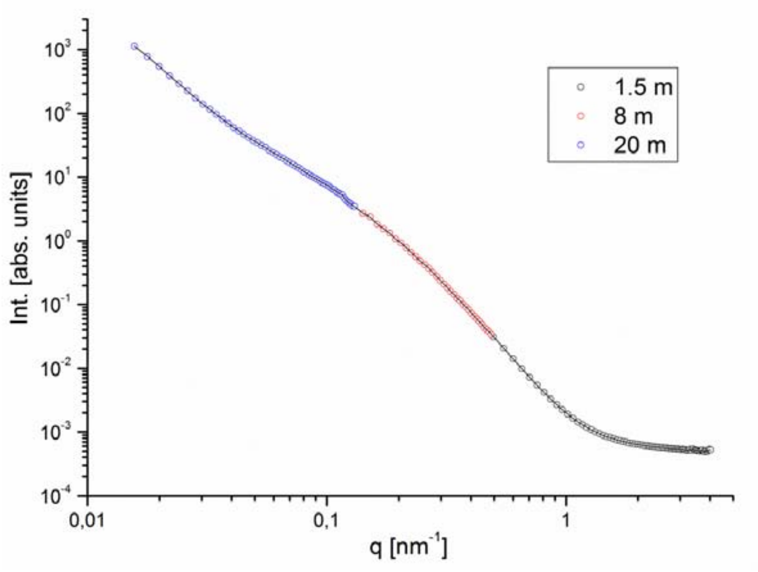

Figure 97. SANS curve of 1st dehydrogenated $Li^{11}BH_4$-MgH_2+0.1NbF_5 sample.

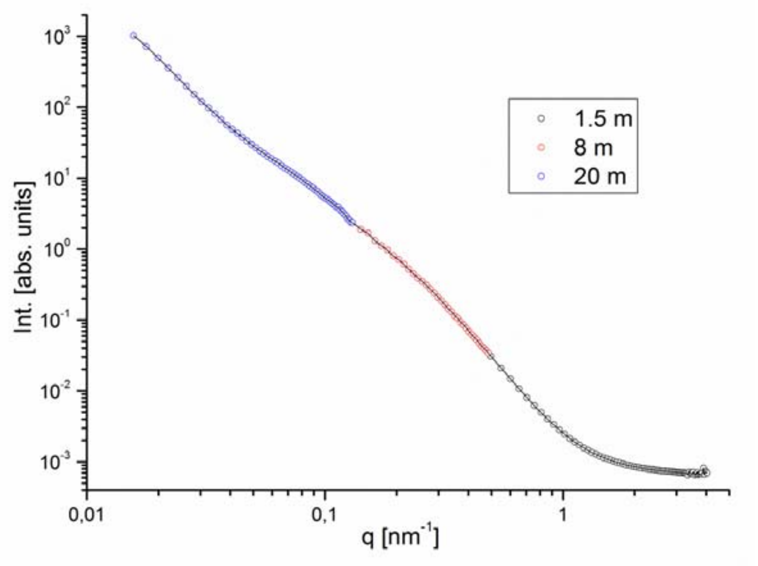

Figure 98. SANS curve of 1st dehydrogenated $^7Li^{11}BH_4$-MgH_2+0.1NbF_5 sample.

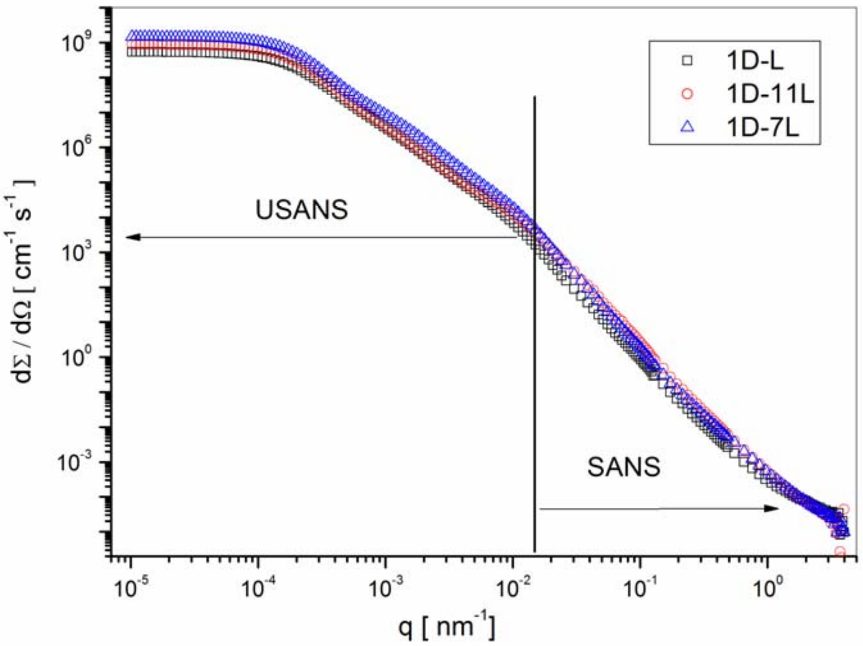

Figure 99. SANS/USANS curves of 1st dehydrogenated $LiBH_4$-MgH_2 (1D-L), $Li^{11}BH_4$-MgH_2 (1D-11L), and $^7Li^{11}BH_4$-MgH_2 (1D-7L) samples.

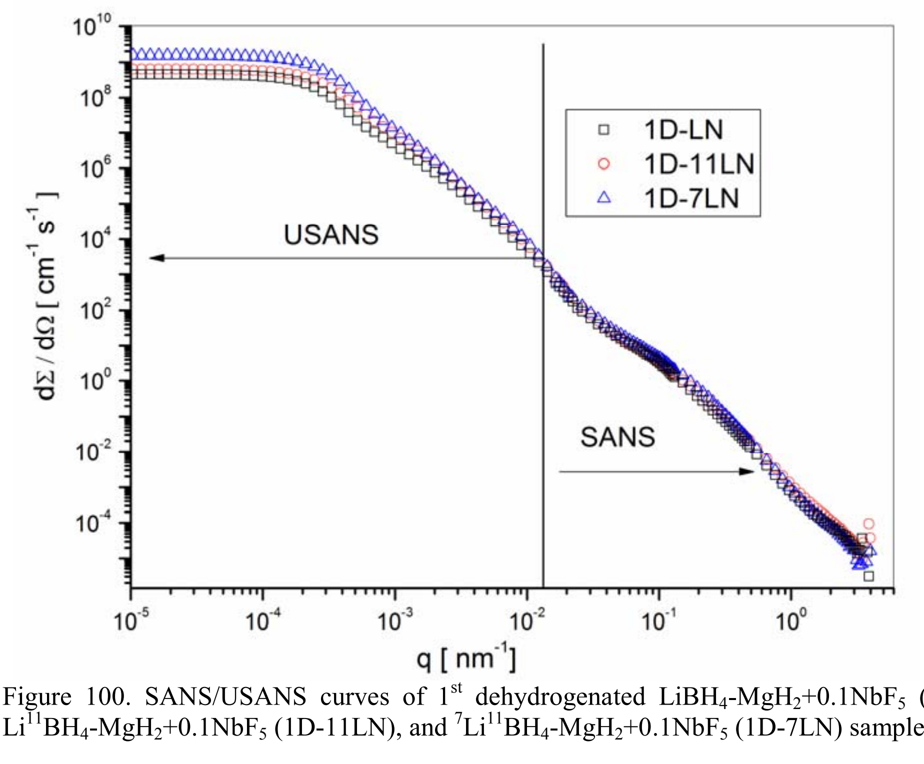

Figure 100. SANS/USANS curves of 1st dehydrogenated $LiBH_4$-MgH_2+0.1NbF_5 (1D-LN), $Li^{11}BH_4$-MgH_2+0.1NbF_5 (1D-11LN), and $^7Li^{11}BH_4$-MgH_2+0.1NbF_5 (1D-7LN) samples.

8. References

1. U. Bösenberg, C. Pistidda, M. Tolkiehn, N. Busch, I. Saldan, K. Suarez-Alcantara, A. Arendarska, T. Klassen and M. Dornheim, *International Journal of Hydrogen Energy*, 2014, **39**, 9899-9903.
2. J. G. Barker, C. J. Glinka, J. J. Moyer, M. H. Kim, A. R. Drews and M. Agamalian, *Journal of Applied Crystallography*, 2005, **38**, 1004-1011.
3. http://www.nist.gov/ncnr/bt5-usans-ultra-small-angle-neutron-scattering.cfm).
4. Alojz Kodre, Iztok Arcon and J. P. Gomilsek, *Acta Chim. Slov.*, 2004, 1-10.
5. D. T. Cromer, *The Journal of Chemical Physics*, 1970, **53**, 1891.
6. D. J. Siegel, C. Wolverton and V. Ozoliņš, *Physical Review B*, 2007, **76**, 134102.
7. J. F. Stampfer, C. E. Holley and J. F. Suttle, *Journal of the American Chemical Society*, 1960, **82**, 3504-3508.
8. R. Gilles, A. Ostermann and W. Petry, *Journal of Applied Crystallography*, 2007, **40**, s428-s432.
9. S. Kato, A. Borgschulte, M. Bielmann and A. Zuttel, *Physical Chemistry Chemical Physics*, 2012, **14**, 8360-8368.
10. J. J. Vajo, S. L. Skeith and F. Mertens, *The Journal of Physical Chemistry B*, 2005, **109**, 3719-3722.
11. A. El Kharbachi, E. Pinatel, I. Nuta and M. Baricco, *Calphad*, 2012, **39**, 80-90.
12. M. Dornheim, *Thermodynamics of Metal Hydrides: Tailoring Reaction Enthalpies of Hydrogen Storage Materials*, 2011.
13. V. Ozolins, E. H. Majzoub and C. Wolverton, *Journal of the American Chemical Society*, 2009, **131**, 230-237.
14. F. E. Pinkerton, M. S. Meyer, G. P. Meisner, M. P. Balogh and J. J. Vajo, *The Journal of Physical Chemistry C*, 2007, **111**, 12881-12885.
15. N. Ohba, K. Miwa, M. Aoki, T. Noritake, S.-i. Towata, Y. Nakamori, S.-i. Orimo and A. Züttel, *Physical Review B*, 2006, **74**, 075110.
16. A. Züttel, A. Borgschulte and L. Schlapbach, *Hydrogen as a Future Energy Carrier*, WILEY-VCH, 1st Edtion edn., 2008.
17. L. Schlapbach and A. Zuttel, *Nature*, 2001, **414**, 353-358.
18. U. S. D. o. Energy and http://hydrogen.pnl.gov/hydrogen-data/hydrogen-properties, *Hydrogen Data Book*.
19. C. o. t. Desert, *Hydrogen Properties*

Module 1, College of the Desert, 2001.

20. A. Züttel, P. Wenger, S. Rentsch, P. Sudan, P. Mauron and C. Emmenegger, *Journal of Power Sources*, 2003, **118**, 1-7.
21. Y. Fukai, *Z. Phys. Chem., 164,165*, (1989).
22. A. E. N. N. Greenwood, *Chemistry of the Elements*, 1997.
23. T. Noritake, S. Towata, M. Aoki, Y. Seno, Y. Hirose, E. Nishibori, M. Takata and M. Sakata, *Journal of Alloys and Compounds*, 2003, **356–357**, 84-86.
24. A. B. A. Züttel, and L. Schlapbach, *Hydrogen as a Future Energy* WILEY-VCH Verlag GmbH & Co. KGaA, Weinheim, ISBN: 978-3-527-30817-0, 2008
25. K.-F. Aguey-Zinsou and J.-R. Ares-Fernandez, *Energy & Environmental Science*, 2010, **3**, 526-543.
26. R. W. Stanley, M. Berube, C. Celik, Y. Ooosaka, J. P. and and M. Avedesian, *Proceedings of the International Magnesium Association, Toronto, Canada*, 1997, **54**, 58-65.
27. H. Imamura, K. Masanari, M. Kusuhara, H. Katsumoto, T. Sumi and Y. Sakata, *Journal of Alloys and Compounds*, 2005, **386**, 211-216.

28. R. Wiswall, in *Hydrogen in Metals II*, eds. G. Alefeld and J. Völkl, Springer Berlin Heidelberg, 1978, vol. 29, ch. 5, pp. 201-242.
29. A. Zaluska, L. Zaluski and J. O. Ström-Olsen, *Appl Phys A*, 2001, **72**, 157-165.
30. Y. Fukai, *The Metal-Hydrogen System, Basic Bulk Properties*, Springer Verlag, Springer Berin Heidelberg, 2005.
31. J.-P. Bastide, B. Bonnetot, J.-M. Létoffé and P. Claudy, *Materials Research Bulletin*, 1980, **15**, 1215-1224.
32. F. H. Ellinger, C. E. Holley, B. B. McInteer, D. Pavone, R. M. Potter, E. Staritzky and W. H. Zachariasen, *Journal of the American Chemical Society*, 1955, **77**, 2647-2648.
33. F. C. Gennari, F. J. Castro and G. Urretavizcaya, *Journal of Alloys and Compounds*, 2001, **321**, 46-53.
34. P. Vajeeston, P. Ravindran, B. C. Hauback, H. Fjellvåg, A. Kjekshus, S. Furuseth and M. Hanfland, *Physical Review B*, 2006, **73**, 224102.
35. P. Vajeeston, P. Ravindran, A. Kjekshus and H. Fjellvåg, *Physical Review Letters*, 2002, **89**, 175506.
36. W. H. Zachariasen, C. E. Holley and J. F. Stamper, *Acta Crystallographica*, 1963, **16**, 352-353.
37. M. Bortz, B. Bertheville, G. Böttger and K. Yvon, *Journal of Alloys and Compounds*, 1999, **287**, L4-L6.
38. E. Akiba, K. Nomura, S. Ono and Y. Mizuno, *Journal of the Less Common Metals*, 1982, **83**, L43-L46.
39. B. Bogdanović, S.-t. Liao, M. Schwickardi, P. Sikorsky and B. Spliethoff, *Angewandte Chemie International Edition in English*, 1980, **19**, 818-819.
40. K. J. Gross, P. Spatz, A. Züttel and L. Schlapbach, *Journal of Alloys and Compounds*, 1996, **240**, 206-213.
41. J. Lu, Y. J. Choi, Z. Z. Fang, H. Y. Sohn and E. Rönnebro, *Journal of the American Chemical Society*, 2009, **131**, 15843-15852.
42. J. J. Reilly and R. H. Wiswall, *Inorganic Chemistry*, 1968, **7**, 2254-2256.
43. R. W. P. Wagemans, J. H. van Lenthe, P. E. de Jongh, A. J. van Dillen and K. P. de Jong, *Journal of the American Chemical Society*, 2005, **127**, 16675-16680.
44. S. A. Shevlin and Z. X. Guo, *The Journal of Physical Chemistry C*, 2013, **117**, 10883-10891.
45. http://www1.eere.energy.gov/hydrogenandfuelcells/storage/pdfs/targets_onboard_hydro_storage.pdf.
46. K. C. Ott, *Final Report for the DOE Chemical Hydrogen Storage Center of Excellence,<http://www1.eere.energy.gov/hydrogenandfuelcells/pdfs/chemical_hydrogen_storage_coe_final_report.pdf>*, LA-UR-2007.
47. L. Simpson, *Hydrogen Sorption Center of Excellence (HSCoE) Final Report, September, 2010,* <*http://www1.eere.energy.gov/hydrogenandfuelcells/pdfs/hydrogen_sorption_coe_final_report.pdf>*.
48. M. A. K. Lodhi, *International Journal of Hydrogen Energy*, 1989, **14**, 379-411.
49. B. Bogdanović, A. Ritter and B. Spliethoff, *Angewandte Chemie International Edition in English*, 1990, **29**, 223-234.
50. W. Oelerich, T. Klassen and R. Bormann, *Journal of Alloys and Compounds*, 2001, **315**, 237-242.
51. W. Oelerich, T. Klassen and R. Bormann, *Journal of Alloys and Compounds*, 2001, **322**, L5-L9.
52. K. F. Aguey-Zinsou, J. R. Ares Fernandez, T. Klassen and R. Bormann, *International Journal of Hydrogen Energy*, 2007, **32**, 2400-2407.
53. A. Aurora, M. R. Mancini, D. M. Gattia, A. Montone, L. Pilloni, E. Todini and M. V. Antisari, *Materials and Manufacturing Processes*, 2009, **24**, 1058-1063.
54. M. Dornheim, S. Doppiu, G. Barkhordarian, U. Boesenberg, T. Klassen, O. Gutfleisch and R. Bormann, *Scripta Materialia*, 2007, **56**, 841-846.

55. M. Dornheim, N. Eigen, G. Barkhordarian, T. Klassen and R. Bormann, *Advanced Engineering Materials*, 2006, **8**, 377-385.
56. G. Barkhordarian, T. Klassen and R. Bormann, *Journal of Alloys and Compounds*, 2004, **364**, 242-246.
57. I. D. Hughes, M. Dane, A. Ernst, W. Hergert, M. Luders, J. Poulter, J. B. Staunton, A. Svane, Z. Szotek and W. M. Temmerman, *Nature*, 2007, **446**, 650-653.
58. Taylor and M. I. K. N. R. & Darby, *Physics of Rare Earth Solids (60–62)*, London, 1972.
59. S. C. Keeton and T. L. Loucks, *Physical Review*, 1968, **168**, 672-678.
60. J. N. Huiberts, R. Griessen, J. H. Rector, R. J. Wijngaarden, J. P. Dekker, D. G. de Groot and N. J. Koeman, *Nature*, 1996, **380**, 231-234.
61. T. B. Flanagan and W. A. Oates, *Annual Review of Materials Science*, 1991, **21**, 269-304.
62. T. Graham, *Philosophical Transactions of the Royal Society of London*, 1866, **156**, 399-439.
63. W. Bartczak and J. Stawowska, *Structural Chemistry*, 2004, **15**, 447-459.
64. H. Nakatsuji and M. Hada, *Journal of the American Chemical Society*, 1985, **107**, 8264-8266.
65. L. Zaluski, A. Zaluska, P. Tessier, J. O. Ström-Olsen and R. Schulz, *Journal of Alloys and Compounds*, 1995, **217**, 295-300.
66. M. Eryürek, Y. Karadag, N. Taşaltın, N. Kılınç and A. Kiraz, *Sensors and Actuators B: Chemical*, 2015, **212**, 78-83.
67. N. Taşaltın, S. Öztürk, N. Kılınç and Z. Z. Öztürk, *Journal of Alloys and Compounds*, 2011, **509**, 4701-4706.
68. N. Taşaltın, F. Dumludağ, M. A. Ebeoğlu, H. Yüzer and Z. Z. Öztürk, *Sensors and Actuators B: Chemical*, 2008, **130**, 59-64.
69. E. Antolini, *Energy & Environmental Science*, 2009, **2**, 915-931.
70. G. G. Libowitz, H. F. Hayes and T. R. P. Gibb, *The Journal of Physical Chemistry*, 1958, **62**, 76-79.
71. J. J. Reilly and R. H. Wiswall, *Inorganic Chemistry*, 1974, **13**, 218-222.
72. J.-G. Roquefere, B. Chevalier, R. Pöttgen, N. Terashita, K. Asano, E. Akiba and J.-L. Bobet, *Intermetallics*, 2008, **16**, 179-187.
73. X. Hou, R. Hu, T. Zhang, H. Kou, W. Song and J. Li, *International Journal of Hydrogen Energy*, 2014, **39**, 19672-19681.
74. M. Polanski, T. K. Nielsen, I. Kunce, M. Norek, T. Płociński, L. R. Jaroszewicz, C. Gundlach, T. R. Jensen and J. Bystrzycki, *International Journal of Hydrogen Energy*, 2013, **38**, 4003-4010.
75. H. H. Van Mal, K. H. J. Buschow and A. R. Miedema, *Journal of the Less Common Metals*, 1974, **35**, 65-76.
76. R. Martínez-Coronado, M. Retuerto, B. Torres, M. J. Martínez-Lope, M. T. Fernández-Díaz and J. A. Alonso, *International Journal of Hydrogen Energy*, 2013, **38**, 5738-5745.
77. MARTINEZ-CORONADO, #160, R., RETUERTO, #160, M., ALONSO, #160 and J. A., *Simplified mechano-synthesis procedure of Mg[2]NiH[4]*, Elsevier, Kidlington, ROYAUME-UNI, 2012.
78. J. L. Soubeyroux, D. Fruchart, A. Mikou, M. Pezat and B. Darriet, *Materials Research Bulletin*, 1984, **19**, 895-904.
79. D. N. a. P.-E. Werner, *Acta Chemica Scandinavica A*, 1982, 847-851.
80. R. Kataoka, Y. Goto, A. Kamegawa, H. Takamura and M. Okada, *Journal of Alloys and Compounds*, 2007, **446–447**, 142-146.
81. B. Bogdanović and M. Schwickardi, *Journal of Alloys and Compounds*, 1997, **253–254**, 1-9.
82. S.-i. Orimo, Y. Nakamori, J. R. Eliseo, A. Züttel and C. M. Jensen, *Chemical Reviews*, 2007, **107**, 4111-4132.
83. Y. Nakamori, H. W. Li, M. Matsuo, K. Miwa, S. Towata and S. Orimo, *Journal of Physics and Chemistry of Solids*, 2008, **69**, 2292-2296.
84. H. I. Schlesinger and H. C. Brown, *Journal of the American Chemical Society*, 1940, **62**, 3429-3435.

85. H. I. Schlesinger, H. C. Brown, B. Abraham, A. C. Bond, N. Davidson, A. E. Finholt, J. R. Gilbreath, H. Hoekstra, L. Horvitz, E. K. Hyde, J. J. Katz, J. Knight, R. A. Lad, D. L. Mayfield, L. Rapp, D. M. Ritter, A. M. Schwartz, I. Sheft, L. D. Tuck and A. O. Walker, *Journal of the American Chemical Society*, 1953, **75**, 186-190.
86. H. I. Schlesinger, H. C. Brown, H. R. Hoekstra and L. R. Rapp, *Journal of the American Chemical Society*, 1953, **75**, 199-204.
87. K. C. Ott, *Final Report for the DOE Chemical Hydrogen Storage Center of Excellence*, LA-UR-20074.
88. N. C. Hallett and H. L. Johnston, *Journal of the American Chemical Society*, 1953, **75**, 1496-1497.
89. W. D. Davis, L. S. Mason and G. Stegeman, *Journal of the American Chemical Society*, 1949, **71**, 2775-2781.
90. S.-I. Orimo, Y. Nakamori, N. Ohba, K. Miwa, M. Aoki, S.-i. Towata and A. Züttel, *Applied Physics Letters*, 2006, **89**, -.
91. S. Orimo, Y. Nakamori, G. Kitahara, K. Miwa, N. Ohba, S. Towata and A. Züttel, *Journal of Alloys and Compounds*, 2005, **404–406**, 427-430.
92. N. Ohba, K. Miwa, M. Aoki, T. Noritake, S.-i. Towata, Y. Nakamori, S.-i. Orimo and A. Züttel, *Physical Review B*, 2006, **74**, 075110.
93. V. Ozolins, E. H. Majzoub and C. Wolverton, *Physical Review Letters*, 2008, **100**, 135501.
94. S.-I. Orimo, Y. Nakamori, N. Ohba, K. Miwa, M. Aoki, S.-i. Towata and A. Züttel, *Applied Physics Letters*, 2006, **89**, 021920.
95. S.-J. Hwang, R. C. Bowman, J. W. Reiter, Rijssenbeek, G. L. Soloveichik, J.-C. Zhao, H. Kabbour and C. C. Ahn, *The Journal of Physical Chemistry C*, 2008, **112**, 3164-3169.
96. S. Kato, M. Bielmann, A. Borgschulte, V. Zakaznova-Herzog, A. Remhof, S.-i. Orimo and A. Zuttel, *Physical Chemistry Chemical Physics*, 2010, **12**, 10950-10955.
97. F. M. A. Muller, J. Bensoam, , 1980.
98. K. Miwa, M. Aoki, T. Noritake, N. Ohba, Y. Nakamori, S.-i. Towata, A. Züttel and S.-i. Orimo, *Physical Review B*, 2006, **74**, 155122.
99. E. H. Majzoub and E. Rönnebro, *The Journal of Physical Chemistry C*, 2009, **113**, 3352-3358.
100. F. Buchter, Z. Łodziana, A. Remhof, O. Friedrichs, A. Borgschulte, P. Mauron, A. Züttel, D. Sheptyakov, L. Palatinus, K. Chłopek, M. Fichtner, G. Barkhordarian, R. Bormann and B. C. Hauback, *The Journal of Physical Chemistry C*, 2009, **113**, 17223-17230.
101. L.-L. Wang, D. D. Graham, I. M. Robertson and D. D. Johnson, *The Journal of Physical Chemistry C*, 2009, **113**, 20088-20096.
102. C. Bonatto Minella, E. Pellicer, E. Rossinyol, F. Karimi, C. Pistidda, S. Garroni, C. Milanese, P. Nolis, M. D. Baró, O. Gutfleisch, K. P. Pranzas, A. Schreyer, T. Klassen, R. Bormann and M. Dornheim, *The Journal of Physical Chemistry C*, 2013, **117**, 4394-4403.
103. E. Rönnebro and E. H. Majzoub, *The Journal of Physical Chemistry B*, 2006, **110**, 25686-25691.
104. Y. Nakamori and S. I. Orimo, *Journal of Alloys and Compounds*, 2004, **370**, 271-275.
105. F. E. Pinkerton, G. P. Meisner, M. S. Meyer, M. P. Balogh and M. D. Kundrat, *The Journal of Physical Chemistry B*, 2004, **109**, 6-8.
106. S. M. Opalka, O. M. Løvvik, H. W. Brinks, P. W. Saxe and B. C. Hauback, *Inorganic Chemistry*, 2007, **46**, 1401-1409.
107. J. J. Reilly and R. H. Wiswall, *Inorganic Chemistry*, 1967, **6**, 2220-2223.
108. J. Graetz, Y. Lee, J. J. Reilly, S. Park and T. Vogt, *Physical Review B*, 2005, **71**, 184115.
109. J. J. Reilly and R. H. Wiswall, *Inorganic Chemistry*, 1967, **6**, 2220-2223.
110. R. Domènech-Ferrer, M. Gurusamy Sridharan, G. Garcia, F. Pi and J. Rodríguez-Viejo, *Journal of Power Sources*, 2007, **169**, 117-122.
111. J. J. Vajo, F. Mertens, C. C. Ahn, R. C. Bowman and B. Fultz, *The Journal of Physical Chemistry B*, 2004, **108**, 13977-13983.

112. Y. Nakamori, H. W. Li, K. Kikuchi, M. Aoki, K. Miwa, S. Towata and S. Orimo, *Journal of Alloys and Compounds*, 2007, **446–447**, 296-300.
113. L. Seballos, J. Z. Zhang, E. Rönnebro, J. L. Herberg and E. H. Majzoub, *Journal of Alloys and Compounds*, 2009, **476**, 446-450.
114. Z.-Z. Fang, X.-D. Kang, J.-H. Luo, P. Wang, H.-W. Li and S.-i. Orimo, *The Journal of Physical Chemistry C*, 2010, **114**, 22736-22741.
115. H. Grove, H. W. Brinks, R. H. Heyn, F. J. Wu, S. M. Opalka, X. Tang, B. L. Laube and B. C. Hauback, *Journal of Alloys and Compounds*, 2008, **455**, 249-254.
116. J. Huot, D. B. Ravnsbæk, J. Zhang, F. Cuevas, M. Latroche and T. R. Jensen, *Progress in Materials Science*, 2013, **58**, 30-75.
117. O. M. Løvvik and O. Swang, *EPL (Europhysics Letters)*, 2004, **67**, 607.
118. E. Rönnebro, *Journal of Physics and Chemistry of Solids*, 2010, **71**, 1154-1158.
119. M. H. Sørby, H. W. Brinks, A. Fossdal, K. Thorshaug and B. C. Hauback, *Journal of Alloys and Compounds*, 2006, **415**, 284-287.
120. H. Hagemann, M. Longhini, J. W. Kaminski, T. A. Wesolowski, R. Černý, N. Penin, M. H. Sørby, B. C. Hauback, G. Severa and C. M. Jensen, *The Journal of Physical Chemistry A*, 2008, **112**, 7551-7555.
121. R. Černý, G. Severa, D. B. Ravnsbæk, Y. Filinchuk, V. D'Anna, H. Hagemann, D. r. Haase, C. M. Jensen and T. R. Jensen, *The Journal of Physical Chemistry C*, 2009, **114**, 1357-1364.
122. L. George and S. K. Saxena, *International Journal of Hydrogen Energy*, 2010, **35**, 5454-5470.
123. L. H. Rude, T. K. Nielsen, D. B. Ravnsbæk, U. Bösenberg, M. B. Ley, B. Richter, L. M. Arnbjerg, M. Dornheim, Y. Filinchuk, F. Besenbacher and T. R. Jensen, *physica status solidi (a)*, 2011, **208**, 1754-1773.
124. Y. Nakamori, K. Miwa, A. Ninomiya, H. Li, N. Ohba, S.-i. Towata, A. Züttel and S.-i. Orimo, *Physical Review B*, 2006, **74**, 045126.
125. L. M. Arnbjerg, D. B. Ravnsbæk, Y. Filinchuk, R. T. Vang, Y. Cerenius, F. Besenbacher, J.-E. Jørgensen, H. J. Jakobsen and T. R. Jensen, *Chemistry of Materials*, 2009, **21**, 5772-5782.
126. L. H. Rude, O. Zavorotynska, L. M. Arnbjerg, D. B. Ravnsbæk, R. A. Malmkjær, H. Grove, B. C. Hauback, M. Baricco, Y. Filinchuk, F. Besenbacher and T. R. Jensen, *International Journal of Hydrogen Energy*, 2011, **36**, 15664-15672.
127. J. S. G. Myrdal, D. Blanchard, D. Sveinbjörnsson and T. Vegge, *The Journal of Physical Chemistry C*, 2013, **117**, 9084-9091.
128. L. Yin, P. Wang, Z. Fang and H. Cheng, *Chemical Physics Letters*, 2008, **450**, 318-321.
129. L.-C. Yin, P. Wang, X.-D. Kang, C.-H. Sun and H.-M. Cheng, *Physical Chemistry Chemical Physics*, 2007, **9**, 1499-1502.
130. P. K. Pranzas, U. Bösenberg, F. Karimi, M. Münning, O. Metz, C. B. Minella, H.-W. Schmitz, F. Beckmann, U. Vainio, D. Zajac, E. Welter, T. R. Jensen, Y. Cerenius, R. Bormann, T. Klassen, M. Dornheim and A. Schreyer, *Advanced Engineering Materials*, 2011, **13**, 730-736.
131. F. Karimi, P. K. Pranzas, A. Hoell, U. Vainio, E. Welter, V. S. Raghuwanshi, C. Pistidda, M. Dornheim, T. Klassen and A. Schreyer, *Journal of Applied Crystallography*, 2014, **47**, 67-75.
132. I. Saldan, R. Campesi, O. Zavorotynska, G. Spoto, M. Baricco, A. Arendarska, K. Taube and M. Dornheim, *International Journal of Hydrogen Energy*, 2012, **37**, 1604-1612.
133. C. Bonatto Minella, S. Garroni, C. Pistidda, R. Gosalawit-Utke, G. Barkhordarian, C. Rongeat, I. Lindemann, O. Gutfleisch, T. R. Jensen, Y. Cerenius, J. Christensen, M. D. Baró, R. d. Bormann, T. Klassen and M. Dornheim, *The Journal of Physical Chemistry C*, 2011, **115**, 2497-2504.
134. P. Mauron, F. Buchter, O. Friedrichs, A. Remhof, M. Bielmann, C. N. Zwicky and A. Züttel, *The Journal of Physical Chemistry B*, 2007, **112**, 906-910.
135. Y. Nakamori and S.-i. Orimo, *Journal of Alloys and Compounds*, 2004, **370**, 271-275.
136. M. Au, A. Jurgensen and K. Zeigler, *The Journal of Physical Chemistry B*, 2006, **110**, 26482-26487.
137. O. Ruff and H. Goerges, *Berichte der deutschen chemischen Gesellschaft*, 1911, **44**, 502-506.

138. R. Juza and K. Opp, *Zeitschrift für anorganische und allgemeine Chemie*, 1951, **266**, 325-330.
139. P. Chen, Z. Xiong, J. Luo, J. Lin and K. L. Tan, *Nature*, 2002, **420**, 302-304.
140. S. Hino, N. Ogita, M. Udagawa, T. Ichikawa and Y. Kojima, *Journal of Applied Physics*, 2009, **105**, 023527.
141. E. Veleckis, *Journal of Nuclear Materials*, 1979, **79**, 20-27.
142. A. Züttel, *Materials Today*, 2003, **6**, 24-33.
143. A. Züttel, S. Rentsch, P. Fischer, P. Wenger, P. Sudan, P. Mauron and C. Emmenegger, *Journal of Alloys and Compounds*, 2003, **356–357**, 515-520.
144. J. J. Vajo, W. Li and P. Liu, *Chemical Communications*, 2010, **46**, 6687-6689.
145. S. N. L. H. M. Database and http://hydrogendoedev.nrel.gov/.
146. M. Felderhoff and B. Bogdanović, *International Journal of Molecular Sciences*, 2009, **10**, 325-344.
147. G. Barkhordarian, T. Klassen, M. Dornheim and R. Bormann, *Journal of Alloys and Compounds*, 2007, **440**, L18-L21.
148. Y. Kim, D. Reed, Y.-S. Lee, J. Y. Lee, J.-H. Shim, D. Book and Y. W. Cho, *The Journal of Physical Chemistry C*, 2009, **113**, 5865-5871.
149. C. Bonatto Minella, S. Garroni, D. Olid, F. Teixidor, C. Pistidda, I. Lindemann, O. Gutfleisch, M. D. Baró, R. d. Bormann, T. Klassen and M. Dornheim, *The Journal of Physical Chemistry C*, 2011, **115**, 18010-18014.
150. H. Ibach and H. Lüth, *Solid-state physics: An introduction to Principles of Material Science*, Springer Verlag, Heidelberg, Londen, New York, 2009.

151. A. Guinier, *X-Ray Diffraction In Crystals, Imperfect Crystals, and Amorphous Bodies*, W. H. FREEMANN AND COMPANY, San Francisco and London, UNIVERSITY OF PARIS, 1963.
152. C. Kittel, *Introduction to Solid State Physics*, Wiley & Sons, Inc., USA, Eighth edition edn., 2005.
153. C. Kittel, *Einführung in die Festkörperphysik*, Oldenburg Wissenschaftsverlag GmbH, München, 8th edn., 2006.
154. A. Guinier, *Physics Today*, 1969, **22**, 25-30.
155. R. W. James, *The optical principle of the diffraction of X-rays* G. Bell and sons LDT, London, Chap. IV, 1962.
156. R.-J. Roe, *Methods of X-Ray and Neutron Scattering in Polymer Science*, Oxford University Press, Inc., New York, 2000.
157. D. Svergun, *Journal of Applied Crystallography*, 1992, **25**, 495-503.
158. J. S. Pedersen, *Neutrons, X-rays and Light*, 2002, 391-420.
159. F. Gerhard and G. Otto, *Journal of Physics: Condensed Matter*, 2006, **18**, S2403.
160. I. S. Dmitri and H. J. K. Michel, *Reports on Progress in Physics*, 2003, **66**, 1735.
161. W. Reimers, A. R. Pyzalla, A. Schreyer and H. Clemens, *Neutrons and Synchrtron Radiation in Engineering Materials Science*, WILEY-VCH, Weinheim, 2008.
162. O. Kratky, I. Pilz and P. J. Schmitz, *Journal of Colloid and Interface Science*, 1966, **21**, 24-34.
163. G. D. Wignall and F. S. Bates, *Journal of Applied Crystallography*, 1987, **20**, 28-40.
164. H. Stabinger and O. Kratky, *Die Makromolekulare Chemie*, 1978, **179**, 1655-1659.
165. F. Zhang, J. Ilavsky, G. G. Long, J. P. G. Quintana, A. J. Allen and P. R. Jemian, *Metall and Mat Trans A*, 2009, **41**, 1151-1158.
166. F. Lixin, D. Mike, B. Scott, G. Nick and I. Jan, *Journal of Physics: Conference Series*, 2010, **247**, 012005.
167. R. Hendricks, *Journal of Applied Crystallography*, 1972, **5**, 315-324.
168. D. Orthaber, A. Bergmann and O. Glatter, *Journal of Applied Crystallography*, 2000, **33**, 218-225.
169. G. G. Long, P. R. Jemian, J. R. Weertman, D. R. Black, H. E. Burdette and R. Spal, *Journal of Applied Crystallography*, 1991, **24**, 30-37.
170. I. Pilz, *Journal of Colloid and Interface Science*, 1969, **30**, 140-144.

171. J. H. Hubbell, H. A. Gimm and I. O/verbo/, *Journal of Physical and Chemical Reference Data*, 1980, **9**, 1023-1148.
172. H. B. Stuhrmann, *Quarterly Reviews of Biophysics*, 1981, **14**, 433-462.
173. C. E. Bouldin, G. Bunker, D. A. McKeown, R. A. Forman and J. J. Ritter, *Physical Review B*, 1988, **38**, 10816-10819.
174. D. C. Koningsberger and R. Prins, *X-Ray Absorption:*

Principles, Applications, Techniques of EXAFS, SEXAFS and XANES, Wiley-Interscience, 1988.
175. Schulz R., Boily S. and Hout J.
176. U. Bösenberg, S. Doppiu, L. Mosegaard, G. Barkhordarian, N. Eigen, A. Borgschulte, T. R. Jensen, Y. Cerenius, O. Gutfleisch, T. Klassen, M. Dornheim and R. Bormann, *Acta Materialia*, 2007, **55**, 3951-3958.
177. A. P. Hammersley, *FIT2D: An Introduction and Overview*, ESRF Internal Report, ESRF97HA02T, FIT2D: An Introduction and Overview, 1997.
178. R. Allmann and R. Hinek, *Acta Crystallographica Section A*, 2007, **63**, 412-417.
179. K. V. Klementiev, XAFSmass, freeware: www.cells.es/Beamlines/CLAESS/software/xafsmass.html

180. B. Ravel and M. Newville, *Journal of Synchrotron Radiation*, 2005, **12**, 537-541.
181. D. T. Cromer and D. A. Liberman, *Acta Crystallographica Section A*, 1981, **37**, 267-268.
182. U. Keiderling, *Appl Phys A*, 2002, **74**, s1455-s1457.
183. S. Kline, *Journal of Applied Crystallography*, 2006, **39**, 895-900.
184. P. Staron and D. Bellmann, *Journal of Applied Crystallography*, 2002, **35**, 75-81.
185. M. R. Hartman, J. J. Rush, T. J. Udovic, R. C. Bowman Jr and S.-J. Hwang, *Journal of Solid State Chemistry*, 2007, **180**, 1298-1305.
186. J. K. Kang, S. Y. Kim, Y. S. Han, R. P. Muller and W. A. Goddard, *Applied Physics Letters*, 2005, **87**, 111904.
187. H. Brumberger, *Modern Aspects of Small-Angle Scattering*, Springer Science & Business Media, Como, Italy, 2013.
188. G. Goerigk, R. Schweins, K. Huber and M. Ballauff, *EPL (Europhysics Letters)*, 2004, **66**, 331.
189. *Small angle x-ray scattering / edited by O. Glatter and O. Kratky*, Academic Press, London ; New York, 1982.
190. I. Bressler, J. Kohlbrecher and A. F. Thunemann, *Journal of Applied Crystallography*, 2015, **48**, 1587-1598.
191. B. Bogdanović, A. Reiser, K. Schlichte, B. Spliethoff and B. Tesche, *Journal of Alloys and Compounds*, 2002, **345**, 77-89.
192. O. Friedrichs, A. Remhof, S. J. Hwang and A. Züttel, *Chemistry of Materials*, 2010, **22**, 3265-3268.
193. M. P. Pitt, M. Paskevicius, D. H. Brown, D. A. Sheppard and C. E. Buckley, *Journal of the American Chemical Society*, 2013, **135**, 6930-6941.
194. Y. Yan, A. Remhof, S.-J. Hwang, H.-W. Li, P. Mauron, S.-i. Orimo and A. Zuttel, *Physical Chemistry Chemical Physics*, 2012, **14**, 6514-6519.
195. David A. Porter, a. Kenneth E. Easterling and M. Y. Sherif, *Phase Transformations in Metals and Alloys*, CRC Press, New York, Third Edition edn., 2009.
196. S. J. Binnie, S. J. Nolan, N. D. Drummond, D. Alfè, N. L. Allan, F. R. Manby and M. J. Gillan, *Physical Review B*, 2010, **82**, 165431.
197. W.-S. Jung, S.-C. Lee and S.-H. Chung, *ISIJ International*, 2008, **48**, 1280-1284.
198. A. J. Kinloch, *Adhesion and Adhesives, Science and Technology*, Springer Netherlands, 1987.

199. D. Kashchiev, *Nucleation: Basic Theory with Applications*, Butterworth-Heinemann, 2000.
200. W. R. Tyson and W. A. Miller, *Surface Science*, 1977, **62**, 267-276.
201. A. Züttel, A. Borgschulte and S.-I. Orimo, *Scripta Materialia*, 2007, **56**, 823-828.

202. G. Schrauzer, *Naturwissenschaften*, 1955, **42**, 438-438.
203. N. A. Lange, *Lange's Handbook of Chemistry*, McGraw-Hill Education, New York, USA, 16 edition edn., 2005.
204. O. Friedrichs, A. Borgschulte, S. Kato, F. Buchter, R. Gremaud, A. Remhof and A. Züttel, *Chemistry – A European Journal*, 2009, **15**, 5531-5534.
205. C. Pistidda, S. Garroni, F. Dolci, E. G. Bardají, A. Khandelwal, P. Nolis, M. Dornheim, R. Gosalawit, T. Jensen, Y. Cerenius, S. Suriñach, M. D. Baró, W. Lohstroh and M. Fichtner, *Journal of Alloys and Compounds*, 2010, **508**, 212-215.
206. A. N. Kolmogorov, *Bull. Acad. Sci. USSR Ser. Math.*, 1937, **1**, 355-359.
207. J. W. A. a. M. R. F., *rans. Am. Inst. Min. Metall. Eng.*, 1939, **135**, 416-485.
208. M. Avrami, *The Journal of Chemical Physics*, 1939, **7**, 1103-1112.
209. M. Avrami, *The Journal of Chemical Physics*, 1940, **8**, 212-224.
210. M. Avrami, *The Journal of Chemical Physics*, 1941, **9**, 177-184.
211. M. H. Mintz and Y. Zeiri, *Journal of Alloys and Compounds*, 1995, **216**, 159-175.
212. J. Bloch, *Journal of Alloys and Compounds*, 1998, **270**, 194-202.
213. J. Bloch, *Journal of Alloys and Compounds*, 2000, **312**, 135-153.
214. J. Bloch and M. H. Mintz, *Journal of Alloys and Compounds*, 1997, **253–254**, 529-541.
215. S. Suda, N. Kobayashi and K. Yoshida, *Journal of the Less Common Metals*, 1980, **73**, 119-126.
216. I. E. Gabis, A. P. Voit, E. A. Evard, Y. V. Zaika, I. A. Chernov and V. A. Yartys, *Journal of Alloys and Compounds*, 2005, **404–406**, 312-316.
217. N. Koga and J. M. Criado, *Journal of the American Ceramic Society*, 1998, **81**, 2901-2909.
218. H. Sasaki, *Journal of the American Ceramic Society*, 1964, **47**, 512-516.
219. U. Bösenberg, J. W. Kim, D. Gosslar, N. Eigen, T. R. Jensen, J. M. B. von Colbe, Y. Zhou, M. Dahms, D. H. Kim, R. Günther, Y. W. Cho, K. H. Oh, T. Klassen, R. Bormann and M. Dornheim, *Acta Materialia*, 2010, **58**, 3381-3389.
220. D. G. McCartney, *International Materials Reviews*, 1989, **34**, 247-260.
221. P. M. Kelly and M. X. Zhang, *Metall and Mat Trans A*, 2006, **37**, 833-839.
222. M. X. Zhang and P. M. Kelly, *Scripta Materialia*, 2005, **52**, 963-968.
223. C. B. Minella, C. Pistidda, S. Garroni, P. Nolis, M. D. Baró, O. Gutfleisch, T. Klassen, R. Bormann and M. Dornheim, *The Journal of Physical Chemistry C*, 2013, **117**, 3846-3852.
224. M. X. Zhang and P. M. Kelly, *Acta Materialia*, 2005, **53**, 1073-1084.
225. E. Deprez, A. Justo, T. C. Rojas, C. López-Cartés, C. Bonatto Minella, U. Bösenberg, M. Dornheim, R. Bormann and A. Fernández, *Acta Materialia*, 2010, **58**, 5683-5694.
226. E. Deprez, M. A. Muñoz-Márquez, M. A. Roldán, C. Prestipino, F. J. Palomares, C. B. Minella, U. Bösenberg, M. Dornheim, R. Bormann and A. Fernández, *The Journal of Physical Chemistry C*, 2010, **114**, 3309-3317.
227. E. Deprez, M. A. Muñoz-Márquez, M. C. Jimenez de Haro, F. J. Palomares, F. Soria, M. Dornheim, R. Bormann and A. Fernández, *Journal of Applied Physics*, 2011, **109**, 014913.
228. C. S. Smith, *Journal Name: Metals Technology; Journal Volume: Vol: 15, No. 4; Other Information: AIME Technical Publication 2387. Orig. Receipt Date: 31-DEC-48*, 1948, Medium: X; Size: Pages: 37.
229. E. Nes, N. Ryum and O. Hunderi, *Acta Metallurgica*, 1985, **33**, 11-22.
230. W. M. Haynes, *CRC Handbook of Chemistry and Physics, 96th Edition*, CRC Press, 2015.
231. T. Zhang, S. Isobe, M. Matsuo, S.-i. Orimo, Y. Wang, N. Hashimoto and S. Ohnuki, *ACS Catalysis*, 2015, **5**, 1552-1555.
232. Y. Filinchuk, E. Rönnebro and D. Chandra, *Acta Materialia*, 2009, **57**, 732-738.
233. H. E. Kissinger, *Analytical Chemistry*, 1957, **29**, 1702-1706.
234. F. Gingl, F. Bonhomme, K. Yvon and P. Fischer, *Journal of Alloys and Compounds*, 1992, **185**, 273-278.
235. J.-F. Brice, A. Courtois and J. Aubry, *Journal of Solid State Chemistry*, 1978, **24**, 381-387.
236. J.-H. Kim, J.-H. Shim and Y. W. Cho, *Journal of Power Sources*, 2008, **181**, 140-143.

237. R. Gosalawit-Utke, K. Suarez, J. M. Bellosta von Colbe, U. Bösenberg, T. R. Jensen, Y. Cerenius, C. Bonatto Minella, C. Pistidda, G. Barkhordarian, M. Schulze, T. Klassen, R. d. Bormann and M. Dornheim, *The Journal of Physical Chemistry C*, 2011, **115**, 3762-3768.
238. M. Paskevicius, M. B. Ley, D. A. Sheppard, T. R. Jensen and C. E. Buckley, *Physical Chemistry Chemical Physics*, 2013, **15**, 19774-19789.
239. H. Grove, L. H. Rude, T. R. Jensen, M. Corno, P. Ugliengo, M. Baricco, M. H. Sorby and B. C. Hauback, *RSC Advances*, 2014, **4**, 4736-4742.
240. E. Deprez, M. A. Muñoz-Márquez, M. A. Roldán, C. Prestipino, F. J. Palomares, C. B. Minella, U. Bösenberg, M. Dornheim, R. Bormann and A. Fernández, *Journal of Physical Chemistry C*, 2010, **114**, 3309-3317.
241. U. Bösenberg, U. Vainio, P. K. Pranzas, J. M. Bellosta Von Colbe, G. Goerigk, E. Welter, M. Dornheim, A. Schreyer and R. Bormann, *Nanotechnology*, 2009, **20**.
242. H. Rietveld, *Acta Crystallographica*, 1966, **20**, 508-513.
243. L. Lutterotti, D. Chateigner, S. Ferrari and J. Ricote, *Thin Solid Films*, 2004, **450**, 34-41.
244. T. A. Baser, M. Baricco, S. Enzo, G. Vaughan and A. R. Yavari, *Journal of Materials Research*, 2008, **23**, 2166-2173.
245. C. J. Sparks, Jr., *Physical Review Letters*, 1974, **33**, 262-265.
246. J. Tulkki and T. Aberg, *Journal of Physics B: Atomic and Molecular Physics*, 1982, **15**, L435.
247. U. Vainio, K. Pirkkalainen, K. Kisko, G. Goerigk, N. E. Kotelnikova and R. Serimaa, *Eur. Phys. J. D*, 2007, **42**, 93-101.
248. I. B. J. Kohlbrecher, *http://kur.web.psi.ch/sans1/SANSsoft/sasfit.html*.
249. G. Goerigk and N. Mattern, *Acta Materialia*, 2009, **57**, 3652-3661.
250. G. F. A. Guinier, *Small-Angle Scattering of X-raxs*, John Wiley & Sons Inc., New York, 1955.
251. S. Haas, G. Zehl, I. Dorbandt, I. Manke, P. Bogdanoff, S. Fiechter and A. Hoell, *The Journal of Physical Chemistry C*, 2010, **114**, 22375-22384.
252. E. Deprez, A. Justo, T. C. Rojas, C. López-Cartés, C. Bonatto Minella, U. Bösenberg, M. Dornheim, R. Bormann and A. Fernández, *Acta Materialia*, 2010, **58**, 5683-5694.
253. M. D. Riktor, M. H. Sørby, J. Muller, E. G. Bardají, M. Fichtner and B. C. Hauback, *Journal of Alloys and Compounds*, 2015, **632**, 800-804.
254. Y. Luo, P. Wang, L.-P. Ma and H.-M. Cheng, *Journal of Alloys and Compounds*, 2008, **453**, 138-142.
255. K. Suarez-Alcantara, M. H. Sørby, C. Pistidda, F. Karimi, I. Saldan, B. C. Hauback, T. Klassen and M. Dornheim, *The Journal of Physical Chemistry C*, 2015, **119**, 11430-11437.
256. C. Pistidda, F. Karimi, S. Garroni, A. Rzeszutek, C. Bonatto Minella, C. Milanese, T. T. Le, L. H. Rude, J. Skibsted, T. R. Jensen, C. Horstmann, C. Gundlach, M. Tolkiehn, P. K. Pranzas, A. Schreyer, T. Klassen and M. Dornheim, *The Journal of Physical Chemistry C*, 2014, **118**, 28409-28417.
257. C. Suryanarayana, *Progress in Materials Science*, 2001, **46**, 1-184.
258. T. N. Kobayashi KF, Shingu PH., *J Mater Sci* 1990, 3149-3154.
259. M. B. Davis RM, Koch CC., *Metall Trans* 1988, 2867-2874.
260. A. Bassetti, E. Bonetti, L. Pasquini, A. Montone, J. Grbovic and M. Vittori Antisari, *The European Physical Journal B - Condensed Matter and Complex Systems*, 2005, **43**, 19-27.
261. Q. Gu, G. Krauss and W. Steurer, *Advanced Materials*, 2008, **20**, 3620-3626.
262. A. H. Üçisik and C. Bindal, *Surface and Coatings Technology*, 1997, **94–95**, 561-565.
263. S. Otani, M. M. Korsukova and T. Mitsuhashi, *Journal of Crystal Growth*, 1998, **194**, 430-433.
264. Y. Wang, H. Y. Wang, Y. F. Yang and Q. C. Jiang, *Materials Science and Engineering: A*, 2008, **478**, 9-15.
265. J. L. Bobet, C. Even, Y. Nakamura, E. Akiba and B. Darriet, *Journal of Alloys and Compounds*, 2000, **298**, 279-284.

266. N. Busch, J. Jepsen, C. Pistidda, J. A. Puszkiel, F. Karimi, C. Milanese, M. Tolkiehn, A.-L. Chaudhary, T. Klassen and M. Dornheim, *Journal of Alloys and Compounds*, 2015, **645, Supplement 1**, S299-S303.
267. T. N. W. Qin, and Y. Umakoshi *J. Appl. Phys.*, 2007, 124303.
268. Z. Li, H. Hahn and R. W. Siegel, *Materials Letters*, 1988, **6**, 342-346.
269. P. M. Kelly and M. X. Zhang, *Scripta Materialia*, 2005, **52**, 679-682.
270. F. von Zeppelin, M. Hirscher, H. Stanzick and J. Banhart, *Composites Science and Technology*, 2003, **63**, 2293-2300.
271. C. Pistidda, G. Barkhordarian, A. Rzeszutek, S. Garroni, C. B. Minella, M. D. Baró, P. Nolis, R. Bormann, T. Klassen and M. Dornheim, *Scripta Materialia*, 2011, **64**, 1035-1038.
272. C. Pistidda, D. Pottmaier, F. Karimi, S. Garroni, A. Rzeszutek, M. Tolkiehn, M. Fichtner, W. Lohstroh, M. Baricco, T. Klassen and M. Dornheim, *International Journal of Hydrogen Energy*, 2014, **39**, 5030-5036.
273. Y. Kim, S.-J. Hwang, J.-H. Shim, Y.-S. Lee, H. N. Han and Y. W. Cho, *The Journal of Physical Chemistry C*, 2012, **116**, 4330-4334.
274. E. Rönnebro and E. H. Majzoub, *The Journal of Physical Chemistry B*, 2007, **111**, 12045-12047.
275. J.-H. Kim, S.-A. Jin, J.-H. Shim and Y. W. Cho, *Scripta Materialia*, 2008, **58**, 481-483.
276. Y. Kim, S.-J. Hwang, Y.-S. Lee, J.-Y. Suh, H. N. Han and Y. W. Cho, *The Journal of Physical Chemistry C*, 2012, **116**, 25715-25720.
277. Y. Yan, A. Remhof, D. Rentsch, A. Zuttel, S. Giri and P. Jena, *Chemical Communications*, 2015, **51**, 11008-11011.
278. K.-B. Kim, J.-H. Shim, K. H. Oh and Y. W. Cho, *The Journal of Physical Chemistry C*, 2013, **117**, 8028-8031.
279. G. Barkhordarian, T. R. Jensen, S. Doppiu, U. Bösenberg, A. Borgschulte, R. Gremaud, Y. Cerenius, M. Dornheim, T. Klassen and R. Bormann, *The Journal of Physical Chemistry C*, 2008, **112**, 2743-2749.
280. S. V. Alapati, J. K. Johnson and D. S. Sholl, *The Journal of Physical Chemistry C*, 2007, **111**, 1584-1591.
281. S. Shang, T. Wang and Z.-K. Liu, *Calphad*, 2007, **31**, 286-291.
282. Z.-K. Liu, Y. Zhong, D. G. Schlom, X. X. Xi and Q. Li, *Calphad*, 2001, **25**, 299-303.
283. Z. Dehouche, R. Djaozandry, J. Goyette and T. K. Bose, *Journal of Alloys and Compounds*, 1999, **288**, 269-276.
284. C. Pistidda, PhD, Technischen Universität Hamburg-Harburg, 2011.
285. U. Bösenberg, D. B. Ravnsbæk, H. Hagemann, V. D’Anna, C. B. Minella, C. Pistidda, W. van Beek, T. R. Jensen, R. Bormann and M. Dornheim, *The Journal of Physical Chemistry C*, 2010, **114**, 15212-15217.
286. F. Cova, E. C. E. Rönnebro, Y. J. Choi, F. C. Gennari and P. A. Larochette, *The Journal of Physical Chemistry C*, 2015, **119**, 15816-15822.
287. J.-H. Shim, J.-H. Lim, S.-u. Rather, Y.-S. Lee, D. Reed, Y. Kim, D. Book and Y. W. Cho, *The Journal of Physical Chemistry Letters*, 2010, **1**, 59-63.
288. C. Pistidda, G. Barkhordarian, A. Rzeszutek, S. Garroni, C. B. Minella, M. D. Baró, P. Nolis, R. Bormann, T. Klassen and M. Dornheim, *Scripta Materialia*, 2011, **64**, 1035-1038.
289. S. Garroni, C. Pistidda, M. Brunelli, G. B. M. Vaughan, S. Suriñach and M. D. Baró, *Scripta Materialia*, 2009, **60**, 1129-1132.
290. D. Pottmaier, C. Pistidda, E. Groppo, S. Bordiga, G. Spoto, M. Dornheim and M. Baricco, *International Journal of Hydrogen Energy*, 2011, **36**, 7891-7896.
291. J. F. Mao, X. B. Yu, Z. P. Guo, H. K. Liu, Z. Wu and J. Ni, *Journal of Alloys and Compounds*, 2009, **479**, 619-623.
292. K. Ikeda, Y. Nakamori and S. Orimo, *Acta Materialia*, 2005, **53**, 3453-3457.
293. D. Pottmaier, E. R. Pinatel, J. G. Vitillo, S. Garroni, M. Orlova, M. D. Baró, G. B. M. Vaughan, M. Fichtner, W. Lohstroh and M. Baricco, *Chemistry of Materials*, 2011, **23**, 2317-2326.

294. D. A. Sheppard, M. Paskevicius and C. E. Buckley, *Chemistry of Materials*, 2011, **23**, 4298-4300.
295. C. Pistidda, S. Garroni, C. B. Minella, F. Dolci, T. R. Jensen, P. Nolis, U. Bösenberg, Y. Cerenius, W. Lohstroh, M. Fichtner, M. D. Baró, R. Bormann and M. Dornheim, *The Journal of Physical Chemistry C*, 2010, **114**, 21816-21823.
296. A. Fernández, E. Deprez and O. Friedrichs, *International Journal of Hydrogen Energy*, 2011, **36**, 3932-3940.
297. C. C. Nwakwuo, C. Pistidda, M. Dornheim, J. L. Hutchison and J. M. Sykes, *International Journal of Hydrogen Energy*, 2012, **37**, 2382-2387.
298. S. Kato, A. Borgschulte, D. Ferri, M. Bielmann, J.-C. Crivello, D. Wiedenmann, M. Parlinska-Wojtan, P. Rossbach, Y. Lu, A. Remhof and A. Zuttel, *Physical Chemistry Chemical Physics*, 2012, **14**, 5518-5526.
299. S. Kato, M. Bielmann, K. Ikeda, S.-i. Orimo, A. Borgschulte and A. Züttel, *Applied Physics Letters*, 2010, **96**, 051912.
300. L. Zeng, H. Miyaoka, T. Ichikawa and Y. Kojima, *The Journal of Physical Chemistry C*, 2010, **114**, 13132-13135.
301. D. Pottmaier, S. Garroni, M. Brunelli, G. B. M. Vaughan, A. Castellero, E. Menéndez, M. D. Baró and M. Baricco, *MRS Proceedings*, 2010, **1262**.
302. O. Friedrichs, A. Remhof, A. Borgschulte, F. Buchter, S. I. Orimo and A. Zuttel, *Physical Chemistry Chemical Physics*, 2010, **12**, 10919-10922.
303. http://hydrogendoedev.nrel.gov/pdfs/progress09/iv_a_1n_reiter.pdf.
304. K.-B. Kim, J.-H. Shim, S.-H. Park, I.-S. Choi, K. H. Oh and Y. W. Cho, *The Journal of Physical Chemistry C*, 2015, **119**, 9714-9720.
305. H.-W. Li, E. Akiba and S.-i. Orimo, *Journal of Alloys and Compounds*, 2013, **580, Supplement 1**, S292-S295.
306. C. J. Sahle, C. Sternemann, C. Giacobbe, Y. Yan, C. Weis, M. Harder, Y. Forov, G. Spiekermann, M. Tolan, M. Krisch and A. Remhof, *Physical Chemistry Chemical Physics*, 2016, **18**, 19866-19872.
307. J. Mao, Z. Guo, X. Yu and H. Liu, *International Journal of Hydrogen Energy*, 2013, **38**, 3650-3660.
308. Y. Yan, H.-W. Li, H. Maekawa, K. Miwa, S.-i. Towata and S.-i. Orimo, *The Journal of Physical Chemistry C*, 2011, **115**, 19419-19423.
309. P. Mauron, M. Bielmann, A. Remhof, A. Züttel, J.-H. Shim and Y. W. Cho, *The Journal of Physical Chemistry C*, 2010, **114**, 16801-16805.
310. H. Shao, M. Felderhoff and C. Weidenthaler, *The Journal of Physical Chemistry C*, 2015, **119**, 2341-2348.
311. S.-A. Jin, Y.-S. Lee, J.-H. Shim and Y. W. Cho, *The Journal of Physical Chemistry C*, 2008, **112**, 9520-9524.

Acknowledgments

I am grateful to Prof. A. Schreyer and Prof. T. Klassen, who gave me the opportunity to work in their groups on the highly exiting fields of structure analysis and metal hydride system for energy storage. Also I am thankful to Dr. P. K. Pranzas and Dr. M. Dornheim for their guidance throughout this work. I sincerely thank Dr. A. Hoell, from whom I have not only learned a lot about science. I am thankful to Dr. Ulla Vainio, for introducing me to SAXS and ASAXS methods, and for those wonderful and pleasant discussion and conversations aside the work. Also I am obligated to express my appreciation to Dr. T. Emmler, who introduced me to NMR method.

I owe many thanks to Dr. Julián A. Puszkiel and his wonderful wife Dr. María V. C. Riglos for their persistent support during the spectroscopy- and microscopy measurements. I have to thank Dr. C. Pistidda for his constant help during the *in situ* SR-XPD measurements and for his constructive scientific discussions. I genuinely appreciate the enjoyable scientific- and non-scientific discussions with Dr. Antonio Santoru along this work.

Many results of this work would have been not accomplished without collaboration with Prof. C. Milanese and Prof. T. Jensen. Therefore, I want to speak my deepest gratitude to both of them and their co-workers, and to all of those who contributed to this work but who I do not remember at the moment.

Lastly, I want to thank my family for their endless support and patience.